

Optimized design of magnetic septa for the Future Circular Collider

Citation for published version (APA):

Sanz Ull, A. (2019). Optimized design of magnetic septa for the Future Circular Collider Eindhoven: Technische Universiteit Eindhoven

Document status and date:

Published: 14/06/2019

Document Version:

Publisher's PDF, also known as Version of Record (includes final page, issue and volume numbers)

Please check the document version of this publication:

- A submitted manuscript is the version of the article upon submission and before peer-review. There can be important differences between the submitted version and the official published version of record. People interested in the research are advised to contact the author for the final version of the publication, or visit the DOI to the publisher's website.
- The final author version and the galley proof are versions of the publication after peer review.
- The final published version features the final layout of the paper including the volume, issue and page numbers.

[Link to publication](#)

General rights

Copyright and moral rights for the publications made accessible in the public portal are retained by the authors and/or other copyright owners and it is a condition of accessing publications that users recognise and abide by the legal requirements associated with these rights.

- Users may download and print one copy of any publication from the public portal for the purpose of private study or research.
- You may not further distribute the material or use it for any profit-making activity or commercial gain
- You may freely distribute the URL identifying the publication in the public portal.

If the publication is distributed under the terms of Article 25fa of the Dutch Copyright Act, indicated by the "Taverne" license above, please follow below link for the End User Agreement:

www.tue.nl/taverne

Take down policy

If you believe that this document breaches copyright please contact us at:

openaccess@tue.nl

providing details and we will investigate your claim.

Optimized design of magnetic septa for the Future Circular Collider

PROEFontWERP

ter verkrijging van de graad van doctor aan de Technische Universiteit
Eindhoven, op gezag van de rector magnificus prof.dr.ir. F.P.T. Baaijens,
voor een commissie aangewezen door het College voor Promoties, in het
openbaar te verdedigen op vrijdag 14 juni 2019 om 13.30 uur

door

Alejandro Sanz Ull

geboren te Madrid, Spanje

De documentatie van het proefontwerp is goedgekeurd door de promotoren en de samenstelling van de promotiecommissie is als volgt:

voorzitter:	prof.dr.ir. G.M.W. Kroesen
1 ^e promotor:	prof.dr.ir. O.J. Luiten
copromotor:	dr. W. Bartmann (CERN)
leden:	prof.dr. E.A. Lomonova
	prof.dr. N.J. Lopes Cardozo
	prof.dr. S. Stapnes (CERN, Universitetet i Oslo)
adviseur(s):	ir. J. Borburgh (CERN)
	dr. J.I.M. Botman

Het onderzoek of ontwerp dat in dit proefontwerp wordt beschreven is uitgevoerd in overeenstemming met de TU/e Gedragscode Wetenschapsbeoefening.

Optimized design of magnetic septa for the Future Circular Collider

Cover picture: Alejandro Sanz Ull.

A catalogue record is available from the Eindhoven University of Technology Library

ISBN: 978-90-386-4779-1.

Contents

1	Introduction	7
1.1	Motivation of the FCC study and overview of alternatives . . .	7
1.1.1	Brief description of the FCC-hh	10
1.1.2	Brief description of the FCC-hh parameters	11
1.1.3	Injection and extraction requirements	13
1.2	Description of the relevant accelerator parameters	15
1.2.1	Energy	15
1.2.2	Luminosity and emittance	15
1.3	Motivation and structure of this thesis	17
2	Septa catalog	21
2.1	Introduction	21
2.2	Different septa topologies	22
2.2.1	Electrostatic septa	24
2.2.2	Magnetic septa	25
2.2.3	Comparison between electrostatic and magnetic septa .	27
2.3	Description of representative electrostatic septa	29
2.3.1	The 50 GeV electrostatic septum at J-PARC	29
2.3.2	The ZS septum at CERN	31
2.3.3	The SEH23 septum	34
2.4	Description of magnetic septa families	35
2.4.1	Direct drive DC and pulsed septa	35
2.4.2	Eddy current septa	48
2.4.3	Lambertson septa	55
2.4.4	Massless septa	59
2.4.5	Opposite fields septa	61
2.4.6	Permanent magnet septa	65
2.4.7	Superconducting septa	66

2.4.8	A semianalytical method for coil placement in septa . .	76
2.5	Figure of merit	80
3	Lambertson septa	85
3.1	Introduction	85
3.2	ISR Lambertson septa	85
3.3	LHC Lambertson septa description	88
3.3.1	LHC MSI description	88
3.3.2	LHC MSD description	91
3.4	LHC Lambertson septa scaled for the FCC	92
3.4.1	Finding the limiting factor of the existing Lambertson septas	92
3.4.2	Using an unique family of Lambertson septa at the FCC extraction system	99
3.5	Lambertson modifications in 2D	101
3.5.1	Double orbiting beam gap alternative	101
3.5.2	Reducing the leak field by changing the shape of the orbiting beam gap	104
3.5.3	Reducing the leak field by adding high saturation materials	107
3.5.4	Reducing the leak field by adding compensation coils . .	111
3.5.5	Reducing the leak field by adding permanent magnets .	117
3.6	Super ferric design	120
3.7	Figure of merit applied to the Lambertson topology	121
4	Massless septa	123
4.1	Introduction	123
4.2	Pacman septum	123
4.2.1	Introduction	123
4.2.2	Optimization	125
4.2.3	Comparison with Iwashita and Yonemura septa	131
4.3	RF compensation and resonant mode selection	138
4.3.1	RF cavity feasibility	142
4.3.2	Preliminary estimation of the parameters of a pillbox cavity with the required field map	143
4.3.3	Effect of the massless septum and the RF compensation on the orbiting beam	144
4.4	Double massless septum for injection protection	147
4.4.1	Concept	147
4.4.2	Comparison between ideal and real septum field	149
4.4.3	Feasibility	151

4.5	Conclusion	152
5	Truncated Cosine θ septum	153
5.1	Introduction	153
5.1.1	Pure multipoles produced by Cosine θ current distributions	153
5.2	2D design	158
5.2.1	Magnetic design	162
5.2.2	Mechanical design	174
5.3	3D design of the coil ends	181
5.3.1	Magnetic design	182
5.3.2	Mechanical validation	187
5.4	Figure of Merit for the Truncated Cosine θ septum	191
5.5	Conclusions and future work	191
6	Layout optimization	195
6.1	Introduction	195
6.1.1	Figure of merit of different septa topologies presented .	196
6.2	Beam size and beam centre	196
6.2.1	Quench protection	199
6.3	Septa layout in the straight section	200
6.3.1	Septa location with one septum family	201
6.3.2	Derivation of the optimum number of magnet families .	206
6.3.3	Optimization of the injection septa	209
6.3.4	Optimization of the extraction septa	221
6.4	Summary and further studies	233
7	Leak field effects	235
7.1	Introduction	235
7.2	Determination of the permissible leak field	235
7.2.1	Determining the maximum permissible leak field from the emittance growth	235
7.2.2	Determining the maximum allowed leak field from the beam rigidity	237
7.2.3	Adopted method	239
7.3	Leak field of the Lambertson septa	239
7.4	Leak field of the SuShi septum	240
7.5	Leak field of Truncated Cosine θ septum	240
7.6	Conclusions	241

8	Conclusions and future work	243
8.1	Summary	243
8.2	Conclusions and future work	246
A	The finite difference method applied to charged particle tracking	249
A.1	The finite difference method	249
A.2	Application of the finite difference method to charged particle tracking	252
B	Analytical estimation stresses and brief description of the Finite Element validation	255
B.1	2D mechanical analysis	255
B.2	3D mechanical analysis	258
B.3	Inductance calculation	261
	Curriculum Vitae	283
	Publication list	286
	Acknowledgements	288

Chapter 1

Introduction

1.1 Motivation of the FCC study and overview of alternatives

The discovery of the Higgs boson at the Large Hadron Collider (LHC) in 2012 marked an important milestone in particle physics and it provided confirmation of one of the cornerstones of the Standard Model of physics. However, it did not answer all the open issues in the Standard Model and it also opened many new questions. The LHC and High-Luminosity LHC (HL-LHC) will continue to explore the 14 TeV energy region with the goal of testing and confirming the Standard Model and finding new physics beyond the Standard Model [1, 2, 3, 4]. Additionally, prior to the start of the LHC, the situation where the Higgs boson would be found and no discrepancy within the standard model would be discovered was named "the nightmare scenario". The LHC has been incredibly successful in the sense that it made the main discovery it was designed to do at the beginning of its life, and this discovery fit the theory very precisely. With the current physics knowledge, it seems that no new major discoveries are within the LHC energy reach. However, a deeper understanding of the open questions in physics, such as the details of the Higgs mechanism and discoveries on supersymmetry, dark matter, the matter-antimatter asymmetry and the origin of the neutrino masses may be found at higher energies or with a higher precision machine [5, 6, 7]. From the scientific point of view, a new particle collider would produce new discoveries about the fundamental structure of matter and the universe. From past experience, taking into account the timescale of the design and construction of a particle

1.1. MOTIVATION OF THE FCC STUDY AND OVERVIEW OF ALTERNATIVES

collider of this magnitude will most likely take at least two decades, so it is necessary to start designing the machine now in order to start operating at the end of the LHC life.

The European Strategy for Particle Physics (ESPP) stated in 2013: *"To stay at the forefront of particle physics, Europe needs to be in a position to propose an ambitious post-LHC accelerator project at CERN by the time of the next Strategy update"*. The FCC study implements this recommendation by developing a long term program for an accelerator project. The most promising approach is to first build a technology ready, high-intensity lepton collider (FCC-ee), followed by a high energy collider (FCC-hh). These two projects are described in the following paragraphs. This two stage approach has the advantage that the technology required to build FCC-hh can be developed while FCC-ee is built and exploited. These two colliders together, and possibly a third stage colliding protons and electrons (FCC-he), would provide the highest socio-economic impact for science and society, especially if they are combined with other complementary studies, like the neutrino experiments being carried out or planned in Japan and the U.S. Additionally, the staged approach allows to base new design choices of the second stage on results obtained from the first [5].

Ultimately, the impact that the construction of the FCC-ee and FCC-he would have in society can be divided into several categories or communities. For particle physicists, the scientific programme addresses most of the open questions in high-energy physics. Theorists would also be concerned given that very detailed and challenging calculations are needed. Detector designers would have the challenge and the opportunity to develop versatile devices for many different studies. This could also attract scientists and engineers from other fields. In the field of accelerator physics, the interest lies in new developments in automatic operation, luminosity optimization and simultaneous operation of the FCC and the injectors, including all the associated experiments. Other scientific communities, for example astrophysicists, would benefit from the discoveries and new questions produced by the FCC, opening opportunities for collaboration.

The FCC will fuel the development of high-field superconductors and possibly the so-called high-temperature superconductors, allowing to design higher field magnets which will in turn allow to design higher energy colliders. Such a collider would also require developments in cryogenic cooling and high efficiency in grid to RF power conversion. Additionally the FCC would be a great incentive to develop new technologies in material science, surface treatment and finishing, high-efficiency medium voltage DC conversion and transport, energy recovery, communication technologies and data storage and processing.

High performance data analysis and high-speed electronics will be necessary to process the enormous amount of data that will produce, most likely involving new technologies like artificial intelligence. Additionally, advances are required in civil engineering, specifically in tunnelling technology and material recovery. All these technologies are susceptible to be developed in collaboration with industry and would provide a direct and almost immediate benefit for society. Finally, the FCC project allows immense opportunities for training of teachers and students at master, doctorate and post-doc level [5]. For all these reasons, there is a clear interest for society to build the FCC.

There are currently two clear research directions to address the current challenges and questions in High Energy Physics. One of them is to build a particle collider at the energy frontier, to produce heavier particles that have not yet been detected. On the other hand, a machine at the precision frontier would allow to study already known interactions with a higher detail, due to the small background noise produced in the collisions.

The physics case for a hadron collider in the range of 100 TeV is clear in the long term, however, it is not yet clear which is the best way to reach this goal. It may be more interesting to build a lepton collider or a hadron collider with an energy reach between the LHC and the Future Circular Collider (FCC). The decision will be supported by the findings of Run 2 of the LHC and other experiments in the near future. However, it is clear that with the current plan of the HL-LHC, which is scheduled to finish operation in 2036, it is necessary to study and plan the successor of the LHC [8]. A conceptual design report (CDR) of the FCC study is due to be published in the end of 2019, and it will be one of the inputs to the next ESPP in 2020.

If the approach taken is to build a high precision collider, there are two alternatives. It is possible to choose a circular collider or a linear collider. FCC-ee would be a circular electron-positron collider with a collision energy of up to 365 GeV [9] and the Chinese electron-positron Collider (CEPC) would reach a collision energy of 240 GeV [10]. The Compact Linear Collider (CLIC) and the International Linear Collider (ILC) are the two major studies in the field of linear lepton colliders. CLIC would reach an energy of up to 3 TeV, to be reached in three steps, and with a length between 11 km for the initial 500 GeV and 50 km for the final 3 TeV stage. ILC is an option with an energy reach of 250 GeV and possibly a future upgrade to 500 GeV[11, 11]. Both CLIC and ILC would allow to conduct high precision experiments in the LHC energy range.

If it is decided to build a collider in the energy frontier, the two main studies are the FCC-hh, which would produce hadron-hadron collisions and the Chinese Super proton-proton Collider (SppC) [10, 12]. Both colliders are

planned to reach a centre of mass (c.m.) of 100 TeV. The exact location of the SppC has not been decided yet and the FCC-hh would be located in the Geneva area. The FCC-hh will be described in more detail in section 1.1.1.

1.1.1 Brief description of the FCC-hh

The FCC project is a proposal for a new 100 TeV hadron collider in the Geneva area. The study presents three variants, as a proton-proton collider, electron-positron collider and proton-electron collider, named FCC-hh, FCC-ee and FCC-he respectively. In the FCC-hh case, the CERN accelerator complex will be used to inject particles into the FCC. For FCC-ee and FCC-he, new injectors are needed. FCC-he is an alternative in which collisions are produced between hadrons and electrons. The most challenging septa type from the magnetic strength point of view is the FCC-hh due to the enormous beam rigidity that will be achieved by the proton beam, and thus this thesis will focus on FCC-hh, which sometimes is referred to as FCC proton-proton or FCC-pp. The three variants have become more stages than alternatives with time, although the project is still at an early stage to state this with total certainty and at this moment it is not possible to confirm which of the three variants would be built first, given the case.

A schematic of the proposed FCC layout within the Geneva region is presented in figure 1.1.

The FCC is planned to have four different experiments set around the collider rings. Two of them will feature general purpose detectors and will be located on opposite ends of a diameter because of lattice symmetry and integration with experimental regions. They would be the two high luminosity experiments, following the same principle as with ATLAS and CMS in the LHC. Although the goal of both of them will be the same, the technology and detector design will be different in each case. There will be two additional experiments with a more specialized purpose, such as ALICE and LHCb in the LHC [13, 14, 15, 16]. These two experiments in principle, would operate at a lower luminosity than the other two.

Both the LHC and the FCC are circular colliders. A collider is a particular case of a synchrotron, or circular accelerator with constant radius. In a synchrotron, the energy of the particle beam is increased in steps, adding energy to the particle beam at specific points in the collider while the magnetic field of the main bending magnets is increased simultaneously.

Once the particles have reached their final energy, they are extracted and used for experiments or any other purpose. In the case of a circular collider, there are two particle beams which travel in opposite directions. These par-

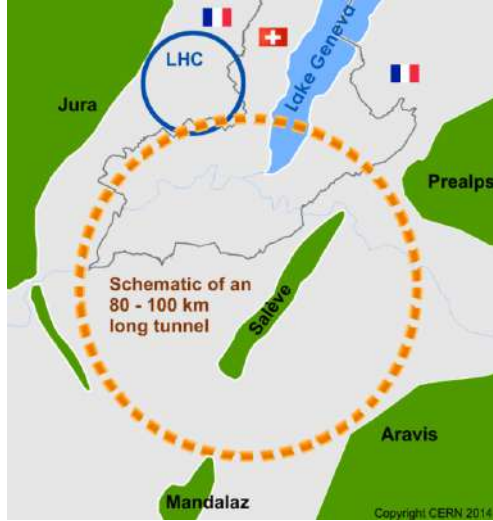


Figure 1.1: FCC layout schematic

ticles are accelerated and they are collided at certain points, usually in the centre of the different detectors. It is possible to have the beams circulating in the same vacuum chamber, although in the LHC and in the FCC there are two different vacuum chambers, one for each beam, and the beams only cross in the interaction point. This is illustrated in figure 1.2 for the case of the LHC. A similar image for the FCC is not available at this moment. The four experiments are also shown in the schematic, with the crossing of the beams and the injection and extraction points in each ring. If the LHC is used as an injector to the FCC, this layout schematic will change while the FCC will maintain the same layout. The injection layout is shown in figure 1.3. The beam will be injected at two different points between two experiments. This layout allows to inject both beams from the outer side of the collider, as shown in figure 1.3, in which the different letters A, B and L show the different straight sections of the planned layout.

1.1.2 Brief description of the FCC-hh parameters

The main beam parameters of FCC-hh are shown in table 1.1. The information of the High Luminosity LHC (HL-LHC) has been included for comparison. The

1.1. MOTIVATION OF THE FCC STUDY AND OVERVIEW OF ALTERNATIVES

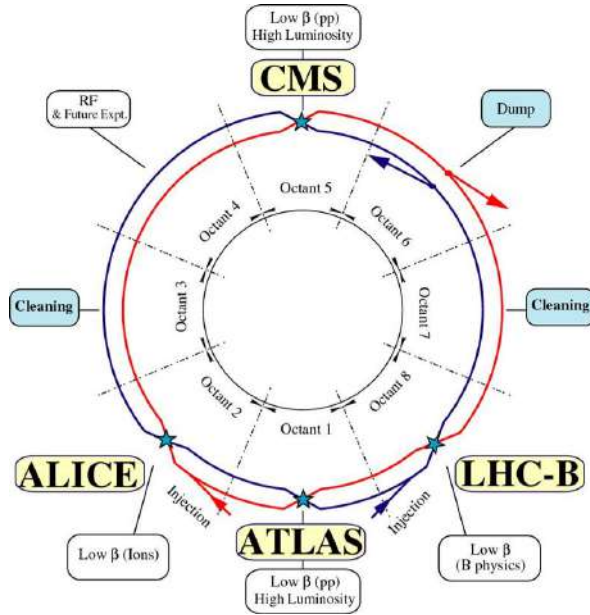


Figure 1.2: LHC layout schematic

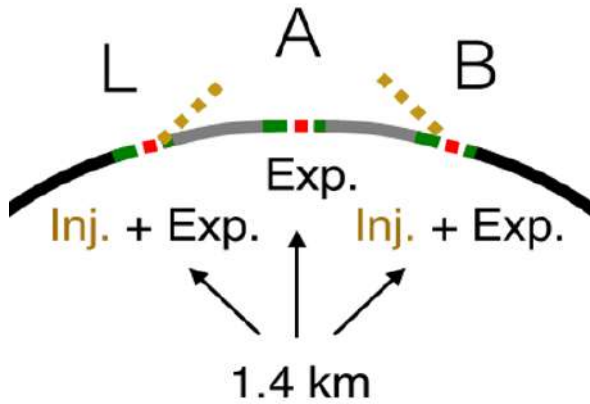


Figure 1.3: FCC injection layout

HL-LHC is the upgrade of the LHC which will provide an integrated luminosity higher than the LHC. It is scheduled to start operating in 2025 [1, 3]. Further information on the FCC study and ongoing R&D areas can be found in [17, 18, 19, 20, 21]. A brief description of the normalized emittance and the luminosity can be found in section 1.2.2.

Table 1.1: Main beam parameters of FCC-hh

Parameter	unit	FCC-hh	HE-LHC	LHC
Collision energy	TeV	100	27	14
Dipole field	T	16	16	8.33
Circumference	km	97.75	26.7	26.7
Beam current	A	0.5	1.1	0.58
Protons per bunch	10^{11}	1	2.2	1.15
Time between bunches	ns	25	25	25
Normalized emittance	μm	2.2	2.5	3.75
Luminosity	$10^{34} \text{ cm}^{-2} \text{ s}^{-1}$	5	5	1
Beam energy	GJ	8.4	0.7	0.36

1.1.3 Injection and extraction requirements

To either inject a beam into or to extract it from a storage ring, kicker magnets are usually employed. However, the extreme beam rigidity of high-energy beams in particle colliders, in particular the rigidity of hadron beams, requires extremely strong pulsed "kicking" fields to impart a sufficiently large deflection angle to be able to merge a particle bunch into or take it out of the storage ring orbit in a controlled way over a reasonable length. In fact the required pulsed field strengths cannot be realized in practice. For this reason so-called (electrostatic or magnetic) septum modules (septa for short) are employed. Septum is a Latin word indicating a partition or a wall between two chambers. A septum in a storage ring is a sharp division between a low-field region (ideally zero) and a high-field region (ideally uniform). During normal operation the beam in the storage ring travels through the low-field region, ideally unperturbed. If, for instance, the beam has to be dumped, a kicker magnet will deflect the orbiting beam by a small angle, pushing it into the high-field region of the septum magnet downstream. In the high field region the deflection angle will be amplified significantly, allowing the beam to be extracted over a relatively short length. The septum module thus acts as a static amplifier of the pulsed kicker magnet. Clearly, septum modules are essential for accelerator operation,

1.1. MOTIVATION OF THE FCC STUDY AND OVERVIEW OF ALTERNATIVES

not in the least because of safety. The importance of the design and development of reliable septum modules can therefore hardly be overstated. The fundamental design challenges are immediately clear: the field in the high-field region should be as high and uniform as possible, the field in the low-field region should perturb the orbiting beam in the storage ring minimally, and the separation between the two, the septum (blade), should be as thin as possible, and also robust against activation and damage by the high-energy particle beam sweeping through during injection or extraction. The septum blade is named in this way because it may slice the orbiting beam, either intentionally or not.

For FCC-hh the baseline injection energy is 3.3 TeV. Although the fields needed for injection are achievable with normal conducting magnets, the main challenge of the injection system lies in obtaining a design with a small septum thickness and very low leak field to avoid emittance growth, which will be explained in later chapters.

The beam parameters at injection and extraction are summarized in table 1.2 and the injection and extraction septa parameters are presented in table 1.3.

Table 1.2: Beam parameters of FCC injection and extraction.

Beam parameters	Unit	Injection	Extraction
Kinetic energy	TeV	3.3	50
Magnetic rigidity	T.m	11011	166785
# bunches	-	10400	10400
Transverse emittances	μm	2.2	2.2
Total beam energy	GJ	0.56	8.5

Table 1.3: Baseline parameters of FCC injection and extraction septa.

Hardware parameters	Unit	Injection	Extraction
Deflection	mrad	9.8	1.15
Integrated field	T.m	92	204
Physical magnet length	m	104	184
Magnetic length	m	84	146
GFR inj. beam h/v (radius)	mm	9/-	23/19
Beam stay clear circ. beam h/v (radius)	mm	9/14 (first unit)	-
Septum thickness (first unit)	mm	8	25

1.2 Description of the relevant accelerator parameters

1.2.1 Energy

It is arguably much simpler to build a synchrotron rather than a particle collider. Having two beams circulating at the same time poses significant constraints in all aspects, such as operations, magnet design, beam crossings, and beam-beam effects. However, the energy reach of a synchrotron with a given radius is significantly lower than the energy of a collider with the same radius. The energy reach in a collider is given by equation 1.1, where E_1 and E_2 are the kinetic energy of the beams and \vec{p}_1 and \vec{p}_2 are the momenta of the respective beams.

$$E_{cm} = \sqrt{(E_1 + E_2)^2 - (\vec{p}_1 + \vec{p}_2)^2 \cdot c^2} \quad (1.1)$$

In the case of a collider both momenta are equal with opposite signs, so the collision energy will be the addition of the kinetic energies.

$$E_{col} = E_1 + E_2 \quad (1.2)$$

If instead of a collider, the experiment is a fixed target, the collision energy becomes much smaller than in the case of the collider as the rest energy of a given particle is usually much smaller than the energy reached when the particle is accelerated up to a relativistic regime (E_1).

$$E_{FT} = \sqrt{2E_1 E_{rest} + 2E_{rest}^2} \approx \sqrt{2E_1 E_{rest}} \ll E_1 \quad (1.3)$$

1.2.2 Luminosity and emittance

Luminosity is one of the key figures to describe the performance of a particle collider. Qualitatively it expresses the rate of relevant events that can be produced at a collision point. It is the density of events per unit of time and transverse cross section. To calculate the luminosity it is necessary to compute some parameters, such as the beam size.

The beam sizes in each plane are given by equation 1.5. The parameters β_{rel} and γ_{rel} are the relativistic parameters, defined as:

$$\beta_{rel} = \frac{v}{c} \quad \gamma_{rel} = \sqrt{1 - \beta_{rel}^2} \quad (1.4)$$

1.2. DESCRIPTION OF THE RELEVANT ACCELERATOR PARAMETERS

$\beta_{x,y}(s)$ are the so called beta functions in the horizontal and vertical direction respectively. The beta function characterizes the beam size along the trajectory. It relates the outer beam envelope with the number of oscillations of a particle around the ideal orbit, and it is a consequence of the focusing action of quadrupoles. Therefore the beam size is determined by the beta function, which is determined by the quadrupole gradients. In other words, the beta function is a product of the boundaries that determine the beam movement, not of the beam itself [22].

The function $D_{x,y}(s)$ is the dispersion function and the term $\frac{\Delta p_{x,y}}{p_{x,y}}$ expresses the momentum spread. Off-momentum particles will oscillate around a closed orbit that is not the nominal one. This phenomenon is caused by an off-momentum particle travelling through a dipole. While a nominal particle will be deflected by the nominal magnetic field integral while it travels along the nominal trajectory, an off-momentum particle will travel a longer or shorter distance and will then be more deflected (or less) than it ideally should be. Its transverse position x can then be calculated by adding a small term to the nominal position, as shown in equation 1.6, where p is the nominal momentum and Δp is the momentum error.

$$\sigma_{x,y}(s) = \sqrt{\frac{\beta_{x,y}(s) \cdot \epsilon_{nx,y}}{\beta_{rel}\gamma_{rel}} + \left(D_{x,y}(s) \frac{\Delta p_{x,y}}{p_{x,y}}\right)^2} \quad (1.5)$$

$$x = x_{nom} + D(s) \frac{\Delta p}{p} \quad (1.6)$$

As usual, s is the longitudinal coordinate along the accelerator ring. This excess or defect in the transverse position translates in a different focusing length when the off-momentum particle reaches a quadrupole. Therefore, its orbit will not be the nominal one. Since $\beta(s)$ and $D(s)$ change along the trajectory of the particles, $\sigma(s)$ is also variable. For completeness, $D(s)$ can be calculated analytically by solving the dispersion equation, while an expression for $\beta(s)$ does not exist [23, 24].

The parameter $\epsilon_{nx,y}$ is the normalized emittance in the x and y axis. Beam quality can be expressed in terms of emittance. The so-called geometrical emittance $\epsilon_{x,y}$ is equal to the product of transverse beam size $\sigma_{x,y}$ and uncorrelated angular spread $\sigma_{\theta x,y}$. For a given beam energy (and assuming linear beam transport and conservative forces) it is a conserved quantity which is a measure for the "focusability" of the beam: the smaller the emittance, the tighter the beam can be focused for a given focusing angle. If the beam energy is increased, then the transverse beam angular spread $\sigma_{\theta x,y}$ automatically goes

down, leading to a decrease in geometrical emittance. This is called adiabatic damping. The so-called normalized emittance is defined as $\epsilon_{nx,y} \equiv \gamma_{rel} \beta_{rel} \epsilon_{x,y}$. The normalized emittance ϵ_{nx} is proportional to the $x-p_x$ phase space area of the beam (and analogously for the y -direction) and as such, it is a measure for beam quality that is Lorentz-invariant, i.e. Independent of the beam energy. The normalized emittance is therefore very convenient for comparing beams at different stages of acceleration.

Assuming that both beams have a gaussian profile, the luminosity is given by:

$$L = G_f \frac{n_b N_1 N_2 f_{rev}}{4\pi \sigma_x \sigma_y} \quad (1.7)$$

In equation 1.7, n_b is the number of bunches circulating in the machine. N_1 and N_2 are the number of particles per bunch and f_{rev} is the revolution frequency. σ_x and σ_y are the beam sizes of the particle distribution in the horizontal and vertical planes respectively. G_f is the geometrical reduction factor, which depends on the crossing angle of both beams. Although it lies outside the scope of this thesis, this angle is known as the Piwinski angle and more information can be found in [25].

It is seen that a smaller beam emittance will increase the luminosity of the collider, increasing also its efficiency. If the beam size is smaller, more particles are closer to the ideal orbit and therefore the probability of an interesting interaction increases and therefore one of the most important figures in a particle collider is the emittance.

The luminosity has units of $[\text{cm}^{-2} \text{ s}^{-1}]$ or $[\text{b}^{-1} \text{ s}^{-1}]$. There are then two lines of action to increase the luminosity of a given accelerator. The first one is to increase the number of particles per bunch and the number of bunches. Alternatively, it is also possible to increase the luminosity by reducing the beam size at the interaction point. Increasing the particle density at a given spot increases the probability of producing a relevant interaction. In the High-Luminosity LHC, the luminosity is increased by acting on both aspects [2].

1.3 Motivation and structure of this thesis

There are many challenging and open questions in the FCC study, one of the most outstanding being the beam dump system (BDS) due to its complexity and to the fact that it is essential to accelerator operation. In the past, only electrostatic septa or normal conducting septa have been used to inject or extract particles due to the relatively low beam energy achieved. However, at

an energy of 50 TeV per beam, the length needed for normal conducting septa, limited to a field of 2 T by the iron saturation, reaches up to 500 m. It is of interest then to investigate more compact and efficient septa topologies and the use of superconducting materials to achieve higher fields while maintaining a low septum thickness. Additionally, if the extraction septa are designed using normal conducting technology, their energy consumption would be too high, in the order of a few MW [17].

Although there are many different components in the BDS, the septa magnets are particularly suitable to be optimized due to the amount of magnets that will be required. A septum magnet is a special type of magnet which is characterized by having two different zones. There is a high-field region which will deflect the beam that is being injected or extracted and a zero field region, where the orbiting beam is located. The orbiting beam must not be perturbed by the magnetic field of the septum magnet. These two zones are separated by a septum or wall, which needs to be as thin as possible in order to relax the requirements on other beam transfer magnets and the required length of the straight section. A thin septum thickness also reduces the beam losses and the activation of the material.

The main challenge of the extraction septa is the enormous strength required at the highest energy level, which makes the use of electrostatic septa not possible. Alternatively, the magnetic strength of the injection septa is not so critical, given that the injection energy is 3.3 TeV, approximately half of the LHC extraction energy. The most critical magnitude at injection is repeatability and field quality, as this will have a direct impact on the luminosity and performance of the collider.

In chapter 2, a review of different septa topologies is required to determine the septa that may be suitable to be installed in the FCC and a figure of merit is proposed as a way of ranking the different septa types systematically. In chapter 3, the parameter space of Lambertson septa is explored and the limitations of this topology are found. The possibilities of massless septa are explored in chapter 4 and the requirements of a pillbox radiofrequency cavity are estimated. This cavity is used to compensate the leak field of the massless septa upstream. Particles are tracked along the longitudinal direction of the cavity to compute the effect of the cavity fields on the orbiting beam.

The superconducting Truncated Cosine θ topology is explored in chapter 5. Electromagnetic and mechanical simulations are carried out to study the effects of the coil ends in the leak field and to quantify the stresses in the septum blade.

Different layout alternatives are investigated in chapter 6. The septa layout of the injection and extraction region are optimized with the goal of reducing the number of magnets necessary and therefore the cost. A general method to

determine the optimum number of families is presented and a general analytical method to identify the most efficient variable to be changed in order to improve the layout of the septa.

The effect of the leak field in the orbiting beam is studied in chapter 7. The permissible leak field is quantified and two methods to determine the maximum permissible leak field are investigated. The first is based on the emittance growth caused by the leak field and the second takes into account the effect of the leak field on the orbiting beam using the beam rigidity. The first method is retained, based on experience with other accelerators.

Finally, future R&D directions are identified in chapter 8.

The charged particle tracking script developed to estimate the effect of the pillbox cavity in the particle beam is described in appendix A. Additional details of the multiphysics TCT septum model simulated in Opera 3D, including an estimation of the inductance, are given in appendix B.1. A short background on the finite element method applied to stress analysis is also included.

Chapter 2

Septa catalog

2.1 Introduction

An overview of the different septa topologies is given in this chapter. A general description of electrostatic and magnetic septa is given in sections 2.2.1 and 2.2.2 respectively. In section 2.2.3. A brief description of the main characteristics and constraints of a direct drive septum is given in section 2.4.1, specifically, the influence of the number of turns in the voltage required to run the septum and the mechanical resistance of the septum blade.

Lambertson septa are presented in section 2.4.3 and SuShi septa are introduced in section 2.4.7.5. Massless septa are described in section 2.4.4. The Truncated Cosine θ (TCT) septum is described in detail in chapter 5.1. These septa topologies are the ones that will be specifically studied in this thesis. The performance of these particular septa topologies will be characterized using the Figure of Merit (FoM) presented in section 2.5. The figure of merit is relevant because the septa topologies that are going to be compared are very different, so a common metric is necessary to rank them.

The rest of the septa topologies described in this chapter are only introduced for completeness, to offer an overview of the existing septa types in different accelerators. All the septa topologies are presented in the same way. First, for each topology, a general description of the topology and its characteristics is presented. Then, some representative examples of that topology are given.

2.2 Different septa topologies

There are two different families of septa. Electrostatic septa and magnetic septa, with several different magnetic septa types [26].

- Electrostatic septa
- Magnetic septa

As a first approximation, one wants to build a septum with the thinnest possible blade, which is to say with the minimum separation between the zero- field region and the high- field region. This will impose less demanding requirements in the kicker magnets or on the preceding septa and will also minimize the beam losses and the radiation caused by those losses. In order to reduce the beam losses, the goal is to achieve an efficiency as close as possible to 100%, either in extraction or in injection, fast or slow. A typical value for the efficiency is between 60 and 70% for multi-turn extraction or about 98% for single turn extraction [27]. For the first iteration, the septum will always be a compromise between those variables, as explained in figure 2.1.

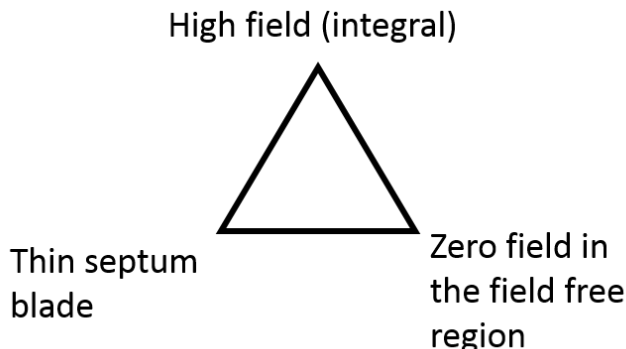


Figure 2.1: Starting point for septa design

In reality, it is also necessary to take into account other different aspects that may be relevant for each septum. In the FCC septa, it will be relevant to consider the use of beam stoppers to protect the superconducting coils in the event of an impact. A direct collision may induce a quench or even drill a hole through the material, which would be fatal for operation. Protection against the heat deposited by the beam tails should also be taken into account when

designing the cryogenic cooling of the superconducting septa. The impact of the beam or its tails in the septum blade may cause radioactive activation, which must be taken into account especially in the case of slow extraction. At this moment, only single-turn extraction is foreseen in the FCC. Activation can degrade the materials and the septum performance, limiting its useful life. It can also be a constraint when repairing or exchanging the septum. For superconducting septa, it is assumed that there is a cryogenic Helium supply for the main lattice magnets which can be used to cool the septa. Therefore, although the septa need to be taken into account for the cryogenic system dimensioning, it should not be necessary to design an ad-hoc cooling system. Additionally, normal conducting septa should also be cooled accordingly. However, energy consumption in this scenario would only be an issue in the case of normal conducting septa, as explained in section 3.6. In the case of the FCC, the cycling of the septa will be slow as they have to follow the energy swing of the accelerator. This means that the septum blade will not be limited by the fatigue of its materials. The septum blade needs to withstand the stresses caused by the Lorentz forces. Septa magnets that operate in a cycle are subject to fatigue, which can be a limiting factor when the cycles are of the order of seconds.

In this study, the main parameters taken into account are the septum blade thickness, the leak field and the maximum magnetic field achieved by the septum magnet. Although passive quench protection devices and quench detection and protection circuits need to be taken into account in the case of superconducting septa. The issues mentioned above will not be fully developed in this thesis although they will be taken into account when relevant. The full studies are being carried out but they lie outside the scope of this thesis [28].

2.2.1 Electrostatic septa

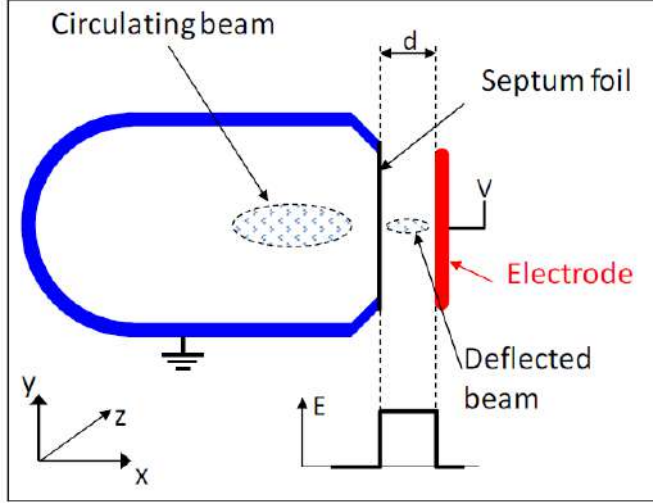


Figure 2.2: Schematic of an electrostatic septum

This family of septa uses an electric field to deflect the particles. The deflection is therefore parallel to the electric field. The electric field is created between the high voltage electrode and the thin septum connected to ground, leaving the enclosed part of the septum as the field-free region, so the orbiting beam can circulate undisturbed.

The septum can be either a foil or a wire array. The foil in the limit can be seen as a wire array with infinite wires with zero distance between them. A schematic to illustrate the working principle of an electrostatic septum is presented in figure 2.2.

Typical values for the electrostatic septa parameters are presented in Table 2.1.

Table 2.1: Typical parameters for an electrostatic septum

Parameter	Unit	Value
Electrode length	mm	500- 3000
Gap width	mm	10- 35
Septum thickness	μm	≤ 100
Vacuum pressure	mbar	$10^{-9} - 10^{-12}$
Voltage	kV	up to 300
Electric field	MV/m	up to 10
Septum foil material	-	Mo or W-Re
Electrode material	-	Ti, St. Steel, Aluminum

Since the particle beam needs ultra- high vacuum to circulate, the main insulator in an electrostatic septum is vacuum. This means the septum itself is inside a vacuum tank and it is susceptible to suffering electrical breakdowns. Vacuum is self- healing after the arc is extinguished but the materials that make the cathode and the anode have to be chosen considering the possibility of flashovers. At high electron emission levels, of the order of $1 \mu\text{A}$, the probability of a vacuum breakdown increases dramatically. The breakdowns can be initiated by the cathode or the anode [29] and it is extremely difficult to predict them [30]. It is also important to take into account that at low pressures, the voltage breakdown departs from Paschen's law [31].

The main reason to use an electrostatic septum is the possibility to achieve very thin septa thickness, down to $50 \mu\text{m}$ instead of the typical value of a few mm for magnetic septa. Additionally, while the supplied voltage can be very high, in the order of 300 kV, the current will be very small. It is a leak current, much smaller than $1 \mu\text{A}$. Thanks to this, the power consumed by an electrostatic septum is very low and will be dominated by the losses in the power converter. The main drawback of electrostatic septa is that the deflection that can be achieved with them is much smaller than with a magnetic device, as explained in section 2.2.3.

2.2.2 Magnetic septa

Regarding the magnetic field configuration, magnetic septa are dipole magnets. The main difference between a traditional dipole and a septum magnet is that in a dipole magnet there is a homogeneous field region while in the septum there is a high- field region and a zero- field region which are separated by

a relatively thin septum, in which the high-field region is less homogeneous than the field in the gap of an equivalent lattice dipole magnet. The septum blade is usually one side of the coil, and making it thinner means that the current density increases. One could increase the number or turns in the coil to reduce the current density but the resistance and the inductance of the magnet depend proportionally on the number of turns and on the square of the number of turns respectively, making it slower or unsuitable to be pulsed, since the load seen by the power converter would be too high. Having more turns also requires more voltage to power the magnet and more space for insulation, which might increase the current density instead of reducing it. Because of this, the coils of pulsed septa in particular are usually built with as few turns as possible so the current in the coil increases and it usually falls in the order of several thousands of amperes. At this point the ratio of conductor and cooling holes becomes important. Using fewer cooling channels will decrease the current density in the conducting part of the coil, which will lower the temperature. Using fewer turns to build the coils will also help to increase the field homogeneity and to reduce the leak field because the current distribution would be more homogeneous and closer to an ideal current wall. This is due to the fact that current densities in septa magnets are usually in the order of 100 to 200 A/mm², and introducing several holes in the septum blade will make the current distribution too different from an ideal current wall. In normal magnets this can be viewed as an optimization problem, and a small saving in material or power in an individual magnet might be a significant saving given that lattice magnets are usually produced in a big series. In septa, since the cooling water circulates in turbulent regime, the optimization needs to be solved numerically and can be very difficult to implement. Besides, in septa usually there is not enough motive to solve this problem because the magnets are produced in small series, or even individually. As an additional remark, in pulsed conductors the current tends to flow on the outer region of the conductor because of skin effect, which suggest the idea to place the cooling ducts in the inner region of the septum blade.

If the power converter is far away from the magnet, the Joule losses originated from transporting such a high current over a few tens of meters will be high. To solve this, for pulsed septa, there is usually a transformer placed near the magnet. The transformer ratio is usually around 1:10, since the Joule losses scale with the square of the current. The power rating of the transformer has to correspond to the power of the magnet, which means that the transformer will have a considerable size, since it typically is in the kW range. The size and placement of the transformer have to be taken into account in the integration phase since, in accelerators that are already built, the space is

limited.

Apart from the current density, the other major cause of the magnet heating will be the power deposition due to beam losses and synchrotron radiation. Cooling then becomes an issue, making these magnets impossible to be air-cooled.

Taking into account the particularities of these devices, one can identify several families of magnetic septa:

- Direct drive DC and pulsed septa
- Eddy current septa
- Lambertson septa
- Massless septa
- Opposite fields septa
- Permanent magnet septa
- Superconducting septa

2.2.3 Comparison between electrostatic and magnetic septa

In theory, for any extraction there are two options that are equivalent, in principle it could be done indistinctly with electrostatic or magnetic septa as long as the particles are deflected as required. However, for the same angle, as the required septum blade becomes thinner, electrostatic septa are able to produce a higher deflection since the magnetic septa will be limited by the current density and the Lorentz force. To illustrate this, we start from the deflection produced by an electrostatic septum for a single particle [32].

$$\theta_E = \frac{q \cdot |\vec{E}| \cdot l}{p \cdot c \cdot \beta} \quad (2.1)$$

Where q is the particle charge, \vec{E} is the electrical field, l is the magnet length, p is the beam momentum, c is the speed of light and β is the relativistic factor. As it is usual in the literature, m_0 is the rest mass of the particle and:

$$\beta = \frac{v}{c} = \frac{|\vec{p}|}{\sqrt{p^2 + (m_0 \cdot c)^2}} \approx 1 \quad (2.2)$$

In a relativistic particle accelerator the approximation $\beta=1$ is reasonable since the particles are travelling at practically the speed of light. For protons in the CERN Accelerator Complex this is not true in the LINAC and Proton Synchrotron Booster (PSB) and Proton Synchrotron (PS). The approximation $\beta \approx 1$ can be considered true from the extraction of the PS at 26 GeV, where $\gamma = 27.7 \gg 1$.

Following this, we can consider the deflection produced by a magnetic septum.

$$\theta_M = \frac{q \cdot \mu_0 \cdot d \cdot J \cdot l}{|\vec{p}|} \quad (2.3)$$

Where d is the septum blade thickness, J is the current density in the blade and the rest of the variables are the same as in equation (2.1). Now making both deflections equal and simplifying the equations, for a given septum thickness, the necessary current density to produce the same deflection as an electrostatic septum is:

$$J = \frac{|\vec{E}|}{\mu_0 \cdot d \cdot c} \quad (2.4)$$

It can be seen that if the blade thickness is too small the current density will be too high to use copper to build the coil, even if the magnet is pulsed, making necessary the use of a superconducting material instead of copper with all the additional challenges that it poses, making an electrostatic septum a much easier solution. However, this advantage in thickness might be shadowed when the required deflection of the particles is too big or the beam rigidity is too high. If we compare the force seen by a particle when it enters the magnetic or electrostatic septum we have:

$$\vec{F}_M = q \cdot \vec{v} \times \vec{B} \quad (2.5)$$

$$\vec{F}_E = q \cdot \vec{E} \quad (2.6)$$

Making those forces equal and considering a magnetic field of 1 T, which is a reasonable value and keeps the calculation simple, we obtain the following relation in modulus between the required electrical field to replace a magnetic field:

$$|\vec{E}| \approx c \cdot |\vec{B}| = 300 MV/m \quad (2.7)$$

The theoretical values of the electrical field in the case of vacuum a breakdown voltage is about 100 MV/m and about 2 MV/m in the case of a dry air. The value of 100 MV/m is rather high but a more realistic value for a septum is 10 MV/m. Taking equation (2.4) and using this value we can observe an inverse relationship between the septum blade thickness and the current density:

$$d = \frac{26.53[A/mm]}{J[A/mm^2]} \quad (2.8)$$

Using equation (2.8) we can obtain a cutoff thickness, above which it would be advantageous to use a magnetic septum instead of an electrostatic septum. Considering that 85 A/mm^2 as the maximum current density that is typically allowed for a DC septum, the septum thickness limit found is 0.31 mm . This cutoff limit is not a hard theoretical limit but a reasonable value that can be used as a general guide in the preliminary phase of the design of a given septum. If the design values are close to this cutoff limit, both alternatives should be studied and other variables such as available space, or energy consumption for example should be considered. Equation (2.8) is plotted in figure 2.3. In the figure, the part of the curve where a magnetic septum is advisable is plotted in blue, while the part where the electrostatic alternative is preferable a priori is plotted in red. If the working point is close to 85 A/mm^2 then both alternatives should be explored. One should keep in mind that figure 2.3 is plotted assuming that the particles are relativistic.

2.3 Description of representative electrostatic septa

2.3.1 The 50 GeV electrostatic septum at J-PARC

As an example, two electrostatic septa are used for the resonant slow extraction at 50 GeV in the MR proton synchrotron, at J- PARC in Japan [33]. The relevant characteristics of these septa are summarized in Table 2.2:

Table 2.2: Characteristics of J-PARC 50 GeV electrostatic septum

Parameter	Unit	Value
Deflection angle	mrad	0.2
Electric field strength	MV/m	6.8
Apparent septum thickness	mm	0.1
Wire diameter	mm	0.08
Inter-wire distance	mm	2
Septum wire material	-	Tungsten- Rhenium

Applying equation 2.4 for the equivalent current density, the obtained value is $J = 225 \text{ A/mm}^2$, which is very high for a septum working in slow extraction

2.3. DESCRIPTION OF REPRESENTATIVE ELECTROSTATIC SEPTA

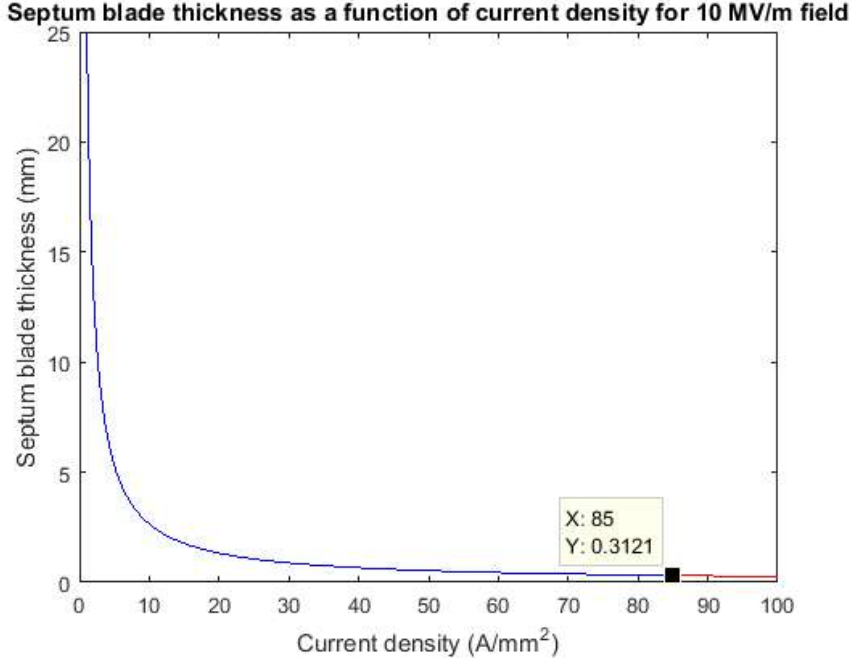


Figure 2.3: Septum blade thickness as a function of the current density
To complement figure 2.3 it is necessary to take into account that electrostatic septa are used when the goal is to produce a long spill of particles, which can last up to a few seconds. They are complemented by a magnetic septum downstream to provide the necessary deflection, which in the case of proton accelerators is not usually possible with electrostatic septa only.

with a duty cycle of almost 20%. However, the option of the electrostatic septum is more appealing since the aim of the extraction system was to minimize the losses [33]. A cross section of this septum can be found in figure 2.4.

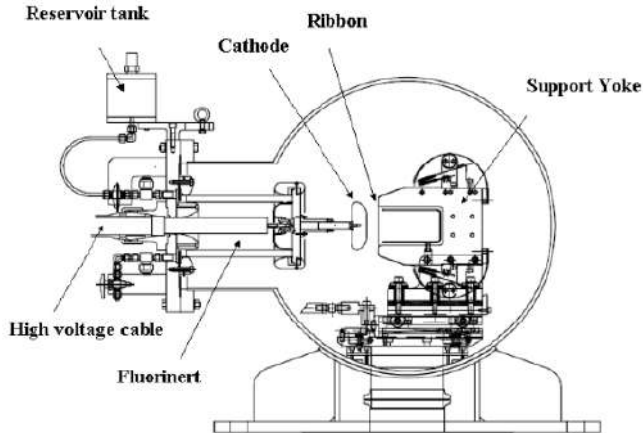


Figure 2.4: J-PARC 50 GeV electrostatic septum cross section

2.3.2 The ZS septum at CERN

The SPS is the accelerator preceding the LHC in the CERN Accelerator Complex. It also delivers beam to the fixed target experiments in the North Area using a third order resonant extraction scheme. The extraction system consists of five individual ZS modules, each 3 meters long, used in the extraction from the SPS at 450 GeV towards the North Area, located in the Long Straight Section 2 (LSS2) which produced a long spill of particles that will be deflected downstream by the MSE magnetic septa. The anode supports of first three modules are made of INVAR® alloy (FeNi36) [34]. The anodes of the last two modules are made of stainless steel. The reason to use INVAR® for the construction of the first two modules is that its thermal expansion coefficient is very low, approximately ten times lower than that of stainless steel, and since the ZS is used in slow extraction mode, the heat deposited is significant, thus using INVAR® the mechanical stability is guaranteed. This heating in the past was also the cause of excessive sparking [35]. Calculations and experience have shown that the heat deposition in the last two modules is low enough to build the anodes using stainless steel, which is cheaper. This is due to the fact that the beam is slightly more separated from the blade as it advances in the extraction line, and it is also the reason to use two different thicknesses for the WRe (76%/24%) wires. The first two modules use $60\mu\text{m}$

2.3. DESCRIPTION OF REPRESENTATIVE ELECTROSTATIC SEPTA

because the first modules practically slice the beam apart and losses have to be minimized. The last three modules are built using $100\mu\text{m}$ wires because the beam has already been partly deflected and the losses are smaller. This small deflection is enough to use less delicate wires in the construction. The most demanding parameter to control in this septum in order to provide the required field quality and deflection is the wire alignment.

The anodes of the ZS septa have been equipped with ion traps. These ion traps are a pair of electrodes which are put in place to remove the ions produced by the interaction between the beam and the residual gases in the vacuum chamber. If they were not installed, the positive ions would eventually penetrate in the high-field region of the septum and would be accelerated towards the cathode, causing voltage discharges which would in the end destroy the septum. Having five modules, the polarities of the ion traps can be alternated to produce a negligible integrated vertical deflection when the machine is operating with electrons or positrons although this is not necessary when operating with protons since they are much heavier. Currently, the upper electrode is powered at -3 kV and the lower one is connected at -6 kV [36]. Full description of the ZS septa, the ion traps and the improvements can be found in [37, 38, 39, 40].

Table 2.3: Characteristics of the ZS septum at CERN

Parameter	Unit	Value
Electrode length	mm	5 x 3000
Gap width	mm	10 to 30
Septum wire diameter	μm	60 or 100
Vacuum pressure	mbar	10^{-9}
Maximum voltage	kV	-300
Electric field	MV/m	10
Septum wire material	-	Tungsten- Rhenium
Inter-wire distance	mm	1.5
Number of wires per module	-	2000

Two views of the septum are presented in figure 2.5 and figure 2.6. In the first picture the cathode has been removed and the anode wire array can be clearly seen. In the second one, the cathode is mounted showing the normal disposition of the septum.

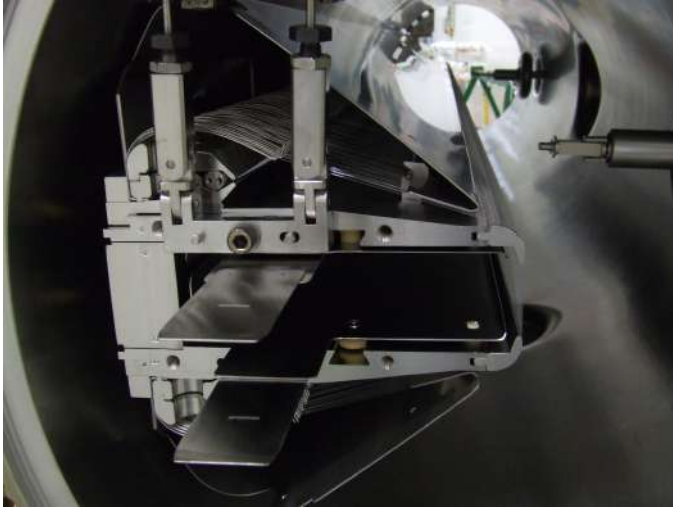


Figure 2.5: The ZS septum anode



Figure 2.6: The ZS septum anode and cathode

2.3.3 The SEH23 septum

The SEH23 is an electrostatic septum used for resonant slow extraction from the CERN PS accelerator towards the East Area. The resonant slow extraction is useful to provide a quasi- continuous beam to fixed target experiments [27]. This septum is built with a 100 μm thick Molybdenum foil instead of a wire array. As an advantage, since a foil is used instead of wires, no ion traps are needed because there is no possibility for charged particle to penetrate in the high-field region. The main parameters of this septum are summarized in table 2.4 and more information can be found in [41].

Table 2.4: Parameters of the SEH31 electrostatic septum

Parameter	Unit	Value
Cathode length	mm	778
Gap width	mm	17
Septum thickness	μm	100
Angular position	mrad	-5 to 5
Septum material	-	Molybdenum foil
Operating voltage	kV	160
Operating electrical field	MV/m	9.4
Conditioning voltage	kV	250
Cathode material	-	Anodized aluminum

A picture of this septum inside its vacuum tank can be seen in figure 2.7.

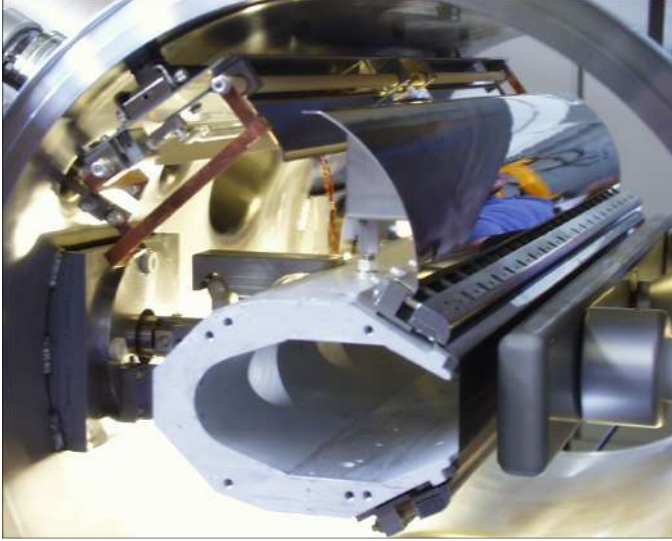


Figure 2.7: Downstream of the SEH23 septum

2.4 Description of magnetic septa families

2.4.1 Direct drive DC and pulsed septa

The traditional construction of these magnets is done as a C-shaped steel yoke closed by a thin copper conductor that separates the high-field and low-field regions of the septum. The thickness of this conductor (the blade) is kept as low as possible to minimize the beam losses. The septum blade has to be thick enough to carry the required current density and to allow space for the cooling circuit. The power dissipated in a DC septum magnet is quite high and typically requires the use of evenly distributed water cooled conductors. The holes of the cooling circuit reduce the cross section of the conductor, increasing the resistance and therefore the power dissipated in the coil. For that reason, the back leg of the coil usually has a bigger cross section.

Another issue with the pulsed septum magnets is that since the current is high, the Lorentz force in the coil is significant. This affects the coil deformation and fatigue and ultimately the field quality in the extracted beam gap. The mitigation of this problem is to hold the coil using springs and clamps. Ultimately DC septa are usually limited by the cooling and pulsed septa will

be dominated by fatigue of the septum blade.

The septum blade can be studied using beam theory. In the case of an in-vacuum septum magnet, the load situation of the septum blade is equivalent to a beam supported at both ends which is subject only to pure flexural stress, as shown in figure 2.8, taken from [42]. The magnet poles will also try to close the separation between them, reducing the gap height. In the case of an in-vacuum septum the deformation is negligible and therefore it will not be considered in this approximation because the error is very small. In equations 2.9 and 2.11, E denotes the Young Modulus' of the material, as it is usual in stress analysis.

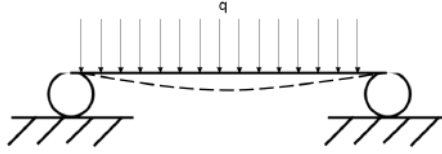


Figure 2.8: Schematic of a beam supported at both ends

The maximum deflection of the beam shown in figure 2.8 is given by equation 2.9, where q is a uniformly distributed load. The full derivation is done in [43].

$$f_{max} = \frac{5}{384EI} qL^4 \quad (2.9)$$

For a beam under pure stress conditions, the elongation is given by equation 2.10 and the elongation is related to the stress by equation 2.11, where E is the Young modulus.

$$\epsilon = \frac{f_{max}}{L} \quad (2.10)$$

$$\sigma = \epsilon \cdot E \quad (2.11)$$

The uniformly distributed load in a magnet is due to the magnetic field and the current, which are considered to be perpendicular in this case. The current considered in the case of a multi-turn septum is the total current, taking the turns into account. The current is considered constant and uniformly distributed, to avoid considering the effect of cooling ducts.

The magnetic field, which in reality varies linearly across the septum blade with from the nominal value to approximately zero, is taken as the average of these values. Although this is an approximation that does not accurately

represent the stresses inside, it is perfectly valid because the total force is not changed. The total load is then calculated according to equation 2.12.

$$q = I \frac{B}{2} \quad (2.12)$$

Combining equations 2.10, 2.11 and 2.12, the maximum stress in the septum blade can be calculated as a function of the septum current and magnetic field. In equation 2.13 I_x stands for the moment of inertia, which should not be confused with the current I .

$$\sigma = \frac{5 \cdot L^3}{768 I_x} B \cdot I \quad (2.13)$$

The desired characteristics of a septum magnet can be deduced from equation 2.13. It is advisable to design a septum with a gap as small as possible. The moment of inertia will be decreased by the need of a thinner septum blade and the magnetic field and the current will be imposed by the magnetic field integral required.

It is important to remember that in the case of pulsed septa the effects of fatigue cannot be ignored and the number of cycles becomes a very relevant factor [44].

The inductance of the magnet can also be estimated analytically. Calculating the exact value of the inductance can be very challenging. The easiest way is to use the definition of magnetic energy and find a relationship with the energy stored in an inductance. The magnetic energy is defined in equation 2.14, where the integral is performed in all the volume where the magnetic field exists and the energy stored in an inductance is presented in equation 2.15.

$$E = \frac{1}{2} \iiint B \cdot H \, dV \quad (2.14)$$

$$E = \frac{1}{2} L I^2 \quad (2.15)$$

In a direct drive septum magnet, the integral in equation 2.14 can be easily approximated analytically. First, it is necessary to use Ampere's law to calculate the H field. Ampere's law states that the magnetic field around a closed loop is proportional to the current enclosed by the loop. This is shown in equation 2.16.

$$\oint \vec{H} \cdot d\vec{l} = N \cdot I \quad (2.16)$$

In a septum, it is advisable to perform the line integral along a loop that allows to simplify the calculations taking advantage of directions and regions where the H field is constant or zero. In the field free region, the magnetic field can be considered non-existent without introducing a significant error. Besides, inside the extracted beam gap, the magnetic field is constant, which reduces the integral to a multiplication. Besides, where the magnetic field is perpendicular to the line path, the scalar product is zero by definition. The path for the integral used is shown in figure 2.9.

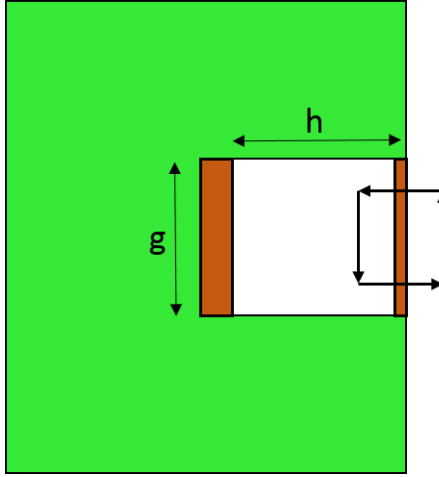


Figure 2.9: Schematic of the application of Ampere's law to calculate the magnetic energy

Once the integral has been performed, the magnetic field H can be calculated, and is given by:

$$H = \frac{NI}{g} \quad (2.17)$$

Where g is the gap height. The magnetic flux density in vacuum (B) is related with the magnetic field (H) via the magnetic permeability of vacuum (μ_0), which is not true in the iron yoke, as shown in equation 2.18. For this reason, it is not easy to perform the line integral in equation 2.16 along a path that travels through the iron yoke.

$$B = \mu_0 H \quad (2.18)$$

Combining these results and introducing them in equation 2.14, the energy can be computed according to equation 2.19.

$$E = \iiint \frac{1}{2} \frac{N^2 I^2}{\mu_0 g} dV \quad (2.19)$$

Since the integral needs to be performed in all the space where the magnetic field exists, it would be necessary to integrate up to infinity. However, the integration can be simplified if one considers that the magnetic field is mostly located inside the extracted beam gap of the septum and there is a small region at the ends of the septum where the field decays rapidly. The volume of this region can be computed as the product of the gap height, the width and the magnetic length of the magnet. The magnetic length of the magnet in a septum, contrary to what happens in normal magnets, is slightly longer than the yoke length. The magnetic length of a septum magnet (a) can be approximated as the yoke length plus the gap height ($l_{yoke} + g$). This is illustrated in figure 2.10, which shows a view from the top of the same septum in figure 2.9 with the volume to perform the energy integral in dashed lines. The velocity of the beam is also drawn for clarity. Therefore, the volume for the integral in equation 2.19 can be approximated as:

$$V = g \cdot h \cdot a \approx g \cdot h \cdot (l + g) \quad (2.20)$$

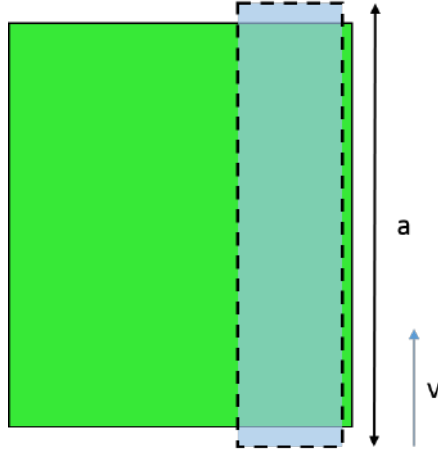


Figure 2.10: Septum view from the top showing the volume where the energy integral is performed

Therefore, the magnetic energy can be computed approximating the volume integral in equation 2.14 by a product and a simple expression for the energy is obtained.

$$E = \frac{1}{2} \frac{N^2 I^2}{\mu_0 g} \cdot h \cdot (l_{yoke} + g) \quad (2.21)$$

Introducing this last result in equation 2.19 and using equation 2.15, an expression for the inductance (L) can be obtained, not to be confused with the length (l).

$$L = \frac{N^2 h (l_{yoke} + g)}{\mu_0 g} \quad (2.22)$$

The interest of this approximation lies in the fact that the error of the calculation lies in the volume integral and ultimately in the calculation of the magnetic length. The magnetic length of a typical 1 m long septum is usually off by a few percent, making a very good trade off with the effort that takes to perform this approximated calculation.

Additionally, the voltage needed to achieve the required rise time for a pulse increases with the inductance. For this reason, septa magnet coils are built with as less turns as possible. Finally, pulsed magnets are always built using a laminated yoke to reduce eddy currents.

2.4.1.1 Direct drive DC septa

Figure 2.11 shows a schematic of a typical DC septum magnet.

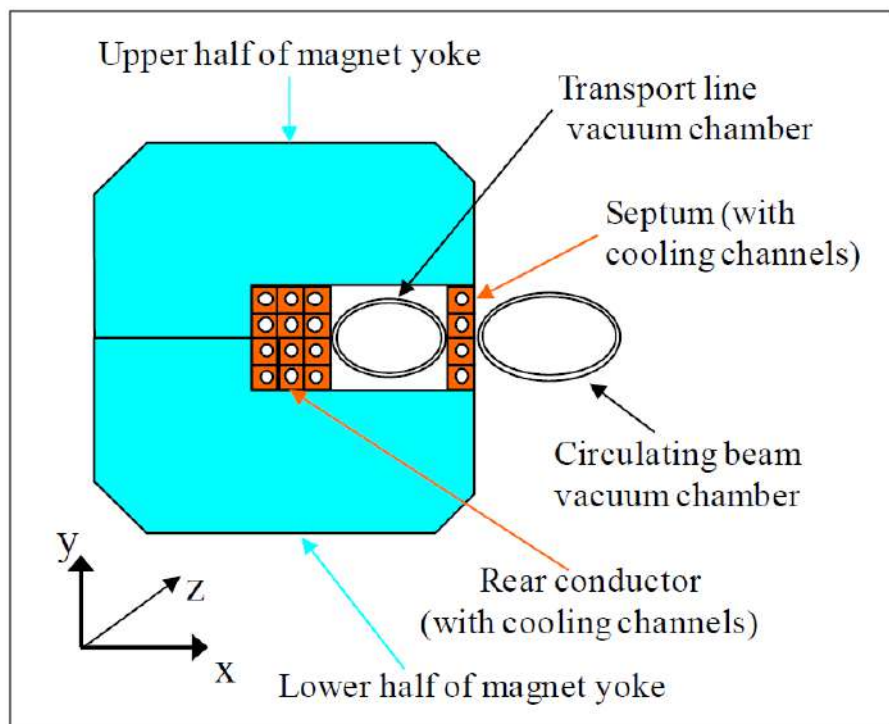


Figure 2.11: Schematic of a DC septum outside vacuum

The septum conductor of a DC septum is typically between 3 and 20 mm in thickness and the current density can be up to 85 A/mm^2 . Coils are usually constructed with as few turns as possible to limit the inductance of the magnet but there is a trade off with the current density and thus the cooling. DC septa are outside vacuum, "clamped" onto the vacuum chamber because many insulation materials can not be used inside ultra high vacuum. This also makes any intervention on the magnets much easier than on an in-vacuum septum because they are more easily accessible and there is no activation due to beam losses. However, this kind of design is only an advantage when the magnetic field is not too intense since the gap height (and therefore the Ampere-turns) and the apparent septum thickness grow significantly. The apparent septum thickness is the addition of the coil thickness, electrical insulation, magnetic shielding (if there is any) and the vacuum chamber walls, and it is to be compared to the beam separation. The typical values for a direct drive DC

septum are summarized in Table 2.5.

Table 2.5: Typical parameters for a DC septum

Parameter	Unit	Value
Magnetic length	mm	400- 1200
Gap height	mm	25- 60
Septum thickness	mm	6- 60
Current	kA	0.5- 4
Current density	A/mm ²	up to 85
Power consumption	kW	up to 100
Number of turns	-	1- 10
Cooling flow	l/min	12- 60

2.4.1.2 Direct drive pulsed septa

A pulsed septum layout is very similar to a DC septum, but with the difference that the magnet is excited only when it is necessary. This saves energy and reduces the cooling requirements. The yoke needs to be laminated to reduce the power dissipated by eddy currents, the number of turns is reduced to minimize the coil inductance and they are generally placed inside vacuum to reduce power consumption and septum thickness. A high inductance produce a slower magnet, which is not desirable and sets unnecessary constraints in the power supply, and inductance is proportional to the coil area and to the square of the number of turns of the coil. Besides, the eddy currents may affect the magnetic field level and homogeneity if they decay too slowly. As in any magnet, the laminations must have the appropriate thickness to allow for full penetration of the magnetic field. Most of the typical values for a pulsed septum are very similar to the ones of a DC septum. However the power is usually supplied by a capacitive discharge power supply (with third harmonic and/or active filters) producing a half- sine pulse with a duration of a few ms. These values are presented in Table 2.6. The schematic of a pulsed septum is the same as for a DC septum, but it will be most likely inside vacuum. Something that one needs to keep in mind when working with pulsed magnets is that while the dissipated RMS power might be lower than if it was a DC septum, the peak power might be higher and that has to be taken into account when designing the power converter.

While pulsed septa loosen the thermal requirements they introduce vibration and fatigue. The reliability of a septum under this new constraints has to be taken into account from the design stage.

Table 2.6: Typical parameters for a pulsed septum

Parameter	Unit	Value
Magnetic length	mm	300- 1200
Gap height	mm	18- 60
Septum thickness	mm	3- 20
Yoke lamination thickness	mm	0.23-1.5
Current (peak)	kA	7- 40
Current density (peak)	A/mm ²	up to 300
Number of turns	-	1- 2
Cooling flow	l/min	11- 80
Vacuum pressure	mbar	10 ⁻⁹

2.4.1.3 The DAFNE 2°septum

The DAFNE accelerator complex is situated at the INFN-LN, in Frascati, Italy. The DAFNE Accumulator and Main Rings are part of an electron-positron collider. There are two mirroring septa installed at the end of the transfer line between the Linac and the Accumulator since the particles will be deflected in one direction or another depending on the charge. The septa are built as a C-shaped yoke closed by a copper conductor, following the principle illustrated in figure 2.11. The design parameters and prototype results, as well as further details on the DAFNE accelerator complex, can be found in [45, 46] and a summary of the relevant parameters of these septa can be found in Table 2.7. The septum is presented in figure 2.12, taken from [45].

Table 2.7: DAFNE septa parameters summary

Parameter	Unit	Value
Nominal field	T	0.104
Bending angle	mrad	38
Gap height	mm	22.5
Magnetic length	mm	623
Septum thickness	mm	1.5
Current density	A/mm ²	55
Peak current	A	1843
Power	kW	2.1
Water flow rate	l/min	6
Pressure drop	atm	3



Figure 2.12: DAFNE 2° septum, as shown in [45], reproduced here for illustration purposes

2.4.1.4 The SM1 septum at the AAC

The Antiproton Accumulator Complex (AAC) at CERN was an accelerator complex used in the 1980's and early 1990's. It consisted of the Antiproton Accumulator (AA), the Antiproton Collector (AC), the Low Energy Antiproton Ring (LEAR) and the ($S\bar{p}\bar{p}S$), which was a modification to use the SPS as a proton-antiproton collider. This is the facility where stochastic cooling was first tested, which led to the discovery of the W^+ , W^- and Z bosons [47, 48, 49]. The AAC was dismantled after the last SPS collider run in 1991, and the LEAR was transformed into the Low Energy Ion Ring (LEIR) while the AA was dismantled and the AC was converted into the Antiproton Decelerator (AD). Today the AD and ELENA constitute the Antimatter Factory [50, 51].

In the AAC there used to be two identical DC septa called the SM1 and SM2. The main parameters of these septa are summarized in Table 2.8.

Table 2.8: Main parameters of the SM1 and SM2 septa

Parameter	Unit	Value
Nominal field	T	0.645
Gap height	mm	77
Yoke length	mm	1000
Septum thickness	mm	11.2
Current density	A/mm ²	69
Current	kA	3.95
Power	kW	110.6
Water flow rate	l/min	2x40
Pressure drop	atm	13

Two views of the SMH61 septum in the PS, a DC septum identical to the SM1 septum, are shown in figure 2.13 and figure 2.14.



Figure 2.13: On the left, a DC septum installed in the CERN PS that is identical to the SM1 septum used in the AA

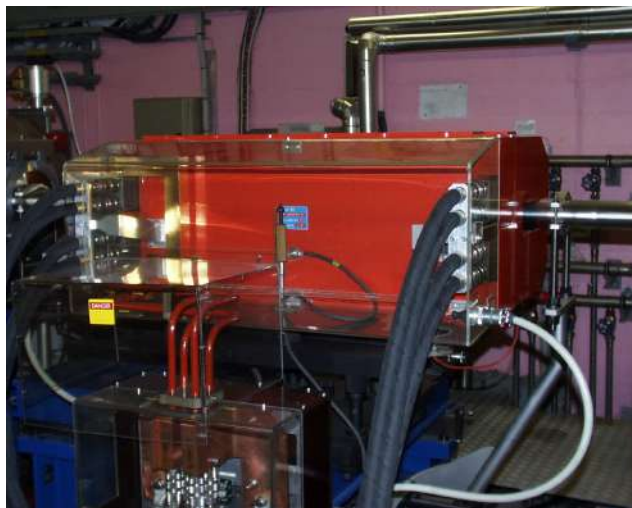


Figure 2.14: Rear view of the DC septum identical to the SM1 septum that used to be installed in the AA

2.4.1.5 The SMH16 septum

The SMH16 is a direct drive pulsed septum installed under vacuum for the extraction of the CERN PS towards the SPS accelerator. It consists of 2 identical modules in a common vacuum tank, with the second one tilted 20 mrad with respect to the first one. The main parameters of this septum are summarized in Table 2.9.

Figure 2.15 shows one of the modules of the SMH16 installed in the tank without the end cover.

Table 2.9: Main parameters of the SMH16 septum

Parameter	Unit	Value
Nominal field	T	1.2
Number of modules	-	2
Angle between modules	mrاد	20
Gap height	mm	30
Yoke length	mm	2x1070
Septum thickness	mm	3
Inductance	μH	5.5
Coil turns	-	1
Peak current	kA	28.7
Pulse duration	ms	3.8
Transformer ratio	-	12
Cooling water flow	l/min	1.2
Pressure drop	bar	22.29



Figure 2.15: One of the SHM16 modules installed in the vacuum tank

2.4.2 Eddy current septa

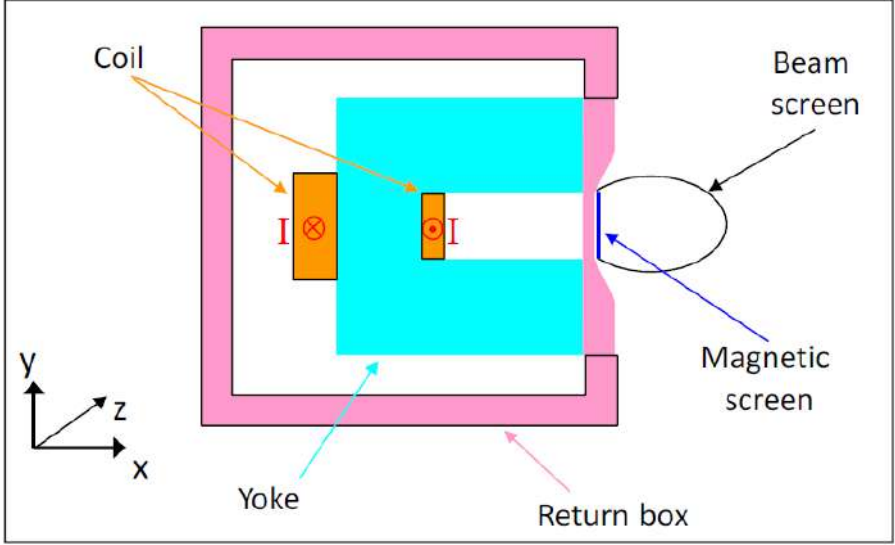


Figure 2.16: Schematic of an eddy current septum with a return box and a magnetic screen

This family of septa relies on eddy currents to shield the leak field. When the magnet is pulsed, the magnetic field induces eddy currents in the septum that try to compensate the leak field. Eddy current septa are usually pulsed with a half-sine waveform between 4 and 15 kHz, or with pulses duration between 66 and 250 μs . These numbers are based on the penetration depth, from equation 2.23. However, since the eddy currents depend on the magnet inductance, they might take a long time to decay. For this reason these are often pulsed using a full sine, taking advantage of the negative part of the waveform to reduce the magnitude of the leak field. However, this strategy will not reduce it to zero, because of the self inductance of the circuit. The coil is also built with as few turns as possible to reduce its inductance. A return box is necessary to create a path for the eddy currents.

The yoke is built as a C-shape and the coil is placed around the back leg, so the dimensions of the return conductor are usually not critical. To reduce the leak field even further, a magnetic screen can be placed around the orbiting beam gap. This allows the leak field seen by the orbiting beam to be as low

as 0.01% of the main field, a significant achievement even for an eddy current septum, which is a topology known for their low leak field. The attenuation of the leak field was studied in detail by P. Lebasque for the eddy current septum of the Soleil storage ring and it is explained in more detail in 2.4.2.2.

The septum blade can be generally made thinner than in a DC septum but it is likely that it will need cooling like a pulsed septum, and if it is too thin the current density might be too big, or the Lorentz forces too high.

One important factor concerning the leak field is the pulse width. The shorter the pulse duration, the less the magnetic field will leak due to the fact that the magnetic field needs some time to establish and magnetize the yoke completely. The working principle of an eddy current septum consists on that the leak field is compensated by the eddy currents, whose magnitude depends completely on the frequency of the driving current. However, if the pulse frequency is high, the voltage needed to operate the magnet will be higher, so the design of the septum and the power converter have to be done in parallel. Electrical insulation becomes a more important issue when the voltage increases, which makes the blade thickness increase. Increasing the thickness of the magnetic shielding will allow for a longer pulse while keeping the same leak field level, thus reducing the voltage of the power converter.

A schematic of an eddy current septum with a return box and a magnetic screen is shown in figure 2.16.

The typical running parameters for an eddy current septum are presented in Table 2.10.

Table 2.10: Typical parameters for an eddy current septum

Parameter	Unit	Value
Magnetic length	mm	400- 800
Main field	T	up to 1.4
Gap height	mm	10- 30
Septum thickness	mm	1- 3
Lamination thickness	mm	0.1- 0.35
Current (peak)	kA	10
Pulse frequency	kHz	4- 15
Number of turns	-	1
Cooling flow	l/min	1- 20

The normal process to design an eddy current septum is illustrated in figure 2.17. It is not a fixed sequence of design steps and it should not be taken as a recipe but as a guideline since every problem is different, and there might

be other requirements or constraints in the design. However, the scheme is useful to illustrate the main steps and the relations between them. The starting point for the design is the parameter d , which is the septum blade thickness, and the deflection angle required by the beam trajectory, that will determine the field integral needed to produce that deflection and are represented in black in the schematic. The derived magnitudes are presented in blue to separate them from the requirements. From the septum thickness one can fix the skin depth for the eddy currents and it is ideally chosen as a tenth or a fifth of the septum thickness to ensure that the eddy currents remain a surface phenomenon and the magnetic field does not penetrate. The skin depth will determine the pulse frequency (f) according to 2.23 where σ is the material conductivity.

$$\delta = \frac{1}{\sqrt{\pi\mu_0\mu_r f\sigma}} \quad (2.23)$$

An eddy current septum has to be designed taking the powering into consideration. The optics will determine the deflection angle, which will produce a value for the magnetic field integral. From that value, in combination with the available length, one can obtain the necessary current to produce the field and, in the end, the inductance of the magnet, which can be derived from 3D finite element simulations as explained in section 2.4.1.

The length of the magnet is not included in the picture because it is usually a constraint, not a requirement, or a derived quantity. The inductance of the magnet is important for the time constants of the eddy currents' decay and because it will be the main load of the power supply. The voltage of the power supply has to be determined both in magnitude and in waveform, which plays an important role in limiting the leak field, as well as the coil insulation design, as stated at the beginning of this section.

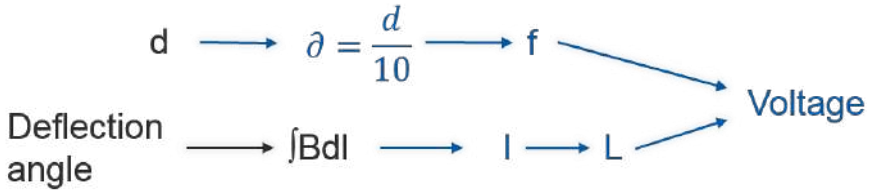


Figure 2.17: Summary of the usual design process for an eddy current septum

2.4.2.1 An eddy current septum for J-PARC

J-PARC is an accelerator complex comprising a Linac, a 3 GeV Rapid Cycling Synchrotron (RCS) and a 50 GeV synchrotron. The injection system into the main ring is composed of two septa, the second one being an eddy current type with the particularity of having a large aperture compared to the typical eddy current septa that are often installed in electron-positron machines. This large aperture poses a problem in terms of leak field and eddy current losses. Besides, one of the reasons to choose an eddy current design instead of any other option is the possibility of having a very thin septum, but the thinner it is, the worse it will be for leak field suppression. The possibilities explored to improve the design and reduce the leak field were to increase the septum thickness, change the pulse width and waveform and include magnetic shielding. The full details of the challenges and possibilities can be found in [52, 53] and further discussion on leak field reduction is carried out in [54]. Table 2.11 summarizes the septum parameters, and a picture of the magnet is shown in figure 2.18.

Table 2.11: J-PARC 50 GeV eddy current septum parameters

Parameter	Unit	Value
Magnet length	m	1.5
Main field	T	0.34
Gap aperture	mm (H x V)	150 x 80
Septum thickness	mm	7
Field homogeneity	-	0.01
Leak field	mTm	0.46
Pulse frequency	kHz	2.86
Deflection angle	mrاد	36
Current waveform	-	full sine
Pulse width	μ s	350
Inductance	μ H	18
Current	kA	10.8
Voltage	kV	5.8
Number of turns	-	2

2.4.2.2 Eddy current septa at SOLEIL

SOLEIL is a synchrotron complex located in Saint Aubin, 20 km South of Paris [55]. The topology chosen for injection or extraction of the electron



Figure 2.18: J-PARC eddy current injector

beam to or from the Booster and to the Storage Ring is the eddy current. The SOLEIL septa system is composed of three magnets with the same cross section. The length of the two septa installed in the Booster (for the injection and extraction) is 300 mm, while the injection septum in the Storage Ring is 600 mm long. In these designs a magnetic screen has been included to reduce the stray field, and the pulse shape has also been investigated. Table 2.12 presents a summary of the main characteristics of the Booster extraction septum, but all the information can be found in [56].

Table 2.12: SOLEIL Booster extraction septum characteristics

Parameter	Unit	Value
Magnet length	mm	300
Main field	mT	286.97
Gap aperture	mm (H x V)	18x15
Peak current	A	3604
Peak voltage	V	290
Coil turns	-	1
Septum thickness	mm	3
Shield thickness	mm	0.5
Field homogeneity	-	$\pm 1.5\%$
Leak field	μTm	54
Pulse duration	μs	120

2.4.2.3 SMH42

An eddy current septum is under development at CERN. It will be placed in the injection to the PS from the PS Booster [57].

The interest of this septum is that the pulse width is very long (2 ms) compared to the usual values and that it has to work together with a bumper magnet. The bumper magnet is one of the five bumper magnets (BSW) that move the orbiting beam slightly to improve the injection quality and reduce beam losses by reducing the deflections required from the kicker and septa magnets, as illustrated in figure 2.19. Further details on the injection scheme can be found in [58].

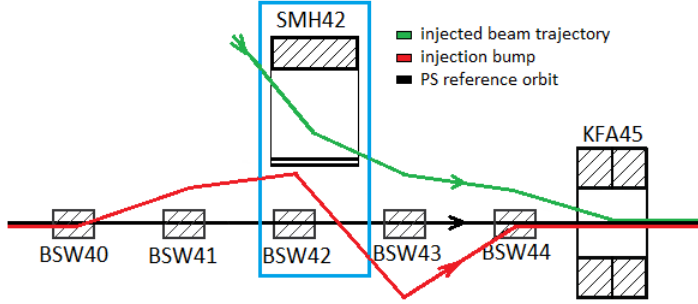


Figure 2.19: Extraction scheme of the SMH42

The functional specification of this septum can be read in [59] and a summary of the relevant parameters is presented in Table 2.13.

Table 2.13: Relevant parameters of the SMH42 injection septum

Parameter	Unit	Value
Physical length	mm	940
Magnetic length	mm	913
Main field	T	0.56
Integrated field	T·m	0.51
Field homogeneity	%	1.2
Integrated leak field (at 10 mm from septum)	mT·m	3.7
Gap aperture	mm (H x V)	70 x 95
Deflection angle	mrاد	54
Pulse width	kHz	1
Current waveform	-	Half-sine
Septum thickness (Downstream extremity)	mm	5.8
Septum thickness (Upstream extremity)	mm	11
Leak field	% of gap field at 10 mm	<1%
Inductance	μH	1.8
Peak current	kA	31.2
Average duty cycle	s	1.2

A prototype of the bumper has been built and it is currently being used to validate simulations.

2.4.3 Lambertson septa

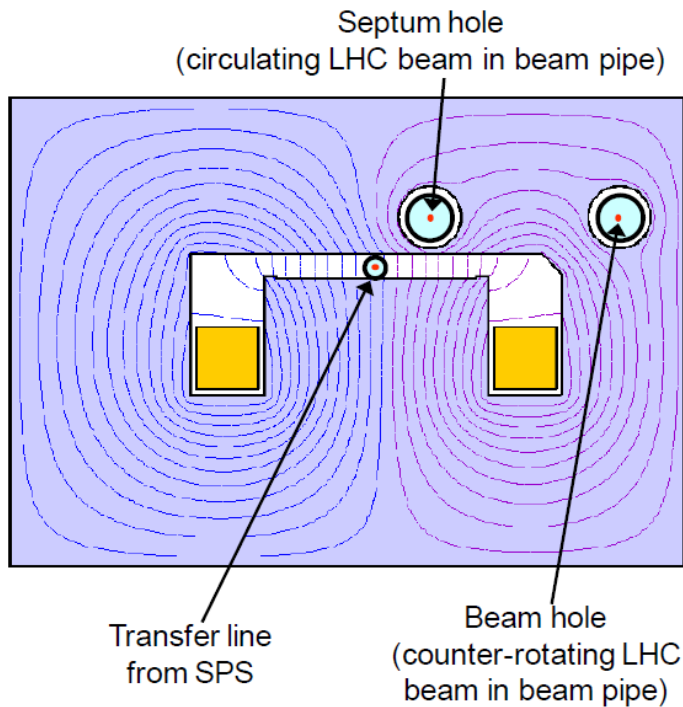


Figure 2.20: Schematic of an LHC injection Lambertson septum (MSI)

A Lambertson septum is an outside vacuum septum magnet which needs to be used in a two-plane injection or extraction scheme. The Lambertson septum produces a deflection in a different plane than the kicker magnets, as shown in figure 3.1. Given the disposition of the magnetic field in the yoke and the upstream or downstream kicker magnets, the Lambertson septum needs to deflect in a different plane.

The main strength of Lambertson septa is that they are robust. The coils are placed far from the radiation of the orbiting beam and inserted into the steel yoke. They are also placed outside vacuum and they are operated as any normal conducting magnet. These magnets are generally run in DC mode, but if they are laminated they can also be cycled or even pulsed. Reducing the

leak field in the orbiting beam gap below the required level can be difficult, since the orbiting beam gap is just another aperture in the magnet. If it is necessary, a magnetic shield can be placed around the gap. In general, the leak field has a tendency to penetrate in the orbiting beam gap, because the gap is embedded in the yoke and the coil is longer than the yoke, so the end effects need to be studied carefully, and shielded has to be designed, if needed. The leak field limits the main field once the yoke starts to saturate, since the orbiting beam gap is inside the yoke, as opposed to a traditional septum in which the field-free region is always outside the yoke. Another advantage of the Lambertson septa with respect to the traditional topology is that a Lambertson will be able to absorb more energy in case of beam losses. In a traditional septum all the losses would be absorbed by a thin copper blade, but in a Lambertson septum they will be absorbed by the iron yoke. A Lambertson septum will not be a collimator but it can protect the equipment downstream, saving costs and increasing the overall reliability of the complex. In figure 2.20, a schematic of the Lambertson septa used for injection into the LHC from the SPS is presented as an example of a typical Lambertson magnet.

The most characteristic feature of the Lambertson topology is that they require a two-plane injection (or extraction) scheme because the plane of deflection is parallel to the plane of the blade. This is due to the coil and the gap disposition given that the magnetic field will always be perpendicular to the iron yoke. There is also a big advantage when designing a Lambertson septum because the coil(s) can be built as a multi-turn water cooled racetrack or bedstead coil, instead of the usual one or two-turn complex coils used in direct drive septa. However, if the magnet is pulsed using a conventional coil will increase the magnetic inductance of the circuit. In summary, Lambertson septa can be seen as a normal conducting window frame magnet with an additional gap, and are suitable for fields up to approximately 1.5 to 2 T like any normal conducting magnet. The limit of a normal conducting magnet is usually determined by the saturation of the Iron yoke.

2.4.3.1 A Lambertson septum at the Hadron Experimental Facility at J-PARC

The Hadron Experimental Facility is part of the Japan Proton Accelerator Complex, located in Tokai, Ibaraki. Protons are extracted at 30 GeV from the Main Ring into the the high-p/COMET beamline by means of a Lambertson septum and two direct drive magnetic septa. The cross-section of the septum is presented in figure 2.21. Full details of the transfer line and the Lambertson septum can be found in [60, 61]. It is outstanding that the poles of the yoke

are not horizontal. This is due to the fact that the deflection plane is not exactly horizontal with respect to the ground. The major specifications for the Lambertson septum are summarized in Table 2.14.

Table 2.14: Major specifications for the 30 GeV Lambertson septum

Parameter	Unit	Value
Iron length	mm	3600
Deflection angle	mrad	38.4
Main field	T	1.1
Leak field	mT	2
Main gap aperture	mm	80
Orbiting beam aperture	mm	30
Peak current	A	1550
Number of turns	-	48

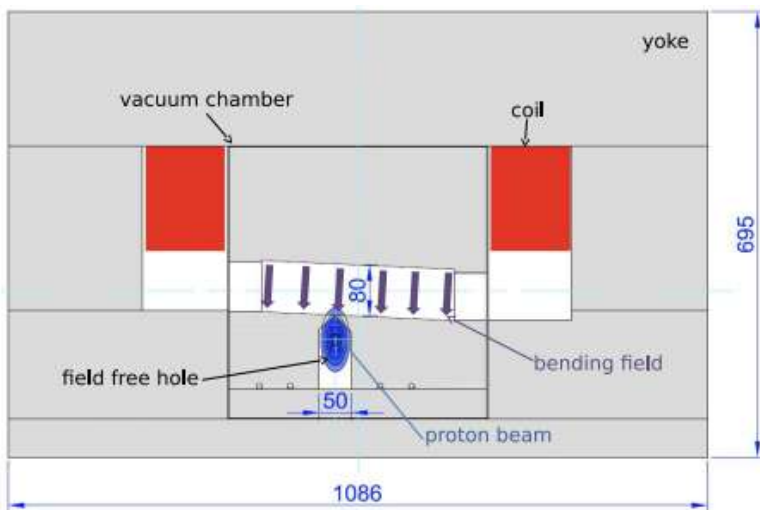


Figure 2.21: Cross section of the J-PARC 30 GeV Lambertson septum

2.4.3.2 LHC MSD Lambertson septa

In the beam dump system of the LHC there are 15 Lambertson septa for each beam line. The MSD magnets are a family with three consecutive different magnet models (MSDA, MSDB and MSDC). The differences between them are the septum thickness and the number of turns in the coil, which allows to connect the magnets in series and use only one power supply for the 15 magnets providing different values of Ampere-turns for the three families. In each dump line there are 15 septa magnet modules, each 4.46 m long. There are 5 modules of the MSDA magnets, followed by 5 MSDB and 5 MSDC downstream. The characteristics of the MSD family are summarized in Table 2.15. The 15 magnets in each beam line are run in series and the difference in the magnetic field comes from the different number of turns in each model. Due to the LHC outstanding performance in the last years there is an ongoing study about the possibility of increasing the collision energy from 14 TeV to 15 TeV (7 to 7.5 TeV per beam), which would be the limit of the main dipoles. For the MSD magnets that means increasing the working point from 880 to 968 A and since the Lambertson is a robust technology and there is a certain margin for operation, there are no major difficulties for this energy increase [62].

Table 2.15: Characteristics of the LHC MSD Lambertson septa

Parameter	Unit	MSDA	MSDB	MSDC
Number of magnets	-	5	5	5
Physical length	m	4.46	4.46	4.46
Septum thickness	mm	6	12	18
Current	A	880	880	880
Number of turns	-	32	40	48
Gap field	T	0.79	0.99	1.16
Leak field (estimated from Flux 2D)	T	$\sim 10^{-6}$	$\sim 10^{-6}$	$\sim 10^{-6}$

The leak field in these magnets has been estimated from simulations performed with Flux 2D [63] and verified with Cobham Opera, but at this field level the calculation is dominated by the software precision. Further details on the design and drawings can be found in [64, 65]. A picture of the MSDA Lambertson septa in back to back configuration are shown in figure 2.22.



Figure 2.22: MSD Lambertson septa in back to back configuration

2.4.4 Massless septa

A massless septum is a traditional septum with no physical septum blade. Since there is no physical blade, the septum blade will be defined as the distance in which the magnetic field decreases from 99% to 1% of the nominal field.

The main advantage of using a massless septum is that in the case of a beam sweep there will be no damage to the septum blade since there are no active parts in the beam path. There is no physical blade that can be subject to any of the typical issues in septa conductors, like thermal or mechanical stress, damage due to beam impact or radioactive activation. In this case, the apparent septum blade thickness can be defined as the region where the magnetic field transitions from 99 to 1% of the nominal value. These values are set arbitrarily and depend on the application, but they are usually taken in massless septa design.

The main drawback however is that the transition from the zero- field region to the high- field region is not sharp but a gradient, and there is no way to avoid the magnetic field leaking to the field-free region. This gradient and the leak field depend on various factors, like the gap and the coil geometry and most importantly the field level, but it will always be inversely proportional to the distance to the high-field region, because it is the propagation of a magnetic field in free space. In iron dominated septa, the higher the field

is, the bigger the transition area becomes. In general the transition region width is very similar to the gap height. Therefore, massless septa are not very common and they are limited to low field applications and with small beam sizes. A reasonable field value for a massless septum is 0.25 T, above that level the transition region becomes too wide or the leak field becomes too high. An easy way to reduce the leak field is to tilt the coils and chamfer the pole tips, increasing the gap height next to the field-free region. This strategy may not reduce the leak field significantly and might reduce the field quality, although when the main field is not strong it can help to improve the design.

2.4.4.1 A massless septum prototype from LANL

Figure 2.23 presents a photograph of a massless septum prototype built for the Proof of Principle (POP) accelerator in Japan. The picture has been taken from [66] for illustration. This magnet is not used in any accelerator but it was used to validate the simulations performed with the FE code POISSON. The gap height, which plays a very important role in the transition region and the leak field value, is 5 mm and it is of the same order as the transition region. The coils are tilted to reduce the magnetic field in the proximity of the transition region, which reduces its width.

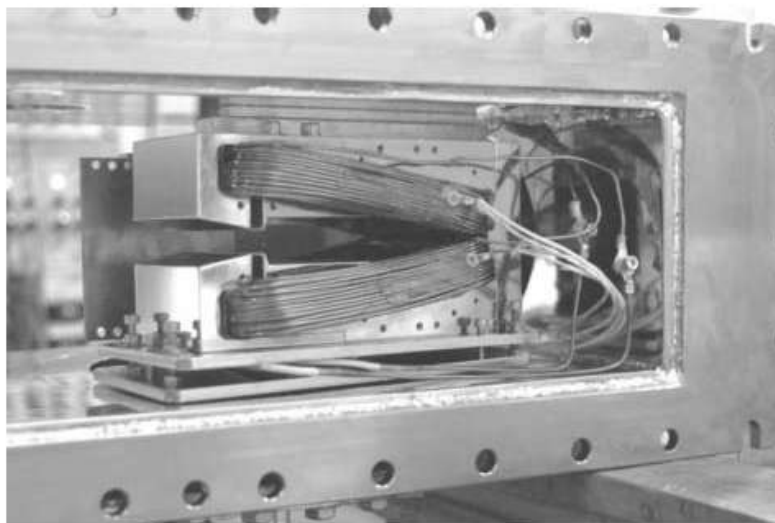


Figure 2.23: Massless septum

2.4.4.2 The hybrid massless septum from NSRF

Apart from tilting the coils there are some other options to reduce the thickness of the transition region in a massless septum. The designer can add compensation coils or permanent magnets to compensate the leak field or improve the field quality in the extracted beam gap. This strategy is studied in depth in [67]. This design achieves a transition width lower than 40 mm for 0.8 T field although the effect of ionizing radiation in permanent magnets has to be taken into account. For clarity, a schematic of the upper half of the magnet is presented in figure 2.24, taken also from [67].

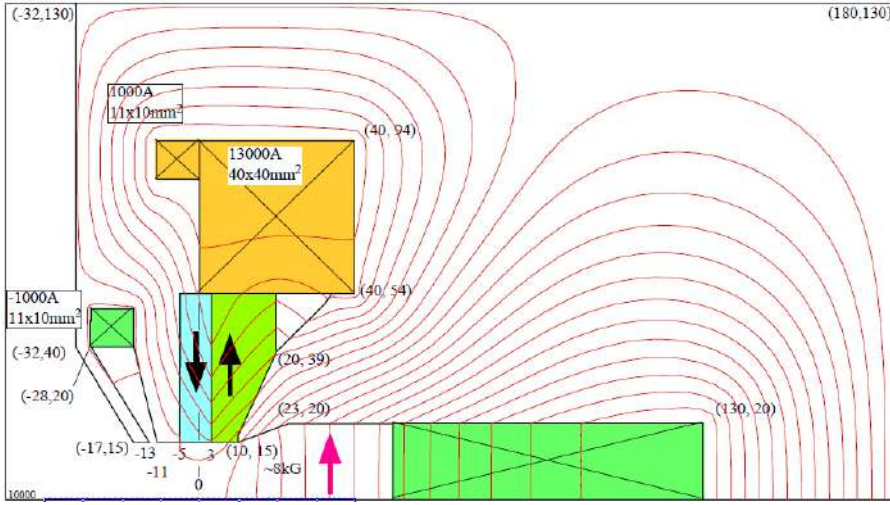


Figure 2.24: Upper half of the hybrid septum magnet

Although a prototype of this septum magnet does not exist yet, the main parameters of the simulations are summarized in Table 2.16. Besides, although they are not septa, hybrid and permanent magnets-based quadrupoles are currently being designed for the CLIC project [68]. In this case the coils are used for fine tuning of the magnetic field gradient.

2.4.5 Opposite fields septa

An opposite fields septum solves the problem of a wide transition region in a massless septum at the expense of adding a blade in the center, losing the massless attribute. The advantage of this kind of septa is that they allow to

Table 2.16: Main parameters of the hybrid septum magnet

Parameter	Unit	MSDA
Magnetic field	T	~ 0.8
Current density (no PM)	A/mm ²	50
Current density (with PM)	A/mm ²	8.1
Transition region thickness	mm	40
PM type	-	NEOMAX 35H
Gap height	mm	30

build a septum with a blade conductor that is under very little stress, which allows to design a very thin blade, as an approximation to a massless septum. Even if the thickness is not zero, it might not be necessary to deal with all the drawbacks of massless septa. In an opposite fields septum the magnetic field reaches zero value at the center of the transition region, thus making the net force in the septum blade also zero or, in the case of a real septum, practically negligible. Figure 2.25 shows the general working principle of the septum described in [69]. This design also has the advantage that can combine two septa into one, saving space and allowing the beam to be deflected into two different transfer lines or targets for example.

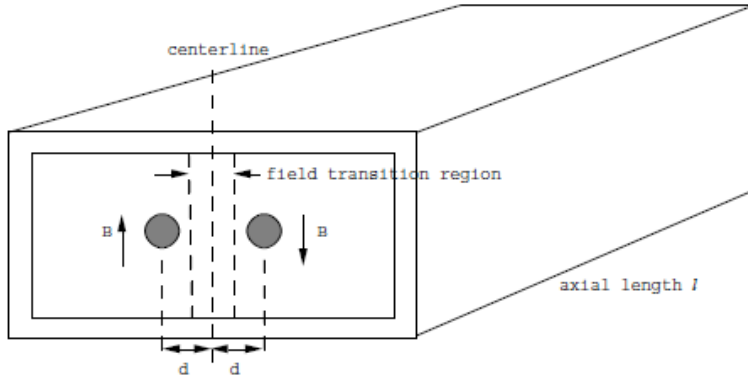


Figure 2.25: Concept of an opposite-fields septum

2.4.5.1 An opposite fields septum magnet at LLNL

As mentioned in section 2.4.5, the width of the transition region is the biggest drawback of using a massless septum in an accelerator. A way to reduce this width is to use an opposite-fields septum magnet. If the flux density is low enough, one of the fields can be shielded using a high permeability material. In figure 2.26, taken from [69] for clarity, the fields simulated with and without shielding are compared.

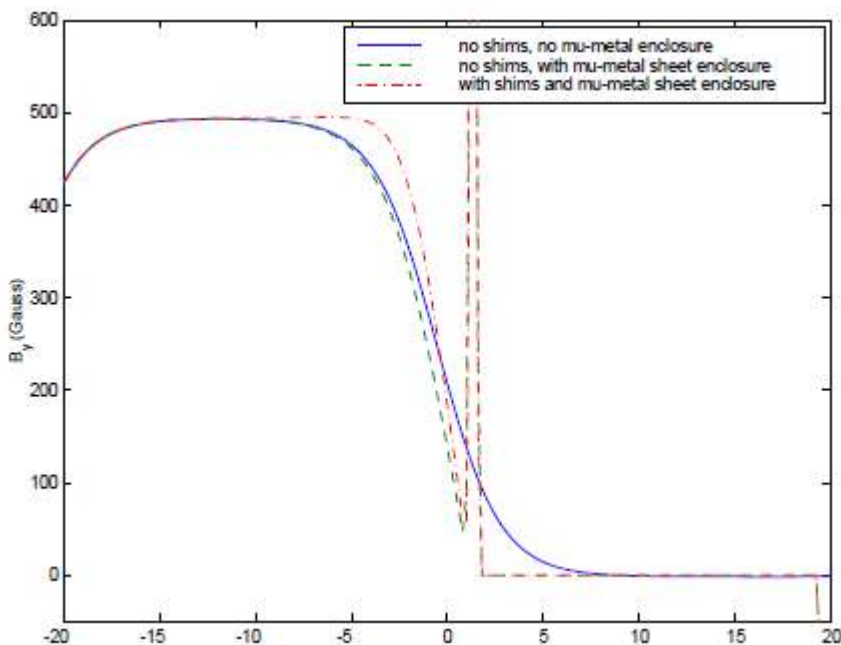


Figure 2.26: Effect of magnetic shielding in an opposite fields septum

For completeness, a small summary of the parameters of this septum is presented in Table 2.17.

Table 2.17: Main parameters of the opposite fields septum at LLNL

Parameter	Unit	MSDA
Magnetic field	T	0.05
Leak field (No shield)	T	0.008
Leak field (With shield)	T	10^{-5}
Beam separation (centers)	mm	56
Transition region thickness (No shield)	mm	100
Gap height	mm	100
Current (N·I)	A·turns	1990
Magnet length	mm	500

2.4.5.2 An opposite fields septum at JHF

The Japan Hadron Facility (JHF) accelerator complex comprises a 50-GeV main synchrotron, a 3-GeV rapid-cycling synchrotron, and a 400-MeV linac. The accelerators provide high-intensity, high-energy proton beams for various scientific fields. These high-intensity, high-energy accelerators, especially the 50-GeV main synchrotron, impose tight demands on the injection/extraction septum magnets for a thin structure, large aperture and high operating field. An opposite-field septum magnet system is one of the solutions to realize a thin septa or very high-field septum magnets. A summary of the magnet parameters is presented in 2.18. Full details of this design can be found in [70]. A cross-section of the model magnet is shown in 2.27.

Table 2.18: Main parameters of the opposite fields septum at JHF

Parameter	Unit	Value
Magnetic field	T	0.188
Field quality	%	1
Transition region thickness (No shield)	mm	16
Gap height	mm	40
Current (N·I)	A·turns	6000
Magnet length	mm	400

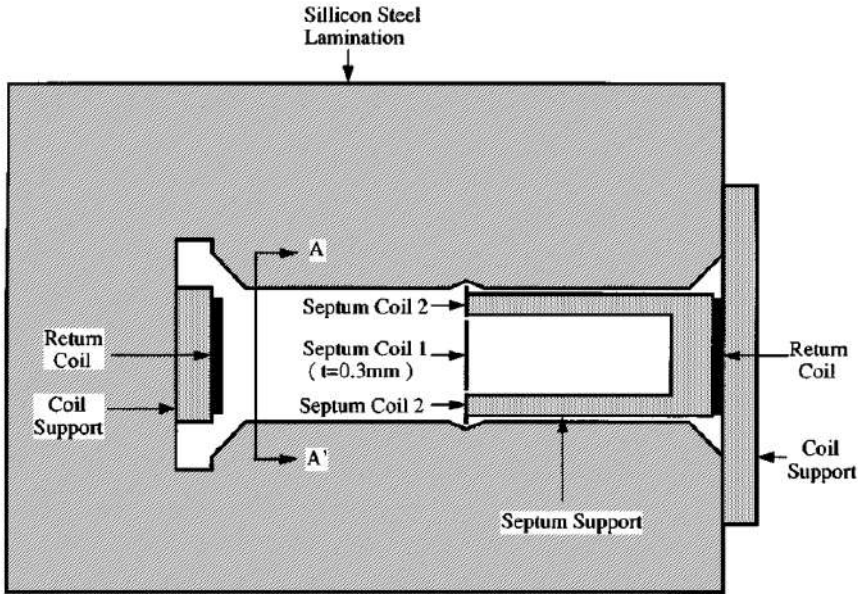


Figure 2.27: Cross-section of the JHF opposite fields model magnet

2.4.6 Permanent magnet septa

Permanent magnet septa use permanent magnet blocks instead of coils to generate a magnetic field. Their main strengths are that the power consumption is zero and the fatigue load does not exist, as opposed to the case of a DC or pulsed septum. The main drawbacks are that the magnetic field can only be slightly adjusted, or in the most simple designs, it can not be regulated at all, and they are relatively weak compared to other types of septa. They can be also quite challenging to assemble. The maximum magnetic field density achieved by this type of magnets is around 1 T usually, although they are extremely rare. Normally they are built using Neodymium- Iron- Boron permanent magnets or Samarium- Cobalt blocks, the latter being a more radiation resistant material [71].

2.4.6.1 The permanent magnet septum at KEK

A schematic of a prototype of a 1:4 prototype built in Japan for the KEK accelerator complex is presented in figure 2.28 and its most relevant characteristics are summarized in Table 2.19. Full details can be found in [71].

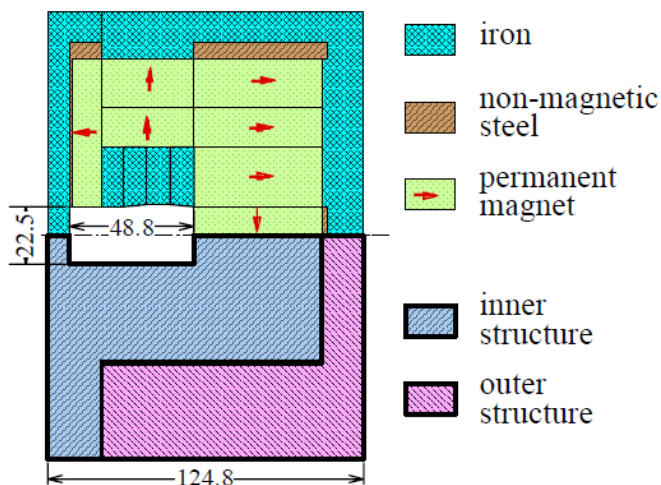


Figure 2.28: Permanent magnet septum schematic

Table 2.19: Major characteristics of the KEK permanent magnet septum

Parameter	Unit	Value
Iron length	mm	227
Main field	T	1
Leak field	% of main field	0.1
Gap aperture	mm (H x V)	48.8 x 22.5
Septum thickness	mm	8.8
Permanent magnets material	-	Nd ₂ Fe ₁₄ B (NEOMAX-32EH)
Variability range	%	-20

2.4.7 Superconducting septa

A superconducting septum, as any superconducting magnet, relies in the placement of the coils rather than in the iron to shape the magnetic field. In fact,

some of them are even ironless designs [72]. The main reasons to use a superconducting design instead of a normal conducting one are the high magnetic field required and the power saving, but a cryogenic system is necessary to operate it plus the risk of quenching has to be dealt with. If the septum is part of the extraction system and it is "lost" temporarily due to a quench it means that the beam needs to be kept in the machine until the superconducting state is recovered and that is a major risk that can not be overlooked. Such a situation is not acceptable for accelerators like the FCC or the LHC, therefore the solution is to dump the beam before the magnetic field decays below the required level. With an adequate quench detection system, it is possible to do so because the time constant of the quench is much longer than the detection itself.

Superconducting septa are the traditional DC septa with the difference of using superconducting cables. Superconducting septa are very uncommon and are mostly conceptual designs and simulations. This is due to the fact that using a superconducting septum poses a problem regarding beam losses since the energy deposited by the losses can make the magnet quench. A septum is inherently prone to losses because the beam travels very close to the septum blade in a curved trajectory. This will cause synchrotron radiation deposited in the septum blade and most importantly, losses from the tails of the beam. In an arc dipole, losses are only due to synchrotron radiation. A quench ideally should be avoided but it will also have to be detected when it happens. Also the electromagnetic force in the conductor might be too high for the septum conductor to be supported if the blade is thin.

2.4.7.1 The NbTi superconducting septum at KEK

An example of a superconducting NbTi septum used in an accelerator is the one installed at KEK in Japan in the 12 GeV proton synchrotron [73]. The main parameters of this septum are presented in Table 2.20. Since the magnet is operated in DC the inductance is not a big issue, but the Lorentz force needs to be taken into account to be sure that the yoke can support the stress without deforming the coil significantly.

Table 2.20: Main parameters of the KEK superconducting septum.

Parameter	Unit	Value
Maximum field	T	2
Aperture (h x w)	mm	134 x 154
Magnetic length	m	1.27
Septum thickness	mm	6.4
Current	A	2220
Current density	A/mm ²	280
Inductance	mH	21
Lorentz force	tonf/m	23

The cross sections of the superconducting septum are shown in figure 2.29.

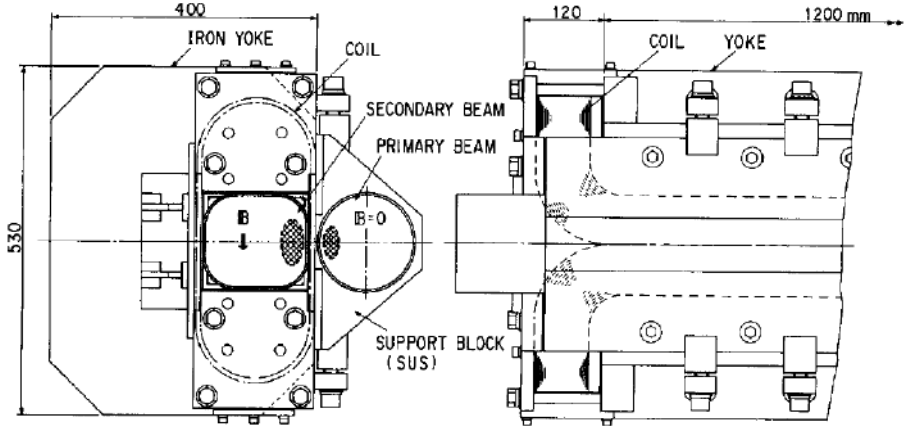


Figure 2.29: Cross section of the 12 GeV superconducting septum at KEK

2.4.7.2 The superconducting septum concept for SIS 300

The FAIR accelerator complex is located at GSI, in Darmstadt, Germany. The accelerator SIS 300 will be built in the near future and there is a project to use a truncated cosine theta superconducting septum [74]. A preliminary cross section with some dimensions is presented in figure 2.30 and a detailed design adapted to the FCC-hh extraction requirements will be described in section 5.1. For clarity, the coil is located on the outer side of the extracted beam.

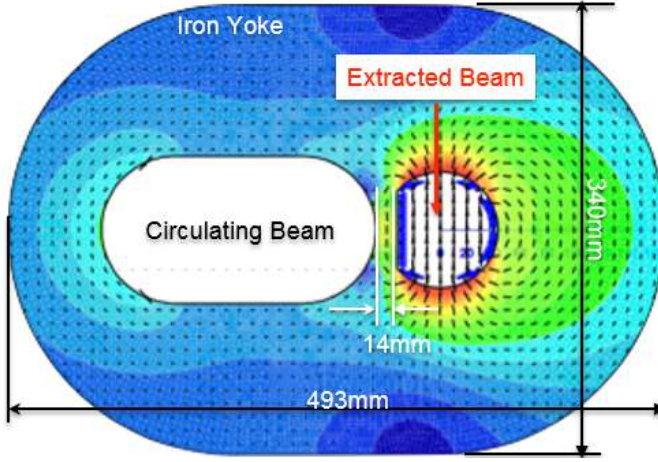


Figure 2.30: Cross section of the SIS 300 superconducting septum

The most relevant characteristics are summarized in Table 2.21.

Table 2.21: Summary of the SIS 300 superconducting septum parameters

Parameter	Unit	Value
Maximum field in the gap	T	3.65
Maximum field in the iron	T	3.45
Septum thickness (without the SC cables)	mm	14
Good field region (h x w)	mm	50 x 35
Leak field	mT	6
Number of strands	-	10
Number of layers	-	2
Current	kA	1.9
Cable type	-	Flat Rutherford
Cable dimensions	mm	1 x 2.5
Turns per pole	-	66
Temperature	k	4.7
Minimum temperature margin	k	1.2
Margin in the load line	%	30

A 2D preliminary design for an 8 T Truncated Cosine θ septum, with a double layer coil in the Cosine θ part of the coil was presented in [75]. The

magnetic simulations achieved an outstanding value of 7.87 T with a leak field below 4 mT in module. The field is generated by 59 turns transporting 15 kA. The mechanical design needs to be studied in depth and a support needs to be designed. The support designed for the 4 T Truncated Cosine θ septum presented in section 5.2.2 can serve as an inspiration for the 8 T support design. Preliminary calculations of the Lorentz forces produce impressive values for the stress in the coil. In the block coil, the Lorentz force per unit length reaches 1100 kN/m, producing a stress of 16 MPa in the coil. The Cosine θ part of the coil needs to withstand a force of 840 kN/m, which results in a 56 MPa stress. The most challenging part of the support design is the block part of the coil because space is very limited. An illustration of the estimated stress in the coil is shown in figure 2.31. The illustration is shown in [75].

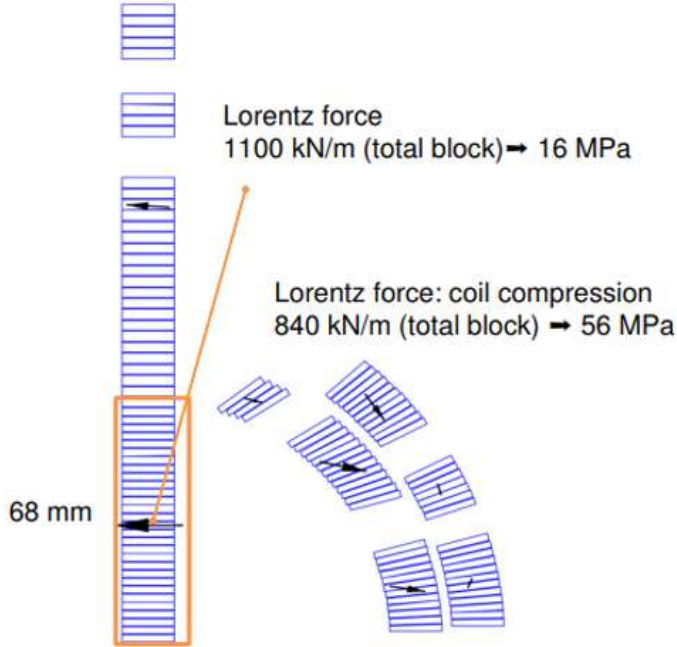


Figure 2.31: Cross section of the SIS 300 superconducting septum

The connection of the coil ends, especially the transition from the block part of the coil to the 2 layers of the Cosine θ part is still to be studied carefully. The design of the coil ends of the 4 T Truncated Cosine θ septum is presented

in section 5.3. This design is inherently complex and a support needs to be designed in parallel.

2.4.7.3 The Muon g^{-2} ironless inflector (Double truncated cosine-theta)

There is an unusual design installed at Brookhaven National Laboratory, in the Muon G-2 experiment [72] which is located in Long Island, New York. This topology is commonly known as double truncated cosine-theta. The coils are made of NbTi and the outer coil acts as a magnetic shield so the circulating beam is not disturbed. The main difference with the Truncated Cosine θ septum showed in the previous section is that the magnet in this case does not need an iron yoke. The magnetic field is contained within the inner and outer layers of the coil. A schematic of said septum and the field distribution is shown for clarity in figure 2.32. Detailed information is available in [76].

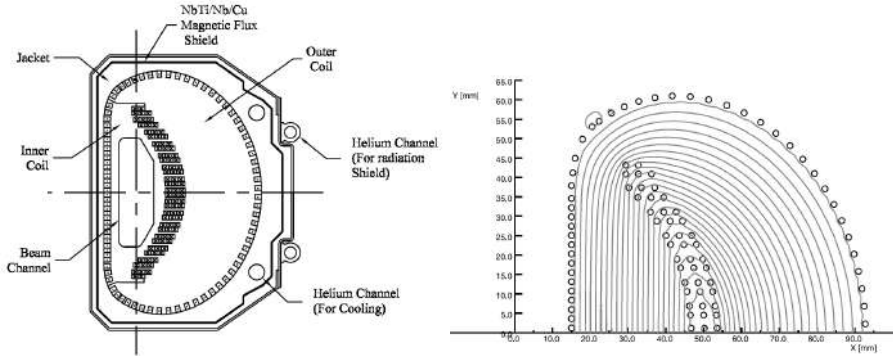


Figure 2.32: Schematic of the Muon G-2 ironless septum and field distribution

This is quite an unconventional design because the main goal of the inflector is to avoid affecting the magnetic field in the muon ring, which poses very strict requirements on the leak field, and the muons will travel through the coil. This would not be possible in a proton machine as the protons would drill a hole in the inflector, but the muons don't interact with matter enough to cause losses. The design is also a so-called self-contained magnet, which ensures that the magnetic field is contained between both conductor layers, allowing to make a design without an iron yoke. The main parameters of this ironless magnet are summarized in Table 2.22.

Table 2.22: g-2 ironless inflector parameters

Parameter	Unit	Value
Maximum field in the gap	T	3.5
Shield capability	T	1.5
Septum thickness (without the SC cables)	mm	14
Beam aperture (h x w)	mm	56 x 18
Leak field	mT	20
Physical length	mm	2025
Number of layers	-	2
Current	kA	3
Cold mass	kg	60
Temperature	k	4.2

2.4.7.4 The stealth dipole

The stealth dipole was introduced by Peter McIntyre in [77]. It can be viewed as a direct drive septum with compensation coils. A 2D design with FCC parameters has been done. A schematic of upper half of the Stealth dipole with the field lines is shown in figure 2.33 and the main characteristics of the septum parameters with a MuMetal shielding around the orbiting beam gap are presented in table 2.23. The bigger set of coils produce the main field in the extracted beam gap, shown in grey with field lines, while the smaller coils cancel the leak field on the orbiting beam gap which is located on the right hand side of the picture, although it is not shown here. The smaller coils can also be viewed as compensation coils which push the leak field into the iron yoke.

Table 2.23: Main characteristics of the stealth dipole

Parameter	Unit	Value
B_0	T	4
B_{leak}	mT	25
Septum thickness	mm	25
Gap height	mm	19
Total current	(A·turns)	86940
Main current / Compensation coil current	(-)	36

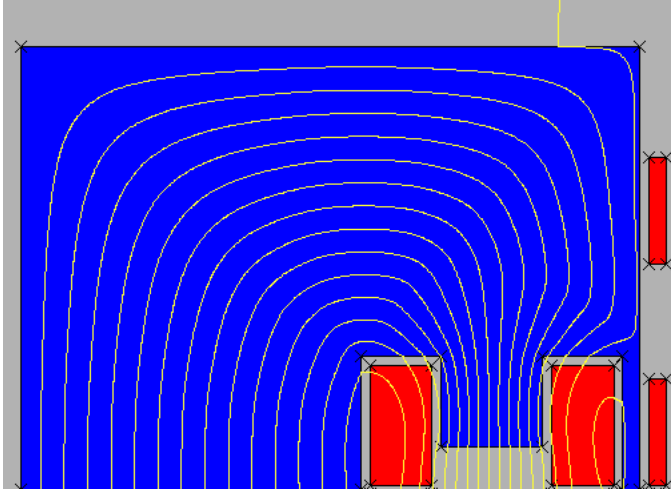


Figure 2.33: Schematic of the FCC stealth dipole design

2.4.7.5 The superconducting shield septum

A different approach to the septa described in the previous section is to use a Superconducting Shield (SuShi) septum. A superconductor is placed around the orbiting beam gap to exclude the magnetic field from that region. The field is excluded by persistent eddy currents generated on the surface of the superconductor when the external magnetic field is changed. The working principle of the shield is shown in figure 2.34.

Preliminary numerical simulations in 2D and 3D have been carried out and more detailed ones are currently being performed. The simulation of Bean's critical state model [78] is implemented by changing the conductivity of the SuShi material at each time step according to the power law shown in equation (2.24).

$$\sigma = |\vec{E}|^{\frac{1-n}{n}} \cdot |\vec{J}| + \sigma_0 \quad (2.24)$$

σ_0 is a very small value to avoid having zero conductivity in a material, which cannot be represented by the software. *sigma* is the electrical conductivity of the material and E is the electric field in the superconducting cable. These simulations are very challenging because the eddy currents are strongly coupled to the electric field in the superconducting material and currently there is no established method to perform them. The challenge of this model

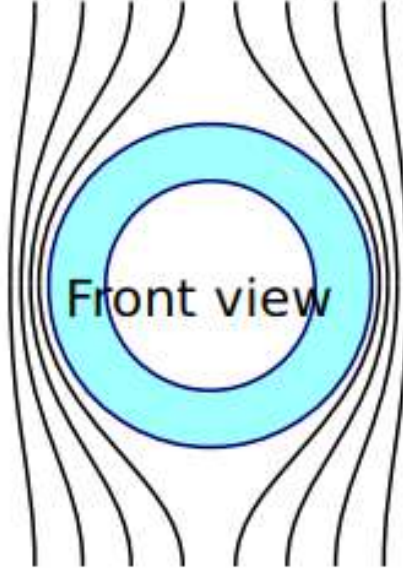


Figure 2.34: Illustration of the SuShi concept

is that the exponent n is usually quite high, in the order of 50 to 100 [79, 80], which results in an almost vertical characteristic, which makes the solution of this equation very long using iterative methods. Every iteration does not take long to calculate, but the time step needs to be reduced to very small amounts, of the order of microseconds. The time steps need to be compared to the full simulation period, which for a preliminary simulation is set to five seconds. However, a promising method to solve this problem has been identified [81] and a simulation is currently being implemented.

The simulations performed using Opera 2D and 3D solve the equation:

$$\nabla \times \left(\frac{1}{\mu} \right) \vec{\nabla} \times \vec{A} - \sigma \left(\frac{d\vec{A}}{dt} + \vec{\nabla} V \right) = \vec{J}_s \quad (2.25)$$

in all space, and in conducting regions:

$$\vec{\nabla} \cdot \sigma \left(\frac{d\vec{A}}{dt} + \vec{\nabla} V \right) = 0 \quad (2.26)$$

Equations 2.25 and 2.26 are the Maxwell equations for the magnetic field, respectively:

$$\vec{\nabla} \times \vec{H} = \vec{J} \quad (2.27)$$

$$\vec{\nabla} \cdot \vec{J} = 0 \quad (2.28)$$

This results in:

$$E = -\frac{d\vec{A}}{dt} - \vec{\nabla}V \quad (2.29)$$

Given that \vec{A} and V are found at each time step and are primary results, they cannot be used in the same time step to calculate additional values. Therefore the conductivity (σ) in equation 2.24 has to be made dependent on the electric field (\vec{E}) and not on the vector potential (\vec{A}).

Measurements have also been performed to validate and complement the simulations. Two successful prototypes have been tested at CERN. One of them is made of bulk MgB₂ [79] and another one made of a multilayer NbTi/Nb/Cu material [79].

At the same time, the magnetic field in the high field region of the septum is shaped by the shape of the superconducting material. The magnetic field is generated by a Canted Cosine-theta (CCT) magnet with an aperture big enough to fit the SuShi and both vacuum chambers. This magnet was not available at the time when the measurements were performed so another magnet was used. Three different superconducting materials are being considered: bulk MgB₂, HTS tape and a multilayer Cu/Nb/NbTi composite. Detailed information on the measurements and the experimental setup of the MgB₂ and HTS tape prototypes is presented in [79]. The results of the measurements performed on the MgB₂ SuShi prototype are listed in table 2.24.

Table 2.24: Main characteristics of the MgB₂ SuShi prototype tested at CERN.

Parameter	Unit	Value
B ₀	T	2.6
B _{leak}	mT	0.1
Septum thickness	mm	8.4
Inner diameter	mm	45

The multilayer material is being tested in SM18 at CERN at the time of writing this text and the preliminary results are shown in table 2.25. Detailed

information on this prototype and the tests performed can be found in [82]. Figure 2.35 shows a picture of the experimental setup with the shield inserted into the MCBY magnet, before insertion in the cryostat.



Figure 2.35: SuShi NbTi prototype assembled in the MCBY magnet prior to insertion in the cryostat.

As a second step of the study, a modified Canted Cosine θ magnet is being designed and the SuShi geometry will change from a tube to a half moon shape to produce outstanding field quality in the orbiting beam gap naturally, using only the geometry of the shield. This concept is illustrated in figure 2.36, reproduced from [82]. Full details of the measurements on both prototypes and the CCT-like septum concept, which is expected to be tested at CERN in 2021, can be found in [83].

2.4.8 A semianalytical method for coil placement in septa

A semianalytical method for finding the coil positions necessary to produce a given magnetic field with a chosen number of current lines is presented in

Table 2.25: Main characteristics of the NbTi SuShi prototype tested at CERN.

Parameter	Unit	Value
B_0	T	3
B_{leak}	mT	0.1
Septum thickness	mm	4
Inner diameter	mm	45

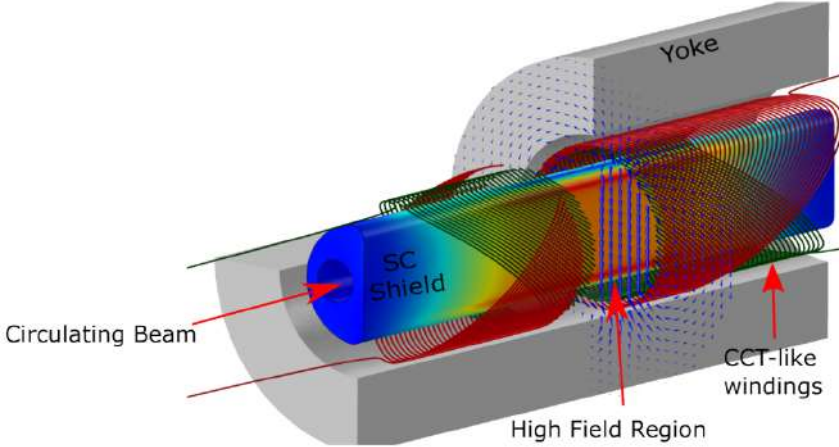


Figure 2.36: Future SuShi prototype to be tested in 2021

[84]. The input of the algorithm is the desired multipole configuration and the number of current lines to be used per pole. The output is a complex variable denoting a position $z = x + i \cdot y$. This should not be confused with a conformal mapping, the complex variable z is only present when the magnetic field multipoles are represented in cartesian coordinates, where $\vec{B} = B_x(x, y) + i \cdot B_y(x, y)$. The advantage of this algorithm is that the only necessary techniques to generate the polynomials are linear algebra techniques. The solution of the polynomials can be easily found using numerical methods and implemented in any mathematical software. The roots of these polynomials will be the positions of the current lines in the complex plane. The method has also some limitations, in particular, it is a 2D method, the magnet ends need to be designed independently. The method assumes the cable size to be zero, which depending on the magnet could not be an acceptable simplification. The method assumes isotropic linear media. Therefore, it is not valid to design an iron dominated

magnet that works near the saturation point. Besides, the method may produce results that are physically impossible to build, some of the current lines might be placed at very short or very long distances from the others or it might be necessary to provide unrealistic currents. Although the method has limitations, it can still be very useful for different applications, like designing air dominated magnets or cancelling stray magnetic fields that can sometimes be present in septa. Traditionally magnet designers have always followed an iterative method, based mostly on experience and optimizing the pole tip shape. It is also common to consider the iron as a linear material in the first simulations to reduce computation time significantly, which is a situation that would benefit from applying this algorithm. The number of iterations to design a magnet can be very high, with hours-long 3D simulations. Using this formalism at the beginning of the design, the number of iterations can be reduced, saving time in the full process. Combined function magnets can also be designed with this method, although superposition can always be applied.

2.4.8.1 Unipolar configuration

There are two different kinds of magnets configurations that can be produced with this algorithm, unipolar (all current lines flow in the same direction), or bipolar (there are positive and negative current lines). The current lines placed with the unipolar configuration need to be closed to produce a coil and it must be done in a way so that the magnetic field multipole produced is not perturbed.

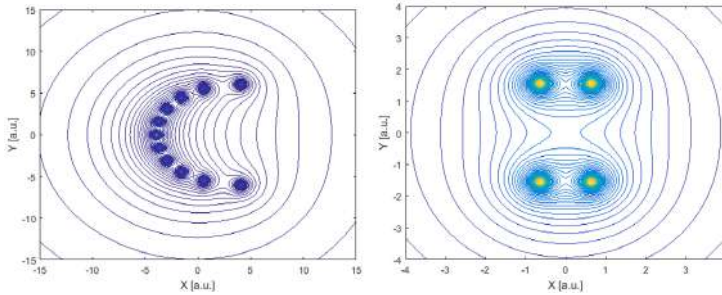


Figure 2.37: Unipolar configuration examples of a dipole and a quadrupole field

2.4.8.2 Bipolar configuration

In the case of bipolar designs, the number of positive current lines is the same as the number of negative current lines, therefore, there will always be an even number of current lines.

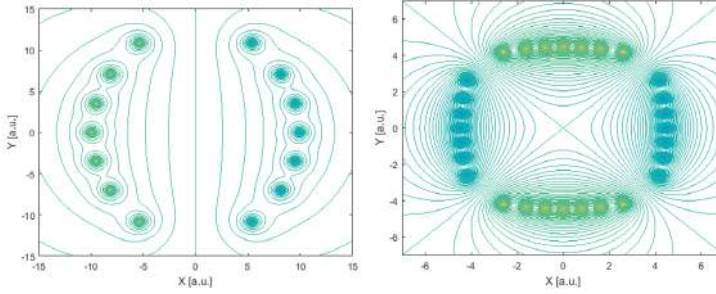


Figure 2.38: Bipolar configuration examples of a dipole and a quadrupole field

A more exotic design with a unipolar configuration can be performed with this method, shown in figure 2.39 [85, 86]. In this case, the orbiting beam gap must be between the coil and the iron yoke. The iron yoke must be designed to provide a return path for the magnetic field lines and avoid saturation.

This preliminary design does not consider the coil support or a further optimization of the coil placements, which have been treated as almost current lines. A 2D finite element simulation was necessary to take into account the saturation of the iron yoke. It is necessary to allow enough width for the iron yoke to remain below saturation level, otherwise the iron permeability would not be significantly greater than the permeability of air and there would be a non negligible magnetic field in the orbiting beam gap. The configuration in this magnet is unipolar, which makes it necessary to close the current lines although this has not been done for this magnet.

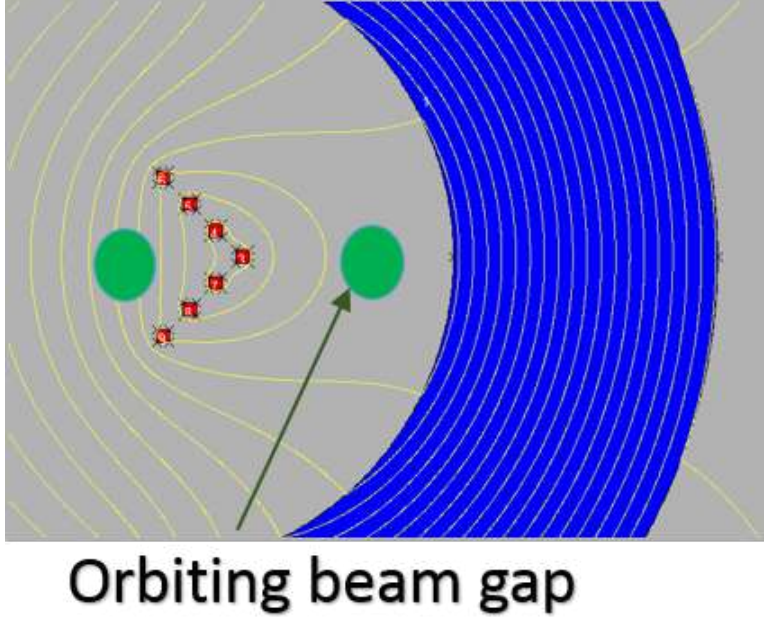


Figure 2.39: Detail of magnet gap and coil layout for the massless septum designed with the analytical method

2.5 Figure of merit

In the previous sections, it has been made evident that there are many different septa topologies with different strengths and weaknesses, which makes it difficult to choose an alternative when starting a design and deciding which is the best technology for a given system. It is of interest to create a common metric with fixed criteria. Parameters of interest related the performance of a septum magnet are the main field, the leak field, the septum thickness, the aperture height and the saturation of the magnetic yoke. The proposed figure of merit is a non dimensional variable that increases with a better septum performance and decreases when the parameters differ from the optimal values. The formula to calculate the figure of merit is presented in equation (2.30).

$$K_{DC} = \frac{B_0}{B_{leak}} \frac{B_{pole}}{B_{sat}} \frac{h}{s} \quad (2.30)$$

The first factor corresponds to the ratio between main field (B) and leak field (B_{leak}), a septum will be better when the main field is strong and the leak field is low. The second factor introduces the saturation of the iron yoke. B_{sat} is the saturation value of the iron and B_{pole} is the magnetic field at the pole. For a normal conducting septum this factor should be close to unity since it is quantifying the efficiency of the iron use in the yoke. In the case of superconducting septa, B_{sat} is taken as the critical field of the superconductor and B_{pole} as the peak field in the coil, regardless of its location. Above the critical field the superconductor will quench and the septum will not work, so it is a factor quantifying the efficiency in the use of superconducting material. A lower factor will indicate an over-dimensioned design, hence increasing the costs and possibly using more space than necessary. In the case of the SuShi septa, there is no coil or iron yoke apart from the external magnet that produces the magnetic field independently of the SuShi, so this factor will be replaced by the ratio between the thickness of the SuShi device and the penetration depth at the corresponding working point. It is obvious that this factor can never be one because there needs to be a margin to the load line. The last factor is a comparison between the gap height (h) and the septum thickness (s). A thinner septum blade is preferable to a thicker one, while a bigger gap height is preferable for impedance and loss reduction.

In the case of superconducting septa, equation 2.30 is adapted as explained above, producing equation 2.31.

$$K_{SC} = \frac{B_0}{B_{leak}} \frac{B_{coil}}{B_{peak}} \frac{h}{s} \quad (2.31)$$

For SuShi septa, the figure of merit is adapted according to equation equation (2.32).

$$K_{SuShi} = \frac{B_{ext}}{B_{leak}} \frac{s}{d_p} \frac{h}{s} \quad (2.32)$$

In this case d_p is the penetration depth of the external magnetic field. Equation equation (2.32) can be simplified but it is presented as the multiplication of three ratios for similarity with equation (2.30).

A description of every septa topology being considered for FCC and some more and a calculation of the figure of merit for every one of them can be found in [87]. The figure of merit calculated for every septum presented in [87]

can be found in table 2.26, which has been reproduced here to better illustrate the scope of the figure of merit and its calculation. The values obtained by the SuShi prototypes are significantly higher than the other topologies because the SuShi operates always at critical current which makes an almost perfect shielding thanks to the persistent eddy currents present in the surface. The shielded Truncated Cosine θ (TCT), Double Truncated Cosine θ (DTCT) and the Stealth dipole present a very low figure of merit. This is due to the fact that both designs produce a leak field that is two orders of magnitude higher than the SuShi prototypes since they rely on compensation coils or iron rather than in a natural phenomenon like eddy currents. However, depending on every individual case, the leak field can be totally or partially mitigated by placing a shield around the zero-field region. It could be argued that since the leak field can be mitigated it has no place in the calculation of the figure of merit. However, since the SuShi prototypes have been measured to reduce the leak field below 0.1 mT, it is fair to allow shielding to septa with a higher leak field.

For comparison, the figure of merit has been calculated for some representative septa to serve as a benchmark of the values that can be achieved by existing septa. The septa used for this benchmark are the eddy current septum at SOLEIL, presented in section 2.4.2.2, the SMH16 at CERN, presented in section 2.4.1.5 and the MSE septum from MedAustron. The SMH16 is a pulsed septum and the MSE septum of MedAustron is a DC septum. These septa have been chosen as reference because they are representative of the different type of septa that are usual in accelerators. Since it is not possible to know which iron was used to build the yokes of these septa, the saturation of the iron has been set at 1.6 T, which is a conservative value for iron in general, but septa normally work far from the saturation point and it is not necessary to choose the highest saturation iron. The saturation could be set to 1.8 or 2 T although that does not change the order of magnitude of the figure of merit.

Table 2.26: Calculation of the figure of merit for the different septa topologies presented.

Septum	B_0/B_{ext} (T)	B_{sat}/B_c (T)	B_{pole}/B_{peak} (T)	B_{leak} (mT)	h (mm)	s (mm)	K (-)
SMH16	1.2	1.6	1.2	14	30	3	0.64
SOLEIL eddy current	0.29	1.6	0.29	0.18	15	3.5	1.23
Shielded TCT	4	6.5	5	0.1	35	30	36
Shielded TDCT	4	6.5	6.5	1	56	30	7.56
SuShi MgB2	2.6	8.4	8.4	0.1	50	8.4	154
SuShi NbTi	3	4	4	0.1	50	4	375
Shielded Stealth	4	6.5	3.76	0.1	19	25	17.5

In the following chapters, the figure of merit will be calculated for the septa topologies being considered for FCC-hh injection and extraction and the design of the injection and extraction septa layout will be based on this figure of merit. Based on the figure of merit, the only septa present in future accelerators should be SuShi type septa. The figure of merit cannot be the only decision tool used when deciding the septum topology to be used in a given case. There are many other factors that are more difficult to be quantified in a single figure, like for example the availability of cryogenic cooling, space constraints or power consumption requirements. The figure of merit then becomes a powerful decision tool although not the final one.

Chapter 3

Lambertson septa

3.1 Introduction

A description of the Lambertson septa used in past and present accelerators (ISR and LHC) will be done in sections 3.2 and 3.3. Then, limitations and possible upgrades of this septa topology will be explored in the following sections. The limitations of the Lambertson septa topology are established in section 3.4.1. A detailed simulation of the cross section of the LHC Lambertson septa, scaled for the FCC, is performed in section 3.4. Different modifications of the cross section to increase the field level are explored. Passive modifications of the cross section, like adding a secondary orbiting beam gap or changing the shape of the orbiting beam gap are studied in section 3.5. The use of high saturation materials in the area around the orbiting beam gap is studied in section 3.5.3. Active compensation of the leak field is explored in section 3.5.4. The use of a super ferric variant of the scaled Lambertson septum is briefly discussed in section 3.6. Finally, in section 3.7, the figure of merit is calculated for the different Lambertson septa variants described in this chapter.

3.2 ISR Lambertson septa

The Intersecting Storage Rings (ISR) was the first Hadron collider in the CERN accelerator complex. It operated between 1971 and 1984 colliding protons at 300 GeV from two independent rings, which intersected at the interaction point [88]. Each ring of the ISR used two Lambertson septa for injection

from the PS to the ISR, with a septum thickness of 14 and 20 mm respectively. An interesting particularity of these magnets is that they were tilted, as shown in figure 3.1. The magnets were tilted because injection into the ISR from the PS was made in a plane inclined from the ground. In the case of the first septum, the tilt angle was 12.5 degrees and for the second septum the tilt was 22.75 degrees. It can also be observed that there is a main coil (1) and a compensation coil (3). The purpose of the compensation coil is to guide the magnetic field lines (2) away from the orbiting beam gap (4) so only the beam that is going to be injected sees the magnetic field (5 and 6). It is necessary due to the high field in the extracted beam gap and the asymmetry of the yoke, which makes the magnetic reluctances of the two halves of the magnetic circuit different. If no action was taken, there would be some stray field leaking into the orbiting beam gap because different field lines would see different magnetic reluctances because the length to be closed by them would be different. In these magnets, a different approach was taken. The cross-section of both halves were made different to make the magnetic reluctance of each side equal. Therefore the vertex of the groove becomes the symmetry axis for the magnetic field and no field lines cross to the opposite side of the magnetic circuit.

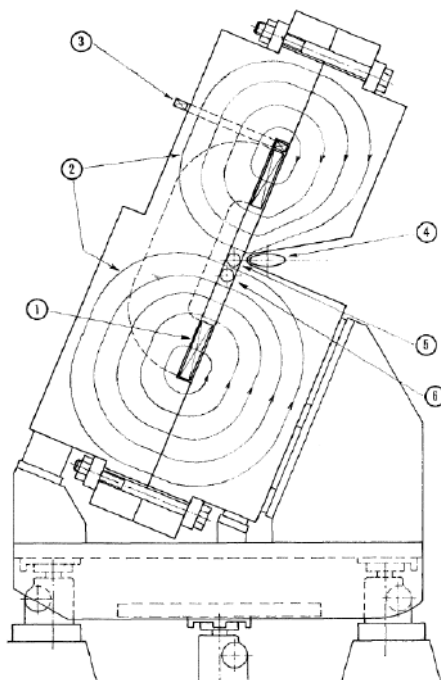


Figure 3.1: Schematic of an ISR Lambertson septum

A picture of one of these septa magnets is also shown in figure 3.2. Although it cannot be appreciated in the drawing, a steel foil with cooling channels was added around the vacuum chamber of the orbiting beam gap. Due to lack of space, the bakeout of the vacuum chamber was done by circulating a current of 1000 A from one end to the other. While this was done, the yoke had to be cooled via the steel foil to avoid degradation of its properties.

The characteristics of the ISR Lambertson septa are summarized in table 3.1 [89].



Figure 3.2: ISR Lambertson septum in storage

Table 3.1: Main characteristics of the ISR Lambertson septa

Parameter	Unit	Value
Septum blade thickness	mm	14/20
Magnetic field	T	1.24/1.48
Inclination angle	Degrees	24.5

3.3 LHC Lambertson septa description

As of today, there are two families of Lambertson septa installed in the LHC. The MSI and the MSD magnets, used for injection and extraction respectively. The MSI has two variants (MSIA and MSIB) while the MSD has three (MSDA, MSDB, MSDC). They were built by CERN in collaboration with IHEP (Protvino). As a particularity, both the MSI and the MSD have a thin (0.9 mm) MuMetal layer around the orbiting beam pipe to reduce the leak field and its influence on the orbiting beam.

3.3.1 LHC MSI description

The 450 GeV proton beam coming from the SPS is injected into the LHC by means of vertically deflecting kicker magnets and horizontally deflecting septum magnets. The constant injection energy explains why these septa are operated in DC. There are five injection septa per injection line, two MSIA

and three MSIB. The differences between the MSIA and MSIB magnets are bifold, the septum thickness of 6 mm for the MSIA versus 15 mm in the case of the MSIB, and the different number of turns. The coil of the MSIA has sixteen turns and the coil of the MSIB has twenty four turns. All magnets in each injection line are connected in series and hence they have the same current and the difference in the field values is due to the different number of turns.

As a particularity, the MSI magnets need to have two orbiting beam gaps to allow both LHC beams to pass through the yoke. A picture and a schematic of the cross section of the MSI magnets are presented in figure 3.3 and figure 3.4 respectively.

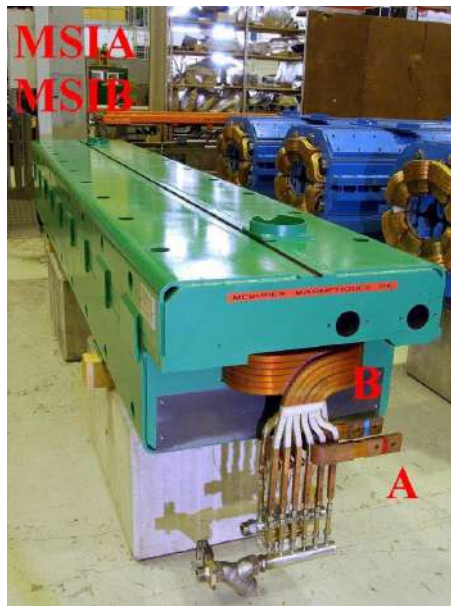


Figure 3.3: Picture of a MSI Lambertson septum

The characteristics of the MSI septa are summarized in table 3.2 and have been taken from [90, 63], where more detailed drawings can also be found. Detailed magnetic measurements can be consulted in [91].

3.3. LHC LAMBERTSON SEPTA DESCRIPTION

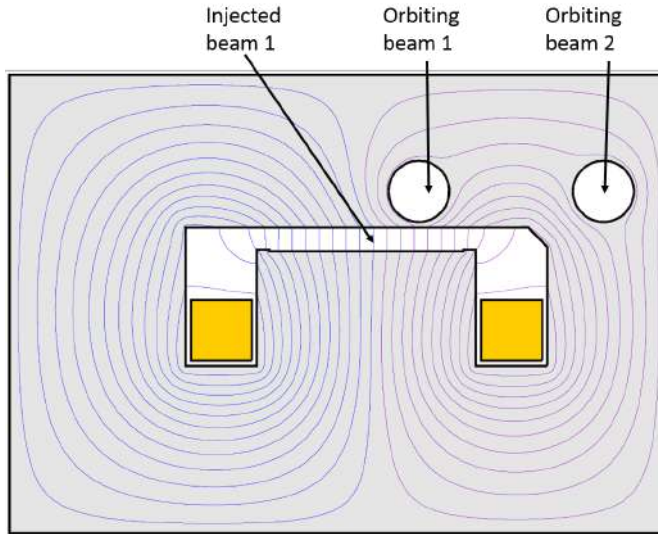


Figure 3.4: Schematic cross section of a MSIA Lambertson septum with field lines

Table 3.2: Summary of the characteristics of the MSI Lambertson septa

Parameter	Unit	MSIA	MSIB
Magnetic field density	T	0.76	1.13
Septum thickness	mm	6	15.5
Pole gap height	mm	25	25
Physical length	mm	4000	4000
Effective length	mm	3718	3718
Orbiting beam gaps diameter	mm	64	64
Current	A	950	950
Number of turns	-	16	24
Power	kW	10.6	15.9
Cooling flow	l/min	7.9	11.8

3.3.2 LHC MSD description

The LHC MSD septa are used to dump the circulating beam at any energy between 450 GeV and 7 TeV. Contrary to the MSI septa, when there is beam in the LHC, they are always on and they must follow the energy swing of the accelerator. The MSD magnets are a family with three consecutive different magnet models (MSDA, MSDB and MSDC). The differences between them are the number of turns in the coil and the septum thickness. For each dump line there are 15 septa magnet modules, each 4.46 m long. There are 5 modules of the MSDA magnets, followed by 5 MSDB and 5 MSDC downstream, all electrically connected in series.

A picture of two MSD septa in back to back configuration was shown in figure 2.22 and a schematic cross section with field lines is presented in figure 3.5.

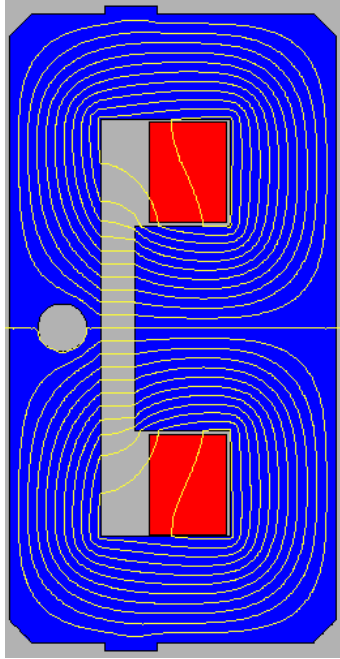


Figure 3.5: Schematic cross section of a MSD Lambertson septum with field lines

The characteristics of the MSD septa are summarized in table 3.3 and have

been taken from [90, 63], where also more detailed drawings can be found. The detailed magnetic measurements can be consulted in [92].

Table 3.3: Summary of the main characteristic of the MSD Lambertson septa

Parameter	Unit	MSDA	MSDB	MSDC
Magnetic field density	T	0.80	0.99	1.16
Septum thickness	mm	6	12	18
Pole gap height	mm	44	44	44
Physical length	mm	4460	4460	4460
Effective length	mm	4095	4095	4095
Orbiting beam gap diameter	mm	64	64	64
Current	A	880	880	880
Number of turns	-	32	40	48
Power	kW	22.7	28.3	34
Cooling flow	l/min	16.5	20.7	24.8
Number of septa per beam	-	5	5	5

While the power dissipated on the MSD magnets is significant, a study was undertaken to assess the performance of these septa and the extraction optics if the LHC is operated at 15 TeV centre of mass energy (c.o.m.) instead of 14 TeV. That is 7.5 TeV per beam instead of 7 TeV per beam [62]. The result is satisfactory, the MSD magnets are not the bottleneck for the operation at 7.5 TeV because there is still some margin to increase the field in the main gap without increasing the leak field significantly. However, to avoid installing an additional power converter the optics of the dump line have to be slightly modified and the centre of the beam moves 0.3 mm vertically, which is not significant. The cooling system and the existing power converter can cope with the parameters at 7.5 TeV without problems.

3.4 LHC Lambertson septa scaled for the FCC

3.4.1 Finding the limiting factor of the existing Lambertson septa

For FCC-hh, the top extraction energy will reach 50 TeV per beam, which will impose very demanding requirements on the septa magnets. A very quick check that can be done easily is to scale up the same magnets from the LHC

requirements to the FCC extraction parameters. The FCC study baseline parameters in March 2017 are summarized in table 3.4 and compared with the LHC values, which can be found in [93]. Being a study project the baseline can be subject to changes but at the moment of writing this document they are the latest values available. The leak field values have been established choosing typical values for Lambertson septa. In section 7.2 they will be validated.

Table 3.4: FCC beam dump baseline parameters as of March 2017

Parameter	Unit	FCC	LHC
Available length	m	120	80
Magnetic field integral	Tm	190	59.2
Total deflection	mrاد	1.2	2.4
Blade thickness	mm	25	12/16/18
Good field region (hor/ver)	mm	28/19	32/32
Leak field	mT·m	1012	96
Average leak field (per magnet)	mT	5	1.6
Total dump line length	km	2.8	975

The scaling of the magnetic field in a FCC version of the LHC Lambertson septa has one hard limit. If the magnetic field in the gap is too high the septum blade will saturate and the leak field will increase. Therefore the main limit for the increase of the magnetic field will be the leak field. To calculate an approximate value of the maximum magnetic field in the extracted beam gap one can use equation 3.1, usually named magnetic Ohm's law:

$$NI = \phi \cdot \mathfrak{R} \quad (3.1)$$

The magnetic reluctance (\mathfrak{R}) is the result of applying the electrical analogy to a magnetic circuit. It is analogous to the resistance in an electrical circuit. The magnetic flux (ϕ) corresponds to the electrical current in Ohm's law and the left term, NI , named usually magneto-motive force, takes the place of the voltage. For the Lambertson limitation, the most interesting term is the reluctance. The magnetic reluctance definition is attributed to Henry Augustus Rowland [94] and for a uniform magnetic circuit it is given by 3.2 [95].

$$R = \frac{l}{\mu_r \mu_0} \quad (3.2)$$

In equation (3.2), the reluctances of the different media in a magnetic circuit will have to be added like electrical resistances, in series or parallel. Since the Lambertson septum is symmetrical, only the upper half of the magnetic circuit is shown in figure 3.7, where the green arrows indicate the mean path of the magnetic flux. Due to the inherent symmetry, equation 3.1 can be applied to the full septum or only to one of the halves. At the orbiting beam gap, the reluctance of the vacuum and the iron are connected in parallel, so the flux will be divided according to the different reluctances. Therefore, while the iron is not saturated, its permeability will be much higher than the permeability of vacuum, so its reluctance will be much smaller than the one of the yoke and practically all the flux will avoid the orbiting beam gap. As the iron starts to saturate and its permeability decreases, the vacuum term becomes more relevant and can not be neglected as when the iron is working in the linear part of the BH curve. That means that while the iron yoke of the septum is not saturated, the equation for the magnetic circuit can be calculated using equation 3.3. The magnetic circuit is shown in figure 3.6.

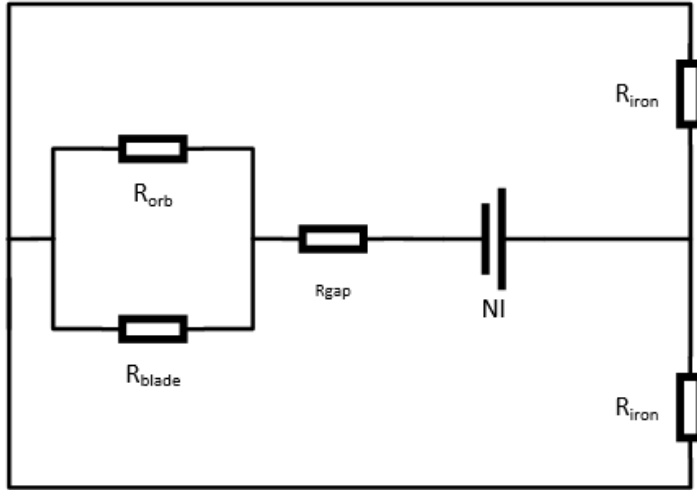


Figure 3.6: Magnetic circuit of the Lambertson septum

$$NI = \phi \cdot \mathfrak{R}_{\text{gap}} + \phi \cdot \mathfrak{R}_{\text{iron}} + \phi \cdot \mathfrak{R}_{\text{orb}} \quad (3.3)$$

It has been assumed in equation 3.3 that no magnetic flux crosses the gap

near the coil. It is a valid assumption as long as the corners of the yoke are not saturated.

Then

$$NI = \phi \cdot \frac{l_{gap}}{\mu_{gap}\mu_0 A} + \phi \cdot \frac{l_{iron}}{\mu_{iron}\mu_0 A} + \phi \cdot \frac{l_{orb}}{\mu_{orb}\mu_0 A} \approx \phi \cdot \frac{l_{gap}}{\mu_{gap}\mu_0 A} \quad (3.4)$$

With

$$\frac{1}{\Re_{orb}} = \frac{1}{\Re_{blade}} + \frac{1}{\Re_{leak}} \approx \frac{1}{\Re_{blade}} \quad (3.5)$$

and

$$\phi = \phi_{blade} + \phi_{leak} \approx \phi_{blade} \quad (3.6)$$

And as the iron, especially the septum blade, becomes more saturated the inequality $\mu_{iron} \gg \mu_{gap}$ becomes less acceptable and therefore it is necessary to take into account the iron part of the circuit, and the orbiting beam gap.

A quick calculation, taking values for the nominal parameters of the MSDA magnets [90, 63] and the relative permeability of non-saturated iron as 4000 [95], the value of the nominal magnetic flux in the MSDA septum magnet can be computed:

$$\phi = \frac{N \cdot I \cdot \mu_{gap} \cdot \mu_0 \cdot A}{l_{gap}} = 434.3 Wb \quad (3.7)$$

The simplest way to increase this value is to scale it linearly, an approximation which is valid if the working point of the iron is in the linear part of the BH curve. A reasonable value for the saturation of magnetic steel is 1.4 T [65, 91, 92, 95]. The precision of this value is not extremely important since this calculation is a linear approximation and will be validated with detailed simulations afterwards. The scaling of the magnetic flux is given by equation 3.8.

$$\phi_{max} = \phi \cdot \frac{1.4T}{0.80T} = 760 Wb \quad (3.8)$$

Introducing this new value for the magnetic flux in equation (3.7) we obtain a new value for the excitation current of 49280 A·turns, which corresponds to a current of 1540 A. To validate this calculation, simulations in 2D have been performed. The septum that meets the FCC requirements is only the MSDC but all three models have been simulated for completeness. The values of the leak field in the centre of the orbiting beam gap are plotted in figure 3.8

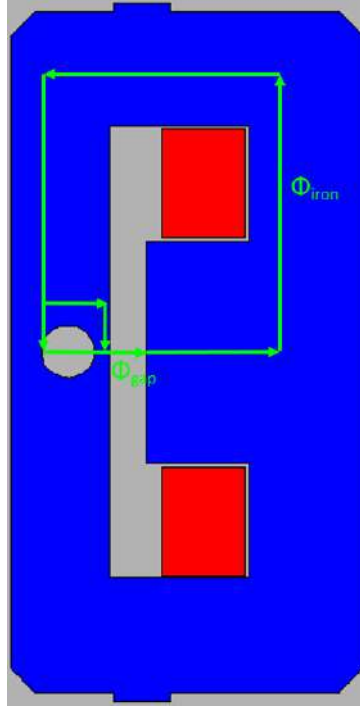


Figure 3.7: Schematic of the magnetic flux in the Lambertson septum

as a function of the main gap. It can be seen that for the MSDC, the maximum leak field allowed is reached when the field in the extraction beam gap is 1.36 T, which is in good agreement with the calculation from equation 3.8. It can be observed that the MSDC model saturates later than the MSDA and MSDB. This is due to the different blade thickness of the three models, the MSDC septa have more space for the flux to circulate through the septum blade. Although the plots show the magnetic field density, which is the common quantity used in magnetic measurements, the quantity that causes the saturation is the magnetic flux, originated by the excitation current.

3.4.1.1 Calculating the leak field

Once the maximum leak field allowed has been estimated analytically, the next step is to simulate the magnets, in this case using Opera 2D, and validate the

calculations explained in this section and in section 7.2.

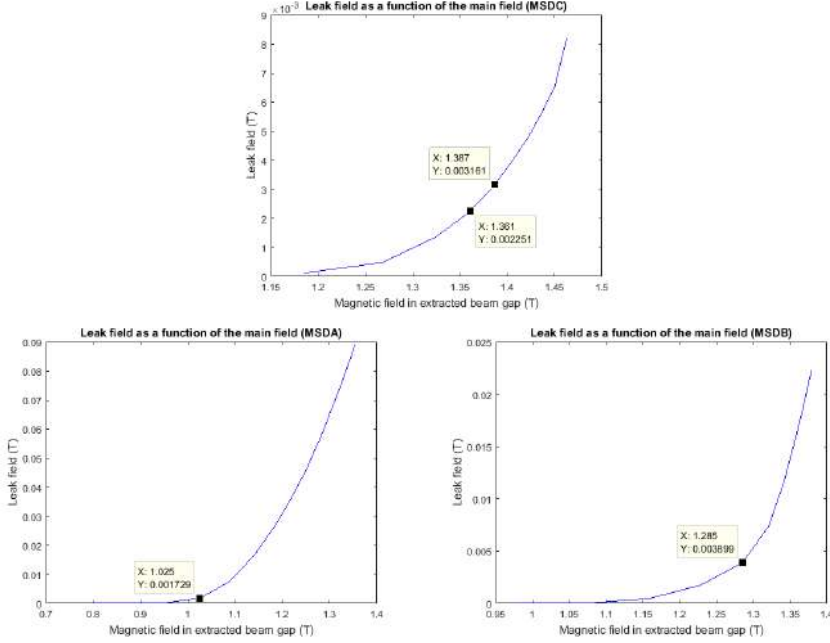


Figure 3.8: Leak field of the MSD Lambertson septa as a function of the main field

In order to reduce the leak field in the orbiting beam gap there is a 0.9 mm MuMetal foil installed around the vacuum chamber. Besides, the space present between this MuMetal foil and the iron yoke is only 2 mm, which is very thin compared to the diameter of the orbiting beam gap but it is necessary to place heating bands for the vacuum chamber bake out. The model has been meshed with enough elements to represent accurately the variation of the magnetic flux across all the different materials [96]. The model used for the MSDC simulation is presented in figure 3.7. The coil has been simplified, and the individual turns have been replaced by a single turn carrying the corresponding current. A detail of the mesh in the area of the orbiting beam gap is shown in figure 3.9.

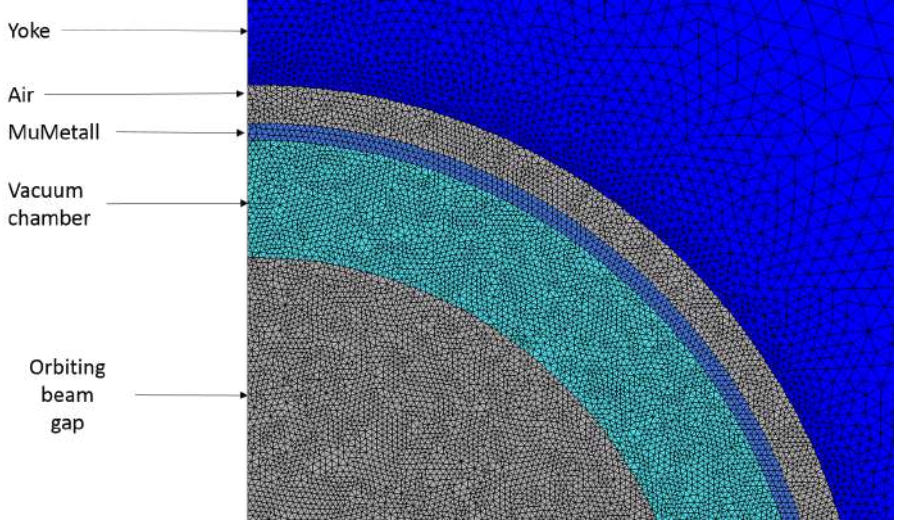


Figure 3.9: Detail of the mesh in the orbiting beam gap and vacuum chamber

Finally, two simulated field maps in the orbiting beam gap produced from the simulations for 1.36 T and 1.38 T in the extracted beam gap, are presented in figure 3.10, where the colour scale is presented in T. The magnetic field component shown is the modulus of the magnetic field. It can be seen that the first simulation, at 1.36 T, has an acceptable leak field while in the second one the leak field increases due to the saturation of the MuMetal foil and it is not an acceptable value which will cause perturbations in the orbiting beam.

Besides, a detailed simulation of the MSDC septum has been performed at 1.36 T to check that it really fulfills the leak field requirements.

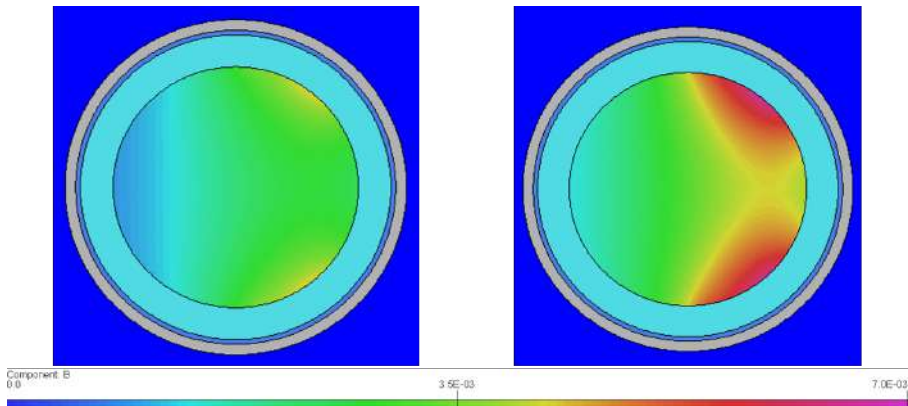


Figure 3.10: Details of simulations of the magnetic field modulus. Left: field map in the orbiting beam gap for 1.36 T in the extracted beam gap. Right: field map in the orbiting beam gap for 1.38 T in the extracted beam gap.

3.4.2 Using an unique family of Lambertson septa at the FCC extraction system

Using 1.36 T as the nominal field results in a magnetic length of 139.70 m. The fact that the physical length is longer than the magnetic length implies that the fill factor of the magnetic line is 85%. The fill factor can be explained by the fact that the coil ends need non negligible space, causing the physical length to be longer than the magnetic length. For comparison, the length ratio in the LHC is approximately 89%, but in the FCC case the coil is expected to be bigger because the number of Ampere-turns is significantly higher than in the LHC case. Continuing these calculations to derive all the parameters of the LHC- like Lambertson septa, we obtain the values presented in table 3.5. These calculations have been done considering the same cross section, magnet length and coil design as in the MSDC model.

3.4. LHC LAMBERTSON SEPTA SCALED FOR THE FCC

Table 3.5: Parameters of the Lambertson septa for the FCC using only one family of magnets

Parameter	Unit	Value
Magnetic field integral	Tm	190
Nominal magnetic field	T	1.36
Leak field	mT	5
Orbiting beam gap diameter	mm	32
Extracted beam gap width	mm	45
Magnetic length	m	139.70
Magnet line fill factor	%	85
Physical length	m	164.36
Mass per magnet (estimated)	tons	9.245
Individual magnet length	m	4.46
Number of magnets per beamline	-	36
Apparent septum thickness	mm	25
Total current (NI)	A·turns	56832
Current	A	1184
Coil turns	-	48
Power consumption per magnet	kW	61.58
Total power consumption (2 dump lines)	kW	2x2217

A simulation using Opera 3D 17R1 shows that the maximum value for the leak field integral at 1.37 T is very close to 10 mT·m, and since the magnet is 4 m long, the average leak field (2.5 mT) is below the limit of 4.5 mT that was established previously. A field map on a 1 x 1 mm² grid of the leak field integral in the orbiting beam gap is shown in figure 3.11, where the plot is centered in the orbiting beam gap and the septum blade is outside the right hand side of the plot.

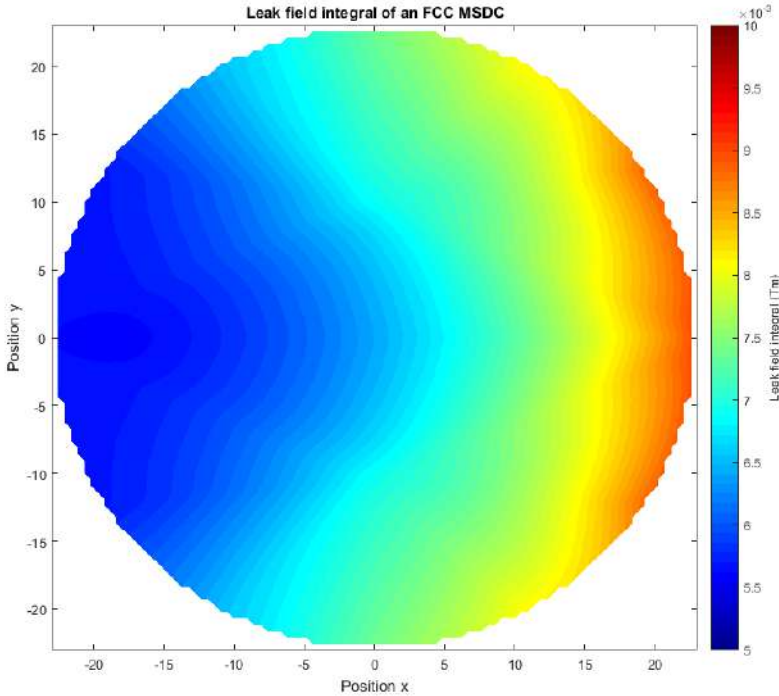


Figure 3.11: Leak field map of a 1.36 T MSDC septum on a $1 \times 1 \text{ mm}^2$ grid located in the orbiting beam gap.

3.5 Lambertson modifications in 2D

3.5.1 Double orbiting beam gap alternative

The most obvious way to increase the magnetic field in the extracted beam gap is to reduce the saturation of the yoke. This will make the permeability of the iron higher, as explained in figure 3.7, and will decrease the proportion of magnetic flux that will penetrate the orbiting beam gap. The proposed cross section of this design is presented in figure 3.12, including the drawing of the magnetic field lines to better illustrate the intended saturation reduction in the yoke, which is the goal of this design. The coil has also been moved

closer to the extracted beam gap to reduce the current needed to produce the magnetic field. This movement has a big drawback, it makes it impossible to use a racetrack coil since the coil would be in the trajectory of the extracted beam gap. The coil type has to be changed to a bedstead or some other shape, which will have an influence on the field at the ends of the yoke. It could be a bedstead coil which would perform well in terms of field quality. The cross section has also been reduced for this simulation to further increase the magnetic field in the gap by reducing the proportion of air and copper, which are non magnetic, with respect to iron. Assuming the same number of turns as the MSDC, 48, it yields a current of 1240 A.

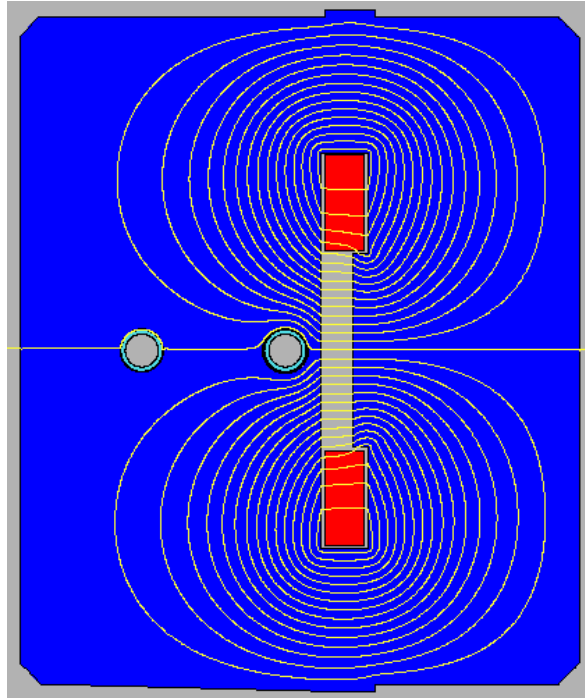


Figure 3.12: Cross section of the proposed double orbiting beam gap Lambertson

septum with field lines

In 2D there is no gain in the magnetic field in the gap since the limiting factor is the saturation of the iron. However, there is a 21% reduction of

the peak power consumption with respect to the scaled-up MSDC before the magnetic field starts penetrating the orbiting beam gap. This is mainly due to the effect of moving the coils closer to the gap and increasing the amount of iron in the yoke to avoid saturating the steel. However this makes the weight of the yoke to increase up to almost 40 tons. Besides, with a double orbiting beam gap, the back to back scheme is not feasible unless additional bumps are included in the beam orbit. This is not interesting because the gain in field does not justify such an important change in the beam optics and very likely in the whole straight section. The characteristics of the beam dump line using the double orbiting beam gap Lambertson are summarized in table 3.6.

Table 3.6: Main characteristics of the double orbiting beam gap Lambertson

Parameter	Unit	Value
Magnetic field integral	Tm	190
Nominal magnetic field	T	1.4
Leak field	mT	5
Orbiting beam gaps diameter	mm	32
Extracted beam gap height	mm	40
Magnetic length	m	135.7
Magnet line fill factor	%	85
Physical length	m	160
Individual magnet length	m	4.46
Mass per magnet (estimated)	tons	39.87
Number of magnets per beam line	-	36
Apparent septum thickness	mm	25
Total current (NI)	A·turns	50602
Current	A	1054
Coil turns	-	48
Power consumption per magnet	kW	48.8
Total power consumption (2 dump lines)	kW	2x1757

It can be estimated that while the power per septum is slightly higher than in the case of the scaled MSDC, the total power consumption of a beam dump line with the double orbiting beam gap is approximately 400 kW lower. This is due to the fact that the required number of septa is lower in this alternative. The main drawback of this design is that the cross section increases significantly and therefore the mass also increases proportionally.

Finally, the field map is shown in figure 3.13. This field map only gives

qualitative information at this resolution although looking at the location of the saturated areas it is possible to deduce where the modifications should be made. The maximum field level in the axis is set at 2.5 T and the leak field in both orbiting beam gaps is 5 times below the maximum allowed. The 0.9 mm thick MuMetal sheet that is present around the vacuum chamber also helps to reduce the leak field.

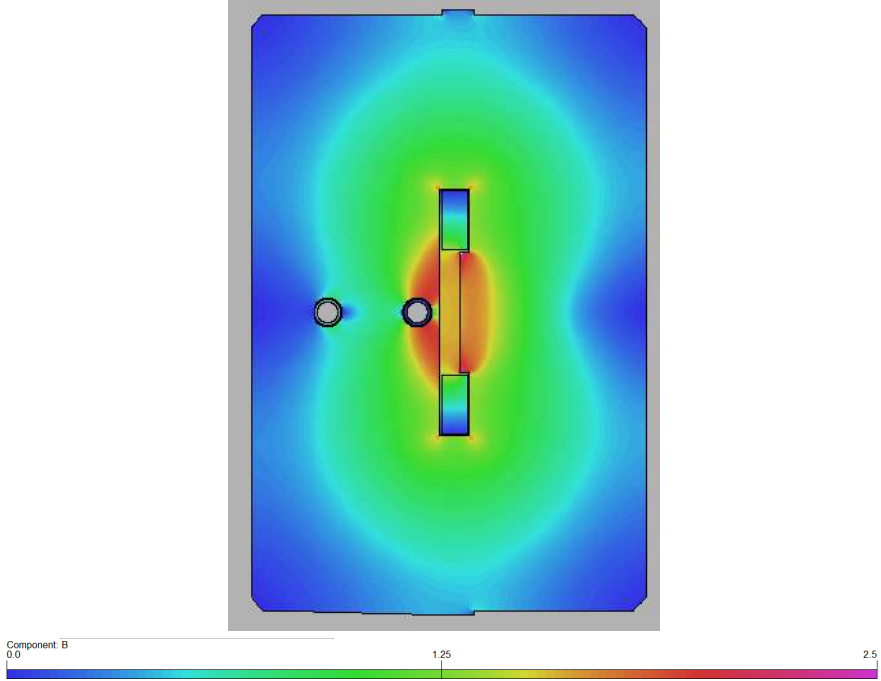


Figure 3.13: Field map of the double orbiting beam gap Lambertson septum

3.5.2 Reducing the leak field by changing the shape of the orbiting beam gap

A priori, an option to reduce the leak field could be to use the shape of the orbiting beam gap to guide the field lines. Two alternatives have been explored, a square shape and a wedge shape. The advantage of the square shape is that it is a very simple geometry that can be used as a first step towards fully under-

standing the other shapes. The disadvantage is that the square geometry acts as a Panofsky quadrupole [97] and it adds a significant quadrupole component to the leak field. This quadrupole component could potentially be introduced into the optics of the FCC lattice. The square shape is therefore not the best alternative conceptually. The wedge shape naturally guides the magnetic field towards the septum blade due to the higher permeability of iron with respect to the air. This will only work while the septum blade is not saturated. Once the iron in the septum blade saturates the permeability of the iron decreases and the shape of the orbiting beam gap loses its influence on the leak field, as explained in section 3.4.1. A detail of the orbiting beam gap with the square and wedge shape is shown in figure 3.14, and the flux lines have been added to the picture to illustrate the intended result.

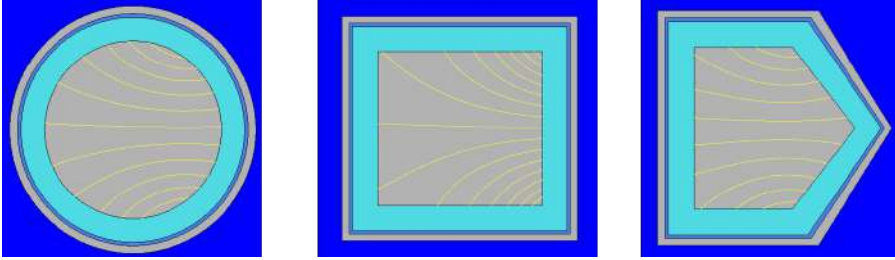


Figure 3.14: Different shapes of the orbiting beam gap considered

Comparing the leak field of the Lambertson septa with the different orbiting beam gap shapes one can see that the difference between the circular shape of the MSDC and the wedge shape is negligible while the square shape is much worse for the leak field. This comparison is plotted in figure 3.15. Although it is difficult to see, the blue and black lines, which correspond to the MSDC and Wedge values are superimposed. The values plotted correspond to the fields next to the septum blade, where the leak field is the highest.

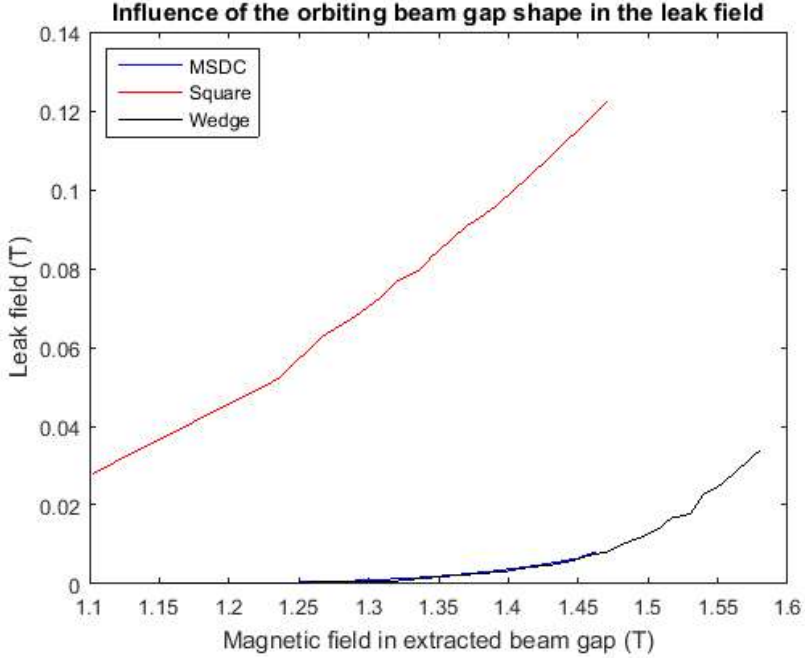


Figure 3.15: Influence of the orbiting beam gap shape in the leak field

Comparing the scaled up MSDC septum and the wedge shape, for the same leak field, there are approximately 20 mT difference in the magnetic field in the gap. These values are presented in table 3.7 to make the comparison easier. The most outstanding result from this comparison is that the leak field when using a square orbiting beam gap is an order of magnitude higher.

Table 3.7: Comparison between the leak fields and the extracted beam gap fields as a function of the shape of the orbiting beam gap

	Leak field (mT)	Extracted beam gap field (T)
Scaled MSDC	2.3	1.36
Wedge shape	2.6	1.38
Square shape	87	1.36

To better understand the differences in leak field one can compare the maps of the magnetic flux density in the yoke in the same conditions as in figure 3.7,

presented in figure 3.16. Taking the scaled MSDC as a base case, it can be seen that in the corners of the square orbiting beam gap the iron is highly saturated while the round and wedge shape reduce the field level by guiding the flux lines smoothly. In all cases, the central part of the septum blade has a low field level, around 1.25 T in most of this area, but the permeability of the iron that is saturated decreases significantly and the magnetic field starts to penetrate inside the orbiting beam gap.

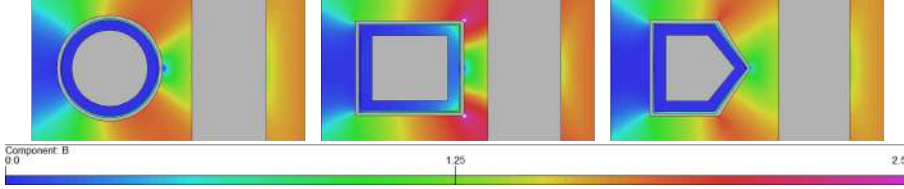


Figure 3.16: Magnetic flux density in the septum blade of the scaled MSDC

Since changing the shape of the orbiting beam gap does not improve significantly the maximum field attainable by a modified MSD Lambertson septa, the next step is to study the influence of high- saturation materials.

3.5.3 Reducing the leak field by adding high saturation materials

The FCC extraction septa will have to follow the energy swing of the accelerator from injection to top energy. The magnets therefore will be slowly ramped, following the increase of field of the main bending magnets. For reasons of limiting core-loss, the magnets will be made of laminated steel sheets. The choice of steel is determined by the saturation, which impacts the penetration of the main field into the field-free region. Most commercially available electrical steels saturate at 2 T or even lower inductions. An exception is ultra pure iron with saturation induction of about 2.15 T, and cobalt steels that can reach up to 2.35 T before saturating [4]. The use of the latter in accelerator environments is strongly discouraged for safety reasons, due to neutron activation to Co-60. Furthermore, the cost and availability of this material in the large quantities required for the FCC septa, cannot justify the small gain in saturation induction.

Several lanthanides are known to exhibit ferromagnetic properties at cryogenic temperatures. It has been reported that Holmium has a saturation magnetization of 3.9 T [98]. Holmium pole tips have been successfully used as flux

concentrators for small superconducting magnets [99]. The Curie temperature for this rare-earth metal however is below 20 K, making its application as a field enhancement material for this particular application impractical. This is also the case for other lanthanides like Dysprosium or Erbium [100]. Holmium properties also vary immensely with production methods, and its cost is very high. The BH curve of Holmium at 4.2 K has been plotted up to almost 6 T in figure 3.17 for better understanding of its magnetic properties, taken from [100]. The BH curve for ISOVAC 1300 100 is plotted in the same figure for comparison. However, the data supplied by the manufacturer of ISOVAC was incomplete, so the curve has been manually extended after the saturation point with relative permeability of 1. Higher B values for ISOVAC shouldn't be taken as an exact value but as an approximation.

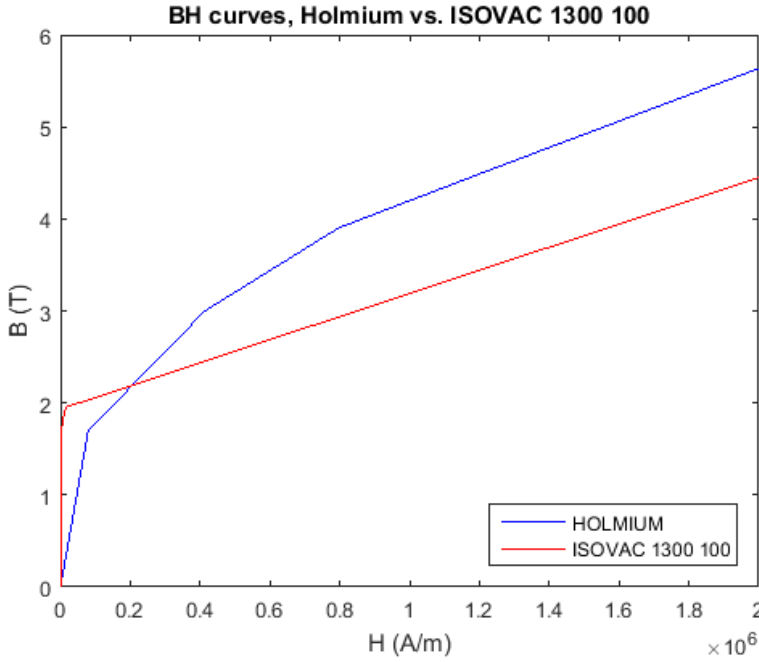


Figure 3.17: BH curve of Holmium at 4.2 K

Even if it is very impractical to add Holmium pieces to a possible FCC Lambertson septum, some simulations have been performed because the Holmium

flux enhancement might be useful for other applications. A picture of the cross section of the Lambertson septum simulated and a detail of the Holmium block is presented in figure 3.18.

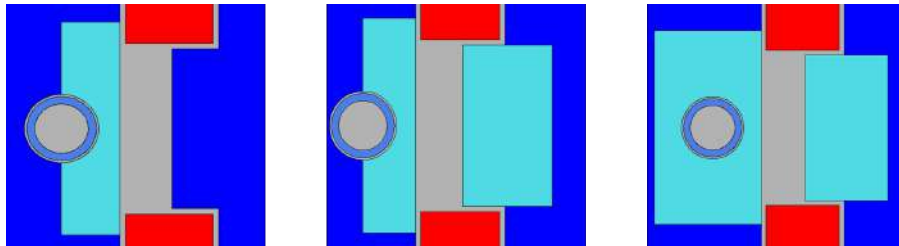


Figure 3.18: Lambertson septum with Holmium tip and septum blade detail

To study the improvement that the Holmium block, in light blue, produces in the Lambertson design, a plot of the leak field as a function of the extracted beam gap field is very useful, and its comparison against the scaled MSDC Lambertson septum. Such comparison is plotted in figure 3.19.

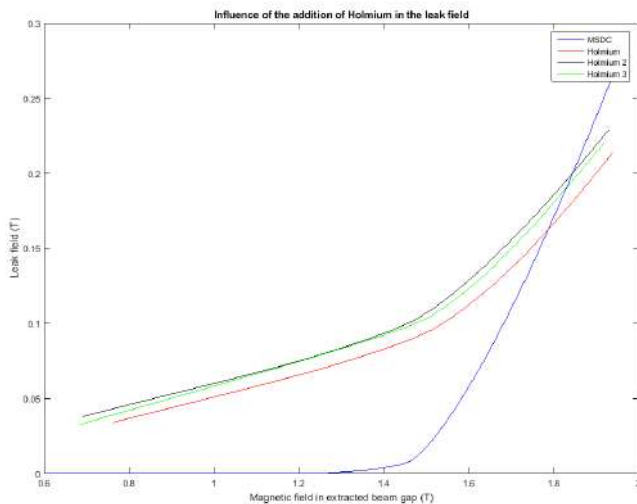


Figure 3.19: Comparison of the scaled Lambertson septum and the design with a Holmium tip

From figure 3.19 it can be deduced that the addition of Holmium to the design would be a good choice for high fields in the extracted beam gap. The leak field is lower at fields above 1.8 T approximately, when an iron septum blade would be highly saturated. For lower fields, and especially for the 1.36 T value that has been established for the scaled MSDC Lambertson septum, the leak field of the Holmium design is approximately 6 times higher than the required FCC baseline value of 5 mT and approximately 20 times higher than the Lambertson septum without Holmium. This might be surprising at a first glance but it is due to the different slopes of the linear parts of the BH curves of Holmium and the steel used (ISOVAC 1300-100). It can also be appreciated indirectly in figure 3.19 that the graphs plotted are symmetric to the BH curves. Although the leak field above 1.6 T is lower with the addition of Holmium in the septum blade, it is still very high and reaches quickly the level of 80 to 100 mT. Depending on the application this value might be acceptable but in the case of the FCC it is not low enough. However, given that at low energy the magnetic rigidity of the beam decreases and the beam is more affected by the leak field and therefore it is not possible to write an absolute statement regarding this matter.

A detail of the saturation of the septum blade is presented in figure 3.20. It can be seen that the Holmium region is mostly not saturated but the iron region on top and bottom of the Holmium largely exceeds 2 T, which means that in order to decrease the leak field the only solution is to add more Holmium around the orbiting beam gap. This is a highly unrealistic solution, but in the future could be feasible.

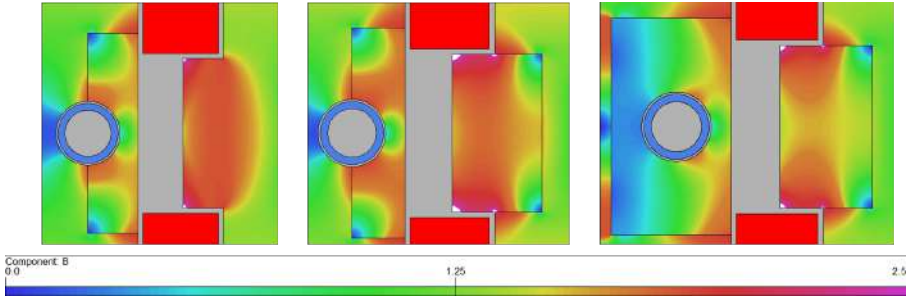


Figure 3.20: Saturation of the septum blade with the addition of a Holmium block

3.5.4 Reducing the leak field by adding compensation coils

After investigating the influence of different materials and the redesign of the orbiting beam gap cross- section, which are passive methods of improvement, the next step is to probe the active compensation of the leak field. The use of compensation coils or perhaps some extra turns to fine-tune the magnetic field is a common practice in magnet design. The danger of this approach is that it can become infinite. The leak field can be seen as an error and theoretically it can be compensated by breaking the error in an infinite number of pieces and compensating each piece independently. This is the approach used to reduce the harmonic content of the magnetic field of the lattice magnets below specification [101, 102] using Fourier or Taylor expansion of the magnetic field. This approach is very convenient when one can use different specialized function magnets since any error can be compensated individually. In the case of septa the aim is to cancel the leak field in modulus and usually the space for compensation coils is very limited.

Taking a step back, for a given magnetic field in free space that needs to be canceled, one could find a position where to place one or more coils and thus fully cancel the original magnetic field. A very easy way of doing this is to use the algorithm described by Fartoukh in [84, 103]. This algorithm is very well suited for homogeneous linear media. If there are two or more linear materials present the equations for the two of them have to be linked and the way to do it is not straightforward. If the geometry is simple enough one can use conformal mapping techniques and the image method to solve for the scalar magnetic potential as if it was an electrostatic potential [95, 104]. For usual geometries of magnet gaps (squares or circles), the most commonly used mapping is the Schwartz-Cristoffel mapping, which is also implemented in many software packages like MATLAB [105, 106]. When the materials considered are not linear, like electrical steel, this algorithm is not useful because the magnetization of the yoke is not uniform. The way to overcome this obstacle is to discretize the material in pieces small enough in which the material can be considered linear, which is nothing else than the well known Finite Element Method. Although it will not be accurate, Fartoukh's method can be used as a first approach if the finite element analysis is foreseen to take long to mesh and solve.

Coming back to compensating the leak field of the scaled version of the Lambertson septum, it is not necessary to compensate all the harmonics of the magnetic field, it is enough to make the harmonic terms small enough, considering the higher order terms tend to be smaller naturally. The first iter-

ation is to use only one compensation coil to make this compensation as simple as possible. Since it is not easy to cancel the leak field with one compensation coil, a second coil can be added, or a third. As stated before, the danger of this method is that it is very easy to keep adding compensation coils to compensate for the effects of the last set of compensation coils added, and this can escalate very quickly to an unrealistic solution, even if the desired compensation is achieved. For this study, the amount of compensation coils has been limited to two. Also, since the main idea of this approach is to use superposition to cancel the leak field there is no MuMetal screen in these designs because it would go against the objective.

The leak field that has to be compensated depends on the shape of the orbiting beam gap. A detail of the different shapes considered and the field lines of the leak field are presented in figure 3.21 to better illustrate the starting point of the compensation coils approach.

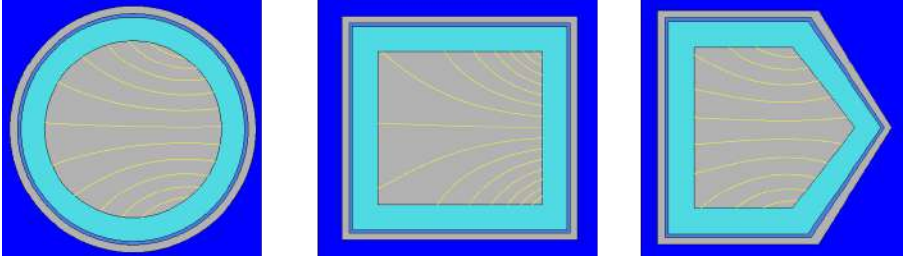


Figure 3.21: Leak field to be compensated depending on the orbiting beam gap shape

It can be seen that the approach in the case of the circular orbiting beam gap has to be different than in the case of the square one. The first one has mainly a dipolar component while the square orbiting beam gap introduces a significant quadrupolar content. The wedge shaped gap produces a magnetic field which is approximately the superposition of the other two. This will impact the positioning of the coils. Another key parameter will be the value of the current in the compensation coils. To have a first idea of the proportion between the main current and the compensation current, an optimization problem has been set up in Opera 2D, using the Opera Optimizer [96] to automate the process. The optimizer performs a grid search although it saves time by reducing the grid to the nodes that produce the best results at each iteration step. The design variables are the two currents and the objective functions are to maximize the magnetic field in the extracted beam gap and

to minimize the surface integral of the leak field over the orbiting beam gap divided by the area of the orbiting beam gap. As explained in section 7.2, this figure of merit is more representative than minimizing the leak field at a given point or minimizing the integral of the leak field along a given line since there are regions of the orbiting beam gap where the leak field is in the order of mT and others where it approaches 0.5 T. This figure is measured in $\text{T}\cdot\text{mm}^2$. This magnitude should not be confused with Wb since the surface vector in the magnetic flux definition is perpendicular to the one used here. However, in tables 3.8 and 3.9, the figure of merit is represented in T because the surfaces are the same, the field is only averaged over the orbiting beam gap.

Using the magnetic field at a given point or integrating along a given line is risking not to obtain a correct design. To reduce computation time, the objective that was minimized was the surface integral of the leak field over the orbiting beam gap and the division by the area was only done to the optimal solution found. This will not change the result since the value will be proportional and due to the way the Opera Optimizer works, saves significant computation time.

3.5.4.1 Adding one set of compensation coils

Using one compensation coil a range for the optimum values was found. There is obviously a relation between the magnetic field in the extracted beam gap and the leak field in the orbiting beam gap.

The results are presented in detail in table 3.8. The negative signs in the compensation coil current expresses that the polarity of the compensation coil is opposite to that of the main coil.

Table 3.8: Results of the optimization using one compensation coil

Parameter	Unit	Minimizing leak field integral	Maximizing the main field
Main coil current	A·turns	$97 \cdot 10^3$	$278 \cdot 10^3$
Compensation coil current	A·turns	-394.95	-540.53
Magnetic field in the extracted beam gap	T	1.50	1.85
Leak field integral over the orbiting beam gap	T	$3.61 \cdot 10^{-5}$	$2.17 \cdot 10^{-4}$

A detailed simulation for the two cases has been performed and although these two designs were the best of all the possibilities, a look at the field maps

of the orbiting beam gap shows that the compensation is not successful. The leak field maps of the lowest and highest ratios identified are presented in figures 3.22 and 3.23 respectively. They are not presented in the same figure because of the difference in the leak field values. The maximum value in the axis of figure 3.22 is 0.1 T and in figure 3.23 the maximum value is 0.5 T.

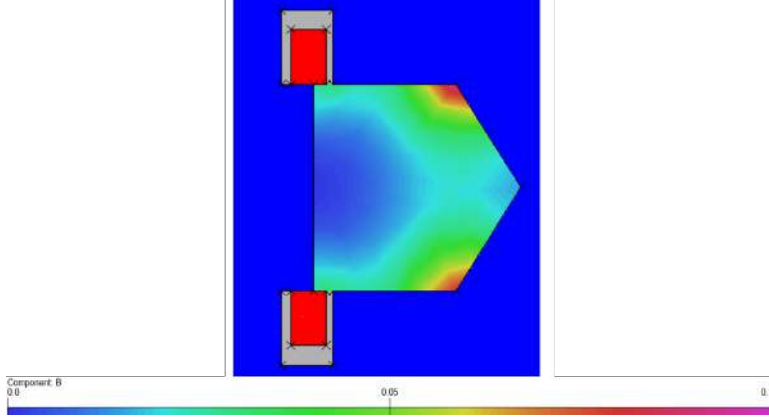


Figure 3.22: Leak map field of the lowest leak field design

The highest ratio design produces a leak field that is at least 0.25 T in almost every part of the orbiting beam gap. This value is not acceptable and achieving a magnetic field in the extraction beam gap of 1.85 T does not justify such a high leak field. The lowest ratio design improves the leak field significantly. The leak field in most of the orbiting beam gap is below 50 mT. This is one order of magnitude less than the highest ratio design and it comes at the expense of achieving a magnetic field in the extracted beam gap of “only” 1.5 T. In terms of main field it is an improvement of 10% with respect to the scaled MSDC Lambertson septum. However, the leak field is still one order of magnitude higher than what is specified in the FCC parameters in table 3.4 and this analysis shows that it is not enough to use only one compensation coil to fully cancel the leak field. This result can not be used in the FCC beam dump line but it might be useful for another application in the future.

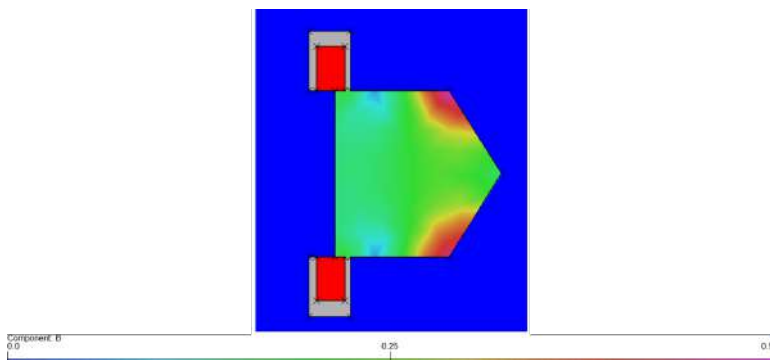


Figure 3.23: Leak map field of the highest magnetic field design

3.5.4.2 Adding two sets of compensation coils

Using two independent compensation coils again no clear optimum was found. After checking the feasibility, a range for the currents ratio was established. It was found that the results did not change significantly with respect to the cases in which only one compensation coil is used. The results are presented in detail in table 3.9. Again the negative sign represents that the coil polarity is opposite to the main one.

Table 3.9: Results of the optimization using two compensation coils

Parameter	Unit	Minimizing leak field integral	Maximizing the field in the extracted beam gap
Main coil current	A·turns	102794.67	422357.76
Compensation coil current	A·turns	-18.7	-18.7
Second compensation coil current	A·turns	-1077.18	-18.7
Magnetic field in the extracted beam gap	T	1.5	2.05
Leak field integral over the orbiting beam gap	T	$2.41 \cdot 10^{-5}$	$2.47 \cdot 10^{-4}$

The leak field map for the highest field design is shown in figure 3.24. It

can be seen that the leak field is approximately 0.5 T almost in every region of the orbiting beam gap, with the white regions of the image being above this value. Even if the magnetic field is above 2 T the leak field is two orders of magnitude above the FCC baseline parameters that can be found in table 3.4.

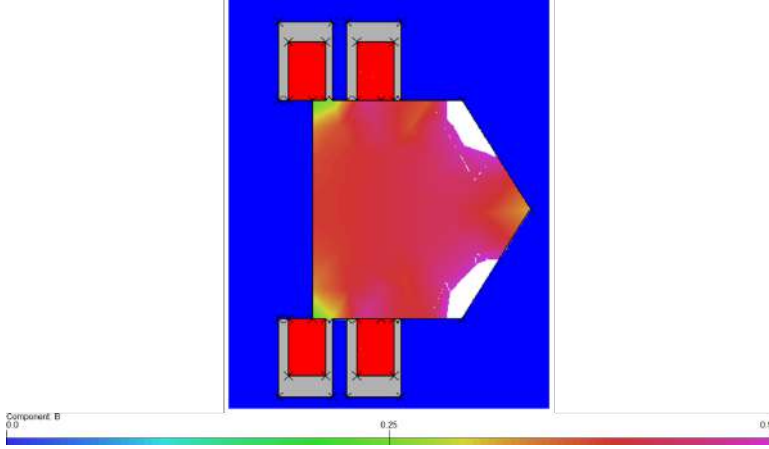


Figure 3.24: Leak map field of the highest leak field design

Since a 2 T Lambertson septum with compensation coils is not acceptable, the other alternative is to try to reduce the leak field as much as possible and accept the resulting magnetic field value in the extracted beam gap. Even a magnetic field of 1.5 T is still a 10% improvement from the 1.36 T scaled MSDC septum. The leak field map of this design is shown in figure 3.25.

Studying the results of using one compensation coil and two independent compensation coils, the conclusion is that it is not possible to cancel the leak field completely. Although the average leak field value used in the optimization seems better than the baseline requirement at first sight, once the field map is produced, it can be seen that the average value does not represent the leak field accurately since it varies abruptly depending on the region of the orbiting beam gap. Besides, looking at table 3.9, one can see that the minimum leak field design is equivalent almost to using only one compensation coil. A further optimization of the two coils approach consists in changing the position of the compensation coils. The improvement is negligible because the leak field stays within the same levels and the field quality in the extracted beam gap decreases. The next idea for compensating the leak field is to use permanent magnet blocks instead of compensation coils. It is not likely that

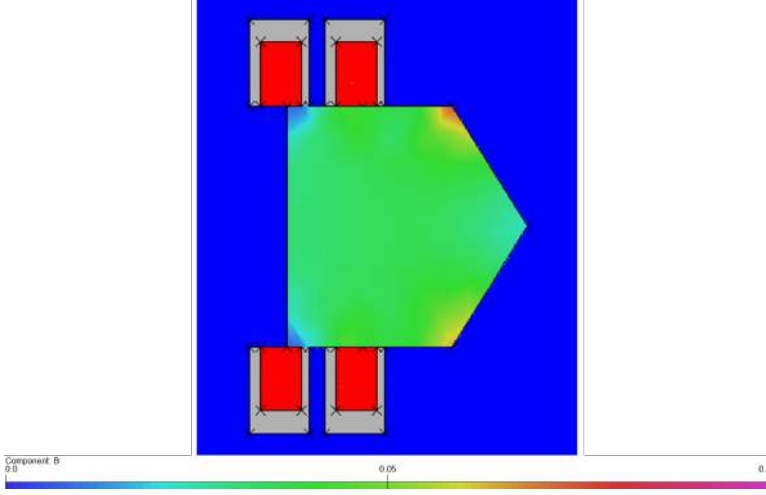


Figure 3.25: Leak map field of the lowest leak field design

the permanent magnets will improve significantly the cancellation of the leak field but since they do not consume any power it is worth studying their use.

3.5.5 Reducing the leak field by adding permanent magnets

As an alternative to compensation coils, simulations were performed using permanent magnets to compensate the leak field. There are new magnet designs at CERN for the DIRAC experiment and LINAC4 that use only permanent magnet blocks to produce the magnetic field [107, 68] and even permanent magnet septa are being investigated at KEK [71]. The main advantage of permanent magnets is that they don't consume any power, but the magnetic field produced is fixed. This could be acceptable for the injection septa since injection always takes place at the same energy but not for the dump line because it has to be possible to extract the beam at any energy. The magnet blocks chosen for the simulation were Samarium- Cobalt permanent magnets ($\text{Sm}_2\text{Co}_{17}$). They are similar to NdFeBo magnets but the Samarium- Cobalt magnets have usually higher coercivity and temperature stability although temperature stability has to be studied carefully and the magnet should be installed in a location with constant temperature [108]. Besides, the radiation hardness of the Samarium- Cobalt magnets is much higher than that of

the Neodymium magnet blocks [71]. Since the operational cost of permanent magnets can be virtually zero given the right conditions, it is worth to study the influence of using permanent magnet blocks to compensate the leak field. The BH curve has been taken from [109] and it is plotted in figure 3.26.

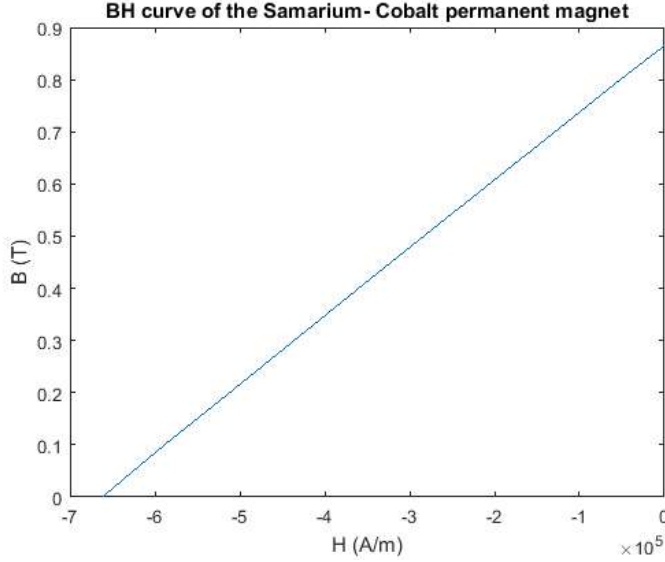


Figure 3.26: BH curve of the Samarium-Cobalt permanent magnet blocks

Four different alternatives for the positioning of the permanent magnet blocks have been investigated and they are all illustrated in figure 3.27. The direction of the magnetization of the permanent magnets is drawn in green arrows. The aim of this positioning is to force the magnetic field lines to avoid the orbiting beam gap. The two cross sections in the top of figure 3.27 are obviously the most inefficient since they will increase the saturation on the left side of the orbiting beam gap. However, they can not be discarded immediately. The two possibilities at the bottom of figure 3.27 are naturally guiding the leak field lines out of the orbiting beam gap. They are in a manner shielding the orbiting beam gap from the leak field with their own magnetic field lines. They rely on superposition of the magnetic field produced by the coil and the magnetic field produced by the permanent magnet blocks to guide the field lines around the orbiting beam gap or if that is not possible, to compensate the leak field inside the orbiting beam gap.

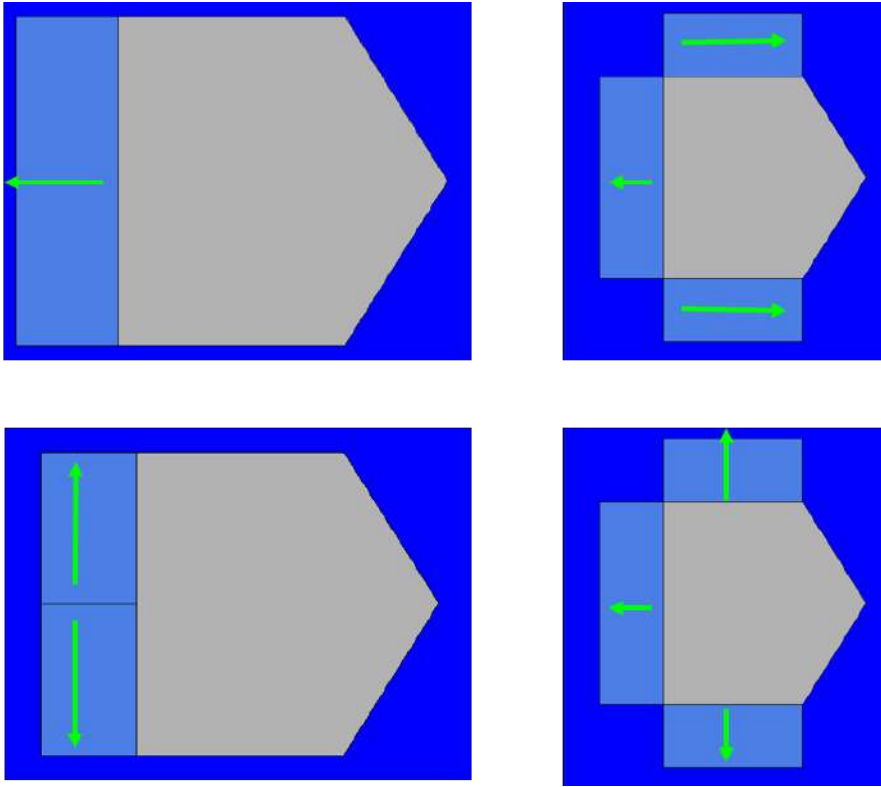


Figure 3.27: Four cross sections considered

Finally, no significant improvement was identified using permanent magnets because in all cases the leak field is too high. The field maps of the four different cross- sections are presented in figure 3.28. All the simulations have been performed for a main field value of 1.36 T in order to compare them with the other alternatives. In all pictures, the white regions are the regions of the orbiting beam gap where the leak field exceeds 0.5 T. It can be seen that the two designs at the bottom of figure 3.28 are much better performing in terms of leak field but there is still a significant region of the orbiting beam gap where the leak field is above 0.25 T. These high values for the leak fields and the fact that the permanent magnets can not be tuned, discourage the use of permanent magnet blocks instead of compensation coils, in spite of the fact that permanent magnets are becoming more common in accelerator

environments, even in the septa domain [107, 68, 71, 110].

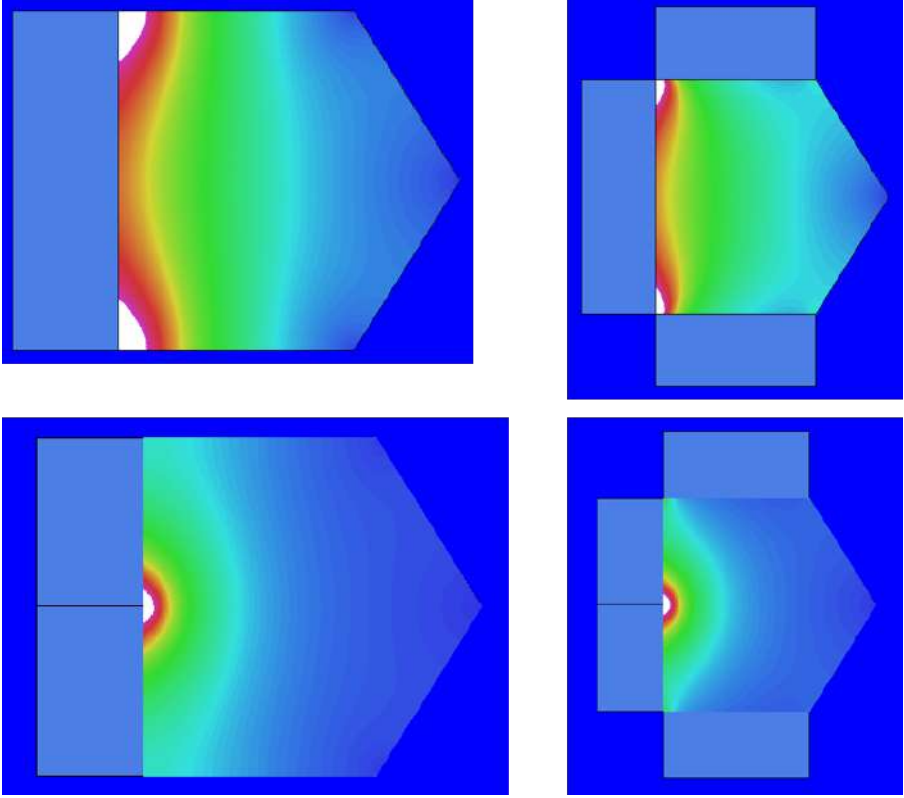


Figure 3.28: Field maps

3.6 Super ferric design

The limiting factor of the Lambertson septa topology have been studied. It has been found that the most critical aspect is the saturation of the yoke in the septum blade. Different ways to reduce this saturation and to compensate the leak field have been investigated. The only further study that could be carried out is to produce a super ferric Lambertson septum. The main advantage of a super ferric design is a potential reduction of the power consumption, since it will be operated in quasi DC mode. However, the septum thickness and the

leak field cannot be reduced while maintaining the same magnetic field in the extracted beam gap because they are only a consequence of the saturation of the septum blade, as explained in section 3.4.1.

3.7 Figure of merit applied to the Lambertson topology

To finalize the study on the Lambertson topology, it is interesting to calculate the figure of merit introduced in 2.5. The figure of merit has been calculated only for the FCC scaled Lambertson septum and for the double Lambertson topology. It has been shown in this chapter that modifying the orbiting beam gap shape, adding high saturation materials, compensation coils or permanent magnet does not produce a better design. The results are presented in table 3.10.

It can be seen that the figure of merit of the superferric Lambertson is one order of magnitude lower than the scaled one and the double Lambertson. The figure of merit rewards minimizing the amount of superconducting material used in the coil design and using it more efficiently, in higher field regions. The second factor of equation 2.31, which measures how efficiently the superconducting material is used, will be equal to one only when the coil is operating at the critical field, that is, never. It will always be lower than one, and in this case it is exceptionally low because the peak field in the coil is about 0.8 T. This is an inherent feature of the Lambertson topology, the coil is far from the high field region and it is protected by the iron yoke. It can be argued that the superferric Lambertson septum is not significantly different than the normal conducting one, only the coil changes from being made from copper to being built from superconducting material. One would expect a superconducting magnet would obtain a higher value in the figure of merit calculation. However, as it was shown in section 3.4.1, Lambertson septa are limited by the septum thickness. For a given thickness the magnetic field cannot increase indefinitely without the leak field increasing, which would be unacceptable. In this calculation, the magnetic field was computed while maintaining the leak field below 0.1 mT. For this reason, the magnetic field of the super ferric Lambertson septum is the same as the normal conducting variant. Following this analysis, from the point of view of the maximum magnetic field, it is always interesting to choose a superconducting dipole, but in the case of a septum this might not be true, and the advantages of using a superconducting materials are in the form of space or energy savings, if any.

3.7. FIGURE OF MERIT APPLIED TO THE LAMBERTSON TOPOLOGY

As a discussion, it can be argued that the figure of merit is not a reliable tool for comparing different magnets because the super ferric Lambertson obtains a much lower value than the normal conducting variants. As described in section 2.5, the figure of merit only takes into account magnetic parameters. In a full injection or extraction region there are many more variables that come into play, such as cost, straight section length, availability of cryogenic installations, etc. One obvious case is when the accelerator is being upgraded and the available space is one of the constraints, which is a different case from when the accelerator is in the study phase as in the case of the FCC. The figure of merit is a useful tool but is not the only tool available and it should not be. Septa design is always an exercise of compromise in itself, as shown in figure 2.1, but it is also a compromise with all the other components of the machine, including the civil engineering and services. If all these aspects are considered, a more detailed analysis is needed.

Table 3.10: Calculation of the figure of merit for the different Lambertson septa presented.

Lambertson type	B_0 (T)	B_{sat} (T)	B_{pole} (T)	B_{leak} (mT)	h (mm)	s (mm)	K (-)
Scaled Lambertson	1.38	1.9	2.9	0.1	46	30	32
Double Lambertson	1.65	1.9	3.15	0.1	46	30	42
Super ferric Lambertson	1.38	6.5	0.8	0.1	46	30	2.6

Chapter 4

Massless septa

4.1 Introduction

In this chapter we will investigate the possibility of using massless septa for the FCC. In section 4.2, the Pacman septum topology is presented and an optimum design is compared with existing massless septa. In section 4.3, the feasibility of using an RF cavity for leak field compensation is explored. Finally, a new injection protection scheme using a double massless septum is briefly studied in section 4.4 to assess the potential of this strategy.

4.2 Pacman septum

4.2.1 Introduction

The concept of the Pacman septum is shown in figure 4.1. It can be seen that, while the iron yoke is not saturated, the magnetic field will not escape to the zero field region.

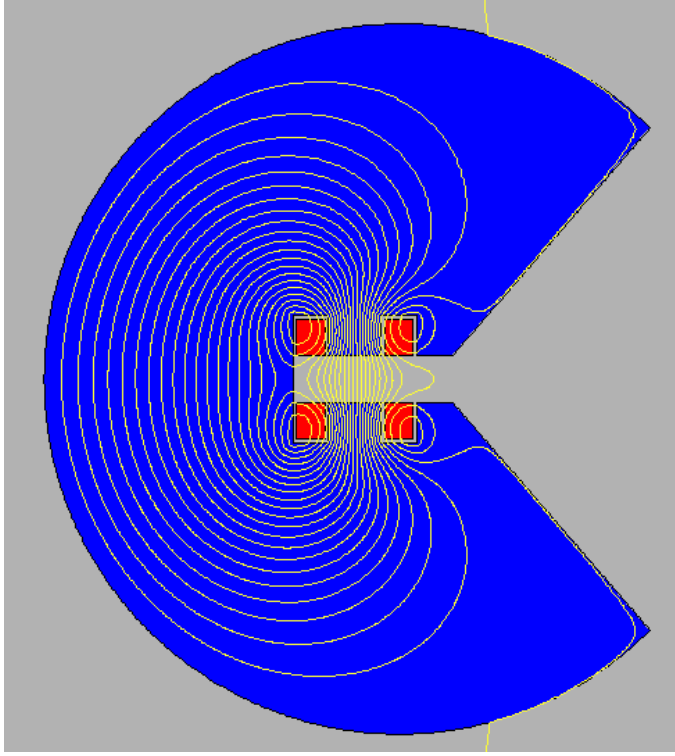


Figure 4.1: Pacman septum with field lines

The injection and extraction beam requirements have been presented in section 1.1.3. It is important to note that the Pacman septum here is assumed to be a super ferric magnet. Being a dump septum, it is necessary to operate the magnet in quasi-DC, following the energy swing of the collider. In order to avoid having enormous coils, the current density needs to be higher than that of copper in a normal conducting magnet, operated in DC, which is in the order of 5 A/mm^2 . For a septum magnet, since it is usually a pulsed magnet, the current density in the coil can be up to 100 A/mm^2 . For a 2 T Pacman septum, the current density considered is in the region of 200 A/mm^2 , which is at least a factor of two above what can be cooled in a resistive coil and therefore needs to be made superconducting.

4.2.2 Optimization

The most interesting question about the Pacman septum is that it can be optimized to reduce the leak field and the septum thickness and increase the magnetic field in the gap with a better field homogeneity. For reference, the field produced by a generic Pacman septum with an angle of 45° and a 38 mm gap height is not homogeneous and presents a septum thickness of about 50 mm counting from the end of the orbiting beam gap, which sometimes is referred to as the beam stay clear region.

The variables used in the optimization are the opening angle, the coil dimensions and the extension of the yoke before the corner of the opening angle of the yoke. This is shown in figure 4.2.

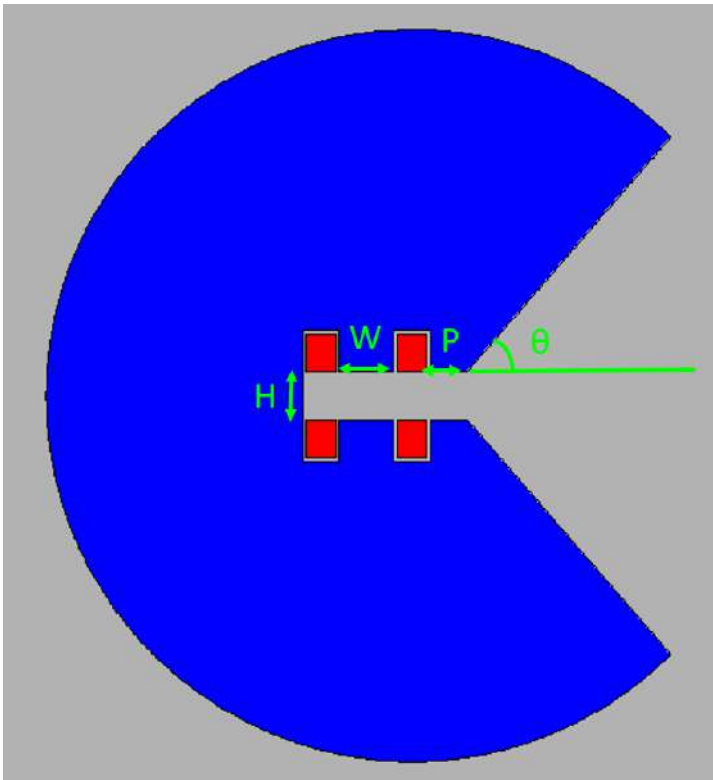


Figure 4.2: Pacman septum variables, angle (θ), gap width (W), pole tip (P) and gap height (H)

It is not surprising to find as a result that the main contribution to the apparent septum thickness is the gap height. The distance needed for the magnetic field to decay to acceptable levels is proportional to the gap height. This is common to most iron-dominated septa. The field magnitude and quality depend on the gap height, and for a bigger gap the deviation of the field lines from the ideal trajectory, straight between the two poles, becomes more evident. In the case of lattice dipoles this means an increase of the higher order field harmonics while in septa it appears as a leak field.

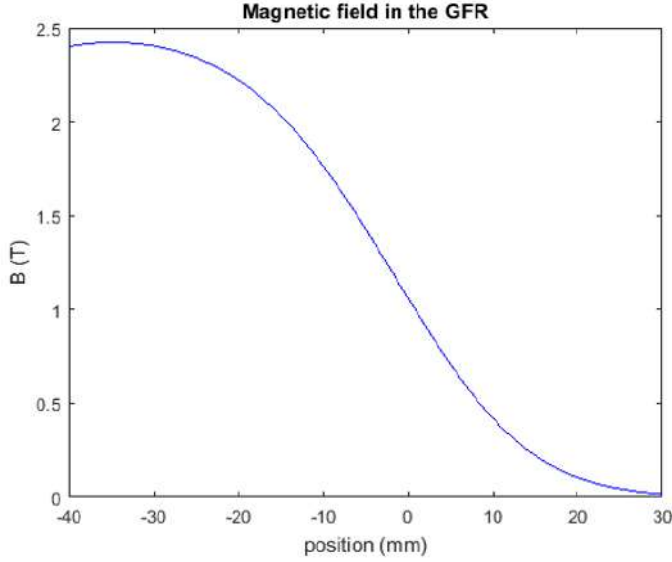


Figure 4.3: Pacman septum field plot along the midplane

A field plot along the midplane is shown in figure 4.3, where the good field region is situated between the coordinates -40 and -10. Then the orbiting beam would be located in the area between the coordinates 10 and 30, which presents a leak field much higher than it would be acceptable. Therefore, it is necessary to optimize the Pacman septum cross section to produce a homogeneous field and reduce the apparent septum thickness, where the magnetic field transitions from the nominal value to zero.

The aperture dimensions on any magnet are determined by the beam parameters, so the only option left is to add passive or active compensation (shims or coils) to optimize a Pacman septum. The optimisation process has

been carried out iteratively in three steps. First, a parametric scan of the three variables was performed, and the best design was kept. The second step was to introduce shims in the good field region to improve the field quality. Last, compensation coils were added to reduce the leak field and the apparent septum thickness and the current in these coils was also set. This process is illustrated in figures 4.4, 4.5 and 4.6 respectively. Figure 4.4 presents the optimization variables of the cross-section shown in figure 4.2. Figure 4.5 shows a detail of the good field region with the addition of shims. Figure 4.6 shows a detail of the cross section with the addition of the compensation coils and the different zones have been marked for clarity.

This approach is acceptable because the Pacman septum can be treated as two almost independent magnets. The magnetic field in the good field region is produced by the main coils. However, the open part of the cross-section, from which the Pacman septum takes its name, acts as a second magnet producing a very low field, which is the leak field. It is also important to note that the shims have been optimized to produce a good field quality at 2 T. When the field is significantly lower, the field quality also decreases significantly. This effect is due to the fact that the magnetic field is dominated by the pole shape and its saturation. For a different pole shape, the field distribution will be different because the local permeability of the iron yoke will vary. Therefore, it is necessary to modify the shims accordingly with the magnetic field obtained in the gap. This makes the use of the Pacman septum in the extraction system very challenging since it needs to operate in an energy range instead of at a fixed energy. Due to this fact, it may be suitable for the injection region.

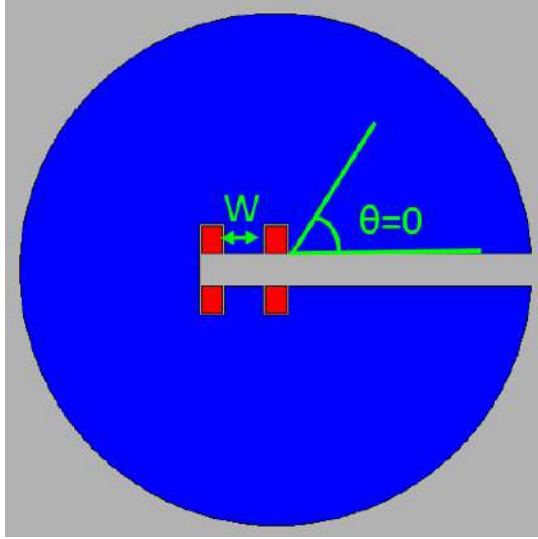


Figure 4.4: Result of the first step of optimization. Opening angle and coil placement.

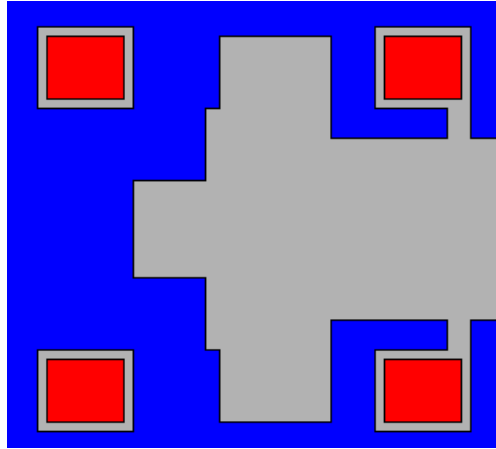


Figure 4.5: Result of the second step of optimization. Shims in the good field region.

Note that the gap height is 38 mm but the poles are shimmed up to a height of 50 mm in the central part. Although the gap size is 38 mm, the magnetic field is generated by a 50 mm gap. The poles could not be shimmed in the opposite way, having a 38 mm gap and adding iron, even outside the good field region since that would reduce the acceptance of the Pacman septum. This increase in height is the key to improve the field homogeneity to an acceptable value. It comes at the expense of having a greater apparent septum thickness and a lower field, since the pole tips are highly saturated. All the Pacman septum characteristics are detailed in table 4.1.

Table 4.1: Parameters of the optimized Pacman septum.

Parameter	Unit	Value
Magnetic field	T	1.34
Leak field	mT	3.26
Apparent septum thickness	mm	55
Gap height	mm	38
NI (main coils)	A·turns	54912
Current density (main coils)	A/mm ²	264
NI (compensation coils)	A·turns	100
Current density (compensation coils)	A/mm ²	5
Gap height/apparent septum thickness	-	1.44

Although the apparent septum thickness (55 mm) is 83% bigger than the required for FCC (30 mm), the ratio (r) between the apparent septum thickness and the gap height is only 1.44. This result is due to the fact that the Pacman septum operates at a 1.34 T field. Reported massless septa in literature present a worse (higher) ratio at a much higher field, such as a ratio of $r=1.3$ at 0.1 T [66] and a ratio of $r=1.6$ at a field of 0.8 T [67]. The optimization process and other massless septa alternatives are described in [85, 86].

The magnetic field along the midplane obtained after the optimization has been completed is shown in figure 4.7. Comparing it with the field obtained before performing any optimization, presented in figure 4.8, it is seen that the field quality has been dramatically improved and the septum thickness is reduced. After the optimization, the field homogeneity is better than 1.5%. Figure 4.7 only shows the leak field up to the end of the orbiting beam gap, although it is higher than the 1% limit chosen in section 2.4.4.

For completeness, both fields are compared in figure 4.8.

It is seen that although the leak field of the optimized version decays over a slightly bigger distance, the field quality in the good field region is significantly

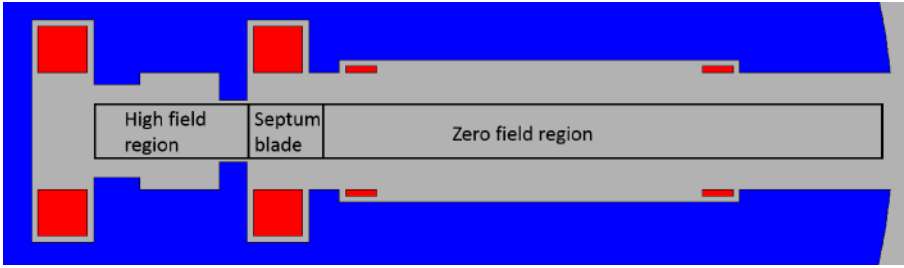


Figure 4.6: Result of the final step of optimization. Addition of compensation coils.

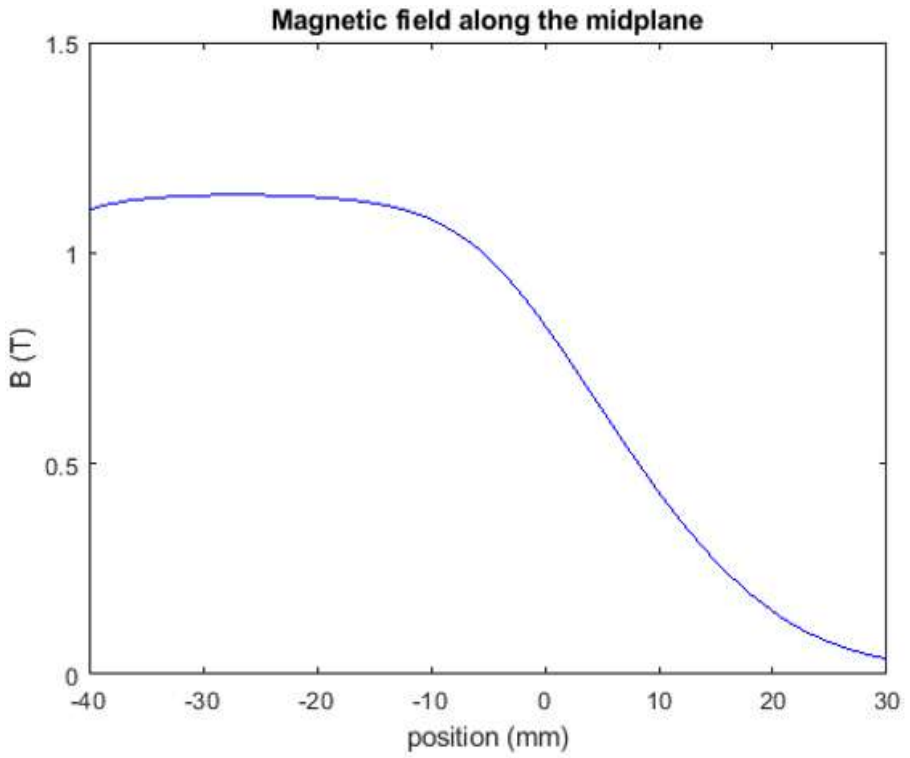


Figure 4.7: Pacman septum field plot along the midplane after optimization

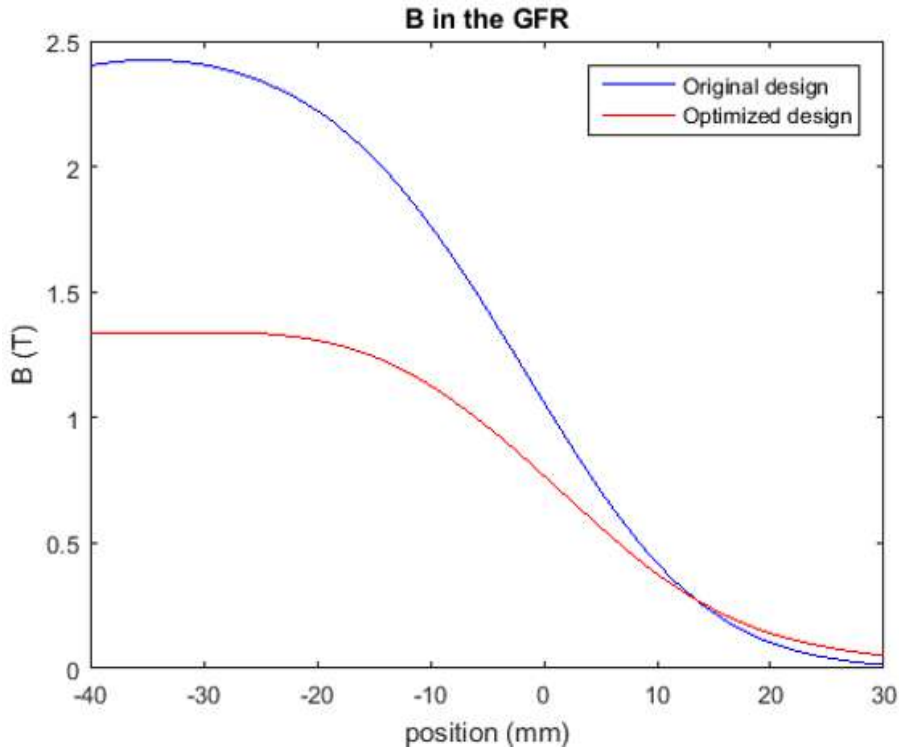


Figure 4.8: Comparison of the Pacman septum magnetic field in the midplane before and after optimization

better. This tradeoff is not ideal since the improvement of the field homogeneity comes at the expense of increasing the leak field level. The original Pacman septum produces a magnetic field that is not ideal for any standard accelerator application, while the optimized Pacman septum could be installed in an given accelerator because there is a homogeneous high field region with a zero field region clearly delimited.

4.2.3 Comparison with Iwashita and Yonemura septa

To put into perspective the Pacman topologies performance, it is useful to compare it with the existing massless septa. The designs by Iwashita and Yonemura [66, 67] have been scaled to have the aperture dimensions required

by the FCC. Additionally, both designs have been pushed to achieve a magnetic field as high as possible and they will be compared with the Pacman septum presented in section 4.2 using the figure of merit. As a second comparison, it is very useful in massless septa to compare the ratio between the gap height and the apparent septum thickness (r).

4.2.3.1 Iwashita type septum scaled for FCC

The full details of this design are presented in [67]. The aperture of this magnet has been increased to fulfil FCC geometry requirements and the current has been increased to find the maximum field achievable with this septum topology, of which a prototype has not been built, only simulations exist.

A detail of the scaled cross section is shown in figure 4.9. Two shims have been added to improve the field quality in the good field region, in which the field homogeneity is better than 3%. These shims do not affect greatly the leak field. The leak field in the orbiting beam gap increases dramatically with the magnetic field increase, from the original 0.8 T to 1.13 T.

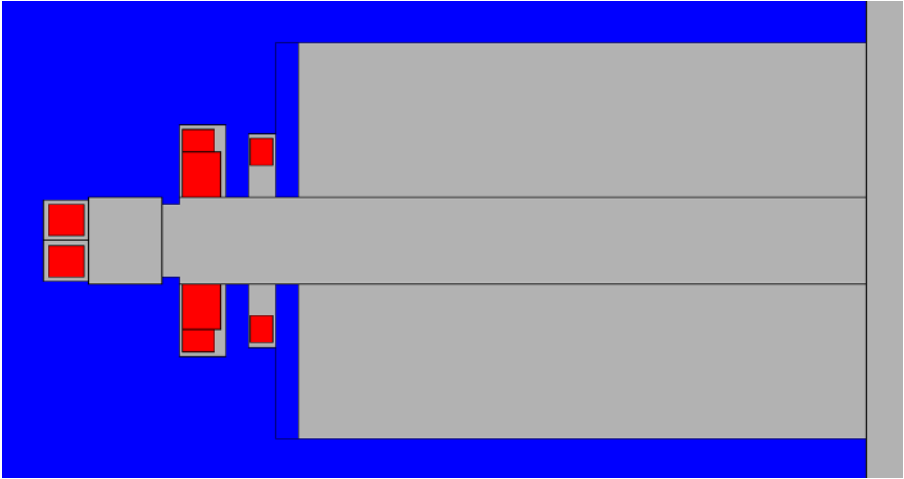


Figure 4.9: Detail of the adapted Iwashita design

The magnetic field along the mid-plane is presented in figure 4.10.

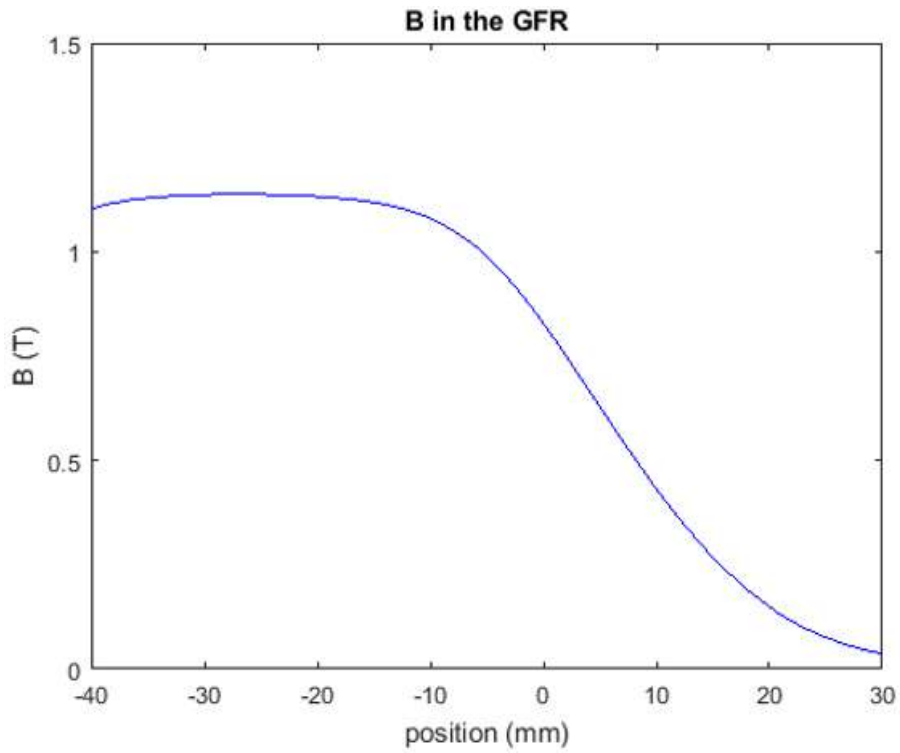


Figure 4.10: Adapted Iwashita septum field plot along the midplane after optimization

The parameters of this septum are summarized in table 4.2.

Table 4.2: Parameters of the optimized Iwashita septum.

Parameter	Unit	Value
Magnetic field	T	1.13
Leak field	mT	0.5
Apparent septum thickness	mm	52
Gap height	mm	38
NI (main coils)	A·turns	17372
NI (compensation coils)	A·turns	3
Gap height/apparent septum thickness (r)	-	1.5
Left shims dimensions (h/v)	mm	8/3
Right shims dimensions (h/v)	mm	-

4.2.3.2 Yonemura type septum scaled for FCC

The full details of this design and the prototype built are presented in [66]. The aperture of this magnet has been increased to fulfil FCC geometry requirements and the current has been increased to find the maximum field achievable with this septum topology.

A detail of the scaled cross section is shown in figure 4.11. Two shims have been added to improve the field quality in the good field region, in which the field homogeneity is better than 3.5%.

The parameters of this septum are summarized in table 4.3.

Table 4.3: Parameters of the optimized Yonemura septum.

Parameter	Unit	Value
Magnetic field	T	0.1
Leak field	mT	7
Apparent septum thickness	mm	65
Gap height	mm	38
NI (main coils)	A·turns	2080
Gap height/apparent septum thickness (r)	-	1.7
Left shims dimensions (h/v)	mm	7/4
Right shims dimensions (h/v)	mm	4/4

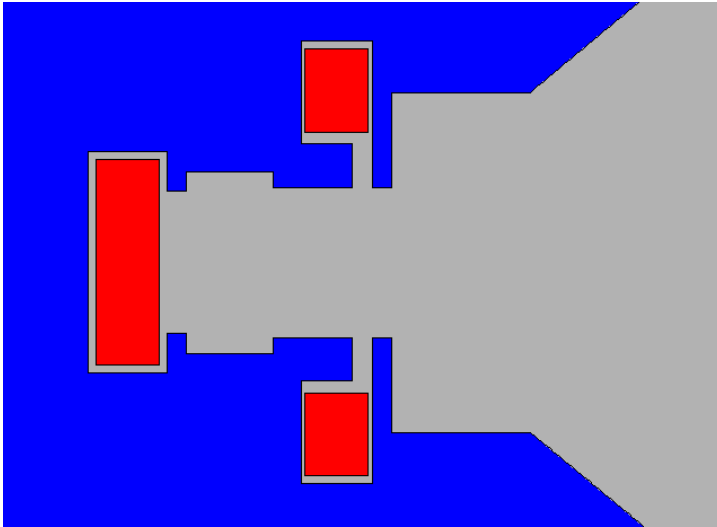


Figure 4.11: Detail of the adapted Yonemura design

4.2.3.3 Comparison of the three massless septa topologies and calculation of the figure of merit

The best way to illustrate the performance of the three septa analysed in the previous paragraphs is to plot the magnetic fields simultaneously in figure 4.12, where the magnetic field from the scaled Yonemura design has been multiplied by a factor of 10 for clarity. The Yonemura design is plotted in the right hand axis due to the difference in the field magnitude with respect to the other two. It can be seen that the scaled Yonemura septum is not useful for FCC since the leak field is in the order of a few mT and it decays very slowly. The scaled Iwashita-like septum achieves a field that is almost 10 times higher and the apparent septum thickness is 1.5 times the gap height, which is a significant improvement compared to the scaled Yonemura-like septum. However, the Pacman septum produces a field that is almost 1.5 T, which is an increment of about 27 % with respect to the Iwashita-like and achieves the apparent septum thickness of 55 mm, which is 9% thinner than the Iwashita-like septum.

As a final step of the comparison, the figure of merit presented in section 2.5 has been calculated for the three septa. The results are presented in table 4.2.3.3. Since the Pacman and the Iwashita septa scaled for the FCC would have to be made super ferric, the FCC Yonemura-like septum could

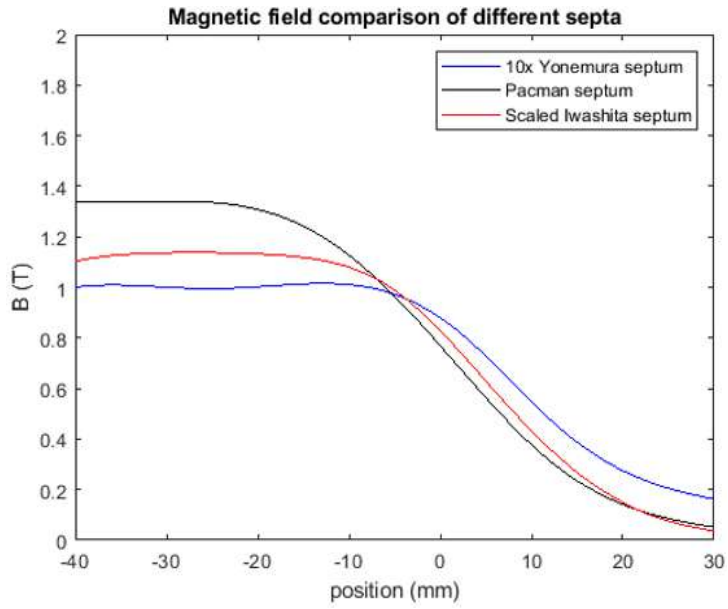


Figure 4.12: Comparison of the different septum fields plot along the midplane after optimization

be made normal conducting for simplicity. In this case, the three figures of merit have been calculated using the normal conducting formula because the only reason to build the septa super ferric is to reduce the coil size and power consumption. Additionally, the Pacman septum would achieve a higher figure of merit if the aperture was reduced, given that the leak field is related to the leak field. This variant of the Pacman septum is also shown in table 4.2.3.3 for completeness, although it would not be possible to install a septum with such dimensions in the FCC. Magnetically, the three septa behave like a direct drive septa, as presented in section 2.4.1.

Table 4.4: Calculation of the figure of merit for the different massless septa presented.

Massless septum	B_0 (T)	B_{sat} (T)	B_{pole} (T)	B_{leak} (mT)	h (mm)	s (mm)	K (-)
Scaled Iwashita septum	1.13	1.8	1.78	0.5	38	52	1.63
Scaled Yonemura septum	0.1	1.8	0.42	7	38	60	0.002
Pacman septum	1.34	1.8	2.31	3.26	38	55	0.36
Pacman septum (reduced acceptance)	2	1.8	2.82	1.26	30	47	2

As a second figure for comparison, and although it is already included in the calculation of the figure of merit, it is common among magnet designers to calculate the ratio between the septum thickness and the gap height (r). For completeness, this ratio has been calculated explicitly in table 4.5.

Table 4.5: Comparison of gap height and septum thickness for massless septa

Septum type	Apparent septum thickness (mm)	Gap height (mm)	Septum thickness/ Gap height (-)
Pacman septum	55	38	1.44
Pacman septum (reduced)	47	38	1.24
Iwashita type	52	38	1.37
Yonemura type	65	38	1.71

From the figure of merit calculated for the three septa types, it is obvious that the Yonemura type is not suitable for FCC since the magnetic field is too weak, although the main use of the prototype was to do phase space stretching, as explained in [66]. The Iwashita type septum and the Pacman septum are also not suitable for FCC, despite the fact that their figure of merit being significantly higher than the Yonemura one, although 1.1 T is not particularly high for the magnetic field of a septum magnet. This is due to the

fact that their operating fields are much higher, in part thanks to the use of compensation coils. It is worth noting that the original design by Yonemura does not include compensation coils because the main goal was not to create the perfect massless septum but to use the field gradient.

4.3 RF compensation and resonant mode selection

One possibility to use a Pacman septum in the FCC is to accept that the virtual septum thickness is bigger than desired and actively compensate its effects.

As an alternative it is of interest to investigate a compensation scheme using a transverse deflecting radiofrequency cavity and to estimate the necessary parameters for such a cavity. The goal is to discard this approach in case the necessary width, length or frequency were not possible to realize and obtain a preliminary assessment of the feasibility of such a system.

Usually in high energy particle colliders, RF cavities are used to accelerate the beam instead of deflecting it. This approach to deflect transversely a beam to compensate a leak field becomes interesting because the cavity can act on some selected bunches and not necessarily on all the bunches of the beam. This may be useful if one wants to use the cavity as a bumper magnet, to create a small bump in the beam orbit at a certain point. The particle deflection is due to the Lorentz force seen by the beam, so it is necessary to have a transverse electric (TE cavity) or magnetic field (TM cavity), or both. However, one should be careful when having both an electric and magnetic field in the transverse plane since their actions can add up constructively or destructively. This cavity does not intend to be a transverse damper, as the ones present in high intensity machines. A transverse damper will operate over several turns and may even be designed with a frequency high enough to act on the head or the tail of a given bunch. In this case, the cavity is assumed to compensate the leak field over one turn and the bunch size is not taken into account. The aim of this study is to investigate the feasibility and estimate the relevant parameters of such a system.

A TE cavity does not have a longitudinal electric field, and according to the Panofsky-Wenzel theorem, the transverse kick of a cavity depends on the transverse variation of the longitudinal electric field, as shown in equation (4.1):

$$V_x = \int \frac{F_x}{q} \cdot dz = \int \left(E_x + (\vec{v} \times \vec{B})_x \right) \cdot dz = -\frac{c}{\omega} \int (\vec{\nabla}_t \cdot E_z) \cdot dz \quad (4.1)$$

In equation 4.1, the particles are travelling along the Z axis. F_x is the force in the x direction and E_x is the electric field in the x direction. The charge of the particle is named q. $\vec{\nabla}_t E_z$ denotes the derivative of the transverse direction. The velocity of the particle is v, which at high energies can be substituted by the speed of light. Then, the product of the velocity of the field can be approximated by:

$$\vec{v} \times \vec{B} = v_z \cdot B_y \approx c \cdot B_y \quad (4.2)$$

This theorem is applicable to any kind of cavity provided that the deviation from the axis is not significant. This is true in this application since the goal of the cavity is to compensate a deflection from a leak field. It has to be taken into account that V_x is not a real voltage as understood in an electric circuit or an electrostatic deflector since part of the deflection comes from the magnetic field. It is fundamentally the work per unit of charge. Additionally, the angular frequency ω is related to the frequency via $\omega = 2\pi f$.

Given that TE modes are characterized by not having an electric field in the direction of propagation, it is not possible then to use a cavity operating in a TE mode to deflect the FCC beam. Since the longitudinal component of the electric field does not exist, therefore there is no variation, transverse or otherwise, of the longitudinal electric field. The simplest mode possible in a TM cavity is the TM_{110} mode. The electrical field on axis is zero but the transverse magnetic field in the axis is most favourable for deflection since both sides of the field add up constructively. The simplest cavity that can be designed is a cylindrical pillbox cavity, and its equations in cylindrical coordinates for the electric and magnetic field of a T_{110} cavity are given by:

$$\begin{aligned} E_r &= 0 \\ E_\theta &= 0 \\ B_z &= 0 \\ E_z &= E_0 J_1\left(\frac{p_{11}r}{a}\right) \cdot \cos(\theta) \\ B_\theta &= i \frac{E_0}{c} J_1'\left(\frac{p_{11}r}{a}\right) \cdot \cos(\theta) \\ B_r &= i \frac{E_0 \cdot a}{c \cdot r \cdot p_{11}} J_1\left(\frac{p_{11}r}{a}\right) \cdot \sin(\theta) \end{aligned} \quad (4.3)$$

In the system of equations (4.3), a is the radius of the cavity, J_1 and J_1' represent the second order Bessel functions of the first kind and its derivative respectively, p_{11} is the first zero of J_1 , with a value of 3.8317, and the imaginary unit in the magnetic fields equations shows that there is a 90° phase difference between the electric and magnetic field. η is the impedance of free space. It can be seen that the radial and azimuthal components of the mag-

netic field are not zero, so they will be able to deflect the beam. It is also necessary to keep in mind that $\vec{B} = \mu_0 \vec{H}$.

A schematic of the pillbox cavity with the relevant dimensions is presented in figure 4.13. The beam travels along the z axis.

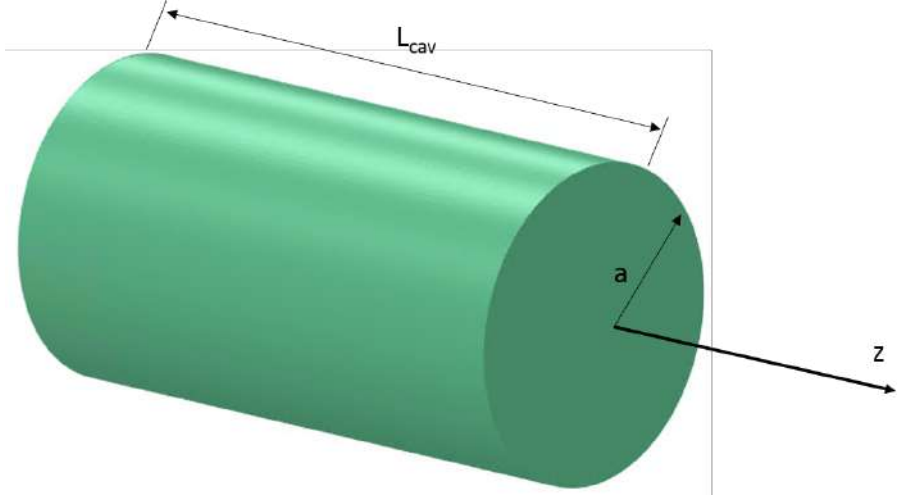


Figure 4.13: Schematic of the cavity dimensions.

The operating frequency determines the cavity radius, according to equation (4.4), which relates the operating frequency to the geometrical parameters of a TM_{nml} cavity. It is clear that if the frequency increases, the radius of the cavity decreases [111, 112].

$$\omega_{nml} = c \cdot \sqrt{\left(\frac{p_{nm}}{a}\right)^2 + \left(\frac{l\pi}{L_{cav}}\right)^2} \quad (4.4)$$

In the case of a TM_{110} cavity, the length is not determined by this equation since the corresponding term is 0. In equation 4.4, a is the cavity radius and L_{cav} is the cavity length and p_{11} is the first zero of the second order Bessel function of the first kind, which has been plotted in figure 4.14. Introducing this value of p_{11} and a frequency of 500 MHz in equation (4.4), the radius a is fixed to 365.7 mm.

$$\eta = \sqrt{\frac{\mu_0}{\epsilon_0}} \quad (4.5)$$

The equations have been adapted to this case from [111].

For illustration, the first and second order Bessel functions of the first and second kind are plotted in figure 4.14.

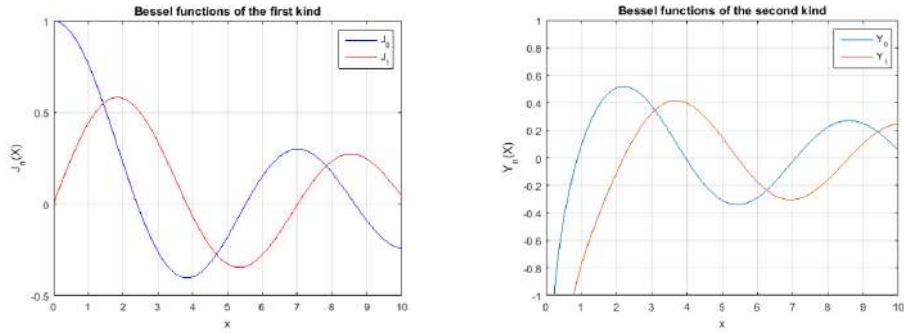


Figure 4.14: Plots of Bessel functions of the first and second kind

The field distribution of a TM_{110} cavity is shown in figure 4.15. A perspective view is shown in figure 4.16. The colour scale is set to one at the maximum field and zero at the lowest point. The directions of the field are indicated with the directions of the arrows.

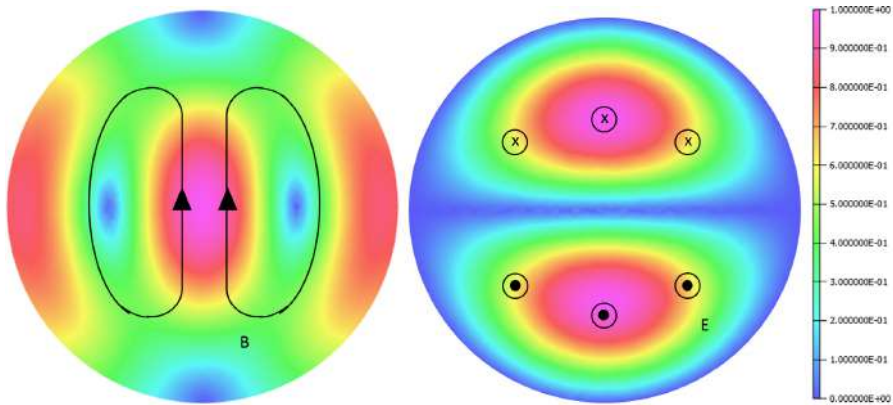


Figure 4.15: Magnetic (left) and electric (right) field distribution in a TM_{110} cavity (arbitrary units)

As expected, the magnetic and electric field have a phase difference of 90

degrees between them and the magnetic field is strongest at the centre, while the electric field is zero along the axis. The maximum of the electric field is located halfway between the axis and the ends of the cavity, while the magnetic field has a global maximum in the axis and two local maxima at the cavity walls, and it vanishes at the midpoints.

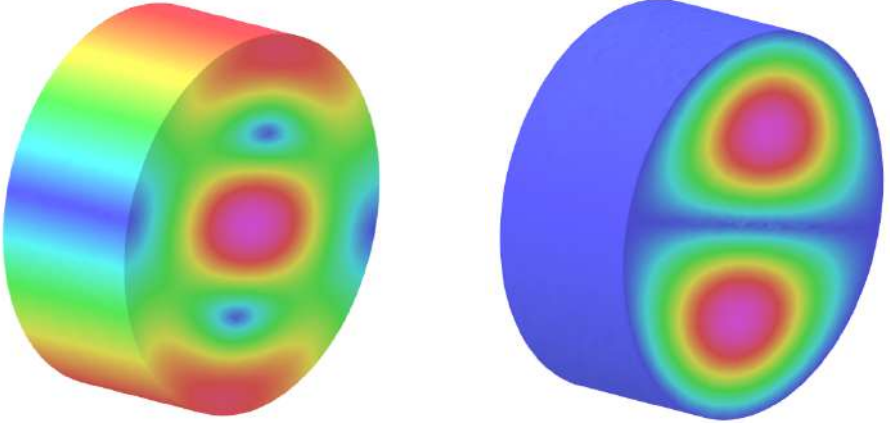


Figure 4.16: Magnetic (left) and electric (right) field distribution in a TM110 cavity in 3D (arbitrary units)

4.3.1 RF cavity feasibility

Once the operating mode of the cavity has been identified, the next step is to define its parameters to achieve a feasible design. The first choice to be made is the technology to be used. A normal conducting cavity is simpler, does not need any quench protection and is weaker than a superconducting cavity. However, if this cavity is used in the beam dump system it should be working permanently and follow the energy swing of the accelerator, which means that it will be challenging to provide sufficient cooling power to the cavity during operation of the FCC. If the cavity is used in the injection system, it can be turned off once the injection is finished. However, the foreseen injection time for the FCC is in the order of tens of minutes. Again, it would be challenging to cool a normal conducting cavity during operation. It is therefore necessary to use a superconducting cavity.

The minimum operating frequency is determined by the beam structure.

That means if the cavity operates at a lower frequency, it will not be able to deflect all the bunches. In the FCC baseline, the bunch spacing is 25 ns, and a bunch, is approximately 8 cm long. That means that a bunch can be seen as a 0.26 ns signal. Therefore, adding the duration of a bunch and the bunch spacing, the cavity should be able to produce a full cycle of the wave with a period between 25 and 26 ns, since the RF wave needs to go through the positive and negative parts of the oscillation. Therefore, the minimum operating frequency of the cavity is around 38 MHz. This estimation of course does not take into account many features of the RF wave, such as rise time, fall time or the duration of the peak. It is also possible to estimate the upper limit of the operating frequency. The cavity needs to deflect one bunch at a time, so the RF wave needs to be positive during approximately 0.5 ns. That produces a maximum operating frequency of 2 GHz. Current technology of superconducting cavities allows for operation at a frequency in the order of 1 GHz, and as an example, the baseline operating frequency for the ILC cavities is set at 1.3 GHz. To include some margin, this cavity will operate at 500 MHz.

In a TM110 cavity the cavity length is not related to the radius, as shown in equation (4.4) where the corresponding term cancels. This is also shown in slide 55 of [113]. Considering only equation (4.4), the length of the cavity can therefore be chosen arbitrarily. The maximum *useful* length corresponds to the distance covered by the particle during half a period of the oscillation, which results in a cavity length:

$$L_{cav} = \frac{c \cdot T}{2} = 300 \text{ mm} \quad (4.6)$$

This length calculation has been verified using Opera 3D. A 300 mm long cavity was simulated using the modal solver to identify the resonant frequencies and modes and, as shown in figure 4.16, the magnetic and electric fields do not depend on the longitudinal position. These results have also been found to agree with those obtained by the CST software.

4.3.2 Preliminary estimation of the parameters of a pill-box cavity with the required field map

A cylindrical cavity has been designed with the parameters presented in section 4.3. The cavity is cylindrical because it is the simplest possible. First, the resonant mode was identified by comparing the desired and obtained field map and the resonant frequency with the Opera 18 HF Modal solver [114]. The cavity is simulated by assuming the walls are a perfect conductor.

The beam rigidity is defined as the relativistic momentum of the beam per unit charge and remains constant at a given energy.

$$B\rho = \frac{\gamma_{rel} \cdot m_0 \cdot c}{q} \quad (4.7)$$

The cavity was excited with a 30 MV/m electric field, as stated in section 4.3, which implies that the peak magnetic field is 0.1 T. For comparison, the leak field of the Pacman septum presented in section 4.2 is 1.26 mT. With these values of magnetic fields, it is possible to neglect the effects of the leak field of the Pacman septum because its effect on the beam will be approximately 80 times smaller. The deflection (α) of a 50 TeV particle due to a 0.1 T magnetic field can be approximated by:

$$B \cdot L_{cav} = \alpha \cdot B\rho \quad (4.8)$$

In equation (4.8) the magnetic field integral has been approximated by the product of the magnetic field by the cavity length. ρ is the radius and the product $B\rho$ is the beam rigidity, which results in $\alpha=180$ nrad. For the leak field of 1.26 mT and a magnet length of 4 m, the achieved deflection obtained from equation 4.8 is $\alpha=30$ nrad. A priori it is possible to use the RF cavity to compensate the deflection from the leak field. However, it is assumed that the leak field is corrected in a single kick, which would require perfect phase advance at every turn. It is therefore necessary to operate the cavity with an orbit feedback system, to relax this constraint.

4.3.3 Effect of the massless septum and the RF compensation on the orbiting beam

A more detailed calculation has been performed using an implementation of the Finite Difference Method in Matlab. It was not possible to perform this check automatically within the modal simulation because the solution provided by Opera contains only the resonance mode, not the fields at every node. To obtain the field values at every point a different simulation needs to be performed. Such a simulation is significantly more time consuming than the modal simulation and does not add any necessary insight at this moment. This preliminary calculations only investigate the feasibility of this compensation scheme. Alternatively, the particle tracking could be performed using general purpose codes like GPT or MAD-X. Again, these simulations would take too much time for this preliminary study.

A thorough description of the finite difference method and its application to this problem can be found in appendix A. The script, which considers only the magnetic field in the cavity, starts by calculating the magnetic force suffered by a particle travelling through the cavity. Considering only the action of the magnetic field, the acceleration of the particle is calculated by dividing the magnetic force by the relativistic mass. The acceleration is then integrated by using the finite difference method to obtain the particle velocity, which is then integrated to obtain the transverse position at each longitudinal step.

his calculation assumes that the deflection happens only at one point, and the particle only sees the maximum magnetic field because its separation from the central axis is negligible. This approximation is necessary although the leak field may vary across the bunch size.

The necessary field maps were extracted from Opera 3D at slices of 1 mm and the trajectory of a 50 TeV particle inside the cavity was calculated using equations (A.15). The separation of the particle from the longitudinal axis is shown in figure 4.17. In the plot, the particle enters the cavity at 0 mm and exits at 300 mm of the horizontal (longitudinal) axis, where the magnetic field is strongest. The final deflection is below 1 nm.

The deflection produced by the cavity is less than 1 nm. Using the approximation for small angles $\tan(\theta) \approx \theta$, this means that the deflection angle is in the order of 1 nrad. This result is expected since 50 TeV is a very high energy. A real beam would have a spread on position and momentum of the particles, but it is seen that there is no need to take it into account at this stage since the deflection of particles in a given starting position different to the axis will be even smaller.

Therefore using an RF separator is not ideal for an accelerator like the FCC, where the beam rigidity is extremely high. It could be useful however for lower energy proton accelerators or for lepton machines. Such plots have been produced for protons and electrons in figure 4.18. It should be taken into account that the vertical axis is in a logarithmic scale. It is important to keep in mind that the rest mass of the electron is approximately $0.51 \text{ MeV}/c^2$, so the plot in figure 4.18 is only valid for energies in which the behaviour of the beam is relativistic, that is, when $\gamma \gg 1$. Below this energies, the assumptions made in these calculations do not hold and therefore the results are not accurate.

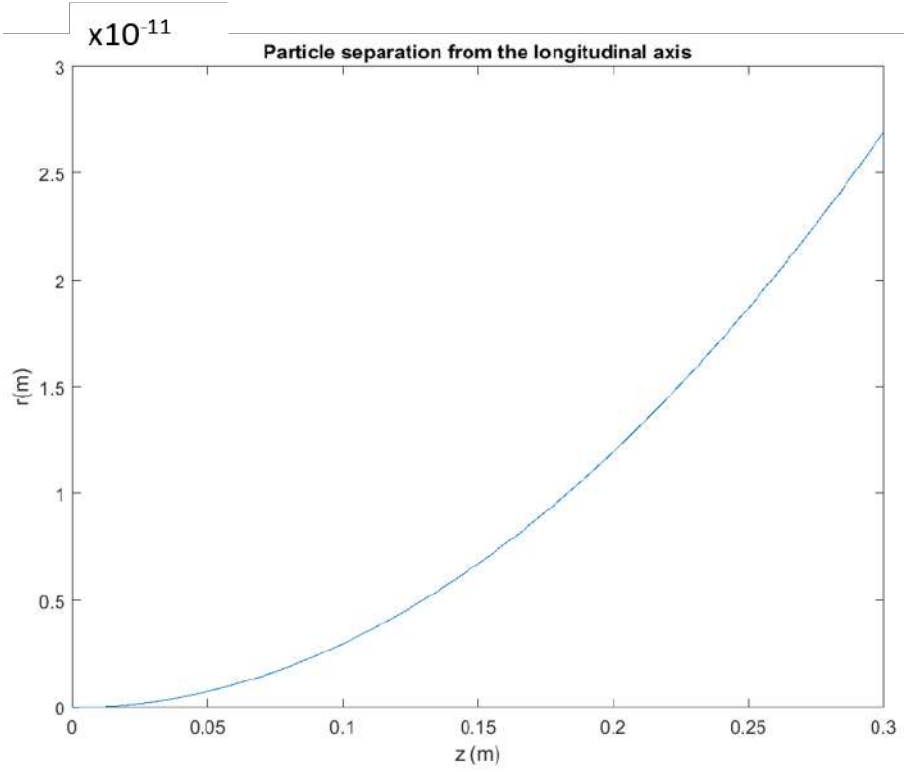


Figure 4.17: Radial separation from the axis of a 50 TeV particle inside the RF cavity

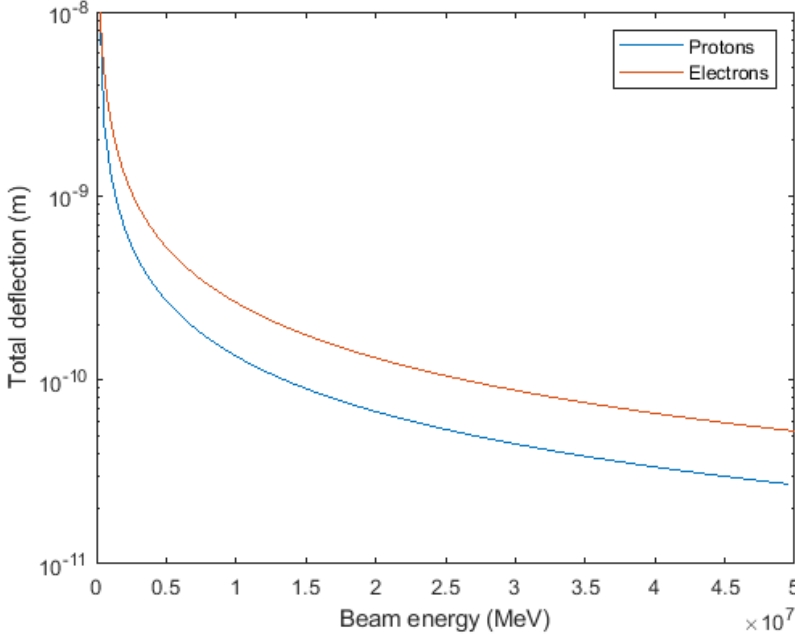


Figure 4.18: Deflection provided by a 30 MV/m RF cavity for a proton and electron beam as a function of the beam energy

4.4 Double massless septum for injection protection

4.4.1 Concept

An unconventional application for massless septa is to use their magnetic field to manipulate the phase space. One possibility is to use the gradient in the apparent septum region to stretch the beam in phase space, to reduce losses at the extraction point in the lattice, as it was proposed in [66]. After the extraction point, a second massless septum with the opposite field returns the beam to the closed orbit in phase space. Using this strategy, the losses of the beam in the extraction septum can be reduced, which has many benefits like reduced stress in the septum and a much lower activation during operation.

Normally in the injection region of a very high energy particle accelerator,

like the LHC or the FCC-hh, there is a quadrupole magnet that helps deflecting a mis-injected beam into an internal dump (TDI), which is capable of absorbing the impact of a certain number of bunches or of the full beam because a staged injection will be blocked as soon as the TDI suffers an impact. The quadrupole is included in the lattice, its function is not only to take part in the optics of the ring, but it also provides an extra deflection thanks to the careful design of the injection region. An impact in the TDI generally indicates a problem upstream in the transfer line or in the injection region, generally a kicker magnet firing failure. A quadrupole magnet is used because the magnetic field grows linearly as the beam is separated from the centre. This quadrupole field is cancelled only at the centre point and affects the beam in all cases given that the beam size of a perfectly injected bunch is not zero, so it needs to be included in the optics.

Alternatively, it is possible to use a double massless septum as an injection protection device [115]. There are two options in this approach. Option A is to use the high-field region of the massless septum to extract a mis-injected beam to an external dump (external TDI). Using an external TDI has the advantage that avoids the hadronic showers to the downstream equipment. The main drawback is that the deflection needs to be sufficient to bypass the first quadrupole magnet seen by the injected beam, whose cryostat has a radius of 540 mm.

The second option (B) is to use the gradient of the magnetic field in the septum region to increase the horizontal size of the beam at the TDI. This would reduce the deposited energy density while not affecting the orbiting beam.

The required field profile is explained qualitatively in figure (4.19), with the indicated dimensions and magnitudes. x_{ZF} is the width of the zero-field region. δB_0 is the allowed leak field in the zero-field region, where the orbiting beam is located. x_{SL} is the width of the apparent septum thickness and B_{max} is the field magnitude in the high field region.

The relevant parameters have been estimated in table 4.6 for both options.

Some of the parameters have been left blank because they are not relevant in the corresponding option. For example, in option B the maximum field (B_{max}) is not relevant, given that the beam will be passing through the gradient region (x_{SL}) and not through the high field region. In the case of option B, both the necessary magnetic field gradient and the magnetic length are given as a range because there is not only one possibility. The aim of this option is to increase the horizontal size of the beam and the lower bound of the range corresponds to an increase by a factor of 2.

It can be seen that in the case of option A, although the gradient of the

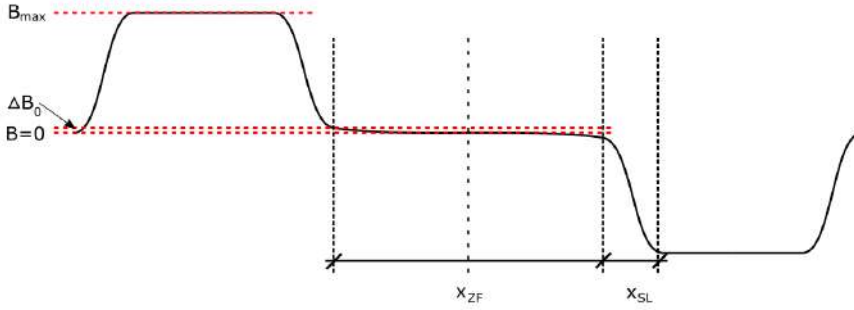


Figure 4.19: Ideal field profile of a double massless septum with the relevant magnitudes

Table 4.6: Estimation of the double massless septum requirements for both options

Parameter	Unit	Option A	Option B
B_{max}	T	2	-
x_{ZF}	mm	9.15	9.15
x_{SL}	mm	5	5
ΔB_0	mT	1	1
dB/dx	T/m	-	10-50
$\int B \cdot dl$	Tm	108	-
Magnetic length	m	54	1-10

magnetic field has been left blank, to express that the gradient is not used in the beam deflection, it is necessary to produce a 400 T/m gradient over a 5 mm distance (x_{SL}), which is not realistic for a massless septum although it is possible to be achieved in a superconducting quadrupole. It is possible to change the optics to further increase the magnitude of x_{SL} by increasing the horizontal β function at the kicker magnet upstream from the TDI. Therefore, only option B will be studied.

4.4.2 Comparison between ideal and real septum field

The most challenging part of designing a double massless septum is to produce a zero-field region in the centre of the gap. The required field profile can be seen as a quadrupole field that has been stretched in the centre. The most

obvious way to change the slope of the field along the midplane of the magnet from a quadrupolar field to a field as shown in figure 4.19 is to place a current wall in the elbows of the plot. If this is done, then the massless septum is not massless anymore. The alternative is then to use compensation coils and create the desired field pattern by superposition.

The magnetic field obtained from the designed septum and the ideal magnetic field are plotted in figure 4.20. Both plots are in the same scale. It is seen that the zero field region can be stretched from a point to an almost 10 mm region, where the leak field stays below a few mT. Besides, the obtained magnetic field gradient reaches the desired 50 T/m. It is necessary to keep in mind that the magnetic field in the high field region is not foreseen to be used in any application, therefore there is no field quality requirement and it is not necessary to optimize it.

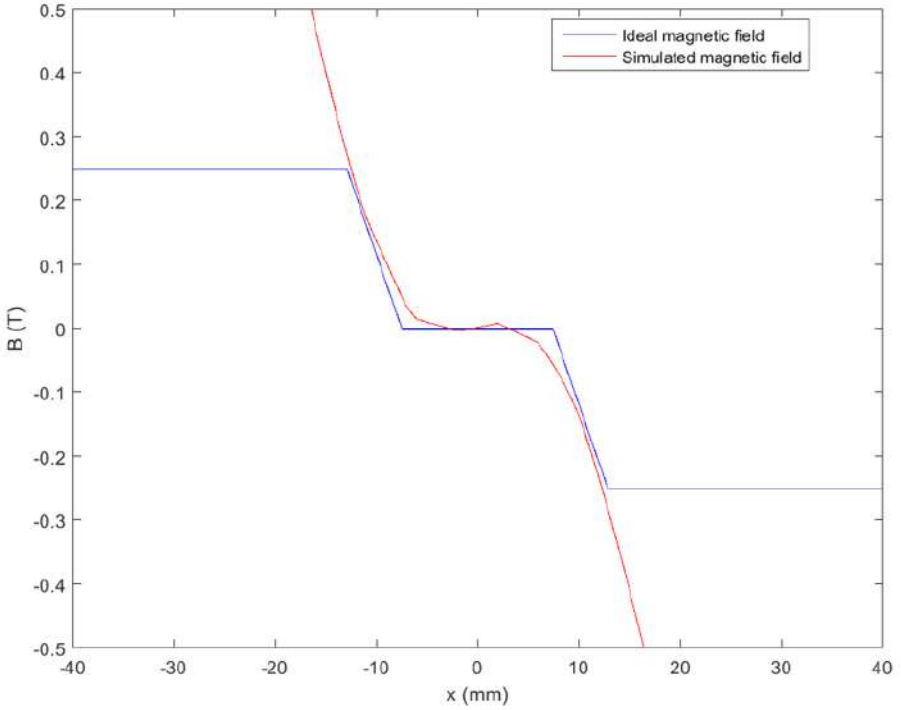


Figure 4.20: Superposition of the ideal and the real magnetic field in the midplane

4.4.3 Feasibility

The main parameters of the double massless septum are presented in table 4.7. The leak field is currently estimated at a level of a few mT, a value comparable to the error of the main dipoles.

Table 4.7: Parameters of the double massless septum.

Parameter	Unit	Value
Magnetic field gradient	T/m	54.6
Leak field	mT	1
Zero-field region thickness	mm	10
Gradient region thickness	mm	5
Gap height	mm	38
NI (main coils)	A·turns	64000
Current density (main coils)	A/mm ²	800
NI (compensation coils)	A·turns	37600
Current density (compensation coils)	A/mm ²	940

A zoom of the cross section is shown in figure 4.21. The bigger coils are the main coils and the smaller ones are the compensation coils.

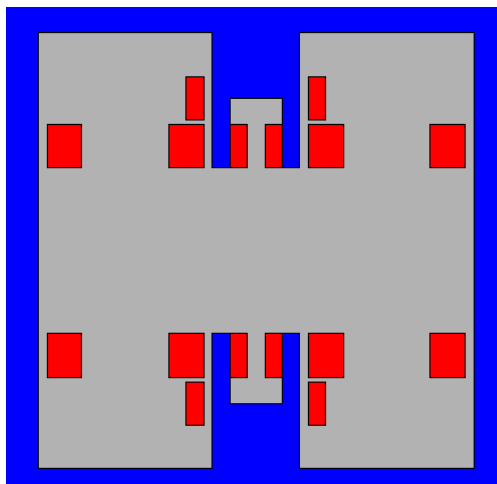


Figure 4.21: Detail of magnet gap and coil layout for the double massless septum

Figure 4.20 shows that the double massless septum presented may be used in the FCC injection protection scheme. All the parameters fall within feasible superconducting technology and the simulated magnetic field follows the required field very closely. Besides, this idea can also be used for lower energy beams, where the integrated field and the gradient required will be lower.

4.5 Conclusion

The Pacman septum has been presented in this chapter. It has been optimized to minimize the apparent septum thickness and to maximize the peak field and the field homogeneity. It has been shown that its performance is better than previously reported massless septa in literature and the figure of merit has been calculated.

It has been shown that the leak field of a 2 T Pacman septum cannot be compensated by a transverse deflecting cavity although such approach may be deployed at lower energies in lepton machines.

Finally, the use of a double massless septum for injection protection has been studied with very promising results. The figure of merit calculated in section 4.2 does not make sense in this application because there is no leak field or apparent septum thickness, in fact, instead of reducing the septum thickness which is the usual approach in septa design, the goal here is to increase the zero field region and producing a magnetic field gradient.

Chapter 5

Truncated Cosine θ septum

5.1 Introduction

In this chapter the concept of Cosine θ magnets is introduced with the aim of explaining the idea of truncation to produce a Truncated Cosine θ septum. The 2D magnetic design of the cross section is performed in section 5.2.1. The mechanical validation is performed in section 5.2.2. Following this, the 3D design of the coil heads is performed in section 5.3. First the magnetic field is simulated and the result is used in the mechanical validation. Finally, the figure of merit is calculated in section 5.4 and future lines of work are identified in section 5.5.

5.1.1 Pure multipoles produced by Cosine θ current distributions

The design of a Truncated Cosine θ (TCT) septum starts from the well known Cosine-Theta dipole with line currents and an iron yoke. One way to generate a pure multipole field in 2D is to place two current cylinders with their centres separated a distance s . One of them carries a current density J_{in} that is travelling into the paper and the other cylinder will carry a current density J_{out} , flowing out of the paper. These current densities will have the same absolute value, so they will cancel in the overlapping region, which can be left empty. This situation is shown in figure 5.1. The magnetic field at any point in the overlapping region, which is the useful aperture, is then given by:

$$\begin{aligned} B_y &= \frac{\mu_0 J}{2} (-r_1 \cdot \cos\theta_1 + r_2 \cdot \cos\theta_2) = \frac{-\mu_0 J s}{2} \\ B_x &= \frac{\mu_0 J}{2} (+r_1 \cdot \cos\theta_1 - r_2 \cdot \cos\theta_2) = 0 \end{aligned} \quad (5.1)$$

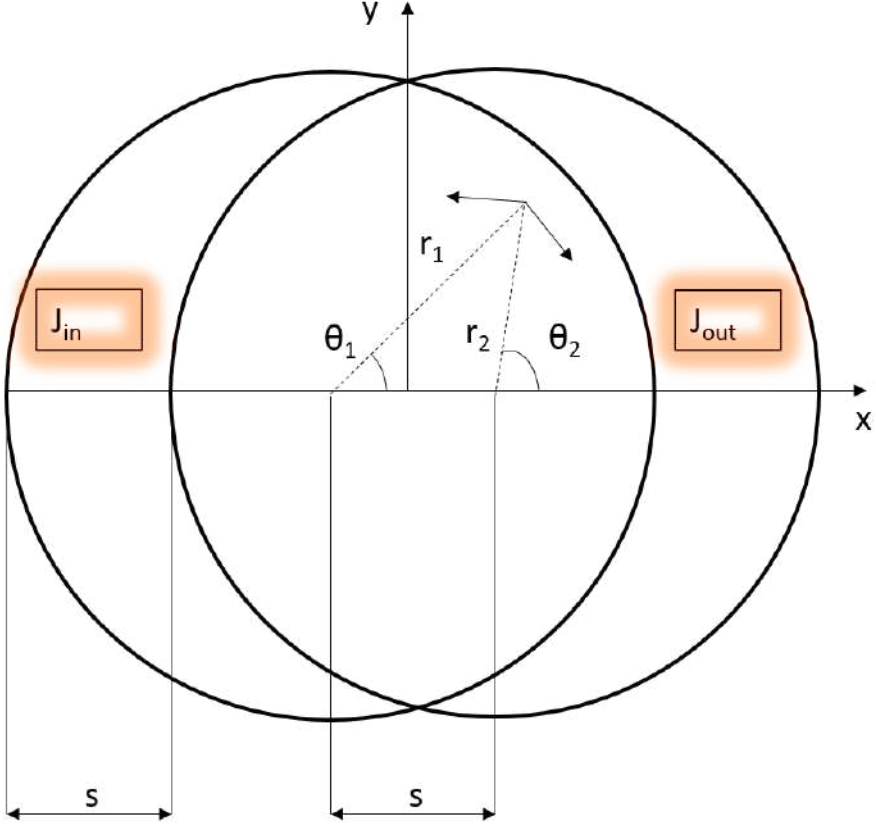


Figure 5.1: Schematic of cross section to produce a perfectly uniform field using two overlapping cylindrical current sheets.

A similar approach can be used with overlapping ellipses, for example two crossing ellipses at 90° can produce a pure quadripole field as explained in [116]. Additionally, the Fourier transform can be applied to a magnetic field to decompose it in multipoles, which can then be generated using cylindrical or

elliptical current sheets. The magnetic field is created by a current distribution at a fixed radius that is scaled according to:

$$J = J_0 \cos(N \cdot \theta) \quad (5.2)$$

Following this, it is possible to produce any field using superposition of the required Fourier multipoles. As it is not possible to produce a superconductor with the shape shown in figure 5.1, in practice a cylindrical sheet is approximated by discrete conductors and the $\cos N \cdot \theta$ distribution of current is achieved by using spacers and grouping the discrete conductors in blocks. Several layers can also be used to further approximate the ideal distribution, typically two.

Starting from a Cosine θ dipole, truncation is necessary to turn the magnet into a septum, as shown on the left side of figure 5.2, which has been reproduced from [75]. In 2D, the magnetic field lines are lines of constant potential. Therefore, the magnet gap can be truncated along a constant potential line and the magnetic field inside the aperture will not leak outside the current wall. In this case, truncation means to place a current wall along the chosen equipotential line. Full derivation of a $\cos(n \cdot \theta)$ multipole can be found in [117, 118] and a derivation of the truncation procedure was done by Krienen et al. [119]. This procedure can be extended to any multipole, allowing to create truncated quadrupoles, sextupoles, etc. If the truncation is not performed along a field line, a combined function magnet can be created, although in this case the leak field will not necessarily be confined into the field free region.

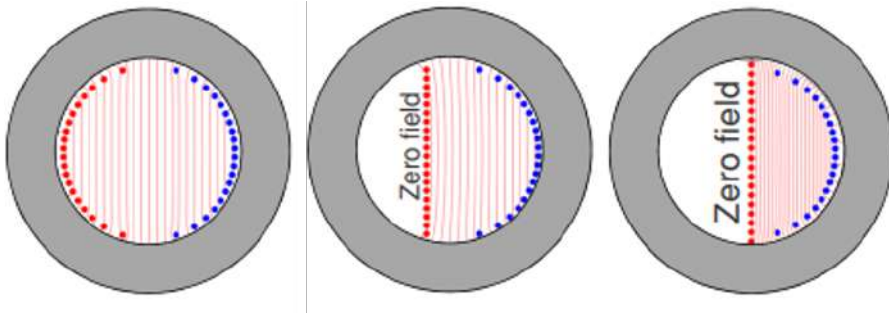


Figure 5.2: Schematic of a Cosine-theta dipole and its truncation

In [119], the image current method, analogous to the mirror charge method in electrostatics, is used to calculate the placement of the current distribution. The image currents can be replaced by an iron yoke that is not saturated and

conducts the return flux of the magnet in the same way as the image currents and its dimensions can be calculated analytically. The analytical calculation is based on two assumptions. The first one is that the permeability of the yoke is much higher than that of vacuum and not yet saturated. The second assumption is that a current wall that extends to the yoke forces the leak field lines to avoid the field free region. In a conventional septum magnet, this current density needs to be constant to avoid the magnetic field leaking into the field free region. This is illustrated in figure 5.3, presented in [120], and in figure 5.4.

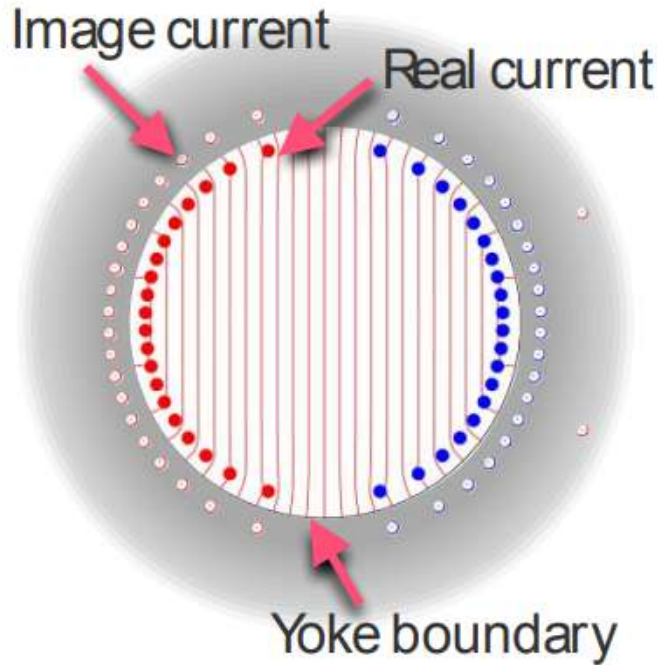


Figure 5.3: Schematic of the image current method

The iron saturation for this calculation is set at 1.6 T. Some soft magnetic steels saturate at a higher level, but taking 1.6 T as a value also provides some margin. It is important to note that this magnetic field value is the peak field that can be allowed at a certain point in the yoke. If the yoke is saturated, even locally, the permeability of that region decreases and eventually becomes

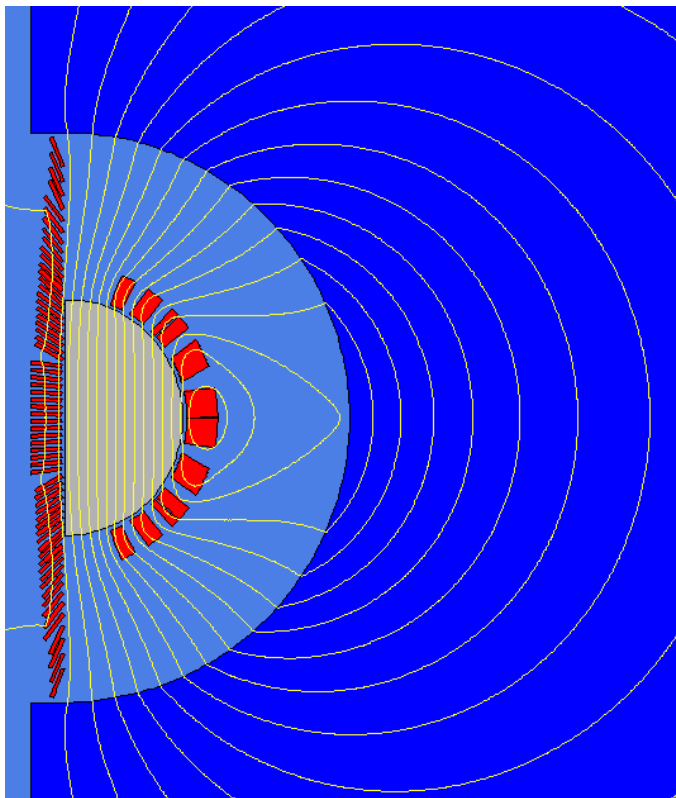


Figure 5.4: Schematic of the TCT septum with the image currents replaced by the iron yoke

comparable to that of vacuum. If the permeability of the yoke is not sufficiently high, the magnetic field will leak into the field free region. It has to be noted that the boundary conditions change when the image currents are substituted by an iron yoke. In the case of the image current, the normal component of the magnetic field is zero while in the case of the iron yoke the magnetic field is fully perpendicular to the iron interface.

5.2 2D design

One of the advantages of the TCT topology is that the geometry of the cross section can be estimated analytically and can be optimized numerically using a finite element code, as opposed to other septa topologies, like massless septa or eddy current septa, which are not easy to study analytically with a good accuracy.

The parameters that are set for this design are the coil radius (R_c) and the magnetic field in the gap (B_0). The inner radius of the yoke (R_y), the number of turns (N) and the current (I) will be calculated. These parameters are shown in figure 5.5.

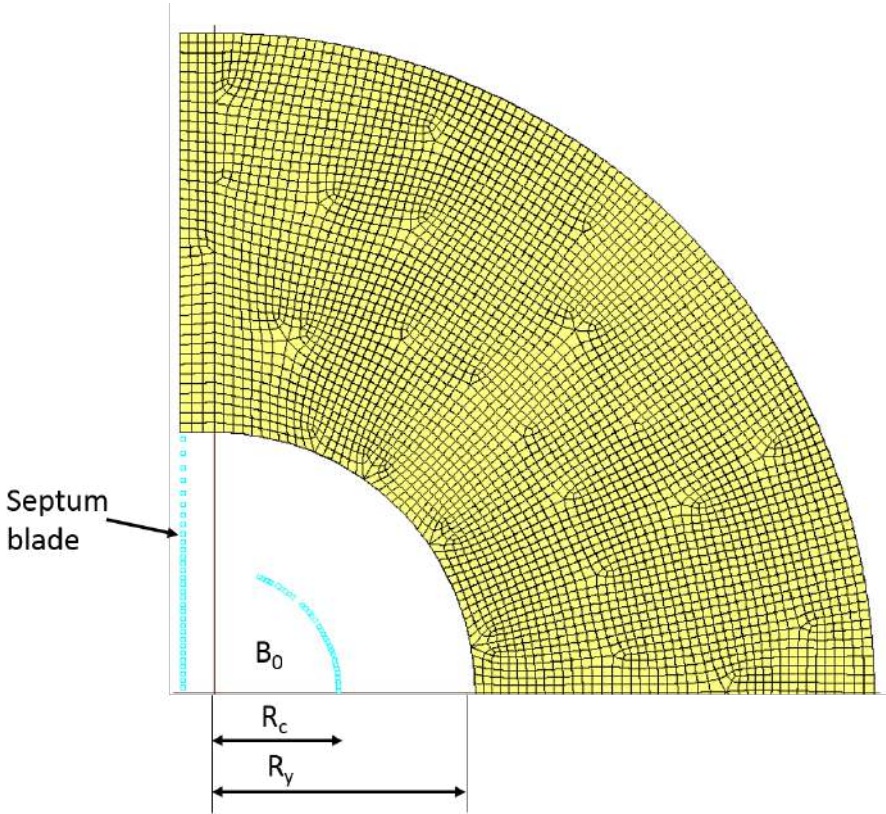


Figure 5.5: Schematic of the TCT septum cross section

The FCC injection and extraction requirements were presented in table 1.3. The inner radius of the coil is set to 35 mm, and the line currents will be approximated by an ideal line at the centre of the cable, that is, at a radius of $R_c = 39$ mm. The inner coil radius is set at 35 mm to make sure that there is space for the orbiting beam to circulate. As explained in [121], the inner magnetic field created by a current sheet at a constant radius with a Cosine-Theta distribution is given by equation 5.3, and the iron yoke, with a radius of R_y can be substituted by an equivalent distribution of image currents carrying a current I_{image} at a distance R_{image} . The full parameters of the image current distribution are written in equations 5.4, and the field produced by the image currents is shown in equation 5.5. This analytical calculation assumes that the magnetic permeability of the iron is much greater than the permeability of vacuum.

$$B_{\text{current}} = \frac{\mu_0 I}{2R_c} \quad (5.3)$$

$$\begin{aligned} R_{\text{image}} &= \frac{R_y^2}{R_c} \\ I_{\text{image}} &= \frac{\mu_r F_e - 1}{\mu_r F_e + 1} I_c \approx I_c \end{aligned} \quad (5.4)$$

$$B_{\text{current}} = \frac{\mu_0 R_c}{2R_y^2} \quad (5.5)$$

The magnetic field inside the coil is calculated by superposition adding the contribution from the coil and the contribution from the iron. The same procedure can be used to calculate the field outside the coil radius, which depends quadratically on distance:

$$\begin{aligned} B_{\text{in}} &= \frac{\mu_0 \cdot I}{2} \left(\frac{1}{R_c} + \frac{R_c}{R_y^2} \right) \\ B_{\text{out}} &= \frac{\mu_0 \cdot I}{2} \left(\frac{R_c}{y^2} + \frac{R_c}{R_y^2} \right) \end{aligned} \quad (5.6)$$

Once the expressions for the magnetic fields are known, it is necessary to calculate the radius of the yoke (R_y). This is done by dividing the total magnetic field by the contribution of the iron to the magnetic field. That is, by dividing the equations system 5.6 by equation 5.5, resulting in:

$$R_y = R_c \cdot \sqrt{\frac{B_{\text{in}}}{B_{\text{iron}}} - 1} \quad (5.7)$$

In fact, since the left side of the yoke is not used by the return magnetic field, it can be removed without any change in the field distribution, as shown in figure 5.2.

Equation 5.7 is valid for a given Cosine-Theta magnet, but the goal is to design a TCT septum. The truncation is done at the centre of the gap, which means that the total magnetic flux is confined to half of the gap area of the original Cosine-Theta magnet. Therefore, the magnetic flux density is doubled because of the reduction in the gap area. Equation 5.7 has to be modified to take this phenomenon into account, and a factor of 2 appears in equation 5.8.

$$R_y = R_c \cdot \sqrt{2 \frac{B_{in}}{B_{iron}} - 1} \quad (5.8)$$

For first approximations it is usually accepted to take the iron saturation at 2 T, but in this case the saturation value has been limited to 1.6 T to allow for some margin in the saturation value and to ensure that the iron remains in the linear part of the BH curve, with a permeability that is much greater than the air permeability. Substituting the value of 39 mm for R_c in equation 5.8, the value obtained for the inner radius of the yoke is $R_y = 78$ mm.

Given that linear media and non-saturated iron are being assumed, the current density necessary to create these fields is proportional to the magnetic fields, by a factor $1/\mu_0$. Therefore the currents necessary to produce the nominal 4 T in the gap are given by equation 5.9, where I_{in} is the current density within the coil radius and I_{out} is the current density needed between the coil radius and the yoke radius. It can be seen that I_{out} is not constant and decays with the inverse of the square of the position of the current lines, exactly like the magnetic field B_{out} in the system of equations 5.6.

$$\begin{aligned} I_{in} &= \frac{I_0}{2} \left(\frac{1}{R_c} + \frac{R_c}{R_y^2} \right) \\ I_{out} &= \frac{I_0}{2} \left(\frac{R_c}{y^2} + \frac{R_c}{R_y^2} \right) \end{aligned} \quad (5.9)$$

From equation 5.6, it follows that the current needed to produce the 4 T magnetic field is given by $N \cdot I = 198625$ A·turns. It is necessary to decide then the number of turns per pole to be used. Using too few turns would imply the need of a high current, above the limits of the superconducting material, and it may be difficult to produce a Cosine-Theta current distribution. This is usually achieved in superconducting magnets by grouping turns in blocks that follow a Cosine-Theta distribution. Using too many turns would make it impossible to design a coil that can be wound because the coil would be too big, especially at the coil ends. Additionally, the magnet inductance would increase significantly, making the energy dissipation in the event of a quench and the design of a quench protection system very challenging, or even impossible.

As a compromise, it has been chosen to use 31 turns per pole. This value means that the current in the coil is 6284 A, which is perfectly achievable in low temperature superconductors. Besides, by maximizing the current in the coil, the space taken by the coil is minimized and it will leave more space in the gap to design a support that holds the coil in place during operation and cool down.

The 3D design of the coil ends would be much simpler using a single strand cable, which could be wound in grooves. Such approach has been used successfully at CERN, LBNL and PSI to wind different Canted Cosine-Theta (CCT) magnets [122, 123, 124]. This strategy has many advantages when the coil shape is simple. It combines the flexibility of a single strand cable with the fact that by introducing several turns in each groove and impregnating the coil with resin makes de facto a Rutherford cable. For simple shapes, the coil former is very easy to machine, and can be 3D printed for more complicated geometries, reducing costs and time. It is very challenging to wind the coil from a continuous single strand cable due to the fragility of the insulation and the cable itself. Therefore the single strand turns need to be connected either in series or in parallel. If they are connected in parallel, a great number of connections has to be made, probably at the ends of the magnet. This is a very challenging point since the splices can be a potential quench point, and their number would be in the order of a few hundred. If they are connected in series, since inductance grows with the square of the number of turns in a coil, a high number of turns would produce a very high inductance. This may be problematic in case of quench, as explained in the previous paragraph. Both the series and parallel connection of many turns has serious drawbacks, but regardless of the connection mode chosen, the coil former of a non-standard shaped coil like the TCT septum may be very difficult to manufacture and 3D printing may be necessary.

Since the single strand approach to wind the coil presents numerous drawbacks, it is more advantageous to use a Rutherford cable to wind the coil, especially if the cable has already been used in another magnet design, and wind it avoiding unnecessary connections. The drawback of this approach is that Rutherford cables are easy to bend on one side, usually called the easy side or easy bend, and are very difficult to bend on the other side, which is usually known as the hard side or hard bend. This challenge will be dealt with in section 5.3. The cable chosen for the TCT septum is the same cable that was used to build the MQM corrector magnets in the LHC. The main parameters of the cable are presented in table 5.1. Details of the MQM corrector magnets can be found in [4].

Once the positioning of each individual cable is calculated, the analytical

Table 5.1: Parameters of the MQM superconducting cable

Parameter	Unit	Value
Cable type	-	Rutherford
SC material	-	NbTi
Cable width (bare)	mm	8.8
Cable height (bare)	mm	0.84
Number of strands	-	2x18
Strand diameter	mm	0.475
Cu/SC ratio	-	1.75
Filament diameter	μm	6
J_c (4.2 K, 5 T)	A/mm ²	2800
Insulation thickness	mm	0.08
Insulation type	-	Polymid

estimation of the design has been completed, a FEM calculation has been carried out to validate and optimize the result.

The characteristics of the TCT septum are summarized in table 5.2.

Table 5.2: Summary of the parameters of the TCT septum

Parameter	Unit	Value
Magnetic field	T	3.8
Inner coil radius	mm	35
Current	A	6284
Number of turns/pole	-	31
Inner yoke radius	mm	82

5.2.1 Magnetic design

The starting point of the numerical design is to design a Cosine θ magnet and optimize the positioning of the cables in the 2D cross section. Then the truncation will be done. The cross section has been optimized using Roxie and Opera 2D [96, 125]. First a Cosine θ magnet was simulated with Roxie and the cables were grouped in blocks. The positioning angles of the blocks, α and β , were further optimized using the Roxie optimizer. These angles are shown in figure 5.6, where the axis are shown for perspective. The full model of the pure Cosine θ magnet is shown in figure 5.7. Having an ideal round yoke

around the coil, the field quality will not be affected. The objective function of the optimization is the addition of the errors at a radius of 15 mm from the origin. It was chosen to optimize the septum cross section in Roxie and compare the results with Opera 2D as a validation.

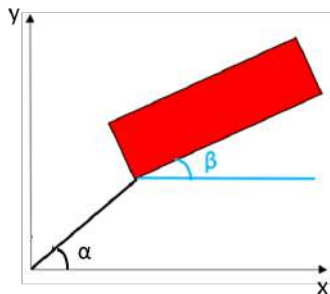


Figure 5.6: Scheme of the variables used in the optimization of the Cosine-Theta cross section for each cable block

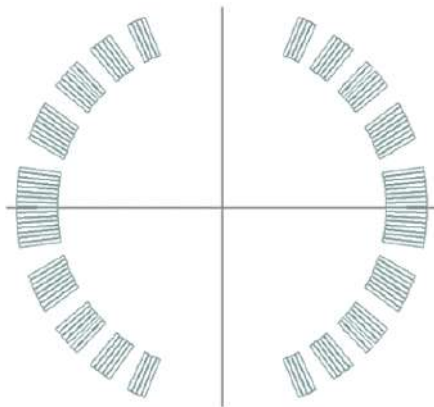


Figure 5.7: Optimization of the Cosine-Theta cross section with the Roxie code

After the Cosine-Theta magnet has been designed, the truncation follows. It is important to notice that magnetically the shape of the yoke is irrelevant. Its only function is to allow the return magnetic flux to travel through a path

with enough permeability, that is, the yoke needs to have enough iron to remain unsaturated. In this case a round outer shape has been chosen for simplicity. The cross section and a zoom of the extracted beam region analyzed in Roxie are presented in figure 5.8. It can be appreciated that only the iron yoke, shown in blue, has been meshed, as explained previously.

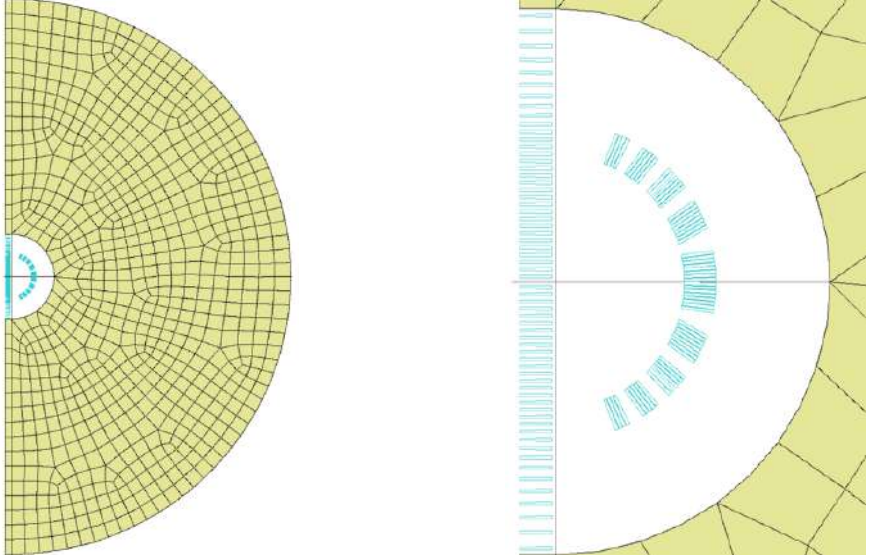


Figure 5.8: Schematic of the cross section model and zoom of the orbiting beam region

The cross section shown in figure 5.8 presents a challenge with the 3D design in mind. It has to be possible to wind the coil without the cables colliding in the coil ends and without blocking the particle beam trajectory. The most important influence in the coil ends design is given by the Rutherford cable having a hard bend side. This produces two immediate ideas for the winding of the coil ends. The strategy is to design a bedstead coil, a usual design in normal conducting magnets when the goal is to reduce the space taken by the magnet and to reduce the influence of the coil ends on the magnetic field. A standard bedstead coil is shown in figure 5.9.

The strategy for winding a bedstead coil with a Rutherford cable would be to first bend the cables upwards on the easy side. Following this bend, the cable would need to be twisted 90 degrees around the vertical axis and

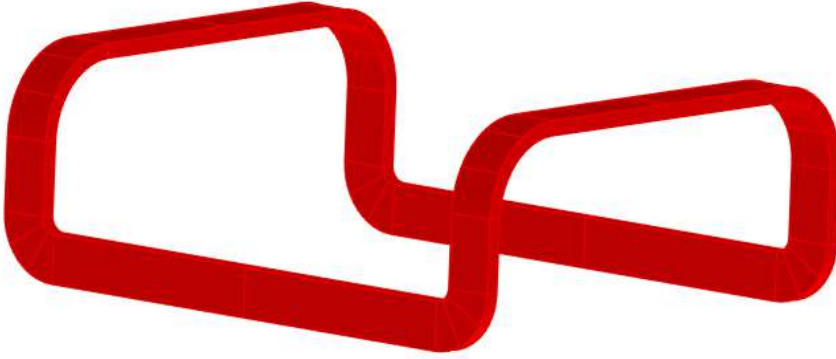


Figure 5.9: Example of a bedstead coil

then bent again on the easy side, which now would be possible. Then the process would need to be repeated in reverse order to obtain the cross section presented in figure 5.8. This bedstead coil would have to be modified given the asymmetry of the coil cross section. In particular, since there is a part of the coil that follows a Cosine θ distribution the easy bend angle of every cable and the twist around the local vertical axis need to be different. This poses many difficulties in the winding process and, assuming that they can be overcome, would increase the height of the magnet dramatically.

In order to keep the magnet length as short as possible and avoid unnecessary difficulties, the strategy will be to connect the cables at the top of the block part of the coil with the cables on the top of the Cosine θ part, as shown in figure 5.10. Alternatively it is also possible to connect the cables on the top of one of the parts with the cables on the lower region of the other part and vice-versa. This is not advisable because it would increase enormously the complexity of the connections and the winding and ultimately it would increase the length of the coil ends beyond reasonable limits.

This connection scheme avoids all the difficulties mentioned previously, but it still maintains a different angle of the cables on both sides of the coil. For this reason, it was chosen to twist each cable in the block part of the coil along the longitudinal axis to match the corresponding angle in the Cosine θ part of the coil, as shown in figure 5.11. The importance of this twist will be explained in more detail in section 5.3.

This change does not have an appreciable impact on the field distribution of

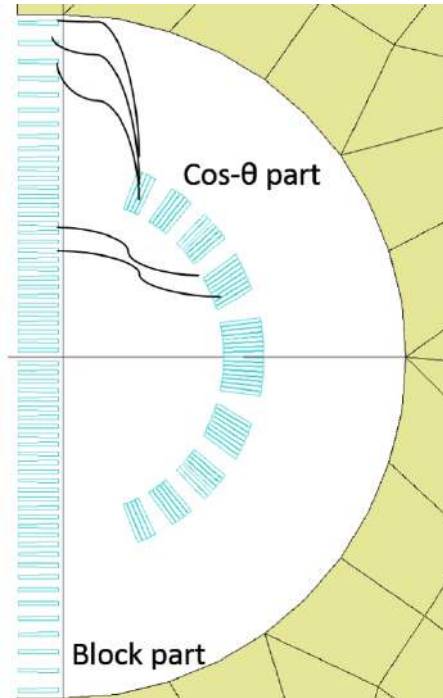


Figure 5.10: Connection scheme of the cables at the coil ends

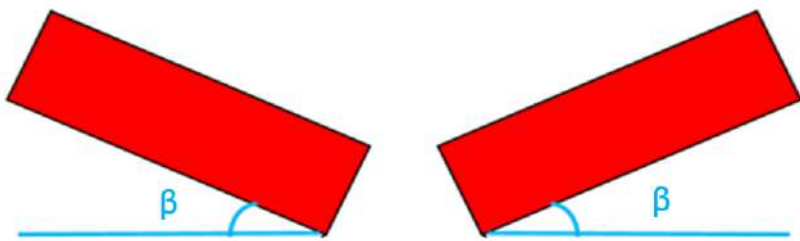


Figure 5.11: Angle matching of the cables in the cross section of the TCT septum

the gap because the current density distribution does not change, as explained in section 5.1. A zoom of the new cross section of the coil implemented both in Roxie (left hand side) and Opera 2D (right hand side) is shown in figure 5.12. In the Opera model, the support (regions coloured in light blue) for the stress analysis has been already implemented. It does not have any impact on the magnetic field distribution since it has been given non magnetic properties. The reason to include this support in the magnetic model is that a multiphysics analysis can be performed, reusing the mesh and automatically transferring the Lorentz force to the stress analysis.

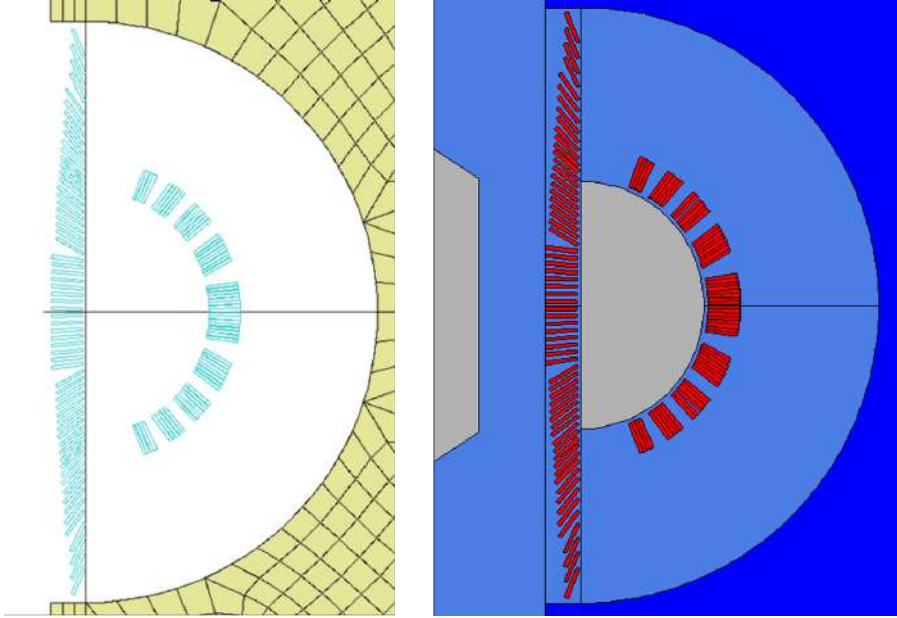


Figure 5.12: Improved coil cross section of the TCT septum model in Roxie (left) and Opera 2D (right)

A comparison between the results obtained with Opera 2D and Roxie are shown in figures 5.13 and 5.14. It can be seen that the magnetic field in the good field region presents a good agreement between the two codes. The Opera simulation presents a small increase near the origin, which is the location of the outer edge of the block part of the coil. The increase is due to the finite element discretization, with the Roxie simulation changing less significantly. On the other side of the gap, the magnetic field rises because the Cosine θ part

of the coil is located in the vicinity. The slight difference between the codes is mostly due to the element quality near the block part of the coil, where it becomes difficult to match these elements with the ones inside the cable. A bad element quality can impact the solution locally, as it is seen in figure 5.14. However, the relative difference between both of them is below 1%.

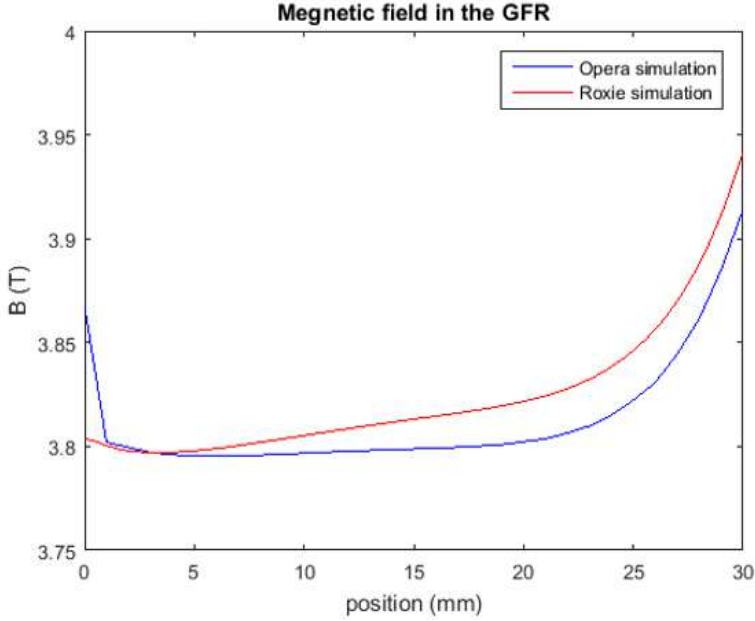


Figure 5.13: Comparison of the magnetic field in the good field region simulated with Opera 2D and Roxie

The leak field obtained with both codes is compared in figure 5.14. The location of the block part of the coil is at $x = -10$ mm. The orbiting beam gap extends to the left of the x-axis and the good field region presented in figure 5.13 extends to the right of the x-axis, with the block part of the coil (not shown for clarity) located between $x = -10$ mm and $x = 0$ mm. The leak field obtained with Roxie is one order of magnitude lower than the one obtained with Opera 2D. The peak observed in the Opera simulation is due to the rapid change of the magnetic field in the vicinity of the cables and the discretization, which is not done by Roxie. The finite element method needs to manage the constraints imposed by interfaces between different materials

with different characteristics. The discretization in the interface region should be done with higher order elements. This is not always possible due to computational complexity. In the Opera 2D model, enough quadratic elements have been used in all the geometry to increase the accuracy of the results, but due to the high number of cables some errors can arise given that the element quality can be poor in the interface regions.

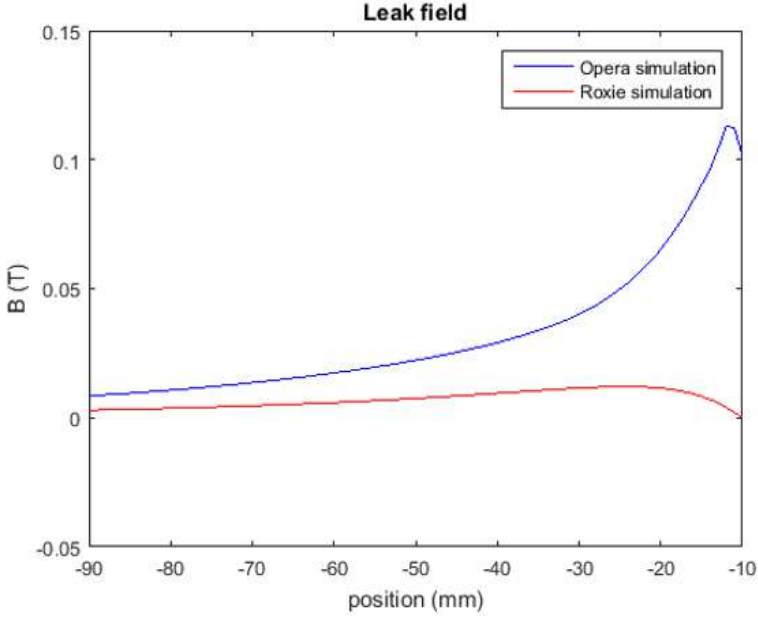


Figure 5.14: Comparison of the leak field in the good field region simulated with Opera 2D and Roxie

Although the Opera 2D model presents a higher leak field, the following analysis will only be performed using Opera. The reason to continue using Opera is its flexibility. A CryopermTM shield can be added around the orbiting beam gap to reduce the leak field, which is not easily implemented in Roxie, and the 2D stress analysis presented in section 5.2.2 can be integrated with the magnetic simulation. CryopermTM is the commercial name for a family of alloys manufactured by different companies which provides an analogous shielding effect as MuMetal, but operates at cryogenic temperatures [126, 127].

A zoom of the model in the orbiting beam gap is shown in figure 5.15, where the CryopermTM shield is shown in light blue. The field map of the

leak field is also shown. It can be seen that the leak field is higher near the inner surface of the shield. This local amplification is due to the fact that the permeability of the CryopermTM is higher than the permeability of air. This results in a short circuit for the leak field lines, which are attracted to the Cryoperm. The shield can become locally saturated and some of the field lines cross the orbiting beam gap near the inner diameter of the shield. The asymmetry in both sides is due to the different distance that the leak field needs to travel depending on the side of the shield in which they are located. The leak field is stronger in the side of the shield that is near the coil, if it was symmetric there would be no asymmetry because the field lines would see the same reluctance. The field map in the CryopermTM shield is shown in figure 5.16.

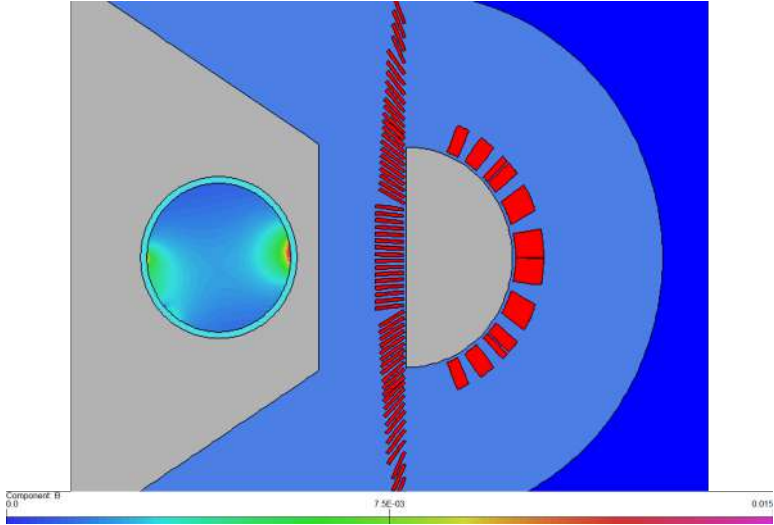


Figure 5.15: Map of the leak field inside the CryopermTM shield

For clarity, a plot of the leak field inside the orbiting beam gap obtained from the Opera 2D simulation including the 2 mm thick CryopermTM shield is shown in figure 5.17. It can be seen that the leak field in the orbiting beam gap is below 3 mT in the central region of the orbiting beam gap and that it only rises when approaching the CryopermTM shield. It can also be seen that the increase is asymmetric, being higher in the side closer to the coil.

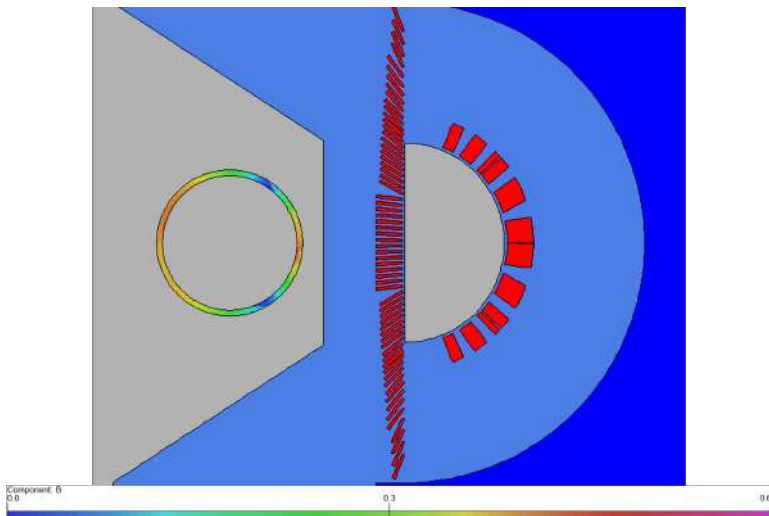


Figure 5.16: Map of the magnetic field in the CryopermTM shield

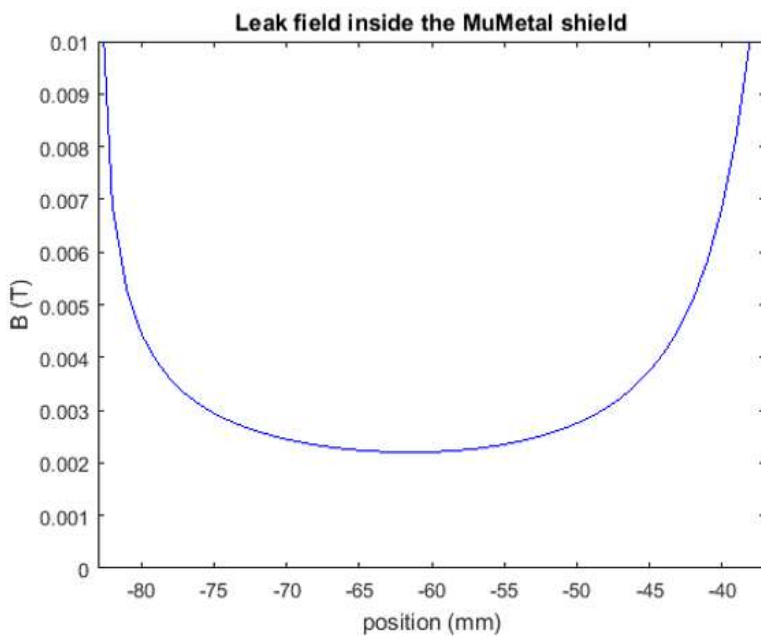


Figure 5.17: Plot of the leak field inside the CryopermTM shield

Since the TCT septum is super ferric, it is necessary to check the working point of the superconducting material to ensure the margin on the load line is enough to avoid unwanted quenches. It is well known that any type II superconducting material is actually superconducting below the critical surface determined by the critical temperature (T_c), below a critical magnetic field (B_c) and below a critical current density (J_c). If the temperature is kept constant, as it is usually the case during the magnetic analysis in steady state, the critical surface becomes a curve relating the critical current density and the critical field. This curve is known as the load line [128]. The margin on the load line for every cable calculated by Roxie is shown in figure 5.18.

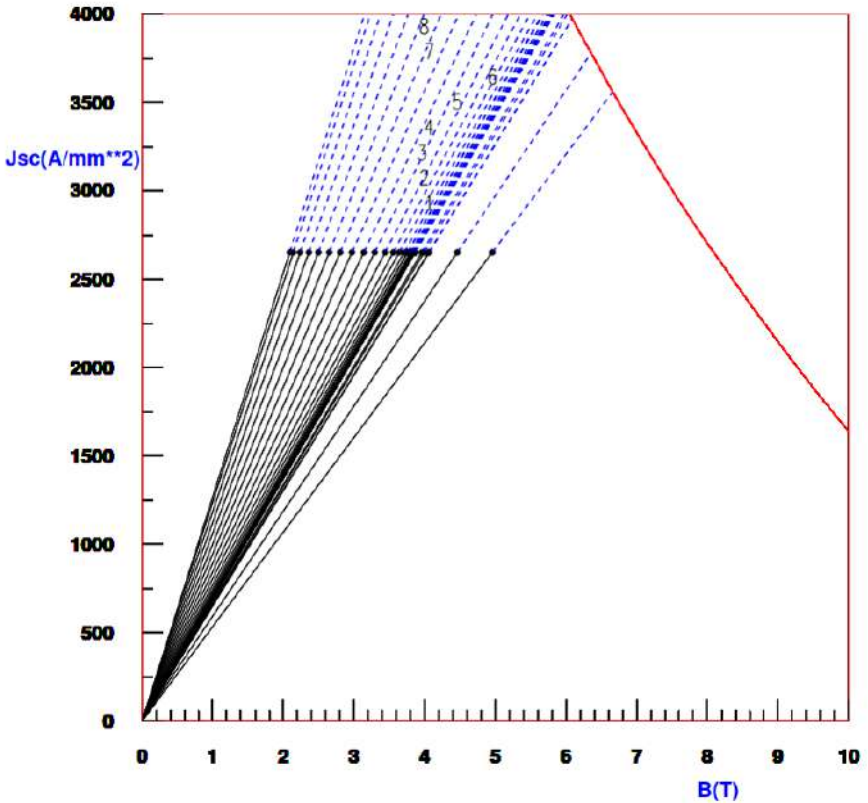


Figure 5.18: Margin on the load line of every cable in the TCT septum coil

The smallest margin on the load line is 28%, which means that the most stressed cable is operating at 70% of its capacity. Increasing the margin on the load line will produce a more robust design, which is desirable from the stability and quench protection point of view. However, the increase in cost is proportional to the increase in margin on the load line. It is common practice to operate the superconducting magnets in the lattice of the accelerator with a margin of 20% to the load line. Operating with a higher margin allows the engineers to understand the magnets performance practically while operating the machine. This is not exactly a technical limit, but a cost limit. For the FCC, there are discussions within the frame of the EuroCirCol project on whether it is possible to decrease the margin to 18% or even 14%. To put these numbers into perspective, the margin on the load line of the main dipoles of the LHC was decreased from 20% to 14% [129, 130]. Since super ferric septa magnets are not usual, there is no standard practice to decide the margin on the load line. In this study, 28% is considered enough margin given that it is twice the margin of the most ambitious design of the EuroCirCol project and an additional 10% margin compared to the most conservative design given that a 10% increase in the margin of a few units will not have a significant impact in the overall cost of the FCC. A 10% increase would have a significant impact in the production cost of the main dipoles and quadrupoles because the number of units projected is in the order of a few thousands. It is not possible to build a superconducting magnet without margin, for thermal stability reasons. This is also the reason the cables are manufactured with a high Copper to superconductor ratio.

To visualize the margin in the coil, the magnetic field distribution in the coil is shown in figure 5.19. It can be appreciated that the most critical cables are situated in at the top of the Cosine θ part of the coil. This is due to the fact that most of the magnetic flux is squeezed in this region to be concentrated in the GFR. It is also evident that the block part of the coil presents a gradient from 4 T to almost 0 T, which is the expected behaviour of the magnetic field in the current wall between the high field region and the field free region of a septum magnet.

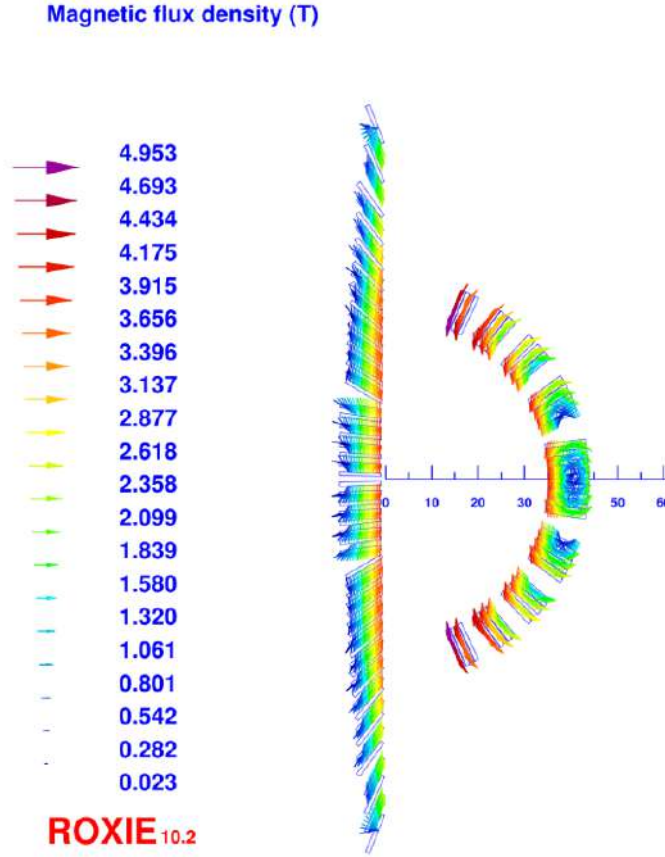


Figure 5.19: Magnetic field distribution on the coil

5.2.2 Mechanical design

Given that no showstopper has been identified in the magnetic study, a mechanical analysis in 2D was performed using Opera 2D. It is not possible to perform this study using the Roxie code, because it is only conceived to perform magnetic analysis, although the Lorentz force in the cables can be calculated. The Lorentz force in the strands is shown in figure 5.20. As it is expected, the force distribution of the Cosine θ part of the coil is trying to flatten the coil and pushing towards the yoke. The block part is pushed outwards and the force

is significantly smaller given that the magnetic field seen by the block part of the coil is much smaller than the field seen by the Cosine θ part of the coil. This asymmetry will not be a problem because the geometrical constraints to design a support are only on the septum blade. Besides, the force distribution in the block part of the coil is uniform, which makes the design of a support simpler than in the Cosine θ part of the coil.

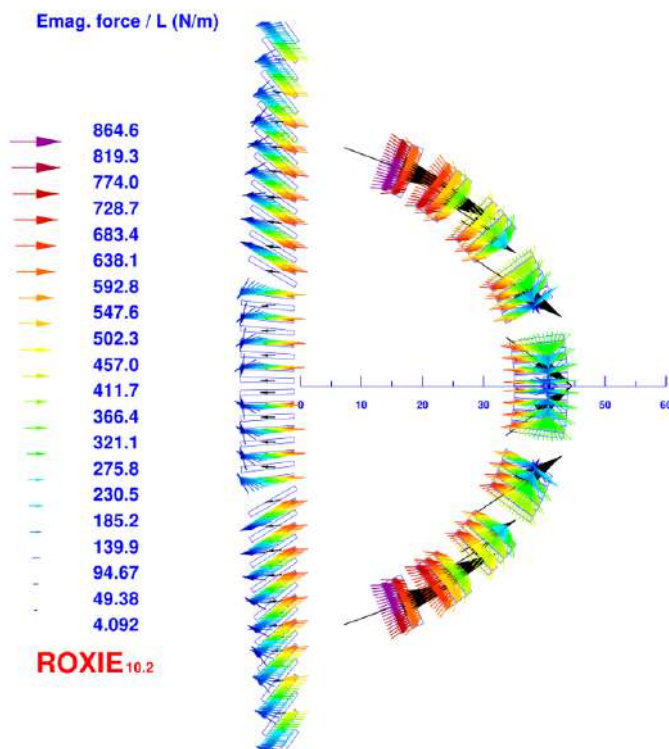


Figure 5.20: Lorentz force in the superconducting strands of the TCT coil

The goal of the support designed is to minimize the deflection produced in the septum blade while the materials remain below the elastic limit. Therefore the support will be split in three parts. The first one will support the Cosine θ part of the coil, the second one will guarantee the separation between the different cables in the block part of the coil and the third one will hold the septum blade in place. It is important to note that the function of the second

part is mainly geometrical since the forces, which are mostly horizontal, will be dealt with by the third part.

The first part of the support does not pose a great difficulty in terms of geometrical constraints, this part can be fixed to the yoke and then the Cosine θ part of the coil can be embedded in the support.

The second part of the support is very close to a uniformly loaded beam, which is very useful when determining the first iteration of the shape of the support. A uniformly loaded beam can be fixed at the ends to make the displacements and the angles at the ends zero.

The maximum deflection in a fixed beam is given by equation 5.10. The maximum deflection is located at the centre of the beam [43].

$$f_{max} = \frac{1}{384EI}qL^4 \quad (5.10)$$

Due to the geometrical constraints of the septum magnet, which is to achieve a septum thickness as small as possible it is not advisable to fix the septum blade support directly in the vicinity of the septum blade area, creating only a fixed beam. However, the support can be fixed to the yoke above and below, and its thickness can be increased to make the support infinitely rigid compared to the septum blade, which is equivalent to a fixed beam. This concept is shown in figure 5.21. The support is shown in light blue and the yoke is coloured in dark blue. The expected behaviour of this support is that there will be a small deflection towards the left in the area of the support that is holding the septum blade in place. The rest of the support will be unaffected by the forces because the rigidity of the top and bottom part of the support is much bigger than the rigidity of the septum blade. The boundary conditions applied on the sides are also shown, although only one support condition per side is shown for clarity. The top and bottom part of the support are not fully optimized, they are made significantly thicker than the coil to simulate an infinitely rigid piece. Most likely the way to build these parts requires the use of enough fixation elements, for example screws.

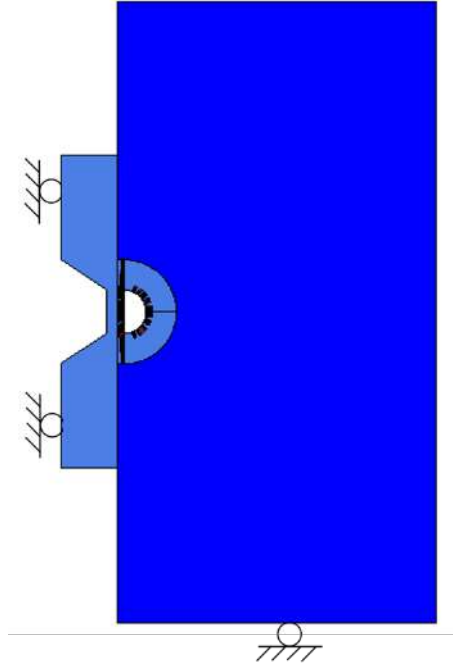


Figure 5.21: Static stress model with schematic of the boundary conditions

The static stress model is created from the magnetic analysis. It shares the geometry and the mesh and only the boundary conditions are changed, while the Lorentz force is used as the mechanical load present in the model. Opera 2D can calculate the Lorentz force directly as the product of the current density and the magnetic field ($J \times B$) but to improve accuracy in the presence of magnetic materials it is recommended to calculate the Maxwell stress integrals around each element. Both magnitudes can be calculated from the magnetic solution and imported into the magnetic model automatically.

The analysis type imposes some assumptions. In the first place, the boundary conditions need to ensure that the model position is fixed. It can be deformed, but it cannot move because being a static analysis there are no kinematic equations involved. If the boundary conditions are not properly set, the solution will never converge. However, the model can be overconstrained (known as a hyperstatic structure) as long as it does not result in a non physical solution. Overconstraining can result in longer convergence times, and this

increase is not necessary linearly.

Once the model has been understood, the only step left before solving it is to choose the materials and include the properties. Since the goal of the septum support is to minimize the deflection in the centre of the septum blade and it has to withstand cryogenic temperatures and not have magnetic properties, the material choice is limited. Materials like aluminium or copper, which is normally used to form spacers in Cosine θ coils might be too ductile for this purpose. Two materials for the support were considered, Aluminium and stainless steel (316LN). They were chosen based on their properties, namely the Young's modulus and Poisson's ratio, while the yield strength at 1.9 K was also considered. The mechanical properties of both materials are summarized in table 5.2.2. The superconducting cables are modelled as copper due to the fact that the copper to superconductor ratio is 1.75, high enough to consider that the behaviour of the cables will resemble that of Copper. Titanium was initially considered but it becomes very fragile at cryogenic temperatures [131, 132, 133, 134]. It is seen that the properties of aluminium are inferior to those of stainless steel, therefore the support will be designed at first using 316LN stainless steel. It is also worth indicating that the uncertainties on the measurements of these properties at cryogenic temperatures can be rather high, up to 5%. 316LN steel has been chosen for this design given the availability of mechanical data at cryogenic temperatures. One may argue that such a high quality material is not necessary and may increase the production cost of the TCT magnet. As it will be shown in the following paragraphs, the stresses in the support are well below the material limits and therefore the use of other steels is possible. Suitable steels would be for example 304 steel or a high-manganese steel like the one developed by Kawasaki steel corporation for the LHC dipoles [135].

Table 5.3: Comparison of material properties

Property (at 1.9 K)	Unit	316LN steel	Aluminium	Copper
Young's Modulus	GPa	207	75	140
Poisson's ratio	-	0.27	0.32	0.34
Yield strength	MPa	570	275	400

Although the material limits are rather high, the maximum stress allowed in superconducting magnets design is usually 200 MPa. The yoke and the coil may be able to withstand such conditions but the insulation might degrade

at cryogenic temperatures. The stress from the cryogenic temperature and most importantly, from the cooldown process are not included in this study. Besides, due to thermal expansion characteristics, using Aluminium to build the magnet support may not be advisable, as the displacements are likely to be much greater than in the case of steel.

Solving the simulation, the results that need to be obtained are the displacements of the septum blade and the stress in the support and the coil, to check that there is enough margin. For illustration, the displacement of the septum blade due to the Lorentz force is shown in figure 5.22. It can be seen that the maximum displacement in the blade is in the order of a few microns. The displacement shown is the modulus of the displacement, not the addition of the x and y components. The deformed mesh is also shown to appreciate qualitatively the behaviour of the septum blade. The displacements in the mesh has been exaggerated for clarity.

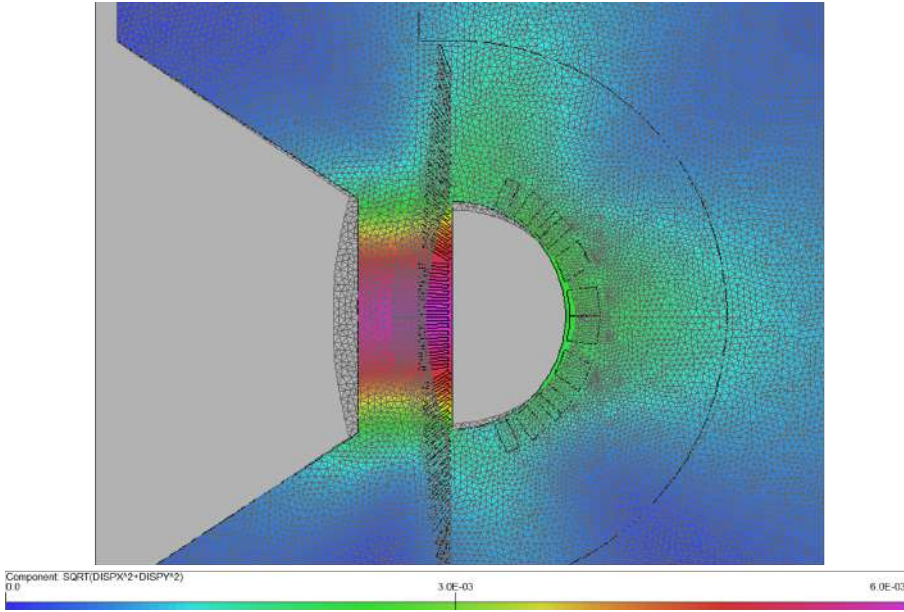


Figure 5.22: Displacement of the septum blade (in mm) with a stainless steel support

The maximum stress is found in the principal directions. A priori in a complex geometry there is no way to know which of the principal stresses

is bigger than the other one. Both need to be calculated. The stresses in the support, in MPa, are shown in figure 5.23. It can be seen that most of the material is in compression and well below the working limits and the hot spots are mostly due to the sharp corners. The support can be optimized to reduce the stress state at given points and this stress can be compensated by pre-stressing the assembled magnet.

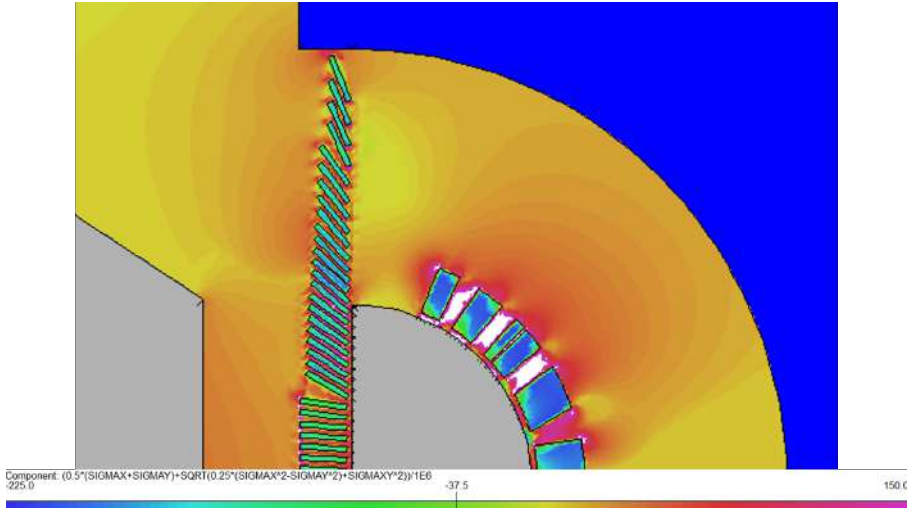


Figure 5.23: Principal stress distribution (in MPa) in the coil support using stainless steel

As a comparison, if the coil support is designed using aluminium, the maximum displacement of the septum blade is approximately 0.015 mm, which is one order of magnitude higher than in the case of 316LN stainless steel. This deflection value is reasonable for a septum blade, although it is preferable to use stainless steel to have a smaller deflection. The maximum stresses in the aluminium support are slightly lower than in the case of stainless steel, but the small decrease in stress does not justify the use of aluminium instead of stainless steel.

Once the 2D analysis is completed and it has been shown that there is no showstopper, the 3D coil ends can be designed.

5.3 3D design of the coil ends

The coil ends of a magnet can be designed applying differential geometry methods as described by Russenschuk in the design of the LHC corrector dipole and quadrupole magnets [136]. Such an approach was used to design the coil ends of the SIS-300 superconducting dipoles [137]. Their treatment is based on a differential geometry approach to a ribbon cable in 3D that can be undeveloped in a plane. The TCT septum magnet is not symmetric, which significantly complicates the mathematical treatment of the cables. However, the coil ends can be designed by allowing the cables to be bent the same way that a Rutherford cable adopts when it is allowed to bend freely. As a first approach, a strip of paper can be used before starting to design the coil ends in Roxie. The cables are bent in a similar way to the cables described by Russenschuk and then modifying the position to match the Cosine θ part of the coil to the block part of the coil.

The 3D design of the coil ends geometry was developed using Roxie. Each of the cables was designed individually starting from a typical Cosine θ magnet coil end. The side of the cable to be connected to the block part of the coil was then moved to match the position on the 2D cross section. The side of the cable to be connected to the Cosine θ part of the coil was adjusted to keep a physical bend in the cable. Once a cable was finally designed in 3D, it was necessary to check that the last cable would not collide with, or go through another cable. This situation would be clearly physically impossible and computationally inaccurate, although the solver may converge. Besides, a spacer for the winding and the support will need to be designed at a later stage. It is therefore necessary to allow enough space between cables to ensure that the material will support the stress. The spacing was checked manually for every cable. As an example, one of the ends of one of the cables imported in Opera 3D is shown in figure 5.24.

It must be noted that the curvature in 3D of the cables on the top and bottom part of the coil are different. Taking this feature into account and adding the fact that the block part of the coil determines half of the cable shape, the mathematical treatment of the TCT coil ends presented by Russenschuk [136] becomes impractical. Moreover, since the adjustment to the block part of the coil is different for every cable, a middle section of the coil was developed to allow the 3D coil ends to be connected to the 2D cross section. Great care was taken to avoid overlap.

A quarter of the coil ends was designed iteratively and then exported to Opera as a set of 1550 conductors. Once a quarter of the full coil was designed, it was reflected to create a the complete upper and lower coils. Opera 3D uses



Figure 5.24: End side of one of the cables of the TCT model in Opera 3D

a Biot-Savart treatment of the conductors. This means that the coil is not meshed and the fields are calculated from the Biot-Savart law. The reason for not meshing the coil is to save time during the meshing and solving steps, thanks to avoiding meshing a complicated geometry and the reduction of the number of elements. As a result, symmetry can be applied to the model, but the full set of coils needs to be included in the model. For more than one coil, the fields are calculated using superposition [114]. This results in a long running time for such a complex geometry.

An image of the full quarter of the coil end is shown in figure 5.25. It can be seen that the coil ends are made smaller than the 2D sector of the coil to reduce overall the size of the septum magnet. The sharp transitions can also be further optimized. For clarity, only a small part of the connection to the 2D cross section is shown.

5.3.1 Magnetic design

In the 3D model implemented in Opera, only a short section of the full coil has been implemented. The coil model is made of the coil ends, the connection section and the straight section. The straight section is an extrusion of the



Figure 5.25: Two views of the full quarter of the TCT coil ends

2D cross section, to model the central part of the TCT septum. The straight part needs to be included in the magnetic model to ensure the magnetic field in the central part of the model is vertical, as in the 2D model. This allows to simulate only the ends of the magnet, saving computation time and memory.

The connection section is the intermediate part of the coil, which connects the straight section and the coil ends avoiding collisions and creating a model which is possible to mesh. It allows enough space in between the cables, which even if they do not overlap might cause problems when meshing the model due to the small insterstices between cables. The connection part of the coil has been modelled as a 3 sets of 20 mm cables that simulate a small cable bending, to avoid the cables crossing each other. The coil ends have already been shown in figure 5.25. A schematic of the coil model with dimensions is shown in figure 5.26. Symmetry is applied when the coil is included in the model. As stated before, the relevant part of the model are the coil ends, the straight part only simulates a long stretch of the real magnet. Simulating the full magnet is not possible. This reduced model is meshed and created in approximately 12 hours and it is solved in 10 hours in a 16 core machine. The computation time in a single core machine is slightly over 6 and a half days. The model can be solved in reasonable time because, for the magnetic solution, the coil does not need to be meshed, reducing the number of nodes of the model and the complexity of the different components present, which ultimately reduces the meshing time significantly.

The 200 mm of the straight part simulated in Opera 3D are only the end of the coil. This length is enough to represent the central part of the magnet, where the 2D simulations presented in sections 5.2.1 and 5.2.2 are very accurate.

Given that the coil size is smaller at the ends, it is interesting to investigate the effect of reducing the yoke radius at the magnet ends as a strategy to

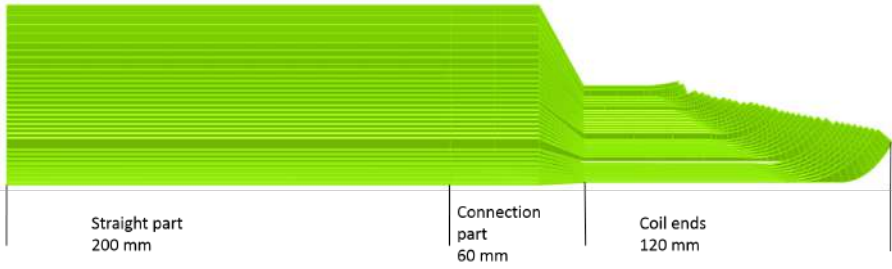


Figure 5.26: Schematic of the coil ends

mitigate the leak field in this region. Besides, the effect of the length of the yoke has also been investigated.

To quantify the effect of reducing the yoke radius, four simulations were run using the cross-section radius as a benchmark. Similarly, the effect of the length is studied by running 4 simulations using the one with the longer yoke (60 mm longer than the coil ends) and an bigger inner radius of 83 mm as a benchmark. The radius was chosen in this case for being the simulation that presents the smaller leak field integral. The results of the simulations are evaluated by calculating the integral of the leak field along the longitudinal axis over a length of 590 mm from the start of the coil ends. Beyond this distance the magnetic field is low enough to neglect its contribution to the integral. The leak field coming from the central part of the magnet has been calculated from the 2D simulation presented in section 5.2.1. Due to computational complexity it is not possible to simulate the full magnet in 3D. The results of the simulations run are summarized in tables 5.4 and 5.5 and the leak field integrals are also included. The leak field integrals presented correspond to one end of the coil, not both.

Table 5.4: Comparison of simulations with different inner yoke radius

Inner yoke radius (mm)	Leak field integral (T·mm)
53	45.63
60	46.57
70	48.03
83	49.91

The leak field along the longitudinal axis (z) has been plotted in figure 5.27. It can be seen that reducing the inner diameter at the coil ends reduces the

leak field. It is not possible to reduce the radius further than 53 mm due to the dimensions of the coil ends. At the coil ends, the iron yoke would not be in contact with the coil, forcing this reduction in radius to be limited to the end region.

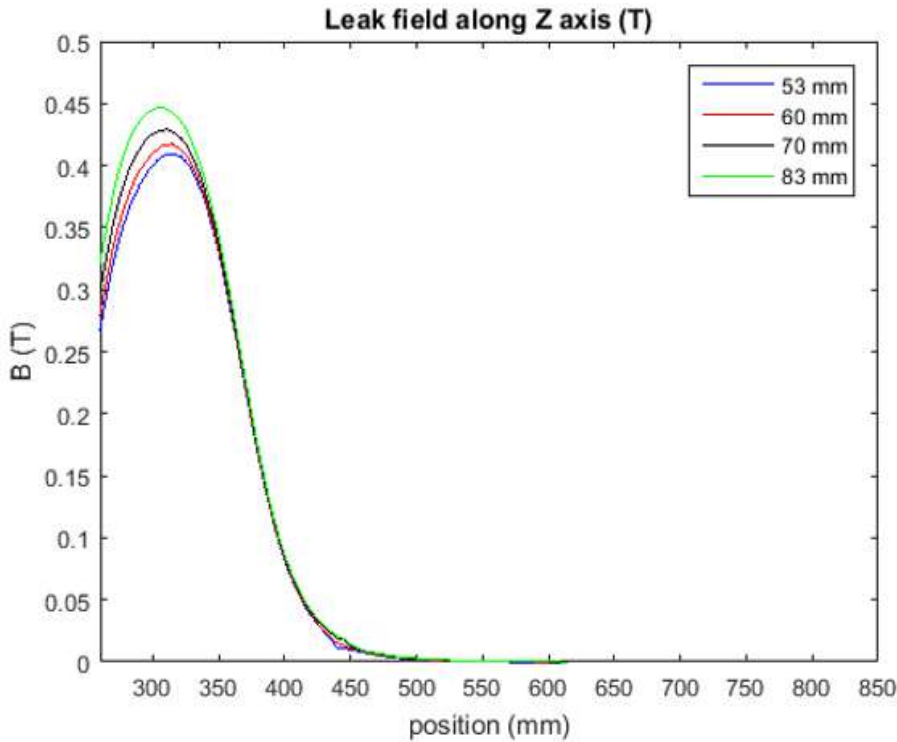


Figure 5.27: Relative leak field values as a function of the yoke inner radius

In table 5.5 a length of 0 means that the coil and the yoke have the same length, with a positive length indicating that the yoke is longer than the coil and a negative length indicates that the yoke is shorter.

The leak field along the Z axis has been plotted in figure 5.28. It can be seen from table 5.5 that increasing the length of the yoke at the coil ends reduces the leak field although it is difficult to appreciate this in figure 5.28. It is not possible to increase the length indefinitely due to space constraints.

Table 5.5: Comparison of simulations with different yoke lengths

Extension of the yoke beyond the coil (mm)	Leak field integral (T·mm)
0	50.59
30	50.05
60	49.91

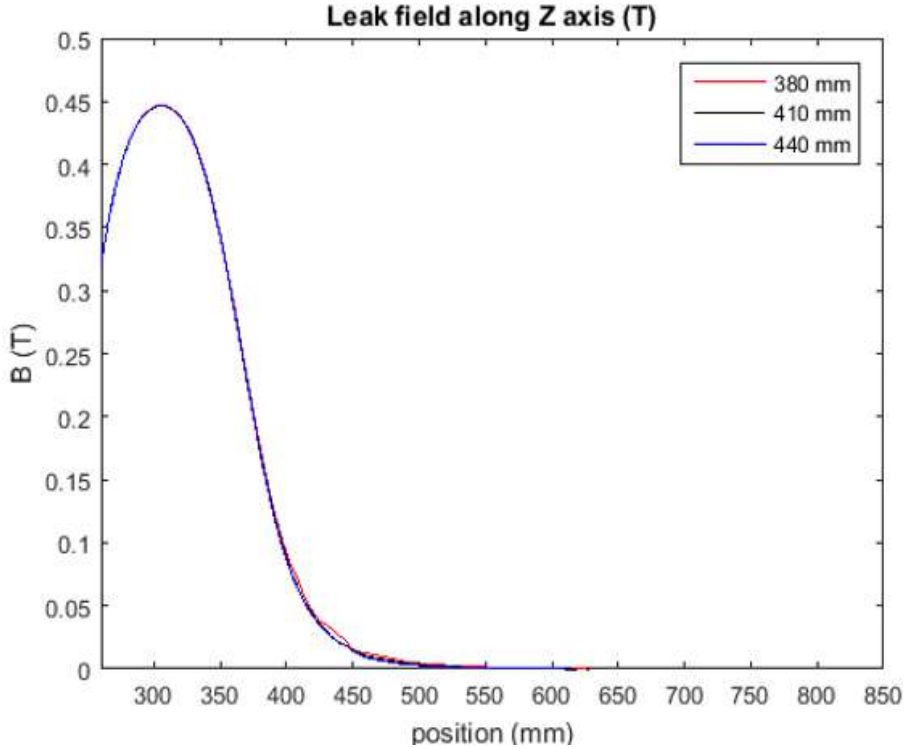


Figure 5.28: Relative leak field values as a function of the yoke length

As an improvement, it is possible to reduce the leak field almost 20% if the yoke is closed at the ends to short circuit the leak field around the orbiting beam gap. This is illustrated in figure 5.29, in which the yoke has been cut to show the principle of the flux short circuit. In this case, keeping the yoke length 60 mm longer than the coil ends and the inner radius of the yoke at 53 mm, the leak field integral decreases to 41 mT·m.

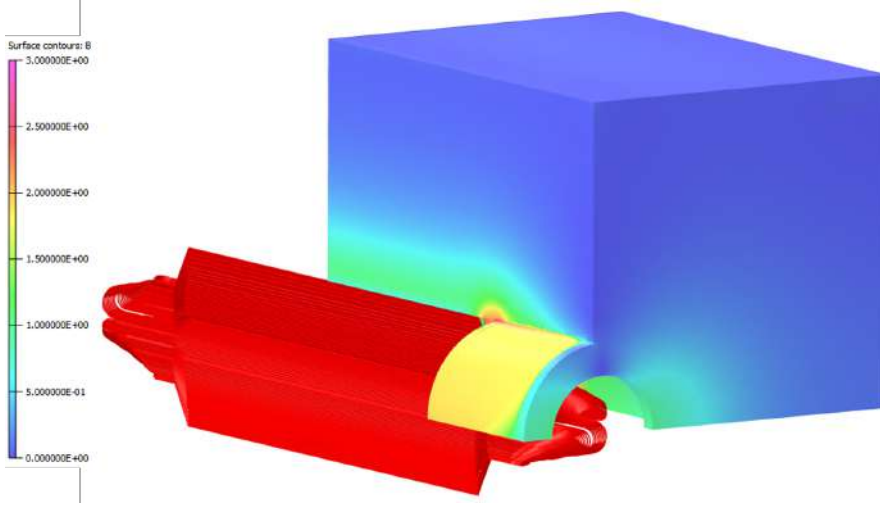


Figure 5.29: 3D model with the short circuit at the coil ends

For completeness, the inductance of the magnet has been estimated and for a magnetic length of 4 m, the total inductance would then be 4.92 mH. The inductance calculation is explained in detail in appendix B.3

5.3.2 Mechanical validation

5.3.2.1 Multiphysics model description

The 3D magnetic model was run as the first part of a multiphysics simulation in which the Lorentz force was used as an input for the stress simulation. As explained before it is done this way to save time and memory. Once the multiphysics method is chosen, it is necessary to mesh the coil and the support.

Before the mesh is created, Opera needs to join all the different components in the model to create the Model Body [114]. In the case of this model, with 1550 conductors, it is not possible to create a Model Body. These 1550 conductors are the 8-node bricks that form the 31 cables of the coil, as explained in section 5.3.

In a computer with 64 GB of RAM, the creation of the Model Body saturates all the memory in approximately 10 hours, when about two thirds of the conductors have been joined. At this point, Opera starts to use the hard drive for the creation of the Model Body, which becomes thousands of times

slower and therefore it is not possible to create a Model Body to be meshed using this geometry of the coil. It would be desirable to substitute the 1550 conductors by the 31 cables and drive the model with a current source.

Such an approach was attempted but the current flow was not solved successfully. The 1550 conductors were exported as step files and then imported into Opera to create the 31 cables maintaining the geometry. However, the conductors do not match perfectly. There are many infinitesimal spaces or overlaps in every block. Since Opera uses Biot-Savart's law to calculate the magnetic field this is not a problem. A small error is introduced in the vicinity of the gap or overlap, which does not cause any effect in the magnetic field. The extent of this error is of the order of a few elements. However, if the coil is driven as a bulk body with a current or voltage source, the current does not find a continuous path to flow and the results obtained are not representative of the reality.

The only possible strategy then is to remove 15 of the 31 cables, or almost one out of every two, and scale the current accordingly to maintain the same number of ampere turns. Removing the cables reduced the number of conductors to 800 and the creation of the Model Body was possible. This operation takes approximately 15 hours and 20 GB of RAM, which is possible to achieve in an ordinary computer. Although with this model the calculation of the Lorentz force and the stresses will not be exact, it will not be far from reality, because the force density in the support will be similar. The force will be more concentrated than in the model with all the conductors, but the stress will be of the same order of magnitude.

The small spaces between cables and their complicated geometry require the use of a very fine mesh in this region, which is not a difficult problem to overcome. The mesh needs to be carefully set and refined to produce an optimum number of elements. The model with the meshed coil produces a mesh with almost 32 million elements and 6.8 million nodes. This is significantly bigger than the previous simulation, when the coil was not meshed. In this case, Opera does not use the Biot-Savart approach to calculate the fields produced by the coil and the algorithm is significantly slower. This, together with the complexity of the model, results in a running time of 23 days for the magnetic simulation and 6 hours to solve the stress simulation in a 16-core machine. In a single core machine, the total CPU solving time amounts to 360 days.

It is therefore not feasible to run several models to optimize the coil ends layout as it is necessary to create a new mesh every time the geometry is changed. The majority of the optimization has been done in 2D and the coil ends have been kept as short as possible to reduce the effect of the leak field.

From the point of view of the end effects, it is also of interest to make the magnet as long as possible to reduce the effect of the field created by the coil ends with respect to the total effect of the field created by the magnet. This is taken into account when calculating the magnetic field integral along the trajectory of the beam.

5.3.2.2 Multiphysics model results

Once the principal components of the stress tensor are known, it is possible to compare the mechanical performance of the coil support with different alternatives and draw meaningful conclusions about the material and the stresses that it can withstand.

The stress analysis of the support and the coil ends in 3D complements the stress analysis in 2D presented in section 5.2.2. The first principal stress in the support and in the coil end is shown in figure 5.30, expressed in MPa. Due to memory availability, only a cut of the support and the coil is displayed. It is seen that the maximum stress obtained is slightly lower than 35 MPa. The stress is in the same order of magnitude as the ones obtained in the 2D analysis although there will be a magnifying effect due to the removal of half of the cables while maintaining the same Ampere·turns. As explained in section 5.3, this simplification was necessary to be able to create the mechanical model. Although the force density in the support will be the same, the stress might be artificially magnified in certain areas. Additionally, the asymmetry of the coil ends will introduce a higher stress component than in the cross section although it will not increase dramatically with respect to the cross section. This stress increase is due to the fact that the magnetic field is amplified in this region, and it is still within manageable limits.

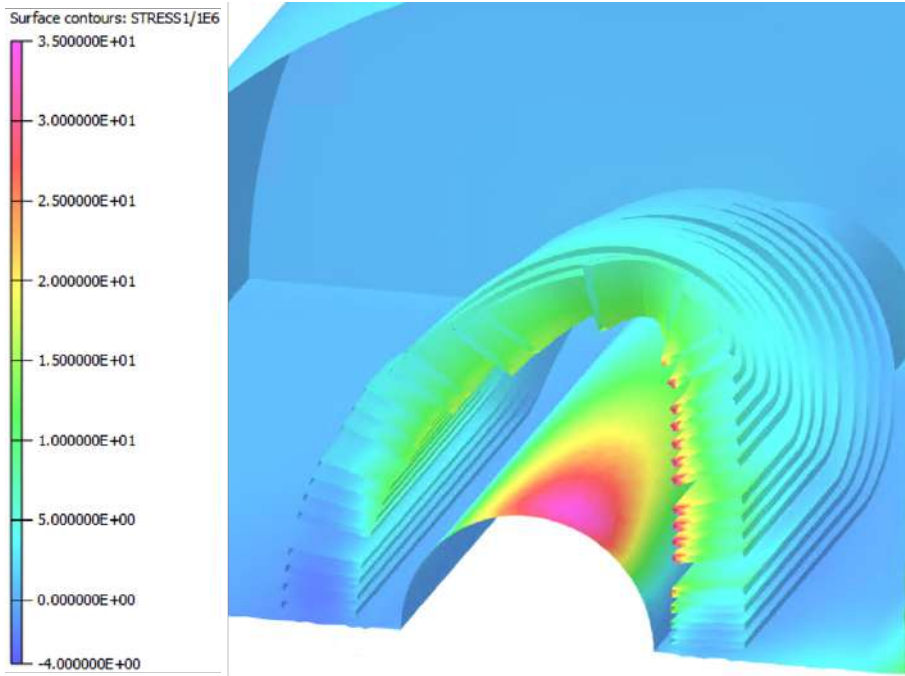


Figure 5.30: First principal stress in the coil end and the support (in MPa)

As expected, the displacement of the coil in the coil ends is in the order of a few microns, as it was shown in figure 5.22 in section 5.2.2. The displacement of the coil ends and the support is shown in figure 5.31. It can be seen that the part with the highest displacement is the septum blade, as expected.

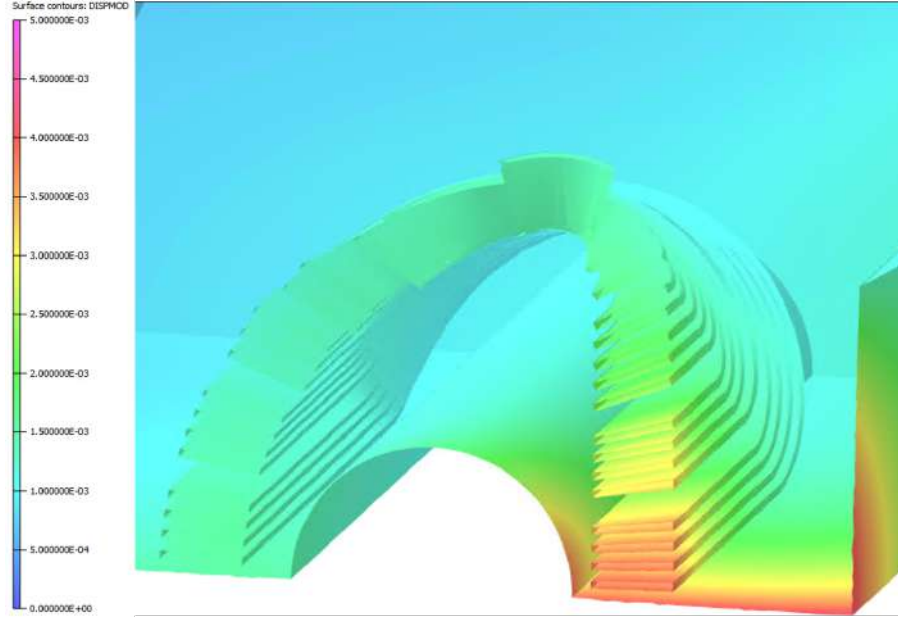


Figure 5.31: Displacement in the coil end and the support (in mm)

5.4 Figure of Merit for the Truncated Cosine θ septum

The figure of merit presented in section 2.5 has been calculated for this septum topology using equation 2.31 with the parameters presented in this chapter. The parameters and the result are shown in table 5.6.

5.5 Conclusions and future work

A conceptual magnetic and mechanical design of a 4 T TCT septum has been produced. It has been shown that the promising analytical 2D results can be validated numerically with great detail and the magnetic design and mechanical validation of the coil ends have been done in 3D despite the simplifications imposed in section 5.3.

The figure of merit introduced in section 2.5 has been calculated for the

Table 5.6: Calculation of the figure of merit for the TCT septum

Parameter	Unit	Value
B_0	T	4
B_{leak}	mT	0.1
B_{peak}	T	5
B_c	T	6.8
h	mm	70
s	mm	35
K	-	58.8

TCT septum and it achieved a value higher than all the other septa topologies presented in this thesis except for the SuShi septum presented in section 2.4.7.5. For this reason, the SuShi and the TCT topologies will be considered in section 6.3.4.

A more detailed model can be created and extended to include the effect of cryogenic temperatures in the material, which opens two lines of future research.

The first one is to calculate the pre-stress that is necessary to apply to the coil to avoid movement of the superconducting filaments, as this might lead to undesired quenches. This is a static simulation that has the same kind of complexity as the simulations performed, and therefore no major obstacle is foreseen, only the same simplifications would be necessary. A method for applying the corresponding pre-stress needs to be identified.

The second challenge that needs to be addressed is the cool-down simulation. It is necessary to ensure that the stress limit of the different materials is not reached at any moment during the cooling process. This will be a transient simulation and the availability of computational resources will be a critical issue. The current model considers the yoke and the coil support as a whole piece but for the cool-down study a model of the full assembly should be used, increasing the complexity of the simulation significantly. For the cool-down simulation the model used need to be an assembly model with the different components connected by sliding contacts, to model the process accurately. If the model used to simulate the cool-down is a single piece model, like the one used in this study, the thermal contraction will introduce artificial stresses that do not exist in reality. Additionally, one of the results provided by the assembly model is residual stress that may remain present in the magnet after cool-down and which would need to be considered for the pre-stress calculation.

Although the simulations are very challenging, they are not impossible to perform. Following these simulations, a prototype could be built to validate the calculations. The most challenging parts of the prototype stage are the winding of the coil ends and the machining of the coil ends support.

Chapter 6

Layout optimization

6.1 Introduction

In this chapter, in section 6.1.1, the septa topologies to be used for injection and extraction are chosen according to their performance measured by the figure of merit. The beam size is calculated in section 6.2.

It is interesting to study the possibility of a staged approach by using different families to design the septa system. In a given injection or extraction system, it is possible to install several groups of septa magnets from the same topology which only differ in some parameters. For example in the LHC beam dump system there are three families of Lambertson septa, with five magnets in each family, as it is explained in section 3.3. The first five magnets form family A, which have a septum thickness of 6 mm and a coil with 32 turns. Family B is formed by the next 5 magnets, which have a septum thickness of 12 mm and a coil of 40 turns. Finally, the last five magnets form family C. They have a septum thickness of 18 mm and 48 turns in the coil. This difference of turns in the coil allows to connect them in series with the same power supply, saving space and reducing costs, while at the same time it is ensured that the deflection produced by every magnet in a given family is the same as the other members. The difference in the septum thickness is due to the fact that the separation between the orbiting beam and the extracted beam is not constant along the dump line. The advantage of this strategy is that placing some weaker septa closer to the kicker magnets may result in a smaller number of magnets required or a shorter straight section length.

The optimum number of magnet families to be used is calculated in sec-

tion 6.3.2. Then in sections 6.3.3 and 6.3.4, the septa layout of the injection and extraction region will be analyzed and an optimized solution will be provided in each case. These optimized solutions will be compared to the current FCC baseline proposals.

6.1.1 Figure of merit of different septa topologies presented

The figure of merit introduced in section 2.5 has been calculated for the Lambertson, the Pacman and TCT septa presented in the previous chapters. The SuShi septum has also been added to the considered topologies to be studied. A summary of the results is shown in table 6.1.

Table 6.1: Summary of figure of merit calculation.

	Lambertson		Pacman	TCT	SuShi	
	NC	SC			MgB2	NbTi
K	32	2.6	0.36	36	154	375

According to the figure of merit, the best topologies are the SuShi septa followed by the TCT. Normal conducting Lambertson septa are also a good option and although the superferric variant has a much lower figure of merit, it may be interesting from the point of view of energy saving. Given that the injection has to be done using a two plane injection scheme, the use of Lambertson septa is necessary. For the extraction, it is clear that the chosen topologies need to be the TCT and the SuShi.

6.2 Beam size and beam centre

The position of the beam will need to take into account the beam size for the different clearances and apparent septa thicknesses, as shown in figure 6.1, where the dashed lines mark the outer dimensions of the beam and the solid lines represent the centre of the beam. Therefore the septum blade thickness, represented in red, cannot be calculated using only the beam centres, but the outer dimensions also need to be taken into account.

In the case of the cryostat clearance (540 mm) the beam size has already been taken into account. This cryostat belongs to the first lattice magnet seen from the septa straight section. The cryostat physical radius is 500 mm.

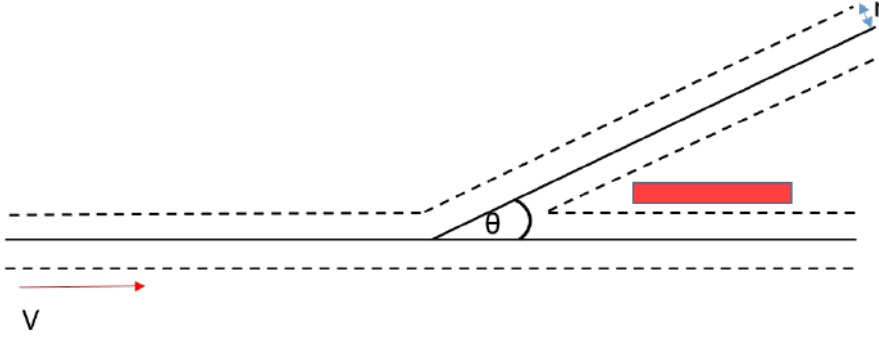


Figure 6.1: Schematic of the beam size

The deflection produced by a magnet can be calculated using the beam rigidity and the magnetic field integral using equation 6.1. The magnetic field is considered constant, hence the integral becomes a multiplication. The angle θ , introduced in radians, is the ratio between the arc length and the radius and the product $B \cdot \rho$ is the beam rigidity. The beam rigidity is the relativistic momentum per unit charge, which was defined in 4.7.

$$\begin{aligned} \theta &\approx \frac{L_s}{\rho} = \frac{B \cdot L_s}{B \cdot \rho} \\ B \cdot l_s &= \theta \cdot B \rho \end{aligned} \quad (6.1)$$

The beam size is considered to have a radius from the centre of 15σ and the additional external tolerance for orbit and alignment is taken as 4 mm, as written in equation 6.2. These values come from optics calculations to obtain the minimum aperture of the different devices. The dimension of σ is given by equation 6.3, where $\beta_{x,y}$ is the beta function in the x and y axis respectively and β_{rel} is the relativistic beta parameter, which at FCC energies can be considered to be 1.

The Lorentz factor is $\gamma_{rel}=3318$ at injection energy and $\gamma_{rel}=50272$ at extraction. These values can be calculated using the parameters reported in table 1.2 and the rest mass of the proton. The normalized emittance is 2.2 mm·mrad. These parameters are taken from the FCC Conceptual Design Report [17]. The beam size is calculated for both the x and y axes according to equation 6.3 [22].

$D_{x,y}$ is the dispersion and $\Delta p_{x,y}/p_{x,y}$ is the momentum spread. This term can be neglected because at injection and extraction the dispersion is deliber-

ately suppressed or kept at very low values, of the order of 10 to 20 cm.

$$r = 15\sigma + 4 \text{ mm} \quad (6.2)$$

$$\sigma_{x,y} = \sqrt{\frac{\beta_{x,y}\epsilon_{nx,y}}{\beta_{rel}\gamma_{rel}} + \left(D_{x,y}\frac{\Delta p_{x,y}}{p_{x,y}}\right)^2} \quad (6.3)$$

One of the main contributions to the required sagitta is the beam size, which needs to be known for the positioning of the septa. However, the beam size will change depending on the location according to equation 6.3. The sagitta is defined as the separation between the centres of the extracted beam and the orbiting beam. Since there is no analytical expression for the beta function [22], but it is known at every point of the line, the strategy is then to calculate the position iteratively.

As a starting point for the calculation, it is possible to calculate the necessary drift space with a σ of zero and still keeping the 4 mm tolerance, which is equivalent to saying that the beam has a 4 mm radius. This will produce a length, at which the beta function, and therefore the beam size, is known. The calculation of the drift space will then be repeated, and a new drift space length will be found at which it is possible to calculate the new beam size and drift space. This procedure, the Gauss-Seidel method, will converge in a few iterations producing an accurate value of the beam size.

As a remark, the function relating L and β has an arbitrary shape since this is only for illustration purposes and the actual shape has little relevance. The vertical blue lines represent the boundaries of the interval in which the problem has to be solved. Solutions outside this interval are not possible. For a general problem there could be more than one solution and the iterative process may diverge, but as explained before, the injection and extraction septa need to be located in within the straight section, so only this region is considered. It is also important to consider that the change in the solution becomes smaller at every iteration, so a reasonable error tolerance has to be set to avoid an excessive number of iterations. The iterations were stopped when the change in position between two consecutive iterations was below 0.5 m. This is sufficiently accurate in view of the fact that the total length of the septa system is in the order of several hundred metres. The Gauss method is one of the slowest converging numerical methods [138, 139] but its strength lies in the simplicity. It can be implemented in a very simple way and even if the required number of iterations to solve a one variable equation is higher than in other methods, each iteration requires very little time.

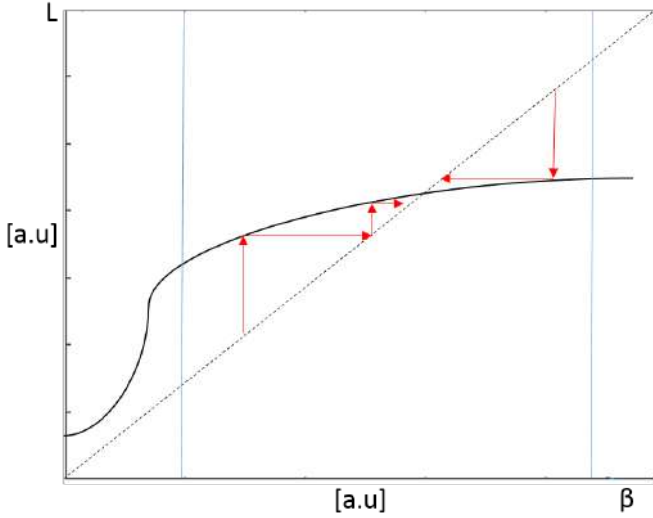


Figure 6.2: Illustration of the Gauss-Seidel iteration concept

6.2.1 Quench protection

Additionally, it is necessary to consider that the superconducting septa need to have a protection device installed upstream from their location. The septum blade needs to be protected regardless of the septum topology but, in the case of superconducting magnets, extra measures are required since the heat deposited by an impact, even if it is not at full energy, might cause a quench. If this is not taken into account the magnet can be destroyed. The Sushi and the TCT septum are both cooled by liquid Helium. The time scale of the impact is orders of magnitude faster than the time required to heat the surrounding area. Therefore the impact is adiabatic and confined to a certain point, not allowing the coil to dissipate the heat of the impact by thermal conduction.

The question in this case is the temperature margin. The critical temperature of NbTi is approximately 10 K [140] and its operating temperature in the TCT septum is 1.9 K. A Sushi built using the multilayer Nb/Cu/NbTi material would have very similar margins. This is the same material used in the LHC and although the margins are not extraordinarily constraining or relaxed they can be dealt with.

A bulk MgB_2 Sushi would have a critical temperature of 39 K [141] and

it can operate at a higher temperature than an NbTi variant, at for example 20 K. Given that the cooling time and the power required do not scale linearly with the the temperature difference, it is interesting to consider operation at a higher temperature as the total time to recover by a quench might be shorter, even if the occurrence of a quench may be more likely, which needs to be studied in detail.

At a first sight, one might think that protection at 50 TeV will be more challenging than at injection, when the energy is 3.3 TeV. This is true regarding the energy values, and protection elements need to be dimensioned accordingly. However, injection protection is also very challenging. If the beam is circulating in steady state, it can be dumped in the case of an emergency and the required reaction time may allow for a few turns before dumping the beam. However, if there is a problem at injection which requires an emergency dump, the beam will need to be dumped immediately and with no error margin to avoid hitting the septum blade, the vacuum chamber or any other equipment in the vicinity. Therefore injection protection is critical and the massless septum presented for injection protection in section 4.4 may be very interesting.

Current calculations estimate the length of the protection devices for 50 TeV energy at 10 m and will very likely require an additional shower protection device of about 1 m [28]. More detailed simulations to calculate the heat deposition will have to be performed in the future using dedicated codes.

6.3 Septa layout in the straight section

For perspective, the injection strategy in the FCC baseline is to use a two plane scheme and inject upstream of an experimental region. The two plane injection is needed due to the use of Lambertson septa. The injected beam comes from above the orbit and it is deflected vertically by the Lambertson septa. Once the beam leaves the Lambertson septa it is travelling in a parallel direction to the orbiting beam. The kicker magnets then deflect the beam horizontally to locate the injected beam in the orbiting beam gap. The beam is always injected in the outer ring of the collider for geometrical reasons. Therefore, each of the transfer lines finishes in a different side of the experiment, where the beams will cross and change between inner and outer ring. The extraction is done in one plane given that the chosen septa topologies are the SuShi and the TCT. The beam in both cases is deflected upwards by the kicker and septa magnets to avoid geometrical constraints due to integration. Additionally, it avoids crossings of the extracted and orbiting beams paths [115], which are not impossible to overcome, but may be a more complex solution. Although

an upwards extraction may seem unsafe a priori, due to the dilution kickers and the beam dump, the number and energy of the surviving particles can be considered negligible. In the case of a dump failure, the beam would be stopped by several km of soil. Since the beam would drill a hole through the dump and its outer envelope and create many associated damages, the beam dump system has to be designed so that such an event is extremely unlikely.

Before doing any study, it is necessary to state that the starting point and work flow when designing an injection or extraction section can be the same. In an injection region the beam arrives at the injection septa, which produce a deflection, and then travels to the quadrupole and kicker magnets, to finish the injection sequence. In an extraction region, the beam is deflected by the kicker magnets in the first place, passes through the quadrupole magnet, and continues to the extraction septa. Both process are analogous and both can be seen as an injection or an extraction, only the travelling direction needs to be inverted, but this trick does not influence the solution in any way. In this study, for simplicity, the injection will be treated as an extraction.

In the following sections the deflection of the different septa families will be calculated in order to achieve a given sagitta at the cryostat. This is a simplification that allows to use analytical expressions that are solvable without the use of symbolic calculus software. As it will be explained in section 6.3.1, the different magnets studied will be considered as thin lenses, in which the magnet is infinitely thin and the full magnetic field integral is concentrated at the centre point. This approximation is not suitable to investigate the detailed trajectory of the beam at every point but it allows to address the positioning of every system analytically.

6.3.1 Septa location with one septum family

The septa magnets, regardless of the topology chosen, need to be placed at a certain point in the straight section of the injection or extraction region. The available space for septa will be divided in three zones, shown in figure 6.3, where the direction of the beam is indicated for reference. The distance L_1 is a drift space, where no magnets will be present. The absorbers and passive protection devices will be placed in this region. The absorbers will be followed by septa magnets, which are located in the zone named L_s . The septa magnets will be followed by a drift space named L_2 which extends to the start of the first stand-alone quadrupole magnet. When the beam is extracted, it is necessary to achieve a separation between the extracted beam and the orbiting beam bigger than the diameter of the quadrupole's cryostat. The sagitta is named d . As a first approximation, the septa will be considered point-like and providing the

full field integral at the centre of the L_s region. This approximation is allowed because the beam follows a circular trajectory with a very large radius while it is travelling through a magnet and the entrance and exit angles will be the same.

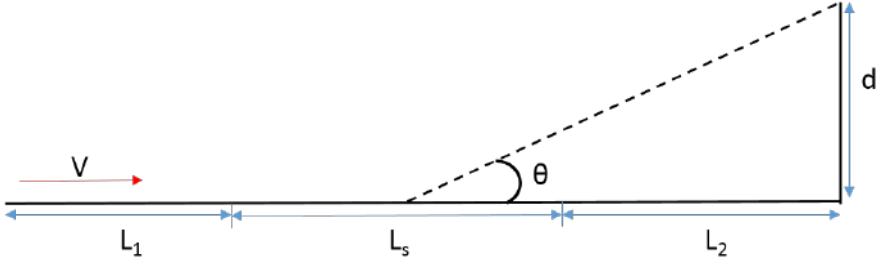


Figure 6.3: Schematic of the extraction straight section

From figure 6.3, one can establish a relationship between the deflection angle θ , the lengths of the different zones of the straight section and the sagitta.

$$\tan \theta = \frac{d}{L_s + L_2} \approx \theta \quad (6.4)$$

The paraxial approximation is allowed because θ is typically in the order of a few mrad. Combining equations 6.1 and 6.4, a second degree equation on θ is obtained.

$$B\rho \cdot \theta^2 + L_2 \cdot \theta - d \cdot B = 0 \quad (6.5)$$

Taking the magnetic field (B) and the drift space (L_2) as independent variables, since the sagitta (d) and the beam rigidity ($B\rho$) are fixed, equation 6.5 can be solved and admits two solutions. However, the second solution with the negative sign of the square root does not make sense since the angle cannot be negative. It is also possible to check that when the drift space L_2 becomes very large, the angle θ tends to zero, and vice-versa.

$$\theta = \frac{-L_2 B \pm \sqrt{L_2^2 B^2 + 4d B \rho \cdot B}}{2B\rho} \quad (6.6)$$

A plot of equation 6.6 is shown in figure 6.4. It can be seen that for a given magnetic field and a desired deflection produced by the septa magnets, the length of the drift space (L_2) is proportional to the desired deflection. The

maximum magnetic field has been set at 10 T for visualization. The maximum length of the drift space has been set to 1 km, significantly longer than the total length planned for septa magnets. These values are significantly over the allowed limits of the working parameters, but it is useful to obtain a more clear understanding of the effect of the different parameters.

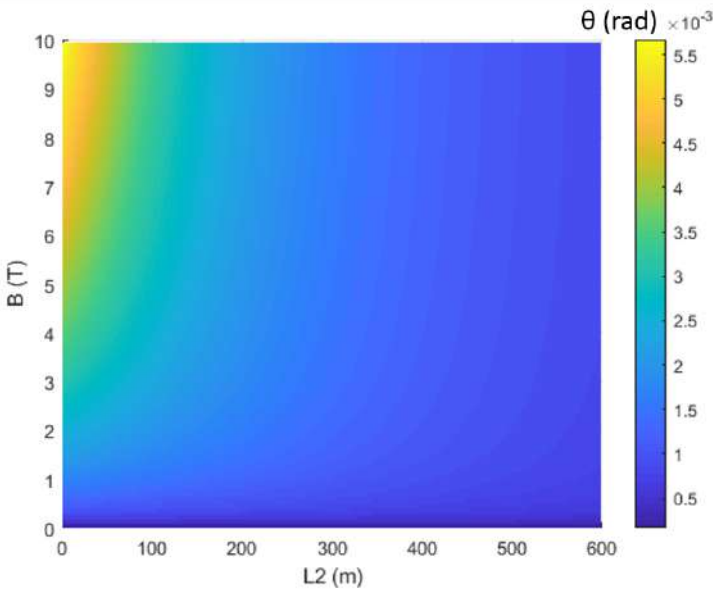


Figure 6.4: Working space of the septa magnets

Figure 6.4 shows the relationship between the drift space length (L_2), the magnetic field of each magnet (B) and the deflection angle necessary to clear the required sagitta. The deflection angle (θ) is determined by the location of the septa and the required sagitta. However, the actual variables that can be used by the magnet designer and by the extraction line designer are the magnetic field integral and the drift space length. The magnetic field can be decomposed as the product of the average field and the total septa length (L_s).

Using equations 6.4 and 6.5 the deflection angle can be eliminated, yielding an analytic expression for the magnetic length L_s in terms of the magnetic field (B), the downstream drift space length L_2 , the sagitta (d) and the beam rigidity ($B\rho$).

$$L_s = \frac{2 \cdot d \cdot B \rho}{\sqrt{L_2^2 B^2 + 4 \cdot d \cdot B \cdot B \rho - L_2 \cdot B}} - L_2 \quad (6.7)$$

The power of equation 6.7 lies in the fact that for a given layout of the extraction line it is possible to know the necessary magnetic field and therefore, which is the best technology to use for the magnetic septa.

Equation 6.7 is plotted in figures 6.4 and 6.5 in two different views. It can be seen that, as expected, for a long magnetic length the magnetic field required decreases, and for a small magnetic field and magnetic length, the necessary drift space increases. It is also possible to realize the required sagitta with a high magnetic field and a short length, which requires a longer drift space.

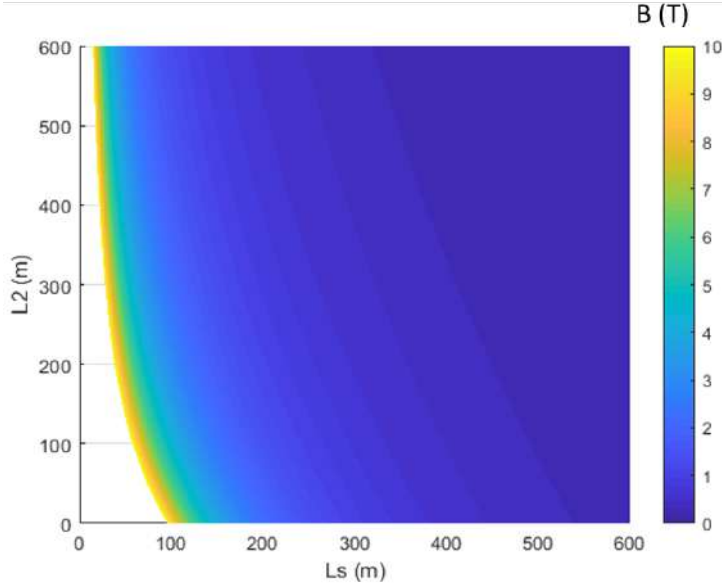


Figure 6.5: Relationship between the required magnetic length, drift space and magnetic field

From figure 6.5 it is also possible to deduce what is the required technology to produce the required sagitta for a given magnetic length and drift space length.

The upper limit of 600 m for the drift space length is set for being high enough and also realistic. It is obviously not possible to operate near the origin, even with a very high field it would not be possible to use a very short magnetic length and drift space, as shown in figure 6.5. Besides, it is possible to design a dump line without a drift space at the end, maximizing the magnetic length but there is a lower limit for the magnetic length. For every magnetic field, it is not possible to extract the beam from the machine with a shorter magnetic length than required by the geometrical separation of the beams. The magnetic length tends to a certain value for an infinite drift space. This is caused by the sagitta that needs to be achieved, as shown in figure 6.3 and equation 6.4. Such an approach is suitable for a 2 plane extraction system, for example using Lambertson septa. Then the kicker deflection angle is independent from the septa. For a single plane extraction scheme, for example using TCT septa, the kicker and quadrupole deflection needs to be taken into account. Besides, a similar calculation can be performed to locate the different septa used in the straight section as a function of the septum thickness.

It is also deduced from figure 6.5 that there is a minimum and a maximum magnetic length necessary when using only one family of septa. Figure 6.6 shows the equivalent plot for the injection system. depending on the septum thickness, a realistic magnetic field for a Lambertson septum is in the vicinity of 1 T. The additional lines have also been plotted for completeness. Figure 6.6 that for a 1 T septum the maximum magnetic length is approximately 75 m if no drift space (L_2) is added. Although there seems to be a lower bound for the magnetic length slightly below 10 m, from equation 6.15 follows that no more than 1466 m drift space would be needed in the extreme case where the full deflection is performed only by the kicker and quadrupole magnets.

The five lines in figure 6.6 are different iso-lines of the surface in figure 6.5. It can be seen that the level curves are closer for higher fields, which means that the slope of the surface along this direction increases sharply with the magnetic field. As stated in section 2.4.1, a normal conducting magnet can produce a magnetic field up to about 2 T. This limit is given by the saturation of the iron yoke. Therefore if the technology chosen for the septa is normal conducting, the minimum lengths of the different zones of the dump line is given by the 2 T line. From the point of view of the layout, this line maximises the magnetic field, producing the minimum possible combination of the lengths of the drift space and the septa magnets. It can be seen that with 2 T magnets and a 1 km drift space, the minimum magnetic length (L_s) required is above 50 m. Any normal conducting septum will operate on the 2 T line or above. If the limit in the magnetic field is set at 4 T, as in the case of the TCT septum presented in section 5.1, it is not possible to design a dump line which lies

below the purple line in figure 6.6.

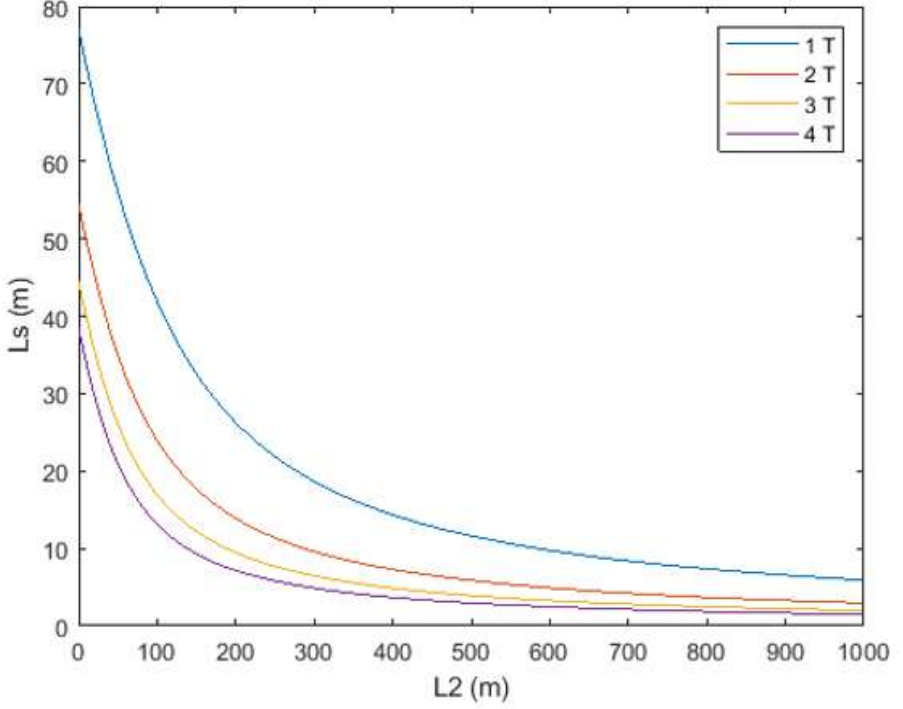


Figure 6.6: Relationship between the required magnetic length and drift space for different injection septa magnetic fields

6.3.2 Derivation of the optimum number of magnet families

For a single magnet family, and fixing the downstream drift space (L_2) for simplicity, it is possible to establish a relationship between the magnetic field and the septa length necessary for the required deflection, starting from equations 6.1 and 6.4:

$$B = \frac{x_c B \rho}{L^2} \quad (6.8)$$

From equation 6.8, the magnetic field can be derived as a function of the required length. Equation 6.8 can then be generalized to n families, resulting in:

$$B_1 L_1 + B_2 L_2 + B_3 L_3 + \dots + B_n L_n = \frac{x_c B \rho}{L_{tot}} \quad (6.9)$$

Assuming that the septa are equally spaced, L_{tot} can be split in n individual lengths (L_i). If the fields are also equally spaced, they follow an arithmetic progression, equation 6.9 becomes then:

$$n \cdot L_i \sum_{i=1}^n B_i = \frac{x_c \cdot B \rho}{n \cdot L_i} \quad (6.10)$$

Using the fact that the sum of the magnetic fields is the sum of an arithmetic progression, equation 6.10 can be modified to calculate the magnetic length of each septum family as a function of the number of families.

$$L_i = \sqrt{\frac{2 \cdot x_c \cdot B \rho}{(B_1 + B_n) n^2}} \quad (6.11)$$

Equation 6.11 is plotted in figure 6.7. The plot has been limited to 20 families because from a design and manufacturing point of view it is advisable to use as few families as possible, as appropriate tooling has to be developed and manufactured for each family, significantly increasing the costs. It is obvious that for one family, equation 6.11 is not valid, one should use equation 6.8, giving a result of 75.66 m for a 1 T Lambertson septum. For 20 families, the magnetic length of each family is slightly over 20 m. That means that for a realistic magnet length of 4 m, five magnets of every family would have to be produced, all with the corresponding tooling. A large number of families, as expected, would increase the production costs significantly. Looking at the slope of equation 6.11, it is more pronounced for lower numbers of families, therefore the biggest gains will be obtained when changing from 2 to 3 or 4 families, and not when changing from 18 to 19 or 20 families.

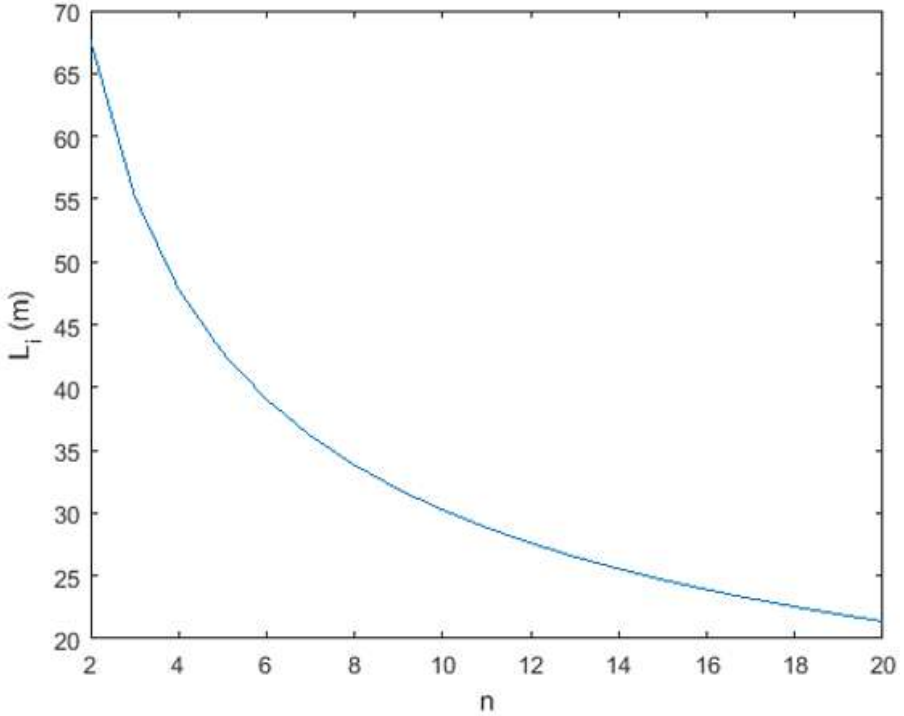


Figure 6.7: Magnetic length of each septa family as a function of the total number of families.

For a magnet length of 4 m, the number of units in each family is plotted in figure 6.8. For two families, the necessary number of magnets is seventeen, for three families the number of magnets required are fourteen and for four families twelve magnets are required. For more than four families the number of magnets required changes significantly less, therefore is not advisable to produce more than three families of magnets because the number of families would increase but the number of magnets per family does not decrease linearly. It can be said that with the assumptions made at the beginning of this investigation, the optimum number of families is either two or three. Although many assumptions were made, and therefore the results obtained will not be exact, they serve as a first step in the study of the injection septa layout, narrowing the parameter choice and allowing to perform a more sophisticated calculation, where more variables will come into play, like different positioning

of the first septa in each family or the drift spaces in the injection line.

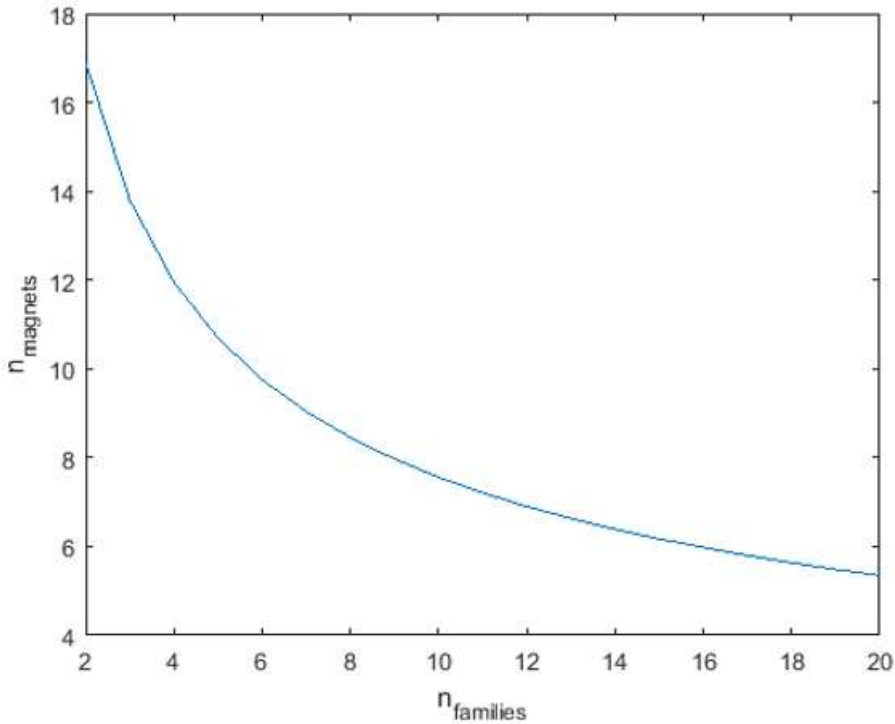


Figure 6.8: Number of magnets required as a function of the number of families

6.3.3 Optimization of the injection septa

The same procedure can be applied to the injection septa system with one difference. Given that the injection scheme is a two plane injection, the kicker and septa deflections are not coupled, as per the previous section. The deflection in the horizontal plane will be the same situation as in figure 6.13. Downstream from the quadrupole no element will produce any deflection. Therefore the septum thickness is determined by the beam separation produced by the kickers and quadrupole magnet. From the geometry point of view, beam injection is an analogous process to beam extraction with the difference that it can be calculated in the opposite sequence. Although the beam will come from the

transfer line, reach the injection septa, then the injection quadrupole and finally the injection kicker magnets, it is possible to think about this system as if the beam is travelling in the opposite direction, as if it was being extracted from the machine. The beam would then start at the kicker magnets, travel through the quadrupole and finally reach the injection septa.

Quadrupole magnets are used in the accelerator lattice to focus the particle beam [22]. Their field cancels in the centre of the aperture and it reaches its peak value at the pole tips. They are characterized by the transverse magnetic field gradient, which results in a magnetic field strength that depends on the position. A particle beam travelling through the centre of a quadrupole magnet will experience a focusing effect in one plane, as the particles that are not in the centre of the aperture will be deflected towards it. The more offset a particle is, the more deflection it will experience. In this case, the use of the quadrupole magnet is not to focus the beam but to deflect it. The beam, previously kicked by the kicker magnets, will be off centre and will experience a deflection proportional to the quadrupole gradient, as if they were travelling through a dipole magnet. Since the deflection increases with the distance from the centre, it is not necessary to place a strong dipole. A quadrupole magnet produces the same effect with less strength, allowing to ease the requirements on the kicker magnets.

The characteristics of the injection kickers and quadrupole system are summarized in table 6.2 [17]. L_K is the length of the kicker stage, L_Q is the length of the quadrupole that increases the deflection from the kicker magnets and L_{dKQ} is the length of the drift space between the kickers and the quadrupole. G_Q is the transverse gradient of the quadrupole field.

Table 6.2: Characteristics of the injection kickers and quadrupole system

Parameter	Unit	Value
$B\rho$	Tm	11011
L_K	m	31.6
L_{dKQ}	m	84.2
L_Q	m	9.1
G_Q	T/m	10.77
θ_K	mrad	0.018

It is necessary to calculate the position at the quadrupole centre to calculate the quadrupole kick. Taking the value of the kickers deflection and the total

length, the transverse position at the quadrupole is given by:

$$x_Q = \theta_k \cdot \left(\frac{1}{2} + L_{KQ} + \frac{1}{2}L_Q \right) = 18.78 \text{ mm} \quad (6.12)$$

The quadrupole kick is then

$$B_Q = G \cdot x_Q = 0.21 \text{ T} \quad (6.13)$$

The deflection angle of the quadrupole is then calculated using equation 6.1.

$$\theta_Q = \frac{B_Q \cdot L_Q}{B\rho} = 0.17 \text{ mrad} \quad (6.14)$$

The total deflection angle of the quadrupole and kickers system is then 0.35 mrad. Given that the magnet cryostat is round, the distance to be cleared at injection will be the same as in the extraction process, 540 mm. Therefore, in the absence of any other deflection, the required drift space distance (L_{\min}) for clearance of the cryostat can be calculated from geometry.

$$x_c = x_Q + \theta_{KQ} \cdot \left(\frac{1}{2}L_Q + L_{\min} \right) \quad (6.15)$$

Solving equation 6.15 produces a value of $L_{\min}=1466 \text{ m}$. However, it is not necessary to clear the cryostat radius in the horizontal and vertical plane simultaneously. By placing the Lambertson septa adequately, this distance can be reduced. L_{\min} can also be seen as the distance in which the beam would clear the cryostat in the horizontal plane.

6.3.3.1 Injection design with two septa families

In this section an optimization of the injection septa will be performed. There will be two families of Lambertson septa, the first will produce a magnetic field of 0.7 T with an apparent septum thickness of only 8 mm and the second one will produce 1.2 T with an apparent septum thickness of 18 mm. These magnetic field values are the maximum values possible for a Lambertson septum with the corresponding parameters.

Given that the kicker magnets produce a horizontal kick, there is no vertical deflection upstream from the first septum magnet. From equation 6.1, it is more advantageous to start installing septa as close to the kicker magnets as possible because the drift space does not produce any significant deflection. The deflection angle is transported downstream of the magnet, so it is interesting to have a long drift space after the magnet, not before. In this case, the

minimum drift space will be determined by the kickers and quadrupole deflections and the septum thickness. A realistic value $L_{\text{dQK}}=23.7$ m is obtained using equation 6.3 and the results from equation 6.14.

Again, the septum thickness of the second family will be determined by the beam separation in the horizontal axis, although the goal of the injection septa is to deflect the beam vertically. This allows to repeat the same procedure and obtain that the minimum distance from the quadrupole to the second family of Lambertson septa is 51.3 m. This means that the available length for the first family and the drift space between the A and B families (L_{AB}) is 27.6 m.

At this point, the only thing left is to optimize the magnetic length of the second Lambertson septa family (L_B) and the drift space downstream of it (L_2). It is straightforward to write an equation providing a relationship between the vertical deflection and the magnetic fields and lengths.

$$x_c = x_Q + \theta_A \left(\frac{1}{2}L_A + L_{AB} + \frac{1}{2}L_B \right) + (\theta_A + \theta_B) \left(\frac{1}{2}L_B + L_2 \right) \quad (6.16)$$

Combining equation 6.16 with equation 6.1, one obtains L_2 and as a function of L_B . This plot is shown in figure 6.9.

$$L_2 = \frac{x_c - \frac{1}{2} \frac{B_A L_A^2}{B\rho} - \frac{B_A L_A L_{AB}}{B\rho} - \frac{B_A L_A L_B}{B\rho} - \frac{1}{2} \frac{B_B L_B^2}{B\rho}}{\frac{B_A L_A}{B\rho} + \frac{B_B L_B}{B\rho}} \quad (6.17)$$

For many possible lengths of Lambertson septa, the required drift space (L_2) becomes negative. This is due to the fact that there is no constraint placed on the lengths stating that lengths need to be positive, therefore if the beam is deflected more than necessary, since the condition is that the deflection at a given length is a given position but not a direction, the equation produces a negative length of drift space. It could be interpreted as an anti septum, which produces an opposite deflection to compensate the excess produced by family B.

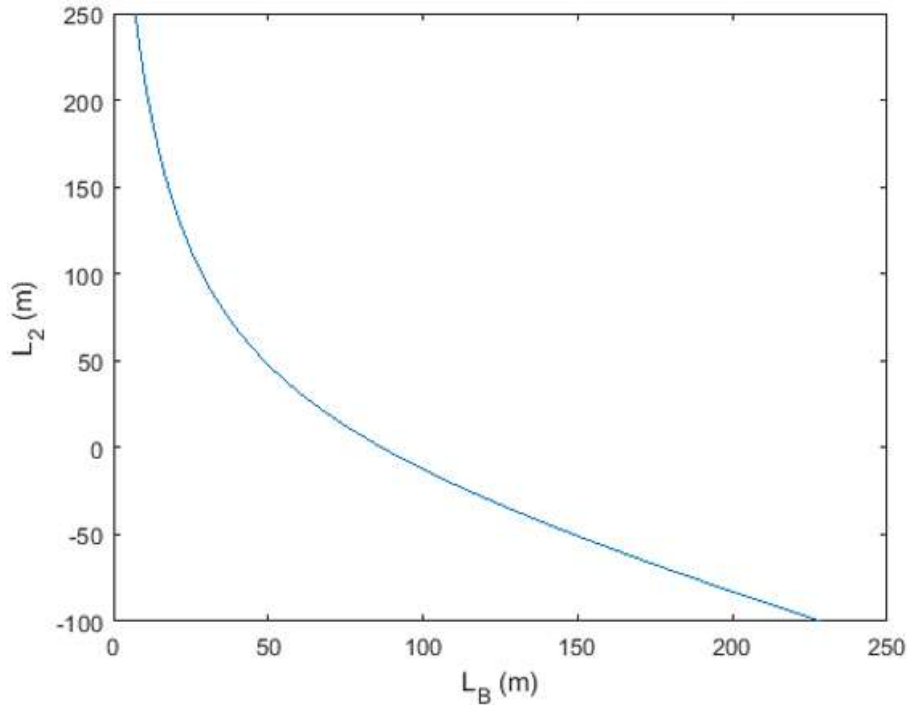


Figure 6.9: Length of the drift space as a function of the length of the second Lambertson septa family

An optimization problem can be set up to minimize the addition of the lengths subject to equation 6.17, which is a non linear equality constraint and complicates the solution significantly. Besides, if the goal was to minimize the total number of magnets, the optimization becomes a mixed integer programming (MIP) problem. MIP problems are significantly harder to solve than linear optimization problems, although there are approximation algorithms based on solving the linear optimization problem and adapting it to obey the integer constraints [142].

However, it is much faster and simpler to plot the addition of the lengths as a function of the second family length and find the minimum. The total length $L_{\text{tot}} = L_B + L_2$ is shown in figure 6.10, which clearly shows a minimum.

We find that the optimum total length is 86.8 m, produced by 87 m of

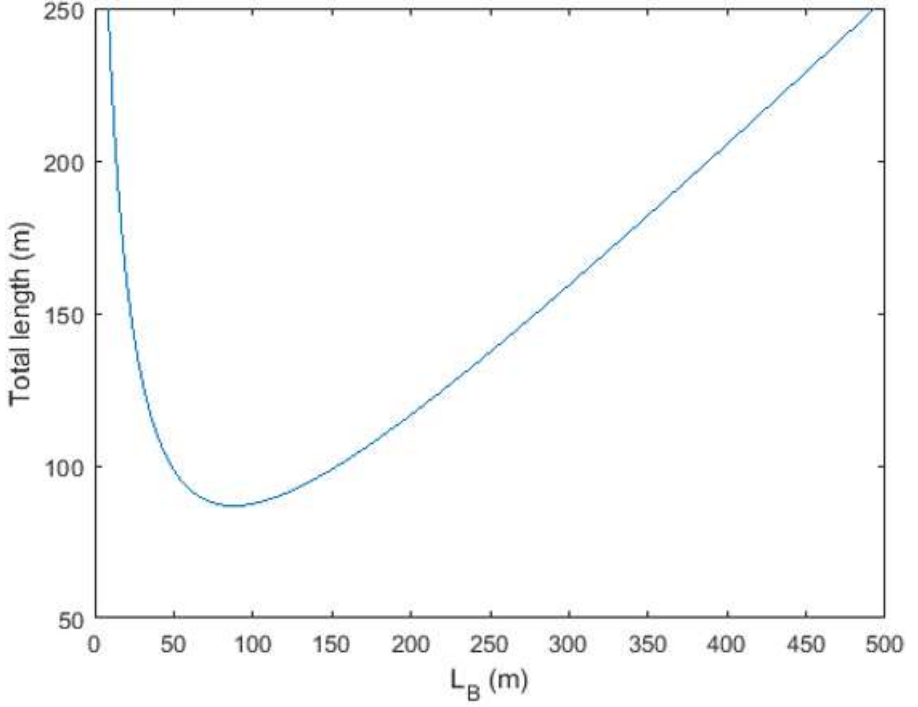


Figure 6.10: Total magnetic length of the B family and the following drift space as a function of the magnetic length of the second family

Lambertson septa from family B and 0.19 m of drift space. This is the optimum solution in terms of length but it might not be the best solution in terms of costs, as the number of magnets to be produced would be 22 assuming realistic 4 m long magnets. It is not an unfeasible number, but running and powering costs may decrease if the number of magnets is reduced. From figure 6.10 one can deduce that it is advisable to find working points towards the left of the optimum and that a small decrease of Lambertson septa length will produce a big change in total length because the slope of the curve is very steep. Some alternatives for both lengths are presented in table 6.3.

From table 6.3 it is seen that decreasing the septa length to 50 m only increases the total length by 10 m but it would require 8 or 9 Lambertson septa less. It is clearly interesting to reduce the length of the second Lambertson septa family to 50 m, which implies that the required number of septa is 13

Table 6.3: Different alternatives for the second Lambertson septa stage

L_B (m)	L_2 (m)	Total length (m)
25	109.9	134.9
50	47.8	97.8
75	12.6	87.6
85	1.8	86.8

instead of 22. The injection system lengths are summarized in table 6.4. It is important to keep in mind that the lengths calculated are all what magnet designers call magnetic lengths. The magnetic field integral in equation 6.1 should be performed along the longitudinal axis for the length at which the magnetic field cannot be neglected. However, it is much simpler to substitute the actual field profile by an average field over a given length, producing a so called hard edge approximation. For the LHC Lambertson septa, the ratio between magnetic and physical length is estimated as 0.9 [63].

Table 6.4: Characteristics of the injection septa system with two Lambertson septa families

Parameter	Unit	Value
L_{dQA}	m	27.3
Magnet length (physical)	m	4.4
L_A (magnetic)	m	27.6
L_A (physical)	m	30.7
Number of magnets (family A)	-	7
L_{AB}	m	1
L_B (magnetic)	m	50
L_B (physical)	m	55.5
Number of magnets (family B)	-	13
L_2	m	47.8
Total length	m	161.3
Total number of magnets	-	20

6.3.3.2 Injection design with three septa families

As a complement to the injection septa scheme proposed in the previous section, and following the result of the estimation of the number of families obtained in section 6.3.2, an alternative using three Lambertson septa families is designed in this section. The Lambertson septa will produce 0.7, 1 and 1.2 T, with an apparent septum thickness of 8, 12 and 18 mm respectively. It can be seen that the difference with the previous alternative is that an intermediate 1 T septum family is introduced with the goal of shortening the injection septa region and, in turn, reduce the total number of magnets and reduce the overall cost as much as possible.

Based on the calculations of the previous section, it is obvious that the first family must be installed at the same position as in the previous case since the minimum distance required for the first Lambertson septum in family A is determined only by the deflections of the kicker and quadrupole magnets and the septum thickness. Therefore, the drift space between the quadrupole magnet and the Lambertson septa (L_{QA}) will be the same, 23.66 m. Repeating the calculation for the 12 mm apparent septum thickness of family B, the minimum length obtained is 35.46 m. And as explained in the previous section, given that the only deflection in the horizontal plane is produced by the kickers and quadrupole magnets, the minimum distance for the first septum of the 18 mm thick family (family C) is the same as before, 57.32 m. Again, since the horizontal and vertical deflections are decoupled, the best strategy is to reduce the drift spaces between the different families (L_{AB} and L_{BC}) as much as possible and place the magnets at the minimum distances calculated.

With the locations of the different families already calculated, the only parameters to be fixed are again the magnetic length of the last family and the length of the drift space downstream (L_2). There is again a relationship between L_C and L_2 , analogous to equation 6.17:

$$x_c = \theta_A \cdot \left(\frac{1}{2}L_A + L_{AB} + \frac{1}{2}L_B \right) + (\theta_A + \theta_B) \cdot \left(\frac{1}{2}L_B + L_{BC} + \frac{1}{2}L_C \right) + (\theta_A + \theta_B + \theta_C) \cdot \left(\frac{1}{2}L_C + L_2 \right) \quad (6.18)$$

Combining equations 6.1 and 6.18 results in an expression L_2 :

$$L_2 = \frac{x_c \cdot B\rho}{\frac{B_A L_A + B_B L_B + B_C L_C}{\frac{1}{2} B_A L_A^2 + B_A L_A L_{AB} + B_A L_A L_B + B_A L_A L_{BC}} + \frac{B_A L_A + B_B L_B + B_C L_C}{B_A L_A + B_B L_B + B_C L_C} + \frac{B_A L_A L_C + \frac{1}{2} B_B L_B^2 + B_B L_B L_{BC} + B_B L_B L_C + \frac{1}{2} B_C L_C^2}{B_A L_A + B_B L_B + B_C L_C}} \quad (6.19)$$

Using equation 6.19, L_2 is plotted in figure 6.11.

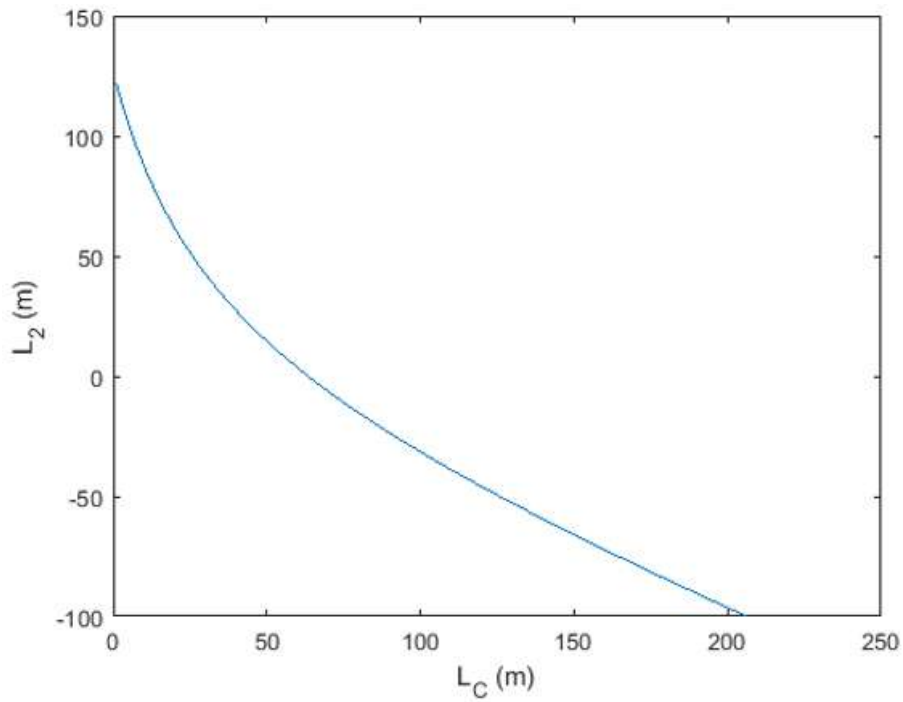


Figure 6.11: Length of the last drift space as a function of the length of the third family of Lambertson septa

And once again, the addition of both distances can be plotted as a function of the length of the third family of Lambertson septa. This plot is show in figure 6.12.

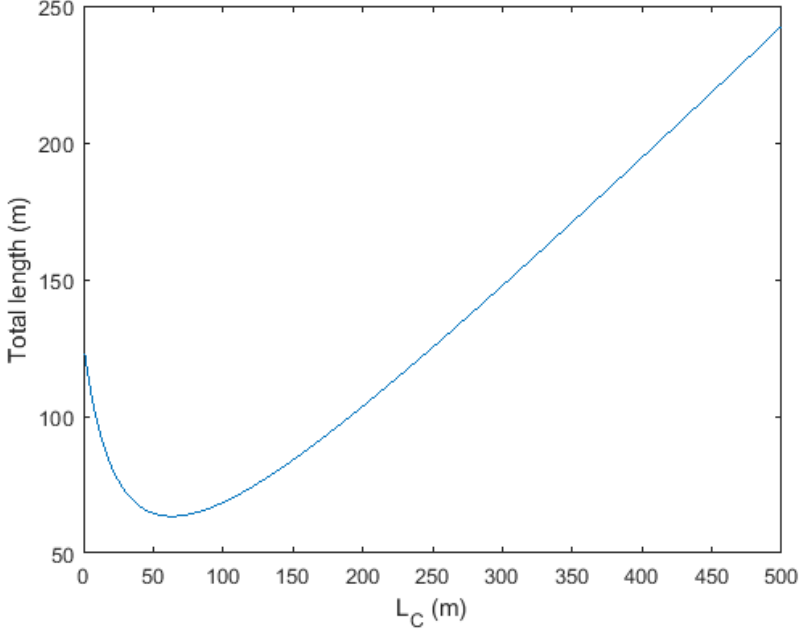


Figure 6.12: Length of the last drift space as a function of the length of the third family of Lambertson septa

From figure 6.12, the minimum length is found to be 63.5 m, which is made up of 63 m of Lambertson septa from the third family and 0.5 m of drift space L_2 . Performing the same analysis of the curve in figure 6.12, some alternatives are provided in table 6.5.

From table 6.5 one can see that there is no interest in increasing the septa length beyond 40 m. The overall length will not change significantly but the number of magnets necessary will increase a 50%. To reduce the cost as much as possible it is advisable to reduce the magnet length L_C to 20 m and increase the drift space distance L_2 to 61.7 m. It can be seen that by reducing the magnet length from 40 to 20 m the increase in overall length is less than 15 m. This reduces the number of magnets that need to be manufactured while not increasing the length of the tunnel significantly.

Table 6.5: Different alternatives for the third Lambertson septa stage

L_C (m)	L_2 (m)	Total length (m)
20	61.7	81.7
30	42.5	72.5
40	27.3	67.3
50	14.6	64.6
63	0.5	63.5

A summary of the different lengths necessary for each stage in this injection alternative is presented in table 6.6. Again, a magnetic length of 4 m per magnet and a ratio between magnetic length and physical length are considered.

Table 6.6: Characteristics of the injection septa system with three Lambertson septa families

Parameter	Unit	Value
L_{dQA}	m	27.3
L_A (magnetic)	m	27.6
L_A (physical)	m	30.6
Number of magnets (family A)	-	7
L_{AB}	m	1
L_B (magnetic)	m	21.8
L_B (physical)	m	24.2
Number of magnets (family B)	-	6
L_{BC}	m	1
L_C (magnetic)	m	20
L_C (physical)	m	22.2
Number of magnets (family C)	-	5
L_2	m	61.7
Total length	m	168
Total number of magnets	-	18

6.3.3.3 Comparison of injection alternatives with the baseline

To summarize the previous section, the injection proposal with two and three families are compared with the proposed baseline in the FCC Condeptual Design Report in table 6.7 [17].

Table 6.7: Comparison of necessary lengths of the injection septa system with with two and three Lambertson septa families and the baseline

Parameter	Unit	2 families	3 families	Baseline
L_{dQA}	m	27.3	27.3	51.5
L_A (physical)	m	30.7	30.7	8
L_{AB}	m	1	1	1
L_B (physical)	m	55.5	24.2	24
L_{BC}	m	-	1	1
L_C (physical)	m	-	22.2	52
L_2	m	47.8	61.7	38.7
Total length	m	161.3	168.1	176.2

It can be seen that both proposals made in this study reduce the length necessary from the FCC-hh baseline. To appreciate fully the improvement, one should also consider the number of magnets necessary to realize each option. These numbers are presented in table 6.8.

Table 6.8: Number of magnets necessary for every injection alternative

Parameter	2 families	3 families	Baseline
Number of magnets A	7	7	2
Number of magnets B	13	6	6
Number of magnets C	0	4	13
Total number of magnets	20	18	21

It can be seen that from the point of view of the number of magnets, it is interesting to use 3 different families of Lambertson septa with the dimensions presented in this study, as the proposal in the baseline requires 3 units more and only uses 2 magnets of the first family, increasing the unit cost of the production. Although the analysis done in section 6.3.2 was simplified, this result confirms that the strategy obtained is correct.

Although it is not shown in figure 1.3, there needs to be a passive quadrupole protection device upstream from the injection quadrupole magnet, and space is reserved in the lattice for this device [28].

6.3.4 Optimization of the extraction septa

From the analysis in section 6.3.2 it follows that it is advisable to use two or three families in the extraction region, instead of one. It is assumed that the deflection of the different magnets is applied at the centre by an infinitely thin magnet with the total strength of that magnet family. The goal of this analysis is to find the best layout possible for the septa stage of the Beam Dump System (BDS). As the two septa families with the highest figure of merit are the SuShi septum and the TCT septum, these two families are the two considered for the BDS. The reason to use two different families is the knowledge obtained in section 6.3.2 that the optimum number of families to use is two or three rather than one. The reason to use two different technologies is that it increases the degrees of freedom such as the magnetic field and septum thickness.

In this study, the deflection provided by the extraction kickers and quadrupole will be taken into account by the apparent septum thickness (s) and the angle θ_K in equation 6.20 and it is not considered a variable.

The starting point of this calculation are the apparent septum thicknesses of the SuShi septum (20 mm) and the TCT septum (35 mm). It is necessary that the beam clears the apparent septum thickness of the SuShi septum as it arrives, which determines the drift space between the quadrupole and the first SuShi septum, although the real limit is the clearance of the cryostat at the end of the straight section. The distance between the kicker magnets and the quadrupole, as well as the strengths are taken as a fixed parameter. They could be changed but then all the optics in the machine would need to be changed accordingly and there is no obvious benefit that could arise from this particular change. There is an interest for the septa magnets to increase the kickers strength, relaxing the septa requirements. This is a trade off and the kickers are usually considered a more risky system due to the possibility of an asynchronous beam dump.

In a first stage, the beam is deflected by the kicker magnets. It travels through a drift space (L_{dKQ}) and arrives at the quadrupole magnet with an angle θ_K . The beam is then deflected by the quadrupole and leaves with an angle $\theta_K Q$. Downstream from the quadrupole, there is a drift space between the quadrupole and the septa (L_{dQS}). The kicker system is highly segmented for reliability reasons. The kicker system is 120 m long (L_K) and has been designed with low voltage kicker magnets to avoid flashovers. Therefore, every

kicker magnet contributes slightly to the system and the loss of one of them will not create unacceptable beam oscillations. This is further explained in [115, 143].

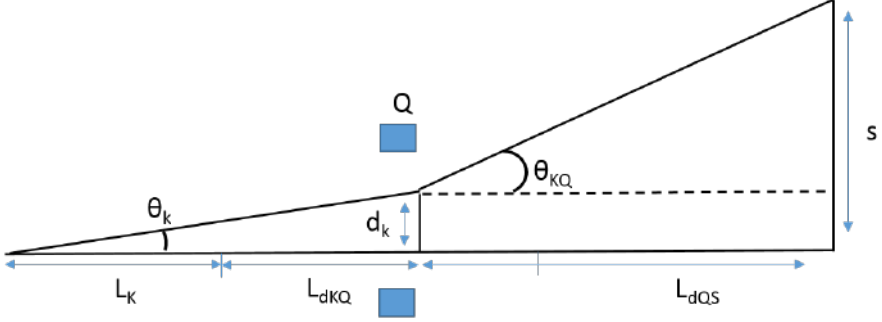


Figure 6.13: Schematic of the kickers and quadrupole system

The characteristics and dimensions of the extraction kickers and quadrupole system are summarized in table 6.9.

Table 6.9: Characteristics of the extraction kickers and quadrupole system

Parameter	Unit	Value
L_K	m	120
L_{dKQ}	m	213
L_Q	m	6.8
G (at 50 TeV)	T/m	70.15
θ_K	mrاد	0.045

As shown in figure 6.14, the beam arrives to the SuShi septa (L_s) with an angle from the kickers and quadrupole magnets (θ_{QK}). It is necessary that the beam clears the SuShi apparent septum thickness (s). At the centre of the SuShi septa, the full deflection is applied, and the beam leaves the SuShi with an angle $\theta_K + \theta_s$ and travels through the drift space between the SuShi and the TCT septa (L_{dST}) stage. The sagitta produced in this stage is x_s . Finally, the beam arrives to the TCT septa stage, which leaves to travel through the last drift space (L_2) with an angle $\theta_K + \theta_s + \theta_T$. The deflection angle produced by

the TCT septa is θ_T . The sagitta at the end of the septa stage is x_c , which is the cryostat radius that needs to be cleared. This is expressed in equation 6.20.

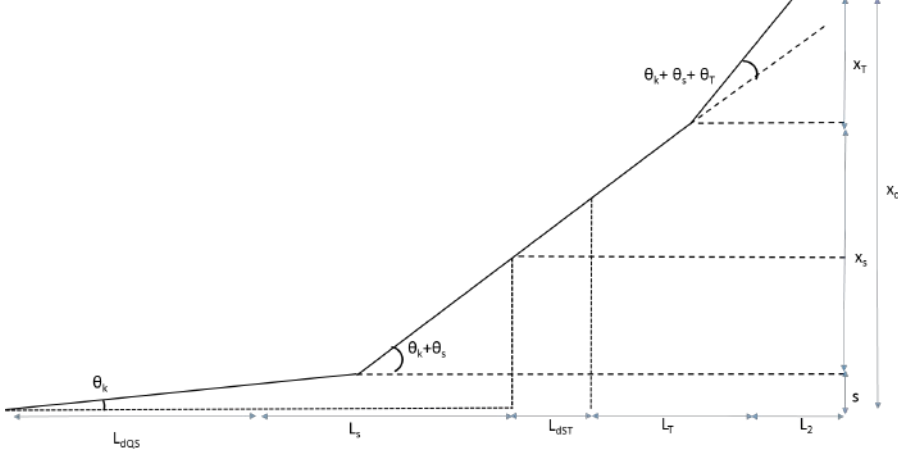


Figure 6.14: Schematic of the extraction region including two septa families

$$x_c = s + x_s + x_T \quad (6.20)$$

The quadrupole in figure 6.13 produces a dipolar kick in the off-centered beam, with a magnitude of $B_Q = G \cdot d_k$. Then d_k can be calculated with the angle θ_k and the geometry of the system.

$$B_Q = \theta_k \cdot \left(\frac{1}{2} L_K + L_{dKQ} \right) = 0.86 \text{ T} \quad (6.21)$$

Using equation 6.1, the angle θ_Q can be calculated.

$$\theta_Q = \frac{0.86 \cdot 6.8}{166.8 \cdot 10^3} = 3.5 \cdot 10^{-5} \text{ rad} \quad (6.22)$$

And the angle θ_{KQ} is calculated by adding both deflections. This is the angle with which the beam arrives to the SuShi septa stage.

$$\theta_{KQ} = \theta_K + \theta_Q = 8 \cdot 10^{-5} \text{ rad} \quad (6.23)$$

Using equation 6.4 again, the total sagitta (s) at the start of the first SuShi septum is given by:

$$s = d_k + \theta_Q \cdot (L_{dQS} + \frac{1}{2}L_Q) \quad (6.24)$$

Knowing that the apparent septum thickness of the SuShi septum is estimated as 20 mm, the thickness of the passive protection device is currently estimated at 25 mm. Its length is foreseen to be 10 m, followed by 10 m of drift space, to allow for work in the absorber and the magnet and with the benefit of using the drift space length to spread the secondary shower from a beam impact on the absorber [28]. The minimum drift space between the quadrupole and the first SuShi septum is obtained from equation 6.24, using the iterative scheme described in section 6.2.

$$L_{dQS} = \frac{s - d_k}{\theta_{KQ}} = 348.3 \text{ m} \quad (6.25)$$

If instead of a 25 mm apparent septum thickness SuShi septum, a TCT septum with a 35 mm apparent septum thickness was used directly, the minimum drift space would be 477 m. It is appropriate then to use a thin septum thickness closer to the extraction point, as it reduces the overall dimensions of the extraction region.

Applying the same reasoning, once it arrives to the TCT septum, the beam needs to clear an apparent septum thickness of 35 mm. It is then possible to obtain a relationship between the SuShi septum length and the drift space between the SuShi septa stage and the TCT (L_{dST}).

$$x_T = s + (\theta_{KQ} + \theta_s) \cdot \left(\frac{1}{2}L_s + L_{dST} \right) = s + \left(\theta_{KQ} + \frac{B_s L_s}{B\rho} \right) \cdot \left(\frac{1}{2}L_s + L_{dST} \right) \quad (6.26)$$

Using the same approach as in section 6.3.3, we obtain an expression for the relationship between the length of the SuShi septum and the drift space between the SuShi septum and the TCT septum:

$$L_{dST} = \frac{10 \cdot 10^{-3} - 8 \cdot 10^{-5} L_s - \frac{1}{2} \frac{B_s L_s^2}{B\rho}}{8 \cdot 10^{-5} + \frac{B_s L_s}{B\rho}} \quad (6.27)$$

It is then possible to find an optimum for the combined length of SuShi septa and drift space. An optimization problem can be set up to minimize the addition of the lengths subject to equation 6.27, which is a non linear equality constraint and complicates the solution significantly. However, it is much faster and simpler to plot the addition of the lengths as a function of

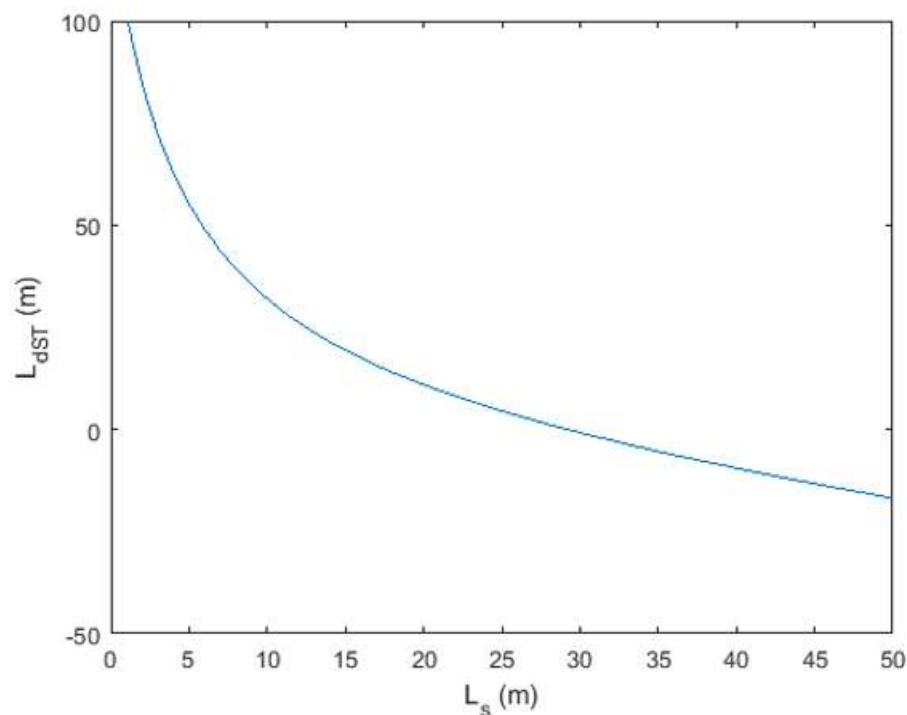


Figure 6.15: Relationship between the required SuShi septum length and the following drift space

the SuShi length and find the minimum. The addition of the lengths is shown in figure 6.16, where the minimum is clearly visible.

The minimum is found for a SuShi length of 30 m and a drift space length of -0.8 m, producing a total length of 29.2 m. This result is clearly not feasible, the drift space cannot be negative. This is caused by the fact that the condition imposed is to clear a distance at a certain length, but there is no condition in the direction of the beam. A negative drift space means that the SuShi septa length is too high and the deflection of the beam is too high, and must be compensated with what could again be seen as a negative septum.

If a minimization problem is set up, one of the constraints must state that lengths need to be positive. Given that the goal of this plot is to avoid the set up and solution of a full optimization problem, this constraints need to be

introduced manually.

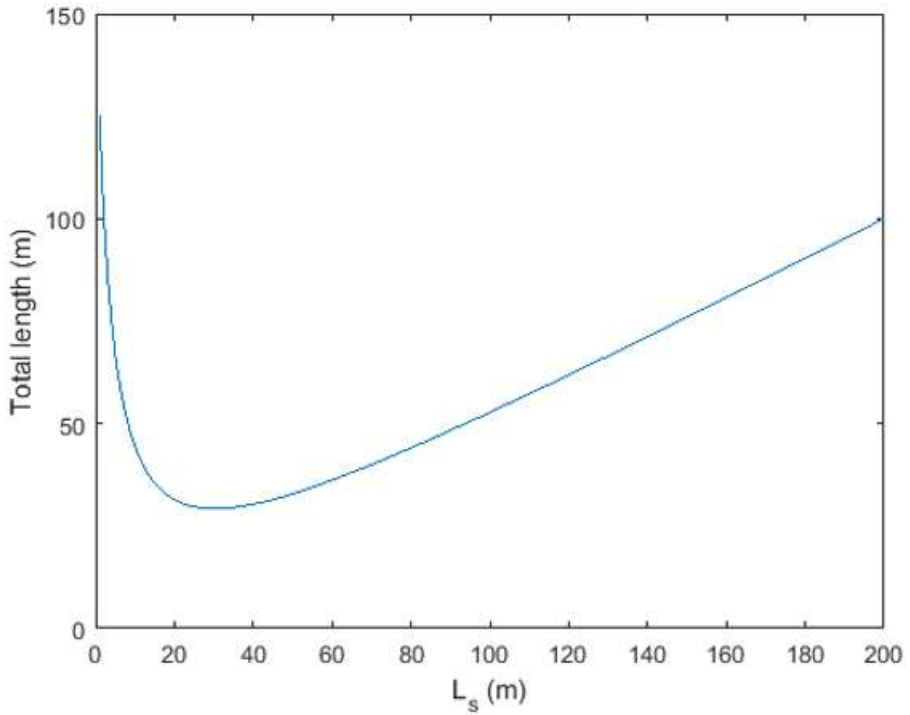


Figure 6.16: Total length of the SuShi septum stage and the following drift space

It can be seen in figure 6.16 that near the minimum of the total distance the slope of the curve is very small, so a small variation in the SuShi septa length will not produce a significant change in the total length. To reduce material costs, it is interesting to increase the drift space and decrease the SuShi length. This trade off is taken into account by calculating the local derivative between the points in figure 6.16. It is then interesting to choose a working point in the curve where the decrease in SuShi length produces an equal increase in overall length, but not more. Otherwise the reduction in SuShi length would be more expensive than the increase in total length. This is achieved for a SuShi septum length of 15 m, where the local derivative is

-1.08. Therefore, the SuShi length is fixed at 15 m and the drift space becomes 20.4 m, producing a total length for this stage of 35.4 m, which is not far from the minimum value in figure 6.16.

The drift space distance of 20.4 m has to be validated with the iterative scheme to calculate that the clearance of the septum thickness considering the beam size is achieved.

Calculating the position of the beam centre at the central point of the SuShi septum, produces a value of 21.8 mm. It is then left to clear a distance that is the difference between 35 mm plus two beam sizes. It is also necessary to keep in mind that at this stage, the deflection angle of the SuShi septa needs to be taken into account, as in equation 6.25. The necessary drift space becomes then 61.7 m. It is almost three times the distance found without considering the beam size, and far from the ideal optimum, but this distance is necessary to install a TCT septum with an apparent septum thickness of 35 mm.

Repeating the same process to find out the minimum length of the TCT stage (L_T) and the last drift space (L_2).

It is also useful to calculate the deflection produced by the SuShi septa (θ_s) using equation 6.1. This produces the value of $\theta_s = 0.27$ mrad.

Combining equations 6.4 and 6.20, the sagitta (x_c) is given by:

$$x_c = s + (\theta_{KQ} + \theta_s) \cdot \left(\frac{1}{2}L_s + L_{dST} + \frac{1}{2}L_T \right) + (\theta_{KQ} + \theta_s + \theta_T) \cdot \left(\frac{1}{2}L_T + L_2 \right) \quad (6.28)$$

Again, the easiest way to understand the relationship between the lengths is to isolate L_2 :

$$L_2 = \frac{0.489 - 4.4 \cdot 10^{-4}L_T - \frac{1}{2} \frac{B_T L_T^2}{B\rho}}{4.4 \cdot 10^{-4} + \frac{B_T L_T}{B\rho}} \quad (6.29)$$

It is necessary to take into account that the 540 mm of clearance at the cryostat already takes into account the beam size. This size has been subtracted in equation 6.29.

Performing the same analysis as before, figure 6.17 shows the relationship between the length dedicated to TCT septa and the following drift space. Again, negative values are plotted to show that the constraint stating that the lengths need to be positive is not taken into account by this simple analysis. The optimum, as seen in figure 6.18, is obtained for a total length of 184 m, which is calculated from a septa length of 187 m and a drift space length of -3 m. It is seen in figure 6.18 that, in this case, the slope is not as pronounced

as in figure 6.16. This means that a change in the septa length will not be as significant as in the SuShi septa case. However, this stage is the main contributor to the total length of the straight section, so it is worth analyzing the consequences of changes in the TCT septa length.

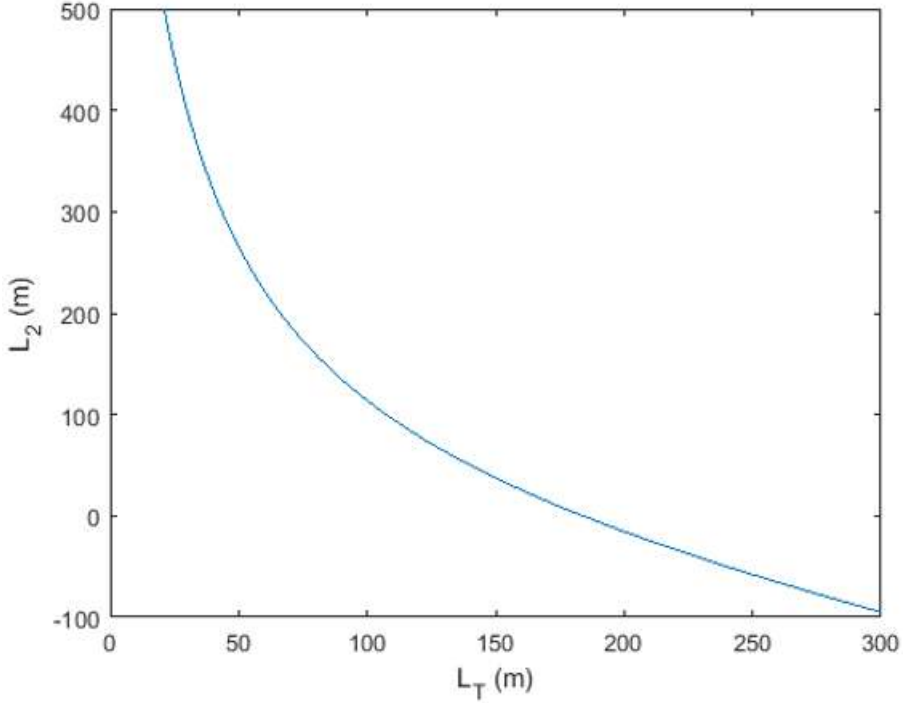


Figure 6.17: Relationship between the required TCT septum length and the following drift space

Following the same reasoning as in the SuShi stage, the local derivative of the total distance is calculated again, but this time the goal is set arbitrarily at a value of -10. This means that a decrease of 1 m of septa length produces an increase of 10 m in the total length. This value is achieved for a TCT septa length of 26 m and a drift space length of 439.5 m. It is more than twice the total length than the minimum obtained from figure 6.18. These values are arbitrarily set and in this case, the approach of using the derivative of the curve in figure 6.18 is more limited than in the case of the SuShi stage. For

this reason, four alternatives are given in table 6.10

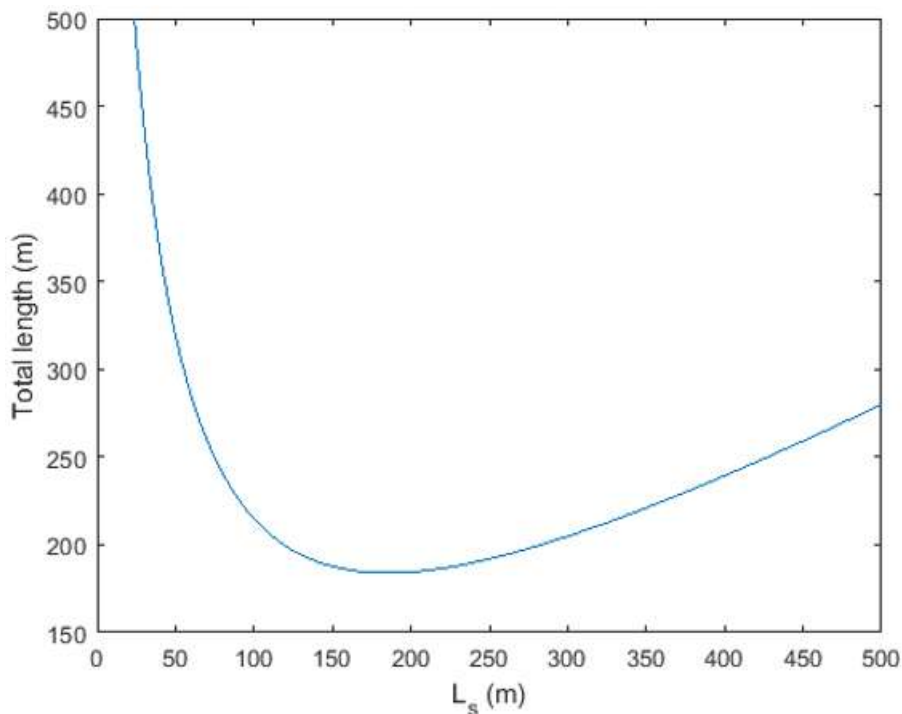


Figure 6.18: Total length of the SuShi septum stage and the following drift space

The length of the different stages are summarized in table 6.10.

It is seen that increasing the length dedicated to TCT septa decreases the overall length. The FCC baseline sets a value of 425 m for the drift space L_2 and 44 m for the space dedicated to the TCT septa (L_T). For this detailed analysis of the extraction line, it is seen that increasing the distance L_T to 50 m reduces the drift space length almost a 35%. The total saving in length is doubled, because there are two extraction lines. It may appear of interest to reduce the total length by increasing the length dedicated to the TCT septa. However, reducing the straight section length significantly would have a non negligible impact in the tunnel layout and could potentially require a change in the tunnel footprint and access shafts. The current FCC layout, explained

Table 6.10: Different alternatives for the TCT stage

L_T (m)	L_2 (m)	Total length (m)
27	428.9	455.9
50	265.41	315.41
75	172.7	247.7
100	113.8	213.8

in section 1.1.1, is geographically constrained by the Alps, the Jura mountains and lake Leman. If the location of the difference access shafts changes, it might impact the required depth of the access shafts, which would now be located in different points, higher than the chosen ones. For this reason, table 6.10 can be used as a starting point of a more complex cost analysis, which is not trivial and would require considerable resources.

6.3.4.1 Comparison of the extraction proposal with the baseline

A comparison of the optimized layout and the FCC baseline is presented in table 6.11. The optimized layout is almost 22% shorter than the baseline, which is a significant improvement. In the LHC dipoles the ratio between magnetic and physical length is 0.94 and in order to have some margin it is taken as 0.9 for this study [144]. The SuShi magnets are assumed to have a length of 2 m per magnet, which is significantly longer than the current prototypes, and the TCT are considered to have a magnetic length of 4 m and therefore a physical length of 4.4 m.

Table 6.11: Comparison between the FCC extraction baseline layout and the layout presented in this study

Parameter	Unit	Optimized layout	FCC baseline
L_S (magnetic)	m	15	20
L_S (physical)	m	16.6	22.2
Number of SuShi magnets	-	12	12
L_{ST}	m	61.7	20
L_T (magnetic)	m	50	39.5
L_T (physical)	m	55.6	43.9
Number of TCT magnets	-	14	11
L_2	m	265.4	425
Septa length	m	399.3	511.1
Total straight section length	m	2800	2800

The proposed layout in this study requires three TCT septa more than the baseline but the total length required for this alternative is almost 22% less than the baseline. As it has been explained before, the cost analysis is quite a complex problem because it involves many other aspects apart from the septa. Given the small difference in the number of septa needed a choice has to be made considering all the implications.

6.3.4.2 Optimization of the beam dump line

Combining equations 6.1 and 6.28, the deflection angles can be expressed as a function of the magnetic fields and the different septa lengths for the full system.

$$x_c = s + (\theta_{KQ} + \frac{B_s \cdot L_S}{B \cdot \rho}) \cdot (\frac{1}{2}L_s + L_{dST} + \frac{1}{2}L_T) + (\theta_{KQ} + \frac{B_s \cdot L_S}{B \cdot \rho}) + \frac{B_T \cdot L_T}{B \cdot \rho} \cdot (\frac{1}{2}L_T + L_2) \quad (6.30)$$

The power of equation 6.30 is that it can be used to calculate which is the parameter change that will be the most profitable to change to optimize the system length. It can be seen as a cost function for the sagitta. Taking partial derivatives with respect to the different variables, and substituting the values calculated previously, a gradient vector can be calculated and normalized. This vector expresses the marginal benefit obtained by changing only one of the parameters. Only the magnitudes relevant to septa are considered, the kickers and upstream drift spaces are taken as fixed parameters as explained

at the beginning of this section. The same analysis can be performed for the case of two and three Lambertson septa presented in section 6.3.3.1, but given that in a single plane extraction all the deflections are linked, it is more interesting to perform this calculation in this case. In a two plane extraction scheme it is not strictly necessary to calculate the partial derivatives and find the gradient vector. Once the number of magnet families has been set, it is possible to optimize the layout by adjusting only the length of the last family and the drift space downstream.

$$\left\{ \begin{array}{l} \frac{\partial x_c}{\partial L_s} = \frac{1}{2}\theta_{KQ} + \frac{B_s L_s}{B\rho} + \frac{B_s L_{dST}}{B\rho} + \frac{B_s L_T}{B\rho} + \frac{B_s L_2}{B\rho} \\ \frac{\partial x_c}{\partial L_{dST}} = \theta_{KQ} + \frac{B_s L_s}{B\rho} \\ \frac{\partial x_c}{\partial L_T} = \theta_{KQ} + \frac{B_s L_s}{B\rho} + \frac{B_T L_T}{B\rho} + \frac{B_T L_2}{B\rho} \\ \frac{\partial x_c}{\partial L_2} = \theta_{KQ} + \frac{B_s L_s}{B\rho} + \frac{B_s L_s}{B\rho} + \frac{B_T L_2}{B\rho} \\ \frac{\partial x_c}{\partial B_s} = \frac{1}{2} \frac{L_s^2}{B\rho} + \frac{L_s L_{dST}}{B\rho} + \frac{L_s L_2}{B\rho} \\ \frac{\partial x_c}{\partial B_T} = \frac{1}{2} \frac{L_T^2}{B\rho} + \frac{L_T L_2}{B\rho} \end{array} \right. \quad (6.31)$$

Taking the values of the partial derivatives of the system of equations 6.31 for this particular extraction system and normalizing with respect to the norm, the gradient vector at this point is found. The results of the system of equations 6.32 means that to increase the sagitta, and therefore reduce the length of the straight section, the most beneficial parameter to increase is the magnetic field of the TCT septa, which has an influence of 88% in the sagitta, followed by the 45% influence from the SuShi septa. This may be surprising at first sight given that the SuShi septa are located upstream in the system and one would expect their importance to be higher than the TCT septa. In this extraction, given that the magnetic field of the TCT and the total length are bigger than the field and length of the SuShi, the TCT septa become more important overall. As a sanity check of this method, one can set the fields and lengths of the SuShi and TCT septa to the same value. If the relative magnitude of the contribution of the SuShi field and length to the gradient vector are not higher than those of the TCT septa, this method will not be correct. Setting both fields to 3 T and both lengths to 20 m, the contribution of the TCT septa field becomes 62 % and the contribution of the Sushi septa field is 76 %. The contributions of the lengths are respectively 11 and 12 %. The method is therefore valid to calculate the relative importance of each magnitude when calculating the contribution of each variable to the total deflection.

It is also seen that the influence of the lengths of both the SuShi and the TCT septa in the final sagitta are below 10%, and the drift spaces downstream

of the SuShi and the TCT septa have very little influence. It is important to keep in mind that this method can be applied to every extraction line, but the results may change depending on the actual values of the different fields and lengths of every particular extraction line. If the magnetic fields of the magnets are currently the limiting factor, it is seen that the strategy to follow is to increase the magnetic length of the SuShi or the TCT magnets instead of the drift spaces, in particular the drift space between the two magnetic stages.

$$\begin{cases} \frac{\partial x_c}{\partial L_s} = 0.071 \\ \frac{\partial x_c}{\partial L_{dST}} = 0.006 \\ \frac{\partial x_c}{\partial L_T} = 0.086 \\ \frac{\partial x_c}{\partial L_2} = 0.024 \\ \frac{\partial x_c}{\partial B_s} = 0.45 \\ \frac{\partial x_c}{\partial B_T} = 0.88 \end{cases} \quad (6.32)$$

Following the gradient study, it is possible to obtain an expression from equation 6.30 in which the the septum thicknesses at a given point is an independent variable, but it would be equivalent to the study performed.

6.4 Summary and further studies

We find that the optimum number of families to be used for a given transfer line is three or less. The actual number will depend on the parameters of every injection or extraction line but it has been shown that the integrated magnetic field does not decrease when increasing the number of families to be used. From a point of view of the manufacturing costs it is obviously more interesting to produce several magnets of each family. It has also been shown that although it is possible to set up an optimization problem to minimize the number total number of magnets or the total length of the straight section, this would require a complex mathematical solution due to the equality constraint present in the problem and the fact that minimizing the total number of magnets would require to solve a MIP problem, which is significantly more difficult than a linear problem. It has been shown that it is easier to minimize the total number of magnets by minimizing the magnets length and then calculate the necessary units of each family. This optimization can be performed graphically. It has also been shown that the influence of the beam size cannot be neglected in these calculations, especially at injection energy.

In this chapter a method has been proposed to determine a layout and the impact of including several septa families. However, considering the rest of

the variables as fixed, the total number of magnets can be reduced to save costs. This is achieved by placing the septa magnets as close to the kickers and quadrupole magnets as possible. For the extraction region, this would require to use a thin septum blade in the first septum or family. Due to the thin septum thickness, the magnetic field produced by this septum cannot be as high as the field produced by the downstream septa with a thicker blade. However, the first deflection angle is transported along all the stages of the transfer line, making an important contribution to the total deflection.

Finally, the most interesting direction for development has been identified. It has been shown that the research effort should be focused on increasing the magnetic strength of the TCT and SuShi septa. A 3.8 T TCT septum was designed in sections 5.2.1 and the following. While such a design is challenging, there is room for improvement. The current TCT septum design allows for some improvement but a significant increase, of the order of 1 T, would require significant work on the cross-section to avoid high magnetic fields in the coil which may provoke unwanted quenches and adequate stress management in the coil areas and the septum blade. A small increase in strength, of a fraction of a Tesla, may be possible by optimizing the septum cross section.

The TCT septum strength can be increased at the expense of increasing the septum thickness, which would require the first magnet to be moved further from the SuShi septa stage, reducing the length of the drift space L_2 . Maintaining the same total distance, this shift in position would imply the reduction of the L_2 drift space. This approach is interesting because it has been shown that the change in the TCT septum has the biggest influence in the total sagitta produced by the whole system, while reducing the length L_2 produces a small impact on the total deflection.

The SuShi septum strength can also be increased by increasing the thickness of the shield. Again, this increase would force the shift of the first SuShi septum further downstream and it would likely require a modification of the design of the external Canted Cosine θ magnet, described in section 2.4.7.5. As in the case of the TCT septum, a decrease on the downstream drift space would be outshined by the increase in magnetic field obtained with a thicker apparent septum thickness.

Chapter 7

Leak field effects

7.1 Introduction

The goal of this chapter is to calculate the leak field produced by the septa used to design the injection and extraction in chapter 6.1 is above or below acceptable limits. The first step is to quantify the maximum allowed leak field at injection and extraction, which is done in section 7.2. Then the leak field of the different injection Lambertson septa options is calculated in section 7.3. For the extraction, the leak field of the SuShi septum is estimated in section 7.4 and finally the leak field of the TCT septum is calculated in section 7.5. The conclusions are summarized in section 7.6.

7.2 Determination of the permissible leak field

The orbiting beam only goes through the extracted beam gap once and it must not be perturbed during normal operation when it travels through the orbiting beam gap. If it is, a small error on the beam orbit can accumulate over many turns and lead to an emittance blow up. It is therefore essential to make a reliable estimate of the fringe fields that leak into the orbiting beam gap.

7.2.1 Determining the maximum permissible leak field from the emittance growth

When a beam is distorted by a non ideal field, filamentation makes its emittance grow. This can be due to an imperfection, such as a misalignment, a

ripple or in this case a leak field [145, 146, 147]. A first consideration, one has to keep in mind that an ideal dipolar kick in normalized phase space is just a vertical displacement of the beam.

The maximum leak field is calculated using equation 7.1, which gives the normalized emittance growth ($\Delta\epsilon$) due to the passage of the beam through a misaligned magnet [148], where Δy is the transverse alignment error and α and β are the Twiss parameters. The goal is to calculate $\int Bdl$ in order to obtain a maximum affordable value for the integral leak field. The transverse alignment error is taken as 0.2 mm, which is 33% higher the allowed transverse alignment error in the LHC [149]. The beam emittance is available in [150] and the Twiss parameters have been calculated using MAD-X [151]. At the extraction point, the parameters of the x-axis and the y-axis are similar and only an average at the middle point of the allocated length for the septa has been calculated. The values introduced in equation 7.1 are summarized in table 7.1. It is assumed that an increase of the beam emittance of 1% is allowed due to the leak field.

$$\Delta\epsilon_n = \frac{\pi}{2} \cdot \left((\Delta y)^2 \frac{(1 + \alpha^2)}{\beta} + \left(\frac{\int Bdl}{B\rho} \right)^2 \beta \right) \quad (7.1)$$

Table 7.1: Parameters for the calculation of emittance growth

Parameter	Unit	Value
Normalized initial beam emittance	mm·mrad	2.2
Allowed emittance increase due to leak field	%	1
Alignment error (Δy)	mm	0.2
α_x	rad	-1.7
β_x	m	1594
α_y	rad	1.8
β_y	m	1740
Beam rigidity at extraction ($B \cdot \rho$)	T·km	166.8
Beam rigidity at injection ($B \cdot \rho$)	T·km	11

Solving equation 7.1 with the values for the x- axis, one obtains: $\frac{\int Bdl}{B\rho} = 1.63 \cdot 10^{-6}$ radians. With the beam rigidity at extraction, the leak field integral obtained is 272 mT·m. If one takes the value of the beam rigidity at injection, the leak field integral obtained is much smaller (30 mT·m) but this is not a relevant value since the main field in the septum will be much smaller and the leak field in each magnet will be negligible, as explained in 3.4.1, which ensures that the leak field is below the limit calculated with equation (7.1). The leak

field does not scale linearly with the main field while the septum blade is not saturated, which is the design constraint.

Solving equation (7.1) with the values for the y-axis produces a maximum leak field integral of $260 \text{ mT} \cdot \text{m}$, which is a very similar value. Since this calculation starts from the approximation of considering only one septum magnet instead of the real system, only the value for the x-axis will be used.

7.2.2 Determining the maximum allowed leak field from the beam rigidity

This method is a simple yet realistic way of approaching the problem. Since there is no clear way of addressing this issue and magnetic fields are not linear due to saturation of the iron, one can consider the beam rigidity which is linear with the energy. The beam rigidity is the beam resistance to be steered by a magnet. It is similar to the inertia in Newtonian mechanics. With this idea in mind one can calculate how much field is necessary to perturb the beam and actually see an effect. That will determine the leak field budget. The beam rigidity was presented in equation 4.7.

From the 2D MSDC simulation at 1.1 T, the value of the leak field obtained in a cross section is 2.3 mT. This is an average value, obtained integrating the leak field over the orbiting beam gap surface and dividing by the surface. It is assumed that this is a constant field and the coil ends effect are negligible since the magnet is long compared to the orbiting beam gap surface. Considering the 15 Lambertson septa installed and a 4 m length per magnet, the integrated leak field seen by the orbiting beam in the LHC is:

$$B_{leakLHC} = 2.3 \text{ mT} \cdot 15 \text{ magnets} \cdot 4 \frac{\text{m}}{\text{magnet}} = 138 \text{ mT} \cdot \text{m} \quad (7.2)$$

The beam rigidity of the LHC at injection has a value of: $B\rho_{LHC}(\text{injection}) = 1501 \text{ T} \cdot \text{m}$. And the beam rigidity of the FCC at injection is calculated from the energy in equation 7.3, as explained in [152].

$$B\rho_{FCC}(\text{injection}) = 11011 \text{ T} \cdot \text{m} \quad (7.3)$$

Then, scaling for the FCC:

$$138 \text{ mT} \cdot \text{m} \cdot \frac{11011 \text{ T} \cdot \text{m}}{1501 \text{ T} \cdot \text{m}} = 1012 \text{ mT} \cdot \text{m} \quad (7.4)$$

This is very robust especially if one takes into account the beam sizes. In the LHC the normalized beam emittance is $3.5 \mu \text{ m}$ while in FCC is $2.2 \mu \text{ m}$.

To make a fair comparison between beam sizes, it is necessary to compare the geometrical emittances, not the normalized ones. The geometrical emittance is calculated dividing the normalized emittance by the product of the relativistic parameters β_{rel} and γ_{rel} . That is, the same kick will be more relevant in the case of smaller beams because while the centers will move the same distance the displacement in phase space will be bigger in the FCC than in the LHC. This is qualitatively explained in figure 7.1, where the blue circumferences represent the phase space with no perturbation and the red circumferences are the result of applying a 1σ kick. The dashed lines represent the emittance growth due to this kick. It can be seen that, for the same kick, the emittance growth in the FCC will be smaller than in the LHC.

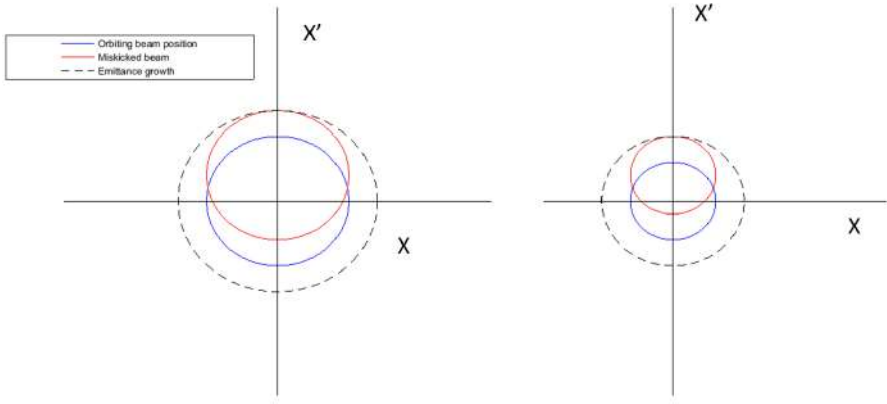


Figure 7.1: Comparison between kicks in the LHC and in the FCC

Which means that, $\epsilon_{g,LHC} > \epsilon_{g,FCC}$ or, considering that the emittance is related to the size of the phase-space. If the beam is kicked a distance L , the ratio between L and the size of the phase space is bigger in the FCC than in the LHC.

The geometrical emittance of the LHC and FCC are respectively:

$$\begin{aligned}\epsilon_{g,LHC} &= \frac{\epsilon_{n,LHC}}{\beta_{LHC}\gamma_{LHC}} = \frac{3.5 \cdot 10^{-6}}{7462} = 0.47 \text{ nm} \\ \epsilon_{g,FCC} &= \frac{\epsilon_{n,FCC}}{\beta_{LHC}\gamma_{FCC}} = \frac{2.2 \cdot 10^{-6}}{53305} = 0.04 \text{ nm}\end{aligned}\tag{7.5}$$

Therefore, the leak field integral for the FCC septa is:

$$1012 \text{ mT} \cdot \text{m} \cdot \frac{0.04 \text{ nm}}{0.47 \mu\text{m}} = 88 \text{ mT} \cdot \text{m}\tag{7.6}$$

7.2.3 Adopted method

The leak field values obtained with the scaling of the emittance growth method and the beam rigidity method are similar. Given that both methods produce similar results, they are a starting point for the septa design at an early stage of the project, in the order of 100 mT·m. Although the beam rigidity method is very reasonable it is only a scaling of the LHC leak field values, which may be overconstraining the FCC design. However, it needs to be taken into account that a 1% value for the allowed emittance growth may also be an excessive constraint. Therefore, the emittance growth method is preferred because the beam rigidity calculation an approximation, while the emittance growth method relies on past operation and experience in different particle accelerators.

7.3 Leak field of the Lambertson septa

The leak field integral is computed along the orbiting beam gap centre for each magnet family and the total leak field integral is added taking the total number of Lambertson septa into account. The total integrated leak field for the three options presented in section 6.3.3.3 is calculated in table 7.2. As a remainder, the different injection layouts were presented in tables 6.7 and 6.8, in section 6.3.3.3. The relevant parameters have been reproduced in table 7.2.

Table 7.2: Comparison of the integrated leak fields for the different injection options

Parameter	Unit	2 Families	3 Families	Baseline
Number of magnets (family A)	-	7	7	2
Number of magnets (family B)	-	13	6	6
Number of magnets (family C)	-	-	4	13
Leak field integral (family A)	mTm	9.8	9.8	2.8
Leak field integral (family B)	mTm	27.3	12.6	12.6
Leak field integral (family C)	mTm	-	9.2	29.9
Total leak field integral	mTm	37.1	31.6	45.3
Maximum allowed leak field	mTm	272		

It is seen that the integrated leak field values obtained for all the three options are significantly lower than the maximum allowed leak field obtained in section 7.2. This means that the septa system will not limit the performance of the FCC significantly. However, even if the leak field is low compared to

other multipole errors, it should be taken into account when designing the necessary corrector magnets.

7.4 Leak field of the SuShi septum

Full 3D simulations of the SuShi septum are not available at this moment. However, different measurements have been performed and the results can be used to estimate the leak field integral in the SuShi stage [79, 82]. It is planned to produce a shield that is longer than the external magnet used to produce the main field in order to avoid leak field penetration at the ends of the shield. Therefore it can be considered that the SuShi leak field is a 2D problem. Since the shield will operate at a field lower than the maximum field that it can shield, the measurements performed present values of leak field below 1 Gauss, and can then be neglected.

7.5 Leak field of Truncated Cosine θ septum

As it has been explained in section 5.3, due to memory limitations it is not possible to solve a full model of the Truncated Cosine θ septum in 3D, even if all the relevant symmetries are applied. The leak field of the total magnet has to be inferred from the 2D and 3D simulations. To calculate a more accurate value, a simulation of the full septum should be solved, although with this approximation the result will be of the same order of magnitude.

The leak field integral is calculated by integrating the contribution of the 2D cross section along the length where the magnet can be considered as 2D and then adding the integral from the 3D coil ends. The leak field integral in the central part of the magnet can be approximated by a multiplication, as the field is constant and the length, as explained in section 5.3, is considered as 3.7 m. In the 3D model, the integration length should extend to infinity, although it will be truncated at a length where the contribution is negligible.

From the results obtained in section 5.3, in figures 5.27 and 5.28, it is clear that the integrated leak field of the Truncated Cosine θ septum will be dominated by the effect of the coil ends. This is due to the geometry of the coil ends, which do not follow the Truncated Cosine θ distribution and the appropriate truncation.

The integrated leak field for both extraction alternatives presented in table 6.11 is shown in table 7.3.

In the case of the optimum extraction proposal presented in section 6.3.4.1

Table 7.3: Comparison of the integrated leak fields for the different extraction options

Parameter	Unit	Optimum proposal	Baseline
Number of SuShi magnets	-	12	12
Number of Truncated Cosine θ magnets	-	14	11
Leak field integral (SuShi)	mT·m	-	-
Leak field integral (Truncated Cosine θ)	mT·m	1573.6	1236.4
Total leak field	mT·m	1573.6	1236.4
Maximum allowed leak field	mT·m	272	

The total integrated leak field is more than 6 times higher than the maximum allowed leak field calculated in section 3.4.1.1. In the case of the baseline proposal, the integrated leak field is more than 5 times higher than the maximum allowed value. It is not possible to shield the orbiting beam gap from the leak field in the region of the coil ends as the different materials (MuMetal or soft iron) would saturate and the leak field would not be attenuated significantly. The leak field then must be actively compensated, either by using compensation coils or with dedicated corrector magnets. Alternatively, it may be possible to reduce the leak field by modifying the geometry of the coil ends. As explained in section 5.3, any modification of the coil ends need to be studied in detail due to the winding and manufacturing challenges that this magnet presents. The compensation coils may be very challenging due to the structure of the leak field. A Fourier analysis of the leak field could be done, but it would be more advantageous to reduce the magnitude of the leak field first. Only after that, the multipole decomposition will be meaningful.

The compensation coils design might be done using the semi-analytical algorithm introduced in [84], which was used to produce exotic septa designs which cancel the magnetic field at a given point [85]. Another alternative for the compensation of the leak field would be in principle to use dedicated magnets upstream and/or downstream of the TCT septa stage. This compensation scheme is simple and it may be possible to reduce the leak field by using very few magnets of reduced power. However, the influence of these corrector magnets in the optics needs to be studied in detail.

7.6 Conclusions

A maximum value for the leak field has been provided in this chapter. The method to calculate it is based in setting a limit to the emittance growth

induced by the leak field of the septa system.

The errors introduced by the leak field in the orbiting beam have been quantified and it has been shown that all the injection alternatives presented in section 6.3.3.3 are below the maximum allowed leak field.

For the extraction system, it has been shown that the SuShi septa introduce errors that can be neglected at this stage and that the Truncated Cosine θ septa presents unacceptable leak field levels, coming from the coil ends. Different alternatives to reduce the leak field of the Truncated Cosine θ septum have been proposed. A geometry modification of the coil ends, the use of compensation coils, dedicated compensation magnets or the use of a massless septum. The use of a set of dedicated corrector magnets to reduce the leak field levels locally, upstream or downstream of the Truncated Cosine θ septa. However, this correction alternative may influence the machine optics.

Assuming successful compensation of the leak field is achieved at the coil ends, the integrated leak field has been estimated. With these assumptions, it is clear that the Truncated Cosine θ septum remains a suitable topology for the FCC dump line with promising performance. Future work should focus on the reduction of the leak field contribution from the coil ends.

Chapter 8

Conclusions and future work

8.1 Summary

In this chapter the results of this study are summarized and future lines of work are outlined. The thesis can be divided in three parts. The first part comprises the exploration of different septa topologies that were initially identified as suitable to be used in the FCC injection or extraction. A figure of merit was developed to provide a common metric to measure their performance. In the second part an optimized layout for the injection and extraction septa is proposed, using the septa with the best performance according to the figure of merit developed. In the last part, the effect of the leak fields on the orbiting beam is investigated to validate the injection and extraction layout. An exhaustive review of existing septa topologies has been carried out, identifying the ones that could be suitable for the FCC-hh BDS.

Given the numerous differences between the different septa topologies, a novel figure of merit was developed to characterize the performance of each septum topology and to enable comparison between them. Three variants of this figure of merit have been developed, for normal conducting septa, superconducting septa and SuShi type septa. As explained in section 2.5, when comparing two different septa, the higher the figure of merit, the better the performance. Although the figure of merit is a powerful tool, it is not the only one that can be used in septum design or comparison. Many other factors such as space limitation or materials choice may be relevant, depending on the particular circumstances of every septum magnet.

Because of its robustness, the Lambertson septa topology has been investi-

gated in particular. The limiting factor of this topology has been found to be the saturation of the septum blade. The operational limit is found when the leak field increases beyond acceptable limits, which in turn limits the septum field. Different shapes of the orbiting beam gap have been investigated, as well as the use of rare earth materials, such as Holmium, as a flux enhancer. Active leak field reduction has also been explored, using one and two sets of compensation coils and permanent magnets although no significant increase on the maximum magnetic field was achieved. A super ferric variant has been studied and it has become an alternative for a low energy consumption injection, taking advantage of the availability of cryogenic cooling.

In the massless septa field, the so called Pacman septum has been introduced and compared with existing massless septa. According to the figure of merit developed, its performance was found to be similar to other existing massless septa although the dimensions and the maximum magnetic field are significantly higher. As a novel concept, active compensation of the leak field has been studied. It is possible to use a transverse deflecting RF pillbox cavity, in TM_{110} mode, to compensate the effect of the leak field in the orbiting beam gap. The parameters of such a cavity were estimated and single particle tracking was performed along the cavity length using the finite difference method. It has been concluded that this idea may possibly be applicable at a lower energy level and a possible energy range has been estimated in the cases of a proton and an electron accelerator.

Other applications for massless septa have been addressed. The possibility of using the leak field for phase space stretching and folding as a way of reducing losses in multiturn slow extraction was studied, as well as the use of a double massless septum for injection protection. These concepts take advantage of the rapid magnetic field variation between the high field region and the zero field region of a septum by using the leak field to blow up the beam and avoid critical beam energy deposition on a downstream equipment. Injection protection has been identified as the most promising application.

A 2D and 3D conceptual design of a 4 T Truncated Cosine θ septum have been produced. This septum may be the first superconducting septum installed. As a first step, 2D electromagnetic and mechanical simulations have been performed to confirm that this septum topology produces a 4 T with a low leak field and a mechanical support concept for the septum coil was designed, including the material choice. The second step of this design was the 3D design of the coil ends. A septum coil where the individual turns do not collide when closing the coil was produced. The coil ends take into account that there needs to be enough space between each cable so they can be supported by a support that can be manufactured. Due to limited computational

resources, it was not possible to simulate the detailed 3D model, so the model had to be simplified. The inductance of the TCT septum was estimated, which will be essential for quench protection studies for example.

A procedure to derive the optimum number of septa families to be used in an injection or extraction line has been established. Although it is obvious that using many different families will increase the cost, it may also be inefficient from the point of view of the necessary length, which will also translate into an increase in cost. This procedure quantifies the total septa length as a function of the number of families. It was found that there is no advantage to install more than three septa families, as the total length of the system will not be reduced and the manufacturing costs will increase.

A new method to calculate the necessary septa length and the length of the drift spaces between them has been established. Although a full optimization problem may be set up, it would involve equality and non linear constraints, which increase the solution complexity significantly. As an added difficulty, physically unfeasible solutions are possible even if the constraints are set up carefully, which would require setting arbitrary limits on the constraints. For example, it may be found that the optimum length for a given drift space is too small to allow for installation of the magnet upstream or downstream. The proposed method breaks the problem into smaller parts and, being sequential, provides a possibility to check the solution at every stage of the septa layout avoiding unnecessary complexity. This method allows for simultaneous optimization of the length of a septum family and the drift space downstream, becoming an approximation of a full optimization problem, with the advantage that the proposed method is significantly simpler than setting up and solving a full optimization problem.

Using the proposed method, a septa layout was produced both for the FCC-hh injection and extraction. The injection has been realized with Lambertson septa due to their robustness and the 2-plane injection scheme. Two possibilities were explored, using 2 and 3 septa families, and the proposed layouts were respectively 9.5 and 5.5% shorter than the initial baseline. An extraction layout was proposed using the same method. For the extraction, the septa topologies chosen were the SuShi septum and the TCT due to their classification according to the figure of merit developed. The proposed extraction layout is almost 22% shorter than the baseline. Additionally, a method to identify the most interesting improvement direction has been introduced. Applying this method to the extraction layout, which would potentially be the system that is more susceptible to reduce its costs, it was shown that the preferred course of action is to increase the magnetic field of the septa, followed by increasing the magnetic length of the Sushi and TCT septa, fol-

lowed by the length of the last drift space. Any modification on the lengths of the other components of the septa system would not produce any significant improvement in the necessary septa length.

Finally, two methods to quantify the maximum allowed leak field integral of a given septum thickness were compared and one of them was chosen based on experience with other accelerators. The injection and extraction integrated leak fields for each alternative were calculated and it was found that the Lambertson septa and the SuShi septum do not introduce a significant leak field. This leak field should be taken into account in detailed studies although it is below acceptable limits. However, the TCT septum introduces a very high leak field due to its coil ends. The design should be optimized before the leak field can fall within acceptable limits.

8.2 Conclusions and future work

In this thesis, an optimized layout of the septa straight section has been produced, which can significantly reduce the cost of the injection and extraction systems. It has also been shown that it is possible to extract the particle beam at peak energy in a moderate space using a reasonable amount of magnets. This work has proven that the BDS is feasible and will not be a reason not to build the FCC. Using the systematic procedure to identify which magnitude has the most impact on the overall system, it has been shown that it is interesting to produce higher field septa magnets, in this case the SuShi and TCT septa. The only possibility to increase the magnetic field produce by a TCT septum is to use high temperature superconductors (HTS), which have the potential of reaching far beyond 16 T.

A design for the first superconducting septum was produced. It was shown that it is necessary to reduce the leak field of the TCT septum while maintaining a compact size of the coil ends and a promising strategy is to use compensation coils at the magnet ends. Since it was not possible to simulate the full magnet due to the computational resources available, a full model without simplifications needs to be developed. Additionally, it is of interest to perform a sensitivity analysis regarding the position of the cables of the TCT septum and its influence on the field quality and leak field. These actions will be necessary to build a first prototype to validate the results obtained from the magnetostatic and mechanical simulations and the septum blade support design.

The building of a TCT prototype could also benefit from the advance of new technologies like 3D printing. It is possible that in the future 3D printed

parts, metallic or not, become suitable for in vacuum installation. This could be of interest to avoid machining the support of the coil ends. If the ends do not need to be machined, a more compact design may be produced, reducing the leak field at the coil ends. Following this advance, in the future it may be possible to 3D print the superconducting cables, which would be an incredible breakthrough. Such a development would open many possibilities such as solving the inverse problem to produce the desired field or cancel the leak field at a certain point.

Although the design of the TCT septum presented uses NbTi cables for reliability reasons, this choice limits the maximum achievable magnetic field. It is possible that the magnet may be built in the future using HTS such as MgB_2 , YBCO or REBCO, to mention the most promising material at this moment. The use of HTS would allow for higher field septa magnets and a higher operating margin, reducing the quench risk. At the moment, HTS materials are available commercially as tapes, allowing to produce Roebel cables. Significant research on how to produce HTS cables is ongoing, the main challenge being that most of the materials are brittle, which makes it difficult to extrude a cable or wind a coil. Under this assumptions, a staged approach in the extraction system becomes possible then. It would consist of a first stage of normal conducting septa followed by a stage of superconducting septa built using HTS materials. The normal conducting septa would produce a small separation of the beam while being very robust. In the case of a kicker magnet malfunction or any beam impact, they could survive or be exchanged in a reasonable time. They could play a protection role for the downstream superconducting septa, which would not be affected by any heat deposition due to radiation or impact of the beam. The superconducting septa would provide most of the required magnetic field integral in a short space thanks to their high fields. In this case, a thick septum thickness is to be expected to contain the stresses produced by the Lorentz forces.

As a result of this thesis, it has been shown that it may be worth to build a super ferric Lambertson septum from the point of view of the energy consumption. However, the iron saturation will still limit the performance of such a magnet.

A detailed design of the double massless septum could be interesting for injection protection, as it has been shown that the required magnetic field gradient for a 3.3 TeV falls within feasible parameters. For a lower energy application the requirements in magnetic field gradient are expected to be more relaxed, although creating the zero field region may be more challenging, as an error in that area would affect the orbiting beam more significantly. However, this challenge does not seem impossible to overcome.

The RF compensation of the leak field may be a very interesting technology for particle accelerators with a lower energy than the FCC. A more detailed design of an RF cavity may be relevant, although the main interest at this point is to perform detailed beam tracking simulations to fully characterize the deflection produced by the cavity and its effect on the beam size and emittance.

Following this topic, detailed numerical simulations of the SuShi shield are necessary and a full simulation of the SuShi shield and the CCT dedicated magnet must be implemented. A full scale prototype of the Canted Cosine θ magnet will be built between 2019 and 2020 and a full size magnetic shield will be installed for testing. This is part of an initiative with the aim of developing a shield material and a manufacturing procedure to produce sufficiently long tubes, more than 1 m long, which is also resistant to flux jumps.

As explained, current studies estimate that the necessary length of the passive protection elements upstream of the septa are approximately 10 m of segmented carbon material, usually referred to as sandwich structure [28]. A more detailed study of the protection elements needs to be undertaken, as well as the study of the segmentation of these elements if this is found to be interesting for the FCC dump line.

For the superconducting septa, quench protection needs to be taken into account. It is not acceptable to operate the accelerator when the dump septa have quenched. Although it is possible to dump the beam without any damage if the quench is detected in time [143], the thermal cycling may take too long, reducing the availability of the machine. Additionally, suitable quench detection and quench protection circuits need to be studied in detail given that they would be protecting critical systems. Quench propagation in HTS is usually significantly slower than in NbTi. This means that with the current quench detection schemes, many more voltage pick-ups are necessary to detect a quench when it occurs. An alternative to avoid the long thermal cycling is to use a HTS material cooled well below the critical temperature would allow for operation with a higher margin, making a quench much less likely.

Appendix A

The finite difference method applied to charged particle tracking

Charged particle tracking script

Although there are many codes available which are capable of performing charged particle tracking, they are far more advanced than what is needed for a preliminary estimation. It is more efficient to develop a simple script which integrates the acceleration and the velocity of a single particle in the presence of a magnetic field. This approach also avoids running long 3D finite element simulations. The application of the finite difference method to particle tracking under the assumption of absence of longitudinal fields is described in this appendix.

A.1 The finite difference method

The Finite difference method is based on the definition of derivative, as shown in equation (A.1), in which h is a sufficiently small value. Qualitatively, the method is based in the fact that if two points of a function are sufficiently close, the next point can be calculated by adding a small quantity to the current point, which is known.

$$\left(\frac{\partial u}{\partial x}\right) \approx \frac{u(x+h) - u(x)}{h} \quad (\text{A.1})$$

If the function u is sufficiently smooth in the vicinity of h , then it can be approximated by a Taylor series.

$$u(x+h) = \sum_{n=0}^{\infty} \frac{(x-x_i)^n}{n!} \left(\frac{\partial u}{\partial x} \right)_i = u_i + h \left(\frac{\partial u}{\partial x} \right)_i + \frac{h^2}{2} \left(\frac{\partial^2 u}{\partial x^2} \right)_i + \frac{h^3}{6} \left(\frac{\partial^3 u}{\partial x^3} \right)_i + \dots \quad (\text{A.2})$$

And truncating after the first derivative, an approximation of the function u_x can be obtained.

From equation (A.1), if the derivative of the function at a given point $\left(\frac{\partial u}{\partial x} \right)$ and the current value $u(x)$ is known, then the value of the function can be approximated as:

$$u(x+h) \approx u(x) + h \cdot \left(\frac{\partial u}{\partial x} \right) + \mathcal{O}(h^2) \quad (\text{A.3})$$

And since the Taylor expansion in equation (A.3), it can be shown that the error associated to the forward approximation is proportional to h , since for a sufficiently small h , the error has an upper boundary, shown in equation (A.4), where C is a positive constant.

$$\left| \frac{u(x+h) - u(x)}{h} - u'(x) \right| \leq C \cdot h \quad (\text{A.4})$$

The Finite Difference Method approximates the function as a succession of n points, and equation (A.3) can be adapted to calculate the next point $u(n+1)$ as a function of the derivative of the function at the current point $u'(x)$ and the current value of the function $u(x)$. Equation (A.5) is usually known as the forward difference approximation. It is important to notice that the \approx symbol in equation (A.3) transformed to a $=$ symbol in equation (A.5) the original function in the forward difference approximation has been substituted by a succession of points, which have no error in the calculation. This is illustrated also by the change of variable, from a continuous variable x to a discrete variable n . The error is in the discretization of the function and the choice of h .

$$u(n+1) = u(n) + h \cdot u'(n) \quad (\text{A.5})$$

There is an analogous approximation known as the backward differentiation approximation, in which the movement along the function is the opposite, shown in equation (A.6). The corresponding error is the same as in the forward approximation.

$$u(x - h) \approx u(x) - h \cdot \left(\frac{\partial u}{\partial x} \right) + \mathcal{O}(h^2) \quad (\text{A.6})$$

The main advantage of using the approximations in equations (A.3 and A.6) is that their complexity is very low, providing very fast results at the expense of a higher error.

To further reduce the error, the central difference approximations is commonly used. The principle of this approximation is shown in equation (A.7) and qualitatively it is seen that instead of taking into account only the precedent or the following point, both are used to calculate the current state of the system. By averaging equations (A.3 and A.6), one obtains that the terms in h of the Taylor expansion vanish and the terms in h^2 reduce their weight. The derivative of the function at a given point is then obtained according to equation (A.7).

$$\left(\frac{\partial u}{\partial x} \right)_i \approx \frac{u(x + h) - u(x - h)}{2h} \quad (\text{A.7})$$

It can be shown that the truncation error in the central difference approximation is proportional to h^2 while in the forward and backward difference approximations the error is proportional to h , following the same principle as in equation (A.4), equation (A.8), in which the upper boundary of the error is given by a positive constant C and h^2 .

$$\left| \frac{u(x + h) - u(x - h)}{2h} - u'(x) \right| \leq C \cdot h^2 \quad (\text{A.8})$$

Applying the same discretization principle as in equation (A.5) to the central difference approximation, the next discrete point in the function, $u(n+1)$ can be calculated from the previous point $u(n-1)$ and the derivative of the function in the current point $u'(n)$.

$$u(n + 1) = u(n - 1) + 2h \cdot u'(n) \quad (\text{A.9})$$

The second derivative of the function u can also be approximated by a finite difference formula. Full details of this derivation can be found in [153]. The final result is shown in equation (A.10).

$$u''(x) \approx \frac{u(x + h) - 2u(x) + u(x - h)}{h^2} \quad (\text{A.10})$$

A.2 Application of the finite difference method to charged particle tracking

The calculation performed starts from the assumptions that the effect of the longitudinal electric field is negligible. Therefore the only acceleration of a particle travelling through the cavity will be transverse to the direction of movement and the energy gain will be neglected. Additionally, the variable m denotes the relativistic mass and the variable m_0 is the rest mass.

Applying the central difference approximation to a particle travelling along the RF cavity, the position is the magnitude that is going to be approximated by the function $u(n)$. Therefore, the position in the x-axis of a single particle travelling through the cavity can be calculated using equation (A.11), where v_x is the speed in the x direction. A similar equation can be produced for the y and z axes.

$$x(n+1) = x(n-1) + 2h \cdot v_x \quad (\text{A.11})$$

To calculate the acceleration in the x-axis, it is straightforward to approximate the second derivative of $x(n)$ using equation (A.10). The result is shown in equation (A.12) and again, a similar equation can be formulated for the y and z axes.

$$a(x) = \frac{x(n+1) - 2x + x(n-1)}{h^2} \quad (\text{A.12})$$

Inside the RF cavity, the acceleration will be produced by the Lorentz force, given by equation (A.13).

$$\vec{F} = q \cdot (\vec{E} + c \times \vec{B}) \quad (\text{A.13})$$

The acceleration is proportional to the relativistic mass of the particle.

$$\vec{F} = \gamma_r e l \cdot m \cdot \vec{a} \quad (\text{A.14})$$

Therefore by combining equations (A.12), (A.13) and (A.14), one can produce the rules to calculate all the points that define the trajectory of the particle inside the cavity. For a TM_{110} it is known that the only non-zero components of the electromagnetic field are E_z, B_r and B_θ , so the resulting Lorentz force is simplified. The trajectory equations are given by the system (A.15), which are coupled equations.

APPENDIX A. THE FINITE DIFFERENCE METHOD APPLIED TO CHARGED PARTICLE TRACKING

$$\begin{aligned}
 x(n+1) &= -x(n-1) + 2 \cdot x(n) - \frac{qB_y h^2}{m} \left(\frac{z(n+1)-z(n-1)}{2} \right) \\
 y(n+1) &= -y(n-1) + 2 \cdot y(n) - \frac{qB_x h^2}{m} \left(\frac{z(n+1)-z(n-1)}{2} \right) \\
 z(n+1) &= -z(n-1) + 2 \cdot z(n) - \frac{qh^2}{m} \left(B_y \frac{x(n+1)-x(n-1)}{2} - B_x \frac{y(n+1)-y(n-1)}{2} \right)
 \end{aligned} \tag{A.15}$$

In equation (A.15), m is the relativistic mass and for highly relativistic beams, the speed of the particle will be the speed of light because it can be considered that all the energy transferred to a particle will be transferred in the form of mass, not of speed. These assumptions are very conservative because in a real cavity one must consider other effects such as the transit time factor and the variation of the electric field. Taking this consideration into account, the motion in the z -axis becomes independent of the cavity, and can be assumed as uniform and can be used as an independent variable for iteration at every step. As a result of these assumptions, solving a highly coupled system of equations can be avoided and two independent explicit equations can be produced to calculate the trajectory of a relativistic particle.

The trajectory of the particle depends on the electromagnetic fields seen by it, its energy and the constant h . It is important to choose h sufficiently small so the error in the approximation is negligible, but choosing a value too small will increase computation time and can produce numerical instability. In this implementation, for simplicity, it was chosen to perform steps of 1 mm. That produces a value of $h = 3.3 \cdot 10^{-12}$.

Appendix B

Analytical estimation stresses and brief description of the Finite Element validation

B.1 2D mechanical analysis

In this section, the choice of the mechanical support shape is explained. The septum blade is very close to a uniformly loaded beam, which is very useful when determining the first iteration of the shape of the support. A uniformly loaded beam can be supported or fixed at the ends. In a support, the displacements at the ends are fixed with a value of zero, while the angles are not. However, in the case of a fixed beam, both the displacements and the angles at the ends are zero. Both situations are illustrated in figure B.1 by Carnicero et al. [42].

The maximum deflection in the supported beam is given by equation B.1 and in the case of the fixed beam is given by equation B.2. In both cases the maximum deflection is located at the centre of the beam [43]. For any given beam cross section, load and material, the deflection of the fixed beam is five times smaller than the supported beam. This indicates clearly that the support has to be designed in a way that resembles a beam fixed at both ends. For this reason, the boundary conditions shown in figure 5.21 are chosen.

$$f_{max} = \frac{5}{384EI}qL^4 \quad (\text{B.1})$$

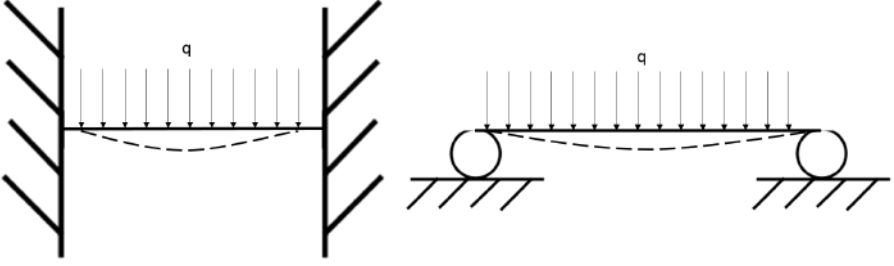


Figure B.1: Uniformly loaded beam, supported at the ends (left) and fixed at the ends (right)

$$f_{max} = \frac{1}{384EI} qL^4 \quad (\text{B.2})$$

The static stress model is created from the magnetic analysis. It shares the geometry and the mesh and only the boundary conditions are changed, while the Lorentz force is used as the mechanical load present in the model. Opera 2D can calculate the Lorentz force directly as the product of the current density and the magnetic field ($\vec{J} \times \vec{B}$) but to improve accuracy in the presence of magnetic materials it is recommended to calculate the Maxwell stress integrals around each element. Both magnitudes can be calculated from the magnetic solution and imported into the magnetic model automatically. In this model, the approach of the Maxwell stress tensor has been chosen to reduce potential inaccuracies.

The finite element method applied to static stress analysis solves equation (B.3) for the displacement vector \vec{D} . It is a matrix equation in which \vec{F} is the load vector and K is the rigidity matrix. K depends on the material properties and it is defined at every node of the mesh, which means that it also depends on the connections between the different nodes. Temperature effects can also be included. Adding the boundary conditions, which are usually balance equations, the matrix K can be inverted and the displacement at every node is then calculated. Other magnitudes can then be derived from the constitutive equations. These equations relate stress or force to strain or deformation [43, 154].

$$\vec{F} = K \cdot \vec{D} \quad (\text{B.3})$$

The analysis type imposes some assumptions. In the first place, the bound-

APPENDIX B. ANALYTICAL ESTIMATION STRESSES AND BRIEF DESCRIPTION OF THE FINITE ELEMENT VALIDATION

any conditions need to ensure that the model position is fixed. It can be deformed, but it cannot move because being a static analysis there are no kinematic equations involved. If the boundary conditions are not properly set, the solution will never converge. However, the model can be overconstrained (known as a hyperstatic structure) as long as it does not result in a non physical solution. Overconstraining can result in longer convergence times, and this increase is not necessary linearly.

The stress in a material is calculated in a given direction, usually in the XY plane. It can be calculated in the x or y axis but it will not necessarily be the maximum stress. The maximum stress is found in the principal directions, which are two perpendicular directions that are characterized for not having any shear stress, as shown in figure B.2.

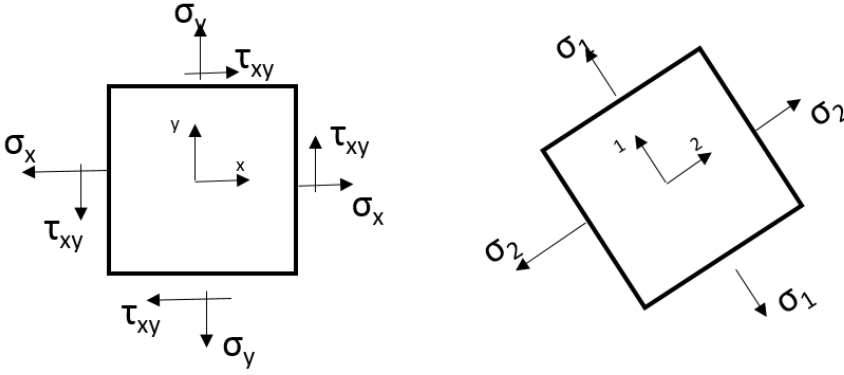


Figure B.2: Principal stresses concept

This can be expressed via the stress tensor of a differential element in a given direction:

$$\sigma = \begin{pmatrix} \sigma_x & \tau_{xy} \\ \tau_{xy} & \sigma_y \end{pmatrix} \quad (\text{B.4})$$

The principal stresses can be calculated from the x and y stress according to equation B.5, which is derived in [43]. It is seen also that the stress tensor is real and symmetric, which implies that all the eigenvalues are real [155]. The principal stresses can also be calculated by numerically by diagonalizing the stress tensor directly using one of the diagonalization algorithms but if

the calculation of the principal stresses has to be performed over numerous elements it is more efficient to use a closed formula.

$$\sigma_{1,2} = \frac{\sigma_x + \sigma_y}{2} \pm \sqrt{\left(\frac{\sigma_x - \sigma_y}{2}\right)^2 + \tau_{xy}^2} \quad (\text{B.5})$$

Equation B.5 is derived by solving the characteristic polynomial of the matrix, which is necessary to diagonalize the stress tensor. The principal stresses are the eigenvalues of the stress tensor and the principal directions are the eigenvectors of this tensor. The stress tensor in the principal directions becomes then:

$$\sigma = \begin{pmatrix} \sigma_1 & 0 \\ 0 & \sigma_2 \end{pmatrix} \quad (\text{B.6})$$

For completeness, in the case of the steel support, the equivalent von Mises stress has been calculated according to equation B.7. The von Mises criterion is widely used to establish a maximum stress in a piece, given a safety coefficient. It is normally used in the case of ductile materials in a bi-axial stress state. Tresca's equivalent stress is also attractive due to the simpler mathematical form, but presents some corners in the $\sigma - \tau$ diagram and might be misleading. When calculating a safety coefficient, the Tresca criterion is also more conservative than the von Mises criterion [156]. Since the equivalent stress is calculated numerically using Opera 2D and the complexity of introducing the equations for both criterions is similar, the von Mises stress is preferred.

$$\sigma_{vM} = \sqrt{\sigma_{xx}^2 + \sigma_{yy}^2 - \sigma_{xx} \cdot \sigma_{yy} + 3 \cdot \tau_{xy}^2} \quad (\text{B.7})$$

B.2 3D mechanical analysis

The concept of principal stresses in 2D, explained in section 5.2.2 in equation (B.5) can be extended to 3D. The 3D stress tensor of a differential element is shown in equation B.8

$$\sigma = \begin{pmatrix} \sigma_x & \tau_{xy} & \tau_{xz} \\ \tau_{xy} & \sigma_y & \tau_{yz} \\ \tau_{xz} & \tau_{yz} & \sigma_z \end{pmatrix} \quad (\text{B.8})$$

Therefore it is possible to find a set of three planes where the shear stress vanishes and there is only normal stresses to these planes, which are also called

APPENDIX B. ANALYTICAL ESTIMATION STRESSES AND BRIEF DESCRIPTION OF THE FINITE ELEMENT VALIDATION

principal stresses. The calculation of the three principal stresses and directions is a bit more complicated than in 2D and it is necessary to introduce the stress invariants.

The same way a vector has different components in different reference systems but its norm does not change, the stress tensor has three invariant quantities, which are presented in equations B.9 [156]. These equations are usually implemented in commercial software and the user can obtain the stress invariants, the principal stresses or the stress in a given direction directly, without any additional programming or calculations. The displacements are also available directly from the FEM calculation. A short description of the principal stresses calculations performed by Opera 3D is provided in the next paragraphs.

$$\begin{aligned} I_1 &= \sigma_x + \sigma_y + \sigma_z \\ I_2 &= \sigma_x \sigma_y + \sigma_x \sigma_z + \sigma_y \sigma_z - \tau_{xy}^2 - \tau_{xz}^2 - \tau_{yz}^2 \\ I_3 &= \sigma_x \sigma_y \sigma_z + 2\tau_{xy}\tau_{xz}\tau_{yz} - \sigma_x \tau_{yz}^2 - \sigma_y \tau_{xz}^2 - \sigma_z \tau_{xy}^2 \end{aligned} \quad (\text{B.9})$$

It is possible to see that the first invariant I_1 is the trace of the stress tensor and the third invariant I_3 is the determinant of the stress tensor. The system of equations (B.9) then can be modified to calculate the principal stresses.

$$\begin{aligned} I_1 &= \sigma_1 + \sigma_2 + \sigma_3 \\ I_2 &= \sigma_1 \sigma_2 + \sigma_1 \sigma_3 + \sigma_2 \sigma_3 \\ I_3 &= \sigma_1 \sigma_2 \sigma_3 \end{aligned} \quad (\text{B.10})$$

Since the system of equations (B.10) is not linear, it can be solved numerically very quickly. However, if a similar system has to be solved many times like in the case of a finite element simulation, it is more efficient to use a set of three closed formulae in terms of trigonometric functions. These formulae were introduced by Viète (1540-1603) for cubic equations with three real roots, Viète also introduced other formulae for different types of cubic equations [157, 158] and they can be particularized for the case of the principal stresses calculations [159]. The three solutions are calculated in terms of the *cosine* and *arccosine* functions and are presented in equations (B.11), in which I_1 , I_2 and I_3 are the stress tensor invariants. For clarity, the angle ϕ is calculated first and then introduced in the three remaining equations.

$$\begin{aligned}
 \phi &= \frac{1}{3} \cos^{-1} \left(\frac{2I_1^3 - 9I_1I_2 + 27I_3}{2(I_1^2 - 3I_2)^{3/2}} \right) \\
 \sigma_1 &= \frac{I_1}{3} + \frac{2}{3} \left(\sqrt{I_1^2 - 3I_2} \right) \cos(\phi) \\
 \sigma_2 &= \frac{I_1}{3} + \frac{2}{3} \left(\sqrt{I_1^2 - 3I_2} \right) \cos\left(\phi - \frac{2\pi}{3}\right) \\
 \sigma_3 &= \frac{I_1}{3} + \frac{2}{3} \left(\sqrt{I_1^2 - 3I_2} \right) \cos\left(\phi + \frac{2\pi}{3}\right)
 \end{aligned} \tag{B.11}$$

Given that the principal stresses are the highest normal stresses states of a given element, it is also useful to order them from higher to lower, just for convention. The principal stresses are also useful to calculate the maximum shear stress at a given point. The maximum shear stress is given by equation B.12, where σ_1 is the highest principal stress and σ_3 is the lowest one. This can also be seen using Mohr's circle, which is shown in figure B.3 [156]. In figure B.3 it is obvious that the principal stresses have zero shear stress.

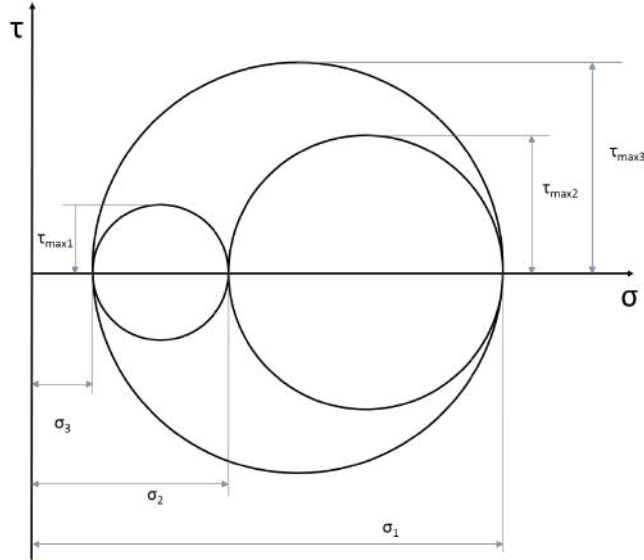


Figure B.3: Mohr's circle with the principal stresses and maximum shear stresses

$$\tau_{max} = \frac{1}{2}(\sigma_1 - \sigma_3) \tag{B.12}$$

By definition, the stress tensor in the principal directions becomes diagonal, which is very useful for finite element calculations and post processing because all the matrix multiplications become scalar multiplications, saving computation time and memory.

$$\sigma = \begin{pmatrix} \sigma_1 & 0 & 0 \\ 0 & \sigma_2 & 0 \\ 0 & 0 & \sigma_3 \end{pmatrix} \quad (\text{B.13})$$

B.3 Inductance calculation

The strategy to calculate the inductance of the magnet is to divide the coil in two parts, the central part and the coil ends. In the central part the magnet can be considered as a 2D magnet and in the coil ends the magnetic flux is dominated by the 3D coil ends. This approach is valid because the inductance can be defined as a ratio between the magnetic flux and the current, according to equation B.14. ϕ is the magnetic flux produced by a magnet of N turns, therefore the total flux linkage is scaled by a factor of N. Qualitatively, every field line goes through the surface and is seen by the N turns.

Since the magnetic flux through a surface is the integral of the flux density through the area of the surface considered, the area can be divided as in figure B.4 and the magnetic flux can be calculated separately.

$$L = \frac{N\phi}{I} \quad (\text{B.14})$$

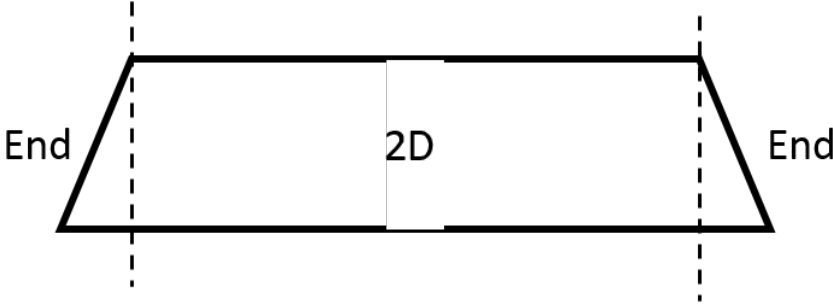


Figure B.4: Schematic of the coil partitioning for the inductance calculation (top view)

Then the inductance per unit length can be calculated from the 2D model. This value corresponds to the area marked as 2D in figure B.4.

The inductance can be calculated as the ratio between the total magnetic flux and the current [160, 161]. It is known that the magnetic field produced by a multiturn coil carrying a current I is proportional to $N \cdot I$, where N is the total number of turns. Additionally, the total magnetic flux through a surface that is interior to the coil is also proportional to the number of turns, making the inductance proportional to the square of the number of turns. This is clearly seen when calculating the inductance of a solenoid with N turns. Therefore it is possible to calculate the flux through a given surface from the Opera 2D simulation and then compute the inductance. The magnetic field calculated from Opera 2D is integrated along a line in the midplane and restricted to the extracted beam gap. The second dimension of the surface is perpendicular to the paper plane and therefore the inductance per metre will be calculated. This plane, including the field lines, is shown in figure B.5.

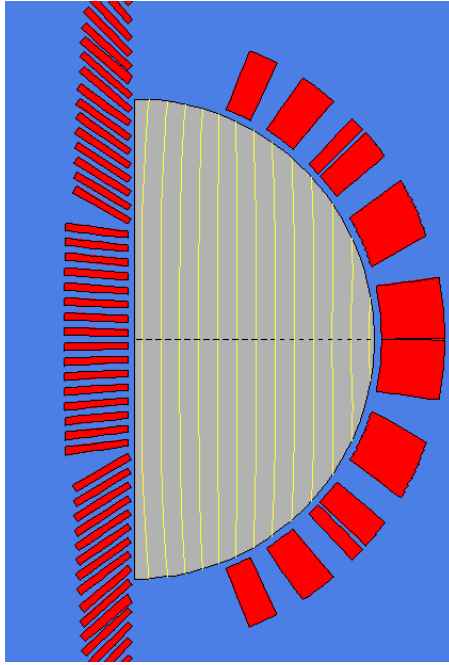


Figure B.5: Schematic of the flux integration for the inductance calculation

APPENDIX B. ANALYTICAL ESTIMATION STRESSES AND BRIEF DESCRIPTION OF THE FINITE ELEMENT VALIDATION

The result of the magnetic flux density integration provided by opera, which can be simplified as a multiplication, is $\phi=0.126$ Wb/m. The inductance is then given by equation B.14.

$$L = \frac{N\phi}{I} = \frac{62 \cdot 0.126}{6284} = 1.24 \text{ mH/m} \quad (\text{B.15})$$

As a comprobation, the inductance is calculated from the energy definition, according to equation 2.15 which has been reproduced here for convenience. The value of the current (I) is the current per cable which is 6284 A. The value calculated will then be the inductance per metre (L').

$$E = \frac{1}{2} L'_{2D} (I)^2 \quad (\text{B.16})$$

The value of the energy per meter calculated from the simulation in Opera 2D is 24072 J/m. Therefore the inductance per unit length calculated is 1.22 mH/m, which is in good agreement with the value obtained from the flux method.

To put this value into perspective, it is interesting to compare it with the inductance of an LHC main dipole, which has 82 turns per aperture. The inductance of an LHC dipole is approximately 100 mH, and the length is 14.3 m [4]. These values produce a result of almost 7 mH/m.

For simplicity, the inductance of the coil ends is calculated from the 3D model using the energy method. The energy is integrated and equation B.16 is solved. However, in this case the value of the energy is in Joules, not in Joules per metre, because the integration is performed in 3D. Besides, it is only possible to integrate the full volume of the model, but as explained in this section, the full magnet cannot be simulated in reasonable time and the central part of the model only represents the full magnet. Therefore, to isolate the contribution of the coil ends to the total inductance, the same scaling of the areas as in figure B.4 is done using the length of the coil end with respect to the total length of the coil in the model. It is not necessary to take into account this scaling in the coil width because this is taken into account by the integration of the energy. Finally, symmetry can be used for the integration or the energy can be integrated in the model and then multiplied by the required symmetry to obtain the total value. In the case of energy this may not be an issue but when the magnitudes integrated are vectors and the direction might change one needs to be very careful to avoid accidental cancellation or addition.

The model simulated in Opera is one quarter of the full model, therefore the value of energy obtained from the post processing will be a quarter of the total energy. In Opera it is possible to integrate the energy with a dedicated

command or to integrate the magnetic energy density in the model volume. They both produce the same result of 4290.7 J for a quarter of the energy. Therefore the total energy is 17162.8 J. It is crucial to keep in mind that the current in the 3D model is not 6284 A, as indicated in table 5.2. As has been explained earlier, the number of cables had to be reduced for the simulation to be solved. Therefore the current that has to be used for the calculation of the inductance is higher by a factor of $31/16$ to keep the NI product and, as a consequence, the magnetic field constant. The current that has to be used is then 12175.25 A and using equation B.16, the total inductance of the model is $231.6 \mu\text{H}$. Finally, to calculate the real inductance of the TCT septum one needs to scale the inductance of the model with the square of the ratio of the number of turns. The real inductance is then $869.4 \mu\text{H}$, which is $(31/16)^2$ times higher than the value obtained from the model.

Scaling the real inductance with the length following the reasoning of figure B.4 will produce the corresponding contribution of the coil ends to the magnetic flux. However, the length of every turn is different. The turns at the top of the coil are shorter and therefore contribute less but the cables closer to the mid plane contribute more. It is possible then to use a mean value and perform the calculations as if all turns had the average length. In this model, the coil ends start at a distance of 200 mm and the average total length of the turns is 352 mm. Therefore, the average coil end is 152 mm and the total inductance of $869.4 \mu\text{H}$ can be scaled with a ratio of $152/352$. The contribution of the coil ends to the inductance is then $375.4 \mu\text{H}$. This value corresponds to the contribution of both ends because the energy used in equation B.16 is the total energy of the magnet, not half.

Finally, it is possible to compute an average inductance per unit length of the magnet by adding the inductance per unit length of two coil ends and the contribution of the central part of the magnet. This value is interesting as a comparison with other magnets and as a guideline for future variants of the TCT septum which might be designed with different strengths and septum thickness for other accelerators. The inductance per unit length of both coil ends (L'_{ends}) can be obtained dividing the inductance by the corresponding length of both coil ends, which is 304 mm. Therefore the inductance per unit length of both coil ends is 1.23 mH/m , which is almost exactly the same as the value obtained from the 2D model. This indicates that the coil ends do not contribute significantly more than the central part to the total inductance and therefore in this case the inductance per unit length does not need to be added with respect to the corresponding lengths, simplifying the calculations.

For a magnetic length of 4 m, the total inductance would then be 4.92 mH.

Bibliography

- [1] *HL-LHC website*. <http://hilumilhc.web.cern.ch>. Accessed: 2018-08-09.
- [2] Apollinari G. et al. *High-Luminosity Large Hadron Collider (HL-LHC): Technical Design Report V. 0.1*. CERN Yellow Reports: Monographs. Geneva: CERN, 2017. URL: <http://cds.cern.ch/record/2284929>.
- [3] *Long term LHC schedule*. <https://lhc-commissioning.web.cern.ch/lhc-commissioning/schedule/HL-LHC-plots.htm>. Accessed: 2018-08-09.
- [4] O. Bruening et al. *LHC Design Report*. CERN Yellow Reports: Monographs. Geneva: CERN, 2004. URL: <https://cds.cern.ch/record/782076>.
- [5] M. et al. Benedikt. *Future Circular Collider - European Strategy Update Documents*. Tech. rep. CERN-ACC-2019-0007. Geneva: CERN, Jan. 2019. URL: <https://cds.cern.ch/record/2653673>.
- [6] M. McCullough. “Physics at FCC”. In: *FCC Week 2017*. 2017. URL: <https://indico.cern.ch/event/556692/contributions/2483388/attachments/1466429/2267366/FCCWeekBerlin.pdf>.
- [7] J. Ruderman. “(Un)known (un)knowns at the FCC”. In: *FCC Week 2018*. 2018. URL: <https://indico.cern.ch/event/656491/contributions/2932030/attachments/1628815/2595795/JoshUnknownKnown.pdf>.
- [8] M. Benedikt. “Future Circular Collider. Status and parameter update”. In: *FCC Week 2016*. 2016. URL: https://indico.cern.ch/event/438866/contributions/1085016/attachments/1255529/1853357/160411_FCC-Status_ap1.pdf.

-
- [9] D. Schulte. “FCC-hh Conceptual machine design, CDR status”. In: 2018. URL: https://indico.cern.ch/event/656491/contributions/2915543/attachments/1628701/2595429/Schulte_Amsterdam.pdf.
 - [10] The CEPC study group. *CEPC Conceptual Design Report*. Beijing: IHEP, 2018. URL: <https://arxiv.org/ftp/arxiv/papers/1809/1809.00285.pdf>.
 - [11] M J et al. Boland. *Updated baseline for a staged Compact Linear Collider*. Tech. rep. CERN-2016-004. CERN-2016-004. Comments: 57 pages, 27 figures, 12 tables. Geneva, Aug. 2016. URL: <https://cds.cern.ch/record/2210892>.
 - [12] The CEPC study group. *CEPC-SPPC progress report*. Beijing: IHEP, 2017. URL: <http://cepc.ihep.ac.cn/ProgressReport.pdf>.
 - [13] *ATLAS experiment webpage*. <https://atlas.cern/>. Accessed: 2018-10-4.
 - [14] *CMS experiment webpage*. <https://cms.cern/>. Accessed: 2018-10-4.
 - [15] *ALICE experiment webpage*. <http://alicematters.web.cern.ch/>. Accessed: 2018-10-4.
 - [16] *LHCb experiment webpage*. <http://lhcb-public.web.cern.ch/lhcb-public/>. Accessed: 2018-10-4.
 - [17] M. Benedikt et al. *FCC conceptual design report*. CERN, 2018.
 - [18] F. Zimmermann. “HE-LHC Machine overview”. In: 2018. URL: https://indico.cern.ch/event/656491/contributions/2915545/attachments/1628887/2596165/HE-LHC_Machine_Overview_-_Frank_Zimmermann_-_FINAL.pdf.
 - [19] M. Boscolo. “FCC-ee Machine overview”. In: 2018. URL: https://indico.cern.ch/event/656491/contributions/2915544/attachments/1628826/2595272/FCCee_Overview_Mboscolo_2.pdf.
 - [20] V. Mertens. “Civil engineering, infrastructure and operation”. In: 2018. URL: https://indico.cern.ch/event/656491/contributions/2915646/attachments/1628719/2595760/FCC_IO_Overview_Amsterdam_VM_090418.pdf.
 - [21] J. M. Jimenez. “Special technologies R&D overview”. In: 2018. URL: https://indico.cern.ch/event/656491/contributions/2915647/attachments/1628831/2595404/FCC_18_Amsterdam-WS_Special_Technologies_v1.0.pdf.

- [22] E. Wilson. *An Introduction to Particle Accelerators*. An Introduction to Particle Accelerators. Oxford University Press, 2001. ISBN: 9780198508298. URL: <https://books.google.fr/books?id=h0seyFa394C>.
- [23] C. Biscari. “Transverse beam dynamics”. In: *Proceedings of the African School of Physics*. 2014. URL: https://indico.cern.ch/event/528094/contributions/2213316/attachments/1322590/1984069/L3-4-5_-_Transverse_Beam_Dynamics.pdf.
- [24] *CERN Accelerator School: general accelerator physics*. CERN. Geneva: CERN, 1987. URL: <https://cds.cern.ch/record/181071>.
- [25] J L Abelleira. “Optics Designs of Final-Focus Systems for Future LHC Upgrades”. Presented 18 Feb 2014. Dec. 2014. URL: <https://cds.cern.ch/record/1742041>.
- [26] M. J. et al. Barnes. “Injection and extraction magnets: septa”. In: *Proceedings, 2009 CAS-CERN Accelerator School: Specialised course on Magnets: Bruges, Belgium, June 16 - 25, 2009*. 2011. arXiv: 1103.1062 [physics.acc-ph]. URL: <https://inspirehep.net/record/891637/files/arXiv:1103.1062.pdf>.
- [27] Janet Susan Schmidt. “Beam injection, extraction and transfer”. In: *Proceedings, CAS-CERN Accelerator School: Introduction to accelerator physics*. 2017. URL: https://indico.cern.ch/event/575505/contributions/2398939/attachments/1403032/2153052/CAS17_InjectionAndExtraction.pdf.
- [28] A. Lechner. “FCC-hh protection absorbers and dumps”. In: *FCC Week 2018*. 2018. URL: https://indico.cern.ch/event/656491/contributions/2930779/attachments/1629787/2597491/2018_10_04_fccabsorbersdump.pdf.
- [29] P. Osmokrovic. “Influence of switching operations on the vacuum interrupter dielectric strength”. In: *IEEE Transactions on Power Delivery* 8.1 (Jan. 1993), pp. 175–181. ISSN: 0885-8977. DOI: 10.1109/61.180334.
- [30] P. Osmokrovic et al. “Stochastic Nature of Electrical Breakdown in Vacuum”. In: *IEEE Transactions on Dielectrics and Electrical Insulation* 14.4 (Aug. 2007), pp. 803–812. ISSN: 1070-9878. DOI: 10.1109/TDEI.2007.4286510.

-
- [31] D. Ilic et al. "Mechanisms of electrical breakdown in low vacuums". In: *Scientific publications of the State University of Novi Pazar Series A: Applied mathematics, informatics and mechanics* 3.2 (Apr. 2011), pp. 85–99.
 - [32] L.N. Blumberg and F. Krausz. "Electrostatics and beam losses for a wire array septum". In: *Internal report, Accelerator department, Brookhaven National Laboratory* (1971).
 - [33] Y. Arakaki et al. "Electrostatic septum for 50 GeV proton synchrotron in J- PARC". In: *Proceedings of IPAC '10, Kyoto, Japan* (2010).
 - [34] Charles E. Edouard. "INVAR and ELINVAR". In: *Nobel Lectures* (1920).
 - [35] R. Oberli R.L. Keizer. "The construction of electrostatic septa with INVAR anodes and ultra-thin wires". In: 1986.
 - [36] R. Dubois et al. "SPS improvement report 196. Electrostatic tests in LSS6 with improved ion traps". In: 1982.
 - [37] Y. Baconnier et al. "Extraction from the CERN SPS". In: *CERN-SPS/ABT/77-4* (1977).
 - [38] X. Altuna et al. "Performance test of the electrostatic septum on 19-11-79". In: *SPS Improvement report No. 168* (1979).
 - [39] R. Dubois et al. "Electrostatic septum tests in LSS6 with improved ion traps". In: *SPS Improvement report No. 196* (1982).
 - [40] Y. Baconnier et al. "Improvement of the extraction channels of the CERN SPS accelerator". In: vol. 3. 1987, p. 1836.
 - [41] J Borburgh, M Hourican, and M Thivent. "Consolidation project of the electrostatic septa in the CERN PS ring". In: CERN-PS-2001-024-PO (June 2001), 5 p. URL: <https://cds.cern.ch/record/505714>.
 - [42] A. Carnicero et al. *Elasticidad y resistencia de materiales. Ingenieros industriales, tercer curso. Formulario de vigas*. https://www.iit.comillas.edu/carnicero/resistencia_materiales/formulario_vigas.pdf. Notes of course: elasticity and materials resistance. MsEng. Electromechanical engineering, ICAI, Madrid.
 - [43] Keith D. Hjelmstad. *Fundamentals of structural mechanics*. English (US). Springer US, 2005. ISBN: 038723330X. DOI: 10.1007/b101129.
 - [44] D. Roylance. *Mechanics of materials*. MIT Open Courseware, 2000. ISBN: 0-471-59399-0. URL: <http://web.mit.edu/course/3/3.11/www/modules/fatigue.pdf>.

- [45] M. Modena et al. “High current density septum prototype for Accumulator and storage rings of DAFNE, the Frascati F-Factory”. In: *4th EPAC* (1994), p. 2304.
- [46] M. Modena et al. “The injection/extraction 2 degrees septum magnets of the DAFNE Accumulator”. In: *DAFNE technical note* (1995).
- [47] R. Billinge and M. C. Crowley-Milling. “The CERN Proton-Antiproton Colliding Beam Facilities”. In: *IEEE Transactions on Nuclear Science* 26.3 (June 1979), pp. 2974–2977. ISSN: 0018-9499. DOI: 10.1109/TNS.1979.4329913.
- [48] G. Brianti. “Experience with the CERN pp complex”. In: *IEEE Transactions on Nuclear Science* 30.4 (Aug. 1983), pp. 1950–1956. ISSN: 0018-9499. DOI: 10.1109/TNS.1983.4332685.
- [49] K. Einsweiler and A. Weidberg. “Standard Model parameters from UA1 and UA2”. In: *CERN-EP/88-152* (Oct. 1988).
- [50] Niels Madsen. “Cold antihydrogen: a new frontier in fundamental physics”. In: *Philosophical Transactions of the Royal Society of London A: Mathematical, Physical and Engineering Sciences* 368.1924 (2010), pp. 3671–3682. ISSN: 1364-503X. DOI: 10.1098/rsta.2010.0026. URL: <http://doi.org/10.1098/rsta.2010.0026>.
- [51] W. Oelert. “The ELENA project at CERN”. In: *Acta Phys. Polon.* B46.1 (2015), pp. 181–189. DOI: 10.5506/APhysPolB.46.181. arXiv: 1501.05728 [physics.acc-ph].
- [52] K. Fan et al. “Design study of a very large aperture eddy current septum for J-PARC”. In: *2007 IEEE Particle Accelerator Conference (PAC)*. June 2007, pp. 224–226. DOI: 10.1109/PAC.2007.4440166.
- [53] M Kikuchi et al. “Beam-transport system of KEKB”. In: *Nuclear Instruments and Methods in Physics Research Section A: Accelerators, Spectrometers, Detectors and Associated Equipment* 499.1 (2003). KEK-B: The KEK B-factory, pp. 8–23. ISSN: 0168-9002. DOI: [http://dx.doi.org/10.1016/S0168-9002\(02\)01785-0](http://dx.doi.org/10.1016/S0168-9002(02)01785-0). URL: <http://www.sciencedirect.com/science/article/pii/S0168900202017850>.
- [54] D. Shuman et al. “Stray Field Reduction of ALS Eddy Current Septum Magnets”. In: *Proceedings of the 2005 Particle Accelerator Conference*. May 2005, pp. 3718–3720. DOI: 10.1109/PAC.2005.1591593.
- [55] *Parametres principaux de l’anneau de stockage Description*. <http://www.synchrotron-soleil.fr/portal/page/portal/SourceAccelérateur/ParametresPrincipaux>. Accessed: 2017-02-14.

-
- [56] P. et al. Lebasque. “Eddy current septum magnets for booster injection and extraction and storage ring injection at synchrotron SOLEIL”. In: *Conf. Proc. C060626* (2006). [,3511(2006)], pp. 3511–3513.
- [57] Z. Szoke et al. “Direct Drive and Eddy Current Septa Magnet Designs for CERN PSB Extraction at 2 GeV”. In: *IEEE Transactions on Applied Superconductivity* 26.4 (June 2016), pp. 1–5. ISSN: 1051-8223. DOI: 10.1109/TASC.2016.2522189.
- [58] M. Serluca J. Abelleira. “PS Injection septum position and injection bump at 2 GeV”. In: *EDMS No. 1557577* (2016).
- [59] J. Abelleira et al. “SPECIFICATION FOR THE 2 GEV PS PROTON INJECTION SEPTA”. In: *EDMS No. 1477011* (2016).
- [60] COMET Collaboration. “COMET Phase-I. Technical design report”. In: (2014). URL: http://comet.kek.jp/Documents_files/IPNS-Review-2014.pdf.
- [61] R. Muto et al. “Development of Lambertson Magnet and Septum Magnets for Splitting 30-GeV Proton Beam in Hadron Experimental Facility at J-PARC”. In: *IEEE Transactions on Applied Superconductivity* 26.4 (June 2016), pp. 1–4. ISSN: 1051-8223.
- [62] A. Sanz Ull et al. “The LHC MSD septa at 7.5 TeV”. In: *EDMS No. 1736186* (2016).
- [63] M. Gyr. “Expected magnetic field quality of the LHC septum magnets used for injection (MSI) and for extraction to the beam dump (MSD)”. In: *LHC project note 129* (1999).
- [64] P. Leclerc D. Cornuet J. Dutour. “Technical specification: The steel septum magnets for the LHC injection and beam dumping system”. In: *CERN Ref: SL-Spec-98-31 MS* (1998).
- [65] P. Leclerc D. Cornuet J. Dutour. “Magnetic measurements of the steel septum magnet used for extraction: MSDC 01”. In: *LHC project note 285* (2002).
- [66] Y. Yonemura et al. “Beam extraction of the PoP FFAG with a massless septum”. In: *Particle Accelerator Conference, 2003. PAC 2003. Proceedings of the*. Vol. 3. May 2003, 1679–1681 vol.3. DOI: 10.1109/PAC.2003.1288634.
- [67] Y Iwashita and Noda. “Massless septum with hybrid magnet”. In: (1998).

- [68] A. Vorozhtsov et al. “Design and Manufacture of a Hybrid Final Focus Quadrupole Model for CLIC”. In: *IEEE Transactions on Applied Superconductivity* 22.3 (June 2012), p. 4000604. ISSN: 1051-8223. DOI: 10.1109/TASC.2011.2182023.
- [69] L. Wang et al. “A prototype dipole septum magnet for fast high current kicker systems”. In: *Proceedings of the 1999 Particle Accelerator Conference (Cat. No.99CH36366)*. Vol. 5. 1999, 3381–3383 vol.5. DOI: 10.1109/PAC.1999.792310.
- [70] I. Sakai et al. “Opposite Field Septum Magnet System for the Separation of Charged Particle Beams”. In: *IEEE Transactions on Applied Superconductivity* 12.1 (Mar. 2002).
- [71] T. Kawakubo et al. “Permanent Magnet Generating High and Variable Septum Magnetic Field and its Deterioration by Radiation”. In: *9th European Particle Accelerator Conference (EPAC 2004) Lucerne, Switzerland, July 5-9, 2004*. 2004. URL: <http://accelconf.web.cern.ch/AccelConf/e04/PAPERS/WEPKF041.PDF>.
- [72] A. Yamamoto et al. “The superconducting inflector for the BNL g-2 experiment”. In: *Nucl. Instrum. Meth.* A491 (2002), pp. 23–40. DOI: 10.1016/S0168-9002(02)01232-9.
- [73] M. Tomizawa et al. “Design of slow extraction from 50-GeV proton synchrotron”. In: *Conf. Proc.* C0206031 (2002). [1058(2002)], pp. 1058–1060.
- [74] K. Sugita. “Design status of a high field superconducting magnet”. In: *FCC Week 2017*. 2017. URL: <https://indico.cern.ch/event/556692/contributions/2488389/attachments/1466268/2271498/Sc-Septum-GSI.pdf>.
- [75] E. Fischer et al. “Design studies for a fast ramped high field superconducting septa”. In: *FCC Week 2016*. 2016. URL: https://indico.cern.ch/event/438866/contributions/1085009/attachments/1257884/1857713/FCC-2016_ScSepta_ID86.pdf.
- [76] J. Grange et al. “Muon (g-2) Technical Design Report”. In: (2015). arXiv: 1501.06858 [physics.ins-det].
- [77] P. McIntyre et al. “Stealth Superconducting Magnet Technology for Collider IR and Injector Requirements”. In: *PP* (Feb. 2018), pp. 1–1.
- [78] C. P. Bean. “Magnetization of Hard Superconductors”. In: *Phys. Rev. Lett.* 8 (6 Mar. 1962), pp. 250–253. DOI: 10.1103/PhysRevLett.8.250. URL: <https://link.aps.org/doi/10.1103/PhysRevLett.8.250>.

-
- [79] D. Barna et al. “First experimental results with the SuShi septum prototypes”. In: 2017. URL: <https://indico.cern.ch/event/556692/contributions/2488390/attachments/1468982/2272308/barna-sushi.pdf>.
- [80] M. Novak et al. “Numerical and experimental studies of the magnetic shielding performance of an MgB2 tube for the superconducting shield septum project”. In: *FCC Week 2018*. 2018. URL: https://indico.cern.ch/event/656491/contributions/2915680/attachments/1628656/2594831/FCCWeek_poster.pdf.
- [81] A M Campbell. “A new method of determining the critical state in superconductors”. In: *Superconductor Science and Technology* 20.3 (2007), p. 292. URL: <http://stacks.iop.org/0953-2048/20/i=3/a=031>.
- [82] D. Barna et al. “Superconducting Shield (SuShi) septum: towards a full prototype”. In: 2018. URL: <https://indico.cern.ch/event/656491/contributions/2947265/attachments/1630674/2599275/barna-sushi-fcc-week-amsterdam.pdf>.
- [83] M. Novak. “Numerical and experimental study of superconducting magnetic shields for the construction of a high field septum magnet”. MA thesis. Budapest, Hungary: Eotvos Lorand University, 2018. URL: <https://wigner.mta.hu/~barna/content/Publications/DiplomaThesis-MartinNovak.pdf>.
- [84] S. Fartoukh. “A semi-analytical method to generate an arbitrary 2D magnetic field and determine the associated current distribution”. In: *LHC project report 1012* (2007).
- [85] A. Sanz Ull. “Septa considered for the FCC-hh beam dump system”. In: *FCC Week 2017*. 2017. URL: https://indico.cern.ch/event/556692/contributions/2488376/attachments/1466298/2272322/High_field_massless_septa_for_the_FCC-hh_beam.pdf.
- [86] A. Sanz Ull. “High field massless septa”. In: *FCC Week 2018*. 2018. URL: https://indico.cern.ch/event/656491/contributions/2947266/attachments/1628552/2597083/Alex_FCCweek2018_Massless_again.pdf.
- [87] A. Sanz Ull et al. “Comparison of superconducting septa topologies and parameter space exploration”. In: *Proceedings of IPAC 18* (May 2018).
- [88] *Report on the design study of Intersecting Storage Rings (ISR) for the CERN proton synchrotron*. French version available. Geneva: CERN, 1964. URL: <https://cds.cern.ch/record/110073>.

- [89] M. Hub. “Measuring machine and results of the magnetic measurements for the steel septum magnets for ISR injection”. In: *ISR/BT/71-19* (1971).
- [90] S et al. Bidon. “Steel septum magnets for the LHC beam injection and extraction”. In: CERN-SL-2002-019-MS (June 2002), 4 p. URL: <http://cds.cern.ch/record/565886>.
- [91] P. Leclerc D. Cornuet J. Dutour. “Magnetic measurements of the steel septum magnet used for injection: MSIB01”. In: *LHC project note 280* (2002).
- [92] P. Leclerc D. Cornuet J. Dutour. “Magnetic measurements of the steel septum magnet used for injection: MSDC01”. In: *LHC project note 280* (2002).
- [93] O. Bruening et al. *LHC Design Report. Beam dump system*. Geneva: CERN, 2004. URL: https://edms.cern.ch/ui/file/445871/5/Vol_1_Chapter_17.pdf.
- [94] Henry A. Rowland. “XIV. On magnetic permeability, and the maximum of magnetism of iron, steel, and nickel”. In: *Philosophical Magazine Series 4* 46.304 (1873), pp. 140–159. DOI: 10.1080/14786447308640912. eprint: <http://iom3.tandfonline.com/doi/pdf/10.1080/14786447308640912>. URL: <http://iom3.tandfonline.com/doi/abs/10.1080/14786447308640912>.
- [95] Edward M. Purcell. *Electricidad y magnetismo. Berkeley physics course-volume 2*. Reverte, 1988.
- [96] Various authors. *Opera 2D Reference Manual*. VectorFields, 2016.
- [97] G. H. Biallas et al. “Combined panofsky quadrupole corrector dipole”. In: *2007 IEEE Particle Accelerator Conference (PAC)*. June 2007, pp. 602–604. DOI: 10.1109/PAC.2007.4440292.
- [98] R. Hoard et al. “Field enhancement of a 12.5-T magnet using holmium poles”. In: *IEEE Transactions on Magnetics* 21.2 (Mar. 1985), pp. 448–450. ISSN: 0018-9464. DOI: 10.1109/TMAG.1985.1063692.
- [99] J. W. Kim, K. W. Shepard, and J. A. Nolen. “A high gradient superconducting quadrupole for a low charge state ion linac”. In: *Proceedings Particle Accelerator Conference*. Vol. 3. May 1995, 1408–1410 vol.3. DOI: 10.1109/PAC.1995.505238.

-
- [100] W. Schauer and F. Arendt. “Field enhancement in superconducting solenoids by holmium flux concentrators”. In: *Cryogenics* 23.10 (1983), pp. 562–564. ISSN: 0011-2275. DOI: [http://dx.doi.org/10.1016/0011-2275\(83\)90198-4](http://dx.doi.org/10.1016/0011-2275(83)90198-4). URL: <http://www.sciencedirect.com/science/article/pii/0011227583901984>.
- [101] Animesh K. Jain. *Basic theory of magnets. CERN 98-05. Proc. CERN Accelerator School on Measurement and Alignment of Accelerator and Detector Magnets, April 11-17, 1997, Anacapri, Italy*. Feb. 1998.
- [102] Nicholas J. Sammut et al. “Mathematical formulation to predict the harmonics of the superconducting Large Hadron Collider magnets. II. Dynamic field changes and scaling laws”. In: *Phys. Rev. ST Accel. Beams* 10 (8 Aug. 2007), p. 082802. DOI: 10.1103/PhysRevSTAB.10.082802. URL: <https://link.aps.org/doi/10.1103/PhysRevSTAB.10.082802>.
- [103] A. Sanz Ull. “Note on the application of Fartoukh’s algorithm”. In: *TE-ABT Internal note* (2016).
- [104] Patricio A. A. Laura Roland Schinzinger. *Conformal mapping: Methods and applications*. 2003.
- [105] Lloyd N. Trefethen Tobin A. Driscoll. *Schwarz-Christoffel Mapping. Cambridge monographs on applied and computational mathematics*. Cambridge University Press, 2002.
- [106] Tobin A. Driscoll. *Schwarz-Christoffel Toolbox User’s Guide. Version 2.3*. Mathworks Inc., 2003.
- [107] A. Vorozhtsov et al. “Design, manufacture and measurements of permanent dipole magnets for DIRAC”. In: *DIRAC note 2013-04* (2013).
- [108] M. Modena A. Bartalesi R. Chritin. “Experimental Test to determine the Magnet Reversible Temperature Coefficient for a Permanent Magnet Quadrupole”. In: *EDMS No. 1240879* (2012).
- [109] Liverpool University and VectorFields. *Manufacturer’s data for a Samarium-Cobalt permanent magnet block*. Opera 18 material data.
- [110] J. A. Clarke et al. “Novel Tunable Permanent Magnet Quadrupoles for the CLIC Drive Beam”. In: *IEEE Transactions on Applied Superconductivity* 24.3 (June 2014), pp. 1–5. ISSN: 1051-8223. DOI: 10.1109/TASC.2013.2289357.
- [111] H. Padamsee et al. *RF superconductivity for accelerators*. Wiley series in beam physics and accelerator technology. New York, NY: Wiley, 1998. URL: <https://cds.cern.ch/record/366783>.

- [112] John Byrd. “Resonant cavities”. In: *USPAS 2009*. June 2009.
- [113] F. Caspers and M. Wendt. “Cavity structures”. In: *JUAS 2018*. Jan. 2018. URL: https://indico.cern.ch/event/683638/contributions/2801789/attachments/1563556/2535357/JUAS2018_RF_lecture.pdf.
- [114] Various authors. *Opera 3D Reference Manual*. VectorFields, 2016.
- [115] E. Renner. “FCC-hh: Transfer lines and injection protection”. In: 2018. URL: https://indico.cern.ch/event/719245/contributions/2956322/attachments/1626410/2595063/Renner_FCC_week_2018_InjTransfer.pdf.
- [116] M.N. Wilson. *Superconducting magnets*. Monographs on cryogenics. Clarendon Press, 1983. ISBN: 9780198548102. URL: <https://books.google.fr/books?id=A0bvAAAAMAAJ>.
- [117] Stephan Russenschuck. *Field computation for accelerator magnets: analytical and numerical methods for electromagnetic design and optimization*. Weinheim: Wiley, 2010. URL: <https://cds.cern.ch/record/1221810>.
- [118] K H Mess, P Schmüser, and S Wolff. *Superconducting Accelerator Magnets*. Singapore: World Scientific, 1996. URL: <https://cds.cern.ch/record/354571>.
- [119] F. Krienen, D. Loomba, and W. Meng. “The Truncated double cosine theta superconducting septum magnet”. In: *Nucl. Instrum. Meth.* A283 (1989), pp. 5–12. DOI: 10.1016/0168-9002(89)91249-7.
- [120] E. Fischer et al. “Superconducting septa and fast ramped cosine-theta magnets”. In: *FCC Week 2015*. 2015. URL: https://indico.cern.ch/event/340703/contributions/802239/attachments/668821/919340/FCC_SC_Septa-FRM_EF_ID48.pdf.
- [121] S. Wolff. “Superconducting accelerator magnet design”. In: *AIP Conference Proceedings* 249.2 (1992), pp. 1159–1197. DOI: 10.1063/1.41989. URL: <https://aip.scitation.org/doi/abs/10.1063/1.41989>.
- [122] G. A. Kirby et al. “Hi-Lumi LHC Twin-Aperture Orbit Correctors Magnet System Optimisation”. In: *IEEE Transactions on Applied Superconductivity* 27.4 (June 2017), pp. 1–5. ISSN: 1051-8223. DOI: 10.1109/TASC.2016.2633424.
- [123] L.N. Brouwer. “Canted-Cosine-Theta Superconducting Accelerator Magnets for High Energy Physics and Ion Beam Cancer Therapy”. PhD thesis. University of California, Berkeley, 2015.

-
- [124] G. Montenero et al. “Mechanical Structure for the PSI Canted-Cosine-Theta (CCT) Magnet Program”. In: *IEEE Transactions on Applied Superconductivity* 28.3 (Apr. 2018), pp. 1–5. ISSN: 1051-8223. DOI: 10.1109/TASC.2017.2787596.
- [125] *Roxie homepage Description*. <https://espace.cern.ch/roxie/default.aspx>. Accessed: 2018-07-14.
- [126] Mushield. *Cryoperm properties*. <https://www.mushield.com/material-sales/cryoperm/>. Accessed on 3-8-2018.
- [127] Mika Masuzawa et al. “Magnetic Shielding: Our experience with various shielding materials”. In: Proceedings of the 16th International Conference on RF Superconductivity.
- [128] . Comments: 23 lectures, 592 pages, published as CERN Yellow Report <https://cds.cern.ch/record/1507630?ln=en>. CERN. Geneva: CERN, 2014. URL: <https://cds.cern.ch/record/1507630>.
- [129] D. Schoerling and S. Izquierdo Bermudez. *Margin in 16 T dipole magnets*. https://indico.cern.ch/event/516049/contributions/2029293/attachments/1270273/1883761/MarginDipoles_Final-EuroCirColReview.pdf. First review of the EuroCirCol WP5.
- [130] D. Schoerling et al. *CONSIDERATIONS ON A COST MODEL FOR HIGH-FIELD DIPOLE ARC MAGNETS FOR FCC*. https://indico.cern.ch/event/536750/contributions/2181089/attachments/1317762/1995811/Cost_Paper.pdf. Cost estimate EuroCirCol collaboration meeting 05.
- [131] E. D. et al. Marquardt. “Cryogenic Material Properties Database”. In: *Cryocoolers 11*. Boston, MA: Springer US, 2002, pp. 681–687. ISBN: 978-0-306-47112-4. DOI: 10.1007/0-306-47112-4_84. URL: https://doi.org/10.1007/0-306-47112-4_84.
- [132] Copper development association Inc. *104/5: Low-Temperature Properties of Coppers and Copper Alloys*. <https://www.copper.org/resources/properties/cryogenic/>.
- [133] P Duthil. “Material Properties at Low Temperature”. In: *Proceedings, CAS - CERN Accelerator School : Course on Superconductivity for Accelerators (CAS 2013): Erice, Italy, April 24-May 4, 2013*. 2014, pp. 77–95. DOI: 10.5170/CERN-2014-005.77. arXiv: 1501.07100 [physics.acc-ph]. URL: <https://inspirehep.net/record/1341650/files/arXiv:1501.07100.pdf>.

- [134] J Sas et al. “The Mechanical and material properties of 316LN austenitic stainless steel for the fusion application in cryogenic temperatures”. In: *IOP Conference Series: Materials Science and Engineering* 102.1 (2015), p. 012003. URL: <http://stacks.iop.org/1757-899X/102/i=1/a=012003>.
- [135] F Bertinelli et al. “Production of Austenitic Steel for the LHC Superconducting Dipole Magnets”. In: *IEEE Trans. Appl. Supercond.* 16.LHC-PROJECT-Report-892. CERN-LHC-Project-Report-892 (May 2006), 1773–1776. 5 p. URL: <https://cds.cern.ch/record/970389>.
- [136] Bernhard Auchmann and Stephan Russenschuck. “Coil End Design for Superconducting Magnets Applying Differential Geometry Methods”. In: 40 (Apr. 2004).
- [137] B Auchmann, Stephan Russenschuck, and N Schwerg. “Discrete Differential Geometry Applied to the Coil-End Design of Superconducting Magnets”. In: *IEEE Trans. Appl. Supercond.* 17.2 (2007), pp. 1165–1168. URL: <http://cds.cern.ch/record/1102023>.
- [138] Romulo Chumacero. *Solving nonlinear equations*. https://www.researchgate.net/profile/Romulo_Chumacero/publication/265633573_Solving_Nonlinear_Equations/links/556e350708aec2268308c3d3/Solving-Nonlinear-Equations.pdf. Universidad de Chile. Notes of Econometria 1 undergrad course.
- [139] Richard Barrett et al. *Templates for the solution of Linear Systems: Building blocks of iterative methods*. SIAM, 1933. ISBN: 9780898713282. URL: <http://bookstore.siam.org/ot43/>.
- [140] Z. Charifouline. “Residual Resistivity Ratio (RRR) Measurements of LHC Superconducting NbTi Cable Strands”. In: *IEEE Transactions on Applied Superconductivity* 16.2 (June 2006), pp. 1188–1191. ISSN: 1051-8223. DOI: 10.1109/TASC.2006.873322.
- [141] M Eisterer. “Magnetic properties and critical currents of MgB₂”. In: *Superconductor Science and Technology* 20.12 (2007), R47. URL: <http://stacks.iop.org/0953-2048/20/i=12/a=R01>.
- [142] Gerald J. Lieberman Frederick S. Hillier. *Introduction to Operations Research*. McGraw-Hill, 2010.
- [143] E. Renner. “FCC-hh: extraction and dilution kicker”. In: 2018. URL: https://indico.cern.ch/event/656491/contributions/2947271/attachments/1631682/2601592/Renner_FCC_week_2018_ExtDil_Kicker.pdf.

-
- [144] L Rossi. “State-of-the-art superconducting accelerator magnets”. In: *IEEE Trans. Appl. Supercond.* 12.LHC-Project-Report-541. CERN-LHC-Project-Report-541. 1 (Mar. 2002), 219–227. 9 p. URL: <https://cds.cern.ch/record/592967>.
- [145] Chiara Bracco. “Injection: Hadron beams”. In: *Proceedings, CAS-CERN Accelerator School: Beam injection, extraction and transfer*. 2017. URL: https://indico.cern.ch/event/451905/contributions/2159032/attachments/1425216/2188137/CAS_ERICE_Hadrons_Injection.pdf.
- [146] Massimo Ferrario. “Recapitulation of relativity and space charge”. In: *Proceedings, CAS-CERN Accelerator School: Beam injection, extraction and transfer*. 2017. URL: <https://indico.cern.ch/event/451905/contributions/2159029/attachments/1426144/2190031/Ferrario.ppt.pdf>.
- [147] Verena Kain. “Emittance preservation”. In: *Proceedings, CAS-CERN Accelerator School: Beam injection, extraction and transfer*. 2017. URL: https://indico.cern.ch/event/451905/contributions/2159070/attachments/1423256/2191040/EmittancePreservation_v1.pdf.
- [148] Various authors. *CAS Third general accelerator physics course. Chapter 3*. CERN, 1988.
- [149] D. Missiaen. “Alignment and metrology- requirements and realisation”. In: *Proceedings, CAS-CERN Accelerator School: Beam dynamics and technologies for future colliders*. 2018. URL: <https://cas.web.cern.ch/sites/cas.web.cern.ch/files/lectures/zurich-2018/surveyalignment.pdf>.
- [150] F. Zimmermann et al. “Beam dynamics issues in the FCC”. In: (July 2016). the paper from the HB2016 workshop provided by Frank Zimmermann. URL: <http://cds.cern.ch/record/2200293>.
- [151] Florian Burkart. Private communication. 2017.
- [152] Helmut Wiedemann. *Particle accelerator physics; 3rd ed*. Berlin: Springer, 2007. URL: <https://cds.cern.ch/record/1083415>.
- [153] P. Frey. *Numerical simulations of PDE problems*. Seminario avanzado de matematicas I. New York, NY: Universidad de Chile, 2008. URL: https://www.ljll.math.upmc.fr/frey/cours/UdC/ma691/ma691_ch6.pdf.

- [154] D. Roylance. *Mechanics of materials*. MIT Open Courseware, 2000. ISBN: 0-471-59399-0. URL: <http://web.mit.edu/course/3/3.11/www/modules/const.pdf>.
- [155] Thomas Hawkins. “Cauchy and the spectral theory of matrices”. In: *Historia Mathematica* 2.1 (1975), pp. 1–29. ISSN: 0315-0860. DOI: [https://doi.org/10.1016/0315-0860\(75\)90032-4](https://doi.org/10.1016/0315-0860(75)90032-4). URL: <http://www.sciencedirect.com/science/article/pii/0315086075900324>.
- [156] Jose Luis Blanco Caraco et al. *Analisis estatico de estructuras por el metodo matricial*. PUBLIDISA, 2012. ISBN: 978-84-9747-448-1. URL: http://ingmec.ual.es/~jlblanco/papers/blanco2012calculo_matricial_estructuras.pdf.
- [157] R. W. D. Nickalls. “Viète, Descartes and the Cubic Equation”. In: *The Mathematical Gazette* 90.518 (2006), pp. 203–208. ISSN: 00255572. URL: <http://www.jstor.org/stable/40378607>.
- [158] *Cubic functions. Trigonometric solution for three real roots*. https://en.wikipedia.org/wiki/Cubic_function#Trigonometric_solution_for_three_real_roots. Accessed: 2018-08-22.
- [159] *Principal Stresses in Two and Three Dimensions*. https://en.wikiversity.org/wiki/Introduction_to_Elasticity/Principal_stresses. Accessed: 2018-08-22.
- [160] John David Jackson. *Classical electrodynamics; 2nd ed.* New York, NY: Wiley, 1975. URL: <https://cds.cern.ch/record/100964>.
- [161] H. Knoepfel. *Magnetic Fields: A Comprehensive Theoretical Treatise for Practical Use*. A Wiley-Interscience publication. Wiley, 2000. ISBN: 9780471322054. URL: <https://books.google.fr/books?id=1n7NPasgh0sC>.

Curriculum Vitae

Alejandro Sanz Ull was born on the 23rd of January, 1989 in Madrid, Spain.

After finishing his high school degree in 2007 at Colegio Nuestra Señora de las Maravillas in Madrid, Spain, he studied Electrical and Mechanical Engineering at ICAI- Universidad Pontificia Comillas in Madrid, Spain. In 2013 he graduated within the Electric Power Systems with a Master Thesis on the design and implementation of the load-frequency control in a synchronous generator. From 2014 to 2016 he worked as an engineer in the CERN Magnet Group where he had the opportunity to work on magnetic design of normal conducting and superconducting magnet and cooling, fatigue and radiation hardness studies. In 2016 he started a PhD project titled “Optimized design of magnetic septa for the Future Circular Collider”, of which the results are presented in this dissertation. The project was carried out in the CERN Septa section and it was supervised jointly by ir. Jan Borburgh, at CERN, and prof.dr.ir. O.J. Luiten at Technische Universiteit Eindhoven.

Publication list

IPAC 2019

- Alternative proposal for FCC-hh extraction septa. **Primary Author.** To be published.
- Upgrade limitations for LHC Lambertson septa for FCC. **Primary Author.** To be published.

IPAC 2018

- Comparison of superconducting septa topologies and parameter space exploration. **Primary Author.**
<http://ipac2018.vrws.de/papers/wepmf083.pdf>
- Validation of the CERN PS Eddy Current Injection Septa. Co-Author.
<http://accelconf.web.cern.ch/AccelConf/ipac2018/papers/tupaf037.pdf>

In preparation

- *"Conceptual design of a high-field septum magnet using a superconducting shield and a canted cosine-theta magnet"*, by Daniel Barna, Martin Novák, Kristóf Brunner, Glyn Kirby, Brennan Goddard, Jan Borburgh, Miroslav Atanasov, Alejandro Sanz Ull, Elisabeth Renner, Wolfgang Bartmann, and Marcell Szakaly

Presentations in conferences

FCC Week 2018

- High field normal conducting massless septa for FCC beam transfer. **Primary author.**
https://indico.cern.ch/event/656491/contributions/2947266/attachments/1628552/2597083/Alex_FCCweek2018_Massless_again.pdf
- Status of truncated cosine-theta septum magnet study. **Presentation** by K. Sugita, **Primary author.**
<https://indico.cern.ch/event/656491/contributions/2938824/attachments/1628601/2596776/FCC18-GSI-CERN-3AMS17C-KS.pdf>
- Numerical and experimental studies of the magnetic shielding performance of an MgB₂ tube for the superconducting shield septum project. **Poster,** co-author.
https://indico.cern.ch/event/656491/contributions/2915680/attachments/1628656/2594831/FCCWeek_poster.pdf

FCC Week 2017

- Septa considered for the FCC-hh beam dump system. **Presentation, primary author.**
https://indico.cern.ch/event/556692/contributions/2488376/attachments/1466298/2272322/High_field_massless_septa_for_the_FCC-hh_beam.pdf
- First experimental results with the SuShi septum prototypes. **Presentation, co-author.**
<https://indico.cern.ch/event/556692/contributions/2488390/attachments/1468982/2272308/barna-sushi.pdf>

Opera EUGM 2016

- Design of an eddy current septum outside of the standard parameter range and current distribution on a conductor. **Presentation, primary author.**
http://bit.ly/Opera_EUGM_2016

Acknowledgements

I want to thank my CERN supervisors, Jan and Miro. Not only for their help with this thesis but for making my time in the Septa section amazing, both professionally and personally. I want to thank Wolfgang for his guidance and support and his patience with my many questions. You have all taught me a lot, about septa and many other topics. I would also like to thank Jom for his support and guidance, always reachable and willing to dedicate all the necessary time despite of being in another country and very busy. This is also extensible to Betty, for all her help with University related issues and to Jim, who answered all my questions very quickly and was very helpful.

I also want to thank Ole and the rest of the Septa section for their human quality, Bruno, Louise, Antoine, Cédric, Thierry, Mike, Patrick, Robert, Henrik, Torstein, Fabrice and James. I have been really lucky to work with all of you, thanks to you I went to work with a smile every day. Many other people also contributed to the happiness, Agnieszka, Andrea, Danilo, Maria and the other Spanish from the building. We have done many things together, at work and outside, and I can only hope we keep on doing them.

During this years I have spent many evenings training with all the people from Laï-Muoï. Training and learning with you kept me in very good shape mentally and physically and apart from all the fun we have had, you all managed to push me and motivate me and I ended up doing things I had never imagined. Especially I want to thank Nico, I have never met someone with such a good heart and so supportive. Pierre, Maurane, Philippe, you have always been there when I needed help to train for the passage or for the compètes and you have all changed my view on many things and you all taught me french.

During these years I have had all the support from my ICAI friends. Fran, Ana, Dani, Bea, Rodri, Ainhoa, Isa and Breo. We cannot meet as much as I would like, but we have always done our best and I know we will keep on doing it. Thanks for all the support and the laughs. Although I have been far

you have always felt very close.

I cannot forget also my friends from Bokatas, Ceci, Nuria, Paya, Sara, Meg, Dr. Bea, Rocio, Ines, Edu, Bea, Samu, Jorge, Danny, Luis, Amaia. It is difficult to express in words all I want to say but you know how much you mean to me. Thanks for all your support and all the laughs and crazy ideas and plans. Also, thanks for being there all these years, especially since I left. I could not wish for better friends than you guys. I have always felt almost like I was in Madrid with you guys. Monica, after all these years we are still close friends and I can say we literally speak (ir)regularly. Let's keep on sending the voice notes.

Sophia, these years would not have been the same without you. You have changed my life in every aspect and you have made it better than I could ever imagine. You have shown me there is much more to life than I thought. Thank you for all your kindness and your support. There are no bad days when I am with you. And I know one day I'll manage to tell you all about my thesis.

Last but not least I want to thank my sister and my parents, you have always given me everything I needed and you have always been there, both to support me and to make life much better. I can never be too grateful to you.